( )	3
Title(English)	Nonlinear Analysis of Reinforced Concrete Structures Subjected to Seismic Loads By Using Three-dimensional Lattice Model
( )	
Author(English)	Tomohiro MIKI
( )	: ( ), : , : 5740 , :2004 3 26 , : , :
Citation(English)	Degree:Doctor of Engineering, Conferring organization: Tokyo Institute of Technology, Report number: 5740 , Conferred date:2004/3/26, Degree Type:Course doctor, Examiner:
( )	
Type(English)	Doctoral Thesis

NONLINEAR ANALYSIS OF REINFORCED CONCRETE STRUCTURES SUBJECTED TO SEISMIC LOADS BY USING THREE-dimensional LATTICE MODEL

by

Tomohiro Miki

Supervisor: Professor Junichiro Niwa

A thesis submitted to the

Faculty of the Graduate School of the

Tokyo Institute of Technology

in partial fulfillment of the requirements for the degree of

Doctor of Engineering

Department of Civil Engineering

Tokyo Institute of Technology

Tokyo, Japan

February 2004

This thesis entitled

Nonlinear Analysis of Reinforced Concrete Structures Subjected to Seismic Loads

by Using Three-dimensional Lattice Model

written by Tomohiro Miki

has been approved for the Department of Civil Engineering

at Tokyo Institute of Technology.

Supervisor:

Professor Junichiro Niwa

Supervising Committee:

Professor Chitoshi Miki

Professor Kazuhiko Kawashima

Professor Nobuaki Otsuki

Associate Professor Hiroshi Yokota

ABSTRACT

In recent year, the numerical evaluation on the performance of reinforced concrete (RC) structures has been performed in a practical design. The procedure used in the evaluation is founded on the developments of the numerical methods based on concrete mechanics and its application as a nonlinear analytical method. On the other hand, in regions frequently subjected to strong earthquake motion, the structural performance is verified based on the seismic performance of structures during the earthquakes. Hence, the dynamic analysis using ground motion recorded during the earthquake has been performed for the seismic performance evaluation. When the actual structures are subjected to the actual earthquake motion, the structure is subjected to combined loads of bilateral bending, shear, and torsion. These conditions cannot be treated by 2D model in which the assumption of plane stress is utilized. Therefore, 3D model is required to verify the seismic performance of RC structures subjected to multi-directional ground motion. In addition, the 3D analytical method with reduced analytical degrees of freedom, which must consider the complex strain histories, is keenly required for practical purpose. This study aims to enhance the abilities of the conventional 2D lattice model into a 3D nonlinear analytical model. To achieve this objective, this study consists of two conceptual categories. One is the development of 3D lattice model and another is its application to the seismic performance verification for RC structural members.

The 3D lattice model, which is based on the 2D lattice model, is proposed and successfully used in the predication of the cyclic response of RC columns. In the model, the arch action is idealized as a compressive strut that is represented by concrete arch members. In addition, as for the truss action, it is assumed that 3D space comprised of an orthogonal coordinate system is defined by three planes. The configuration of 3D lattice model is verified for the static cyclic analysis of laterally loaded RC columns. The reliability of the model including the post-peak behavior is confirmed.

The basic performance of the 2D lattice model that is the foundation of 3D lattice model is verified through several experiments. The analysis by the 2D static lattice model of RC shear dominated columns is carried out. In addition, the dynamic analysis is carried out for shaking table tests. The seismic performance verifications of RC columns with different amount of transverse reinforcement and carbon fiber reinforced plastic sheet are performed. Through the analytical discussions, the reliability of both 2D static and dynamic lattice models in predicting the nonlinear response of RC columns is clarified. Moreover, the significant improvement in predicting the post-peak response is realized by considering the

buckling behavior of reinforcement as the spatially averaged stress-strain model of reinforcement.   The accuracy of prediction is also improved by considering the pull-out behavior of longitudinal reinforcement at the column-footing connection.   The model using the joint elements in which the strain-slip relationship of reinforcement is incorporated into the analysis.

The 3D static lattice model is verified through the experiments of RC columns subjected to lateral forces from the diagonal direction of a section.   The analysis is also carried out for RC beams with solid and hollow cross sections subjected to pure torsion.   From the analysis, the applicability of the model to the prediction of torsional behavior of RC beams is confirmed.   In order to apply to arbitrary loading condition, the analytical simulation of RC columns with hollow cross section subjected to cyclic loading combined torsion and bending is carried out.   It is confirmed that the 3D lattice model analysis can appropriately predict the 3D response of RC columns subjected to the combined cyclic loading of torsion and bending. In addition, the influence of combination of torsional and flexural deformations on the load carrying capacity and the deformation capacity is clarified.

The analysis by the 3D dynamic lattice model is conducted and verified for the RC columns on the bilateral shaking table tests.   The verification analysis on the seismic performance of RC columns is also performed based on the several actual earthquake motions.   The ability of 3D lattice model analysis in predicting the biaxial behavior of RC columns subjected to the bilateral ground motion is clarified.   In addition, the importance of the appropriate constitutive models of concrete and reinforcement are recognized.   The influence of the buckling of reinforcement on the post-peak response of RC columns as well as the cyclic hysteresis representing the energy dissipation capacity is also demonstrated.

The earthquake damage evaluation for actual rigid-frame RC viaducts during Hyogo-ken Nanbu (Kobe) Earthquake is carried out by using the 3D dynamic lattice model.   The reliability of 3D dynamic lattice model in predicting the structural behavior of RC viaducts is verified.   The influence of vertical loads corresponding to the self-weight on the maximum displacement is clarified.   The results of dynamic analysis and the actual damage features of RC viaducts are compared and the reliability of 3D dynamic lattice model on the evaluation of actual damage of RC viaducts subjected to severe seismic motion is confirmed.

ACKNOWLEDGEMENTS

CONTENTS

1   GENERAL INTRODUCTION

1.1   Background

In recent years, several significant progresses of the analytical technology for concrete structures have been achieved.   The progresses are supported by the developments of numerical methods based on concrete mechanics and its application as nonlinear analytical procedure.   In regions subjected to relatively frequent strong ground shaking, the design procedures of structures should be improved along the cutting edge of concrete technology with adequate achievements.   These procedures may result in comparatively good performance of engineered structures.   Although the design procedures are not universally applicable because of the regional differences in construction styles, structural engineers can learn much by studying such procedures.   For structural design in Japan, the standard specification for seismic performance verification of concrete structures (JSCE 2002) is extensively revised after Hyogo-ken Nanbu Earthquake at 1995.   The updated standard specification is established based on the concept that considerable inelastic deformation of reinforced concrete (RC) structures is possible after the longitudinal reinforcement yields, rather than considering only the elastic behavior of the structures subjected to strong earthquake motions.   Although the structural performance at the inelastic region is often experimentally evaluated, the significant development of the analytical technique motivates the designers to use reliable analytical tools for the purpose of performance evaluation. Consequently, in a practice, the analytical prediction has emerged as a powerful help for predicting the behavior of RC structures.

A series of revisions for the standard specifications has been carried out with respect to the seismic design of RC structures.   In the revisions, the ductility design philosophy is adopted to take into consideration the deformation capacity of RC structures in spite of a criterion for load carrying capacity.   It is also specified that designers must perform the verification through the dynamic analysis for a structure.   In the dynamic analysis, since the number of available ground motion recorded near the construction site is generally limited, the input acceleration should be supplemented using the ground motion recorded at other regions having similar geometrical, seismological, and geophysical conditions.   Structural engineers

are concerned mainly with the local (short-period) effect of large earthquake, where the ground motions are intense enough to cause structural damage. These so-called strong-motion earthquakes are too violent to be recorded by the very sensitive seismographs typically used by seismologists. Hence, it is necessary to develop the special types of strong-motion seismographs. Although the prediction of input ground motion seems to be in the field of empirical engineering, in recent year, the estimation of earthquake motion is possible by the contribution of earthquake engineering. Consequently, the dynamic analysis using input ground motion recorded during actual earthquakes can be performed to evaluate the seismic performance of RC structures. The information of fracture mechanism for RC structural members at the nonlinear stage is an important criterion with respect to the seismic evaluation in the performance-based design.

The response of RC columns obtained from the dynamic analysis is quite useful to estimate the state of deformation including the maximum and residual displacements from the viewpoint of the restoration or rehabilitation after earthquake. In the practice, the structural response is considered by analyzing along the principal axes of structural system. However, the actual ground motion will apply to actual three-dimensional (3D) structures from different directions of its principal axes. As a result, the behavior of structures along each axis may be underestimated. In these loading conditions, the structure is subjected to combined loads of bilateral bending, shear, and torsion. Consequently, the behavior becomes more complex than that under the uniaxial motion. 3D analysis is indispensable to clarify the seismic performance of RC columns subjected to multi-directional ground motion. In addition, the efficient and simple 3D numerical tool with the objective outcomes is required to properly evaluate the seismic performance of RC columns.

At present, the research for advanced analytical technology has been presented, in which 3D constitutive model with a special attention to cracking of concrete can be applied to nonlinear finite element analysis using the solid element (Hauke et al. 2000, Maekawa et al. 2001, Tsuchiya et al. 2002). 3D FE solid element analysis with proper constitutive models can reliably capture the response of any RC structures. However, it is very complicated. The main disadvantage of 3D FE solid element analysis lies in the fact that the computation takes very long time and requires powerful computation facility due to large number of degrees of freedom is significantly huge. In contrast, the tendency of designers is toward looking for more efficient and easier ways to tackle the confronted difficulties.

Hence, in the practice, the dynamic analysis is generally performed based on the frame model or the models using fiber technique, which can simulate the mechanical behavior of RC columns even in the nonlinear response region. As for the frame model, such as the Takeda
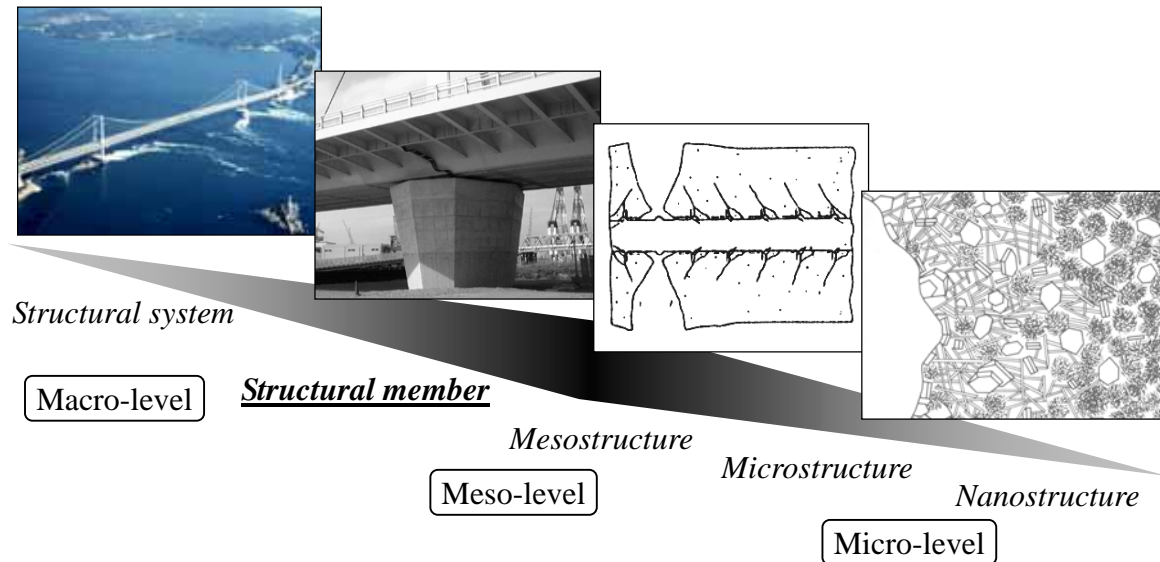
Figure 1.1   Scale of modeling level

model (Takeda et al. 1970), a RC structure is modeled into some individual RC structural members incorporated their restoring characteristics.   On the other hand, as for the model using fiber technique (Dhakal 2000, Spacone et al. 1996a, 1996b), a RC member is discretized longitudinally into several layers and each of which the layer is subdivided into some fiber elements.   Each element consists of uniaxial fibers so that its stress-strain relationship is properly incorporated.   These are recognized as a highly practical method to evaluate the inelastic deformation behavior of flexural RC structures.   However, it is necessary to idealize the both location and size of the plastic hinge region, which should be incorporated into the appropriate fiber elements.   Moreover, the shortcoming of these models is the difficulty in estimating behavior in the post-peak range, particularly when a RC member fails in shear.   In these models, the shear deformation and the changing of torsional stiffness cannot directly be predicted because the in-plane deformation is unconsidered.   Hence, a 3D analytical method with reduced degrees of freedom, which can take into consideration the complex strain-stress histories as well as the nonlinearity of a structure, is keenly required.

1.2   Literature Review

1.2.1   Nonlinear analysis of concrete structures

In the structural analysis to evaluate the performance of concrete structures, a target structure has to be discretized and averaged for simplicity.   With this modeling procedure, spatially averaged smeared models are successfully used in the finite element analysis.   Here, the designer should carefully perform the modeling of concrete and specify the level (scale) of

modeling since concrete can be treated as homogeneous material and sometimes needs to be considered as heterogeneous one. This matter is depending on the averaged size in the modeling. In the analytical modeling, generally, the scale of structure is conceptually divided into three categories, micro-level, meso-level, and macro-level as abstractly shown in **Figure 1.1**. Several modeling methods of concrete structures with respect to the applied constitutive models and the modeling level are briefly expressed below.

Fiber model

The nonlinear analysis using a fiber technique is generally used in the practice. In the fiber technique, a structural member is discretized both longitudinally and transversely at the cross-sectional level into finite regions as shown in **Figure 1.2**. If only small deformations take place and plane sections remain plane, the strain at each fiber can be computed from the curvatures and the distance of the fiber from the neutral axis of a cross-section. The overall response of each element is the integrated response of these fibers and the overall response of the member comprises of all the element responses.

Dhakal et al. (2000, 2002a, 2002b) has proposed the enhanced fiber model that took into account the inelastic material mechanism such as spalling of cover concrete and buckling of longitudinal reinforcement as specially averaged material models. In this research, a method to evaluate the stable buckling length of longitudinal reinforcement inside a RC member was proposed based on the energy balance. The enhanced fiber models were verified for various types of RC flexural members. The comparison of the analytical results using enhanced fiber models with various experimental results proved the reliability of proposed models in predicting the post-peak cyclic behavior and seismic response of RC columns. The degradation of post-peak response due to material and geometrical nonlinearities such as
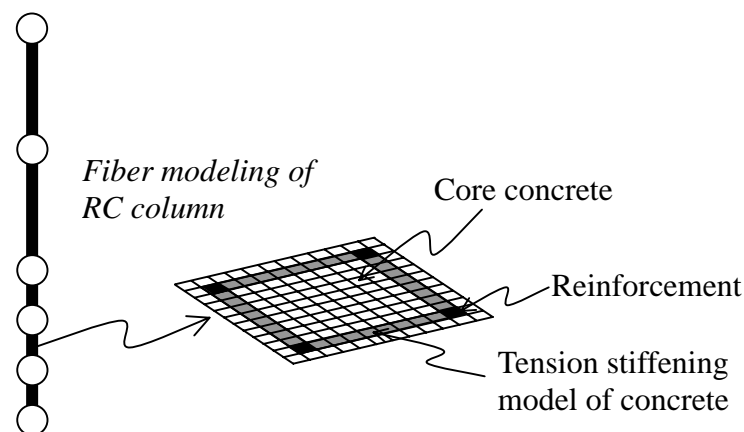
Figure 1.2 Subdivision of cross section into fibers (concrete and reinforcement)

spalling of cover concrete and buckling of longitudinal reinforcement was able to be captured in the analysis as well. However, the fiber model is one of the integration methods assuming the small deformation takes place and plane sections remain plane. This assumption may be unrealistic when a RC member is subjected to large deformation (Ichinose et al. 2001, Kinugasa and Nomura 2000). In addition, the torsional or shear behavior of RC members cannot be predicted reliably due to the simplicity of single degree of freedom in the longitudinal direction.

Nakamura et al. (Nakamura et al. 2003, Yamamoto et al. 2003) have presented the torsional behavior caused by shifting of shear center in a cross section of RC members. This phenomenon is due to the unsymmetrical behavior resulting in the material nonlinearity of concrete and reinforcement even if there is no external torsion. In this study, it is interesting to analyze this behavior by frame elements with the fiber technique based on the thin-walled bending beam theory.

Lattice type model at meso-level

The lattice type fracture model for concrete material has been proposed by Bažant and Tabbara (1990), and Lilliu and van Mier (2002), in which the model allowed a straightforward implementation of the material heterogeneity at the meso-level (**Figure 1.3**). This lattice models assumes usually a linear-elastic material constitutive relationship in the small size element. Based on linear-elastic fracture mechanics, the crack propagation along the interface and the matrix can be described. The numerical results showed that the model was able to reproduce the fracture processes observed in the real physical experiments. In the

(a) Lattice mesh on the generated particle structure

(b) Distinction of lattice mesh between aggregate, matrix, and bond phases
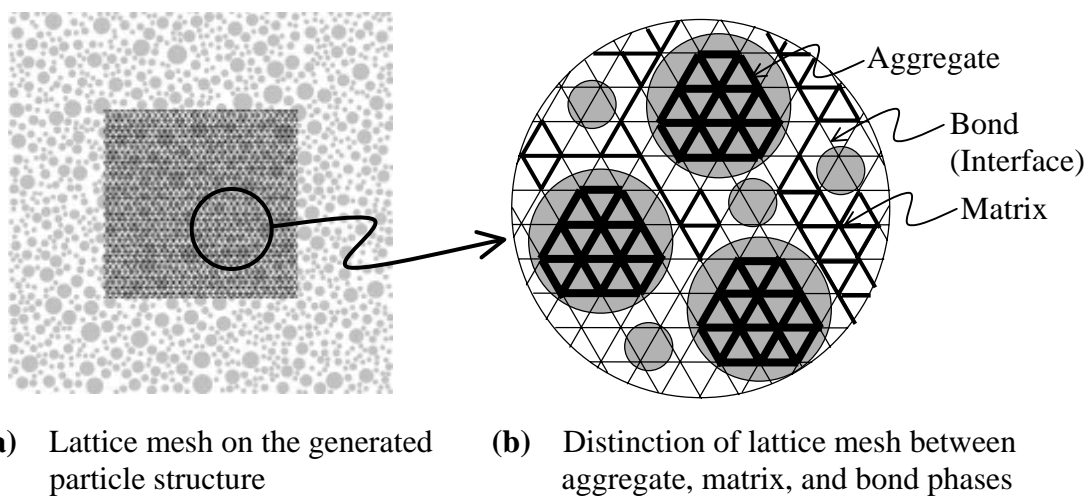
Figure 1.3 Lattice type model for concrete at meso level (Lilliu and van Mier 2003)

load-displacement relationship, the de-bonding corresponded to nonlinear pre-peak behavior, while the crack formation and propagation in the matrix corresponded to the softening branch. The disadvantage of this model is that initial cracks must be defined at the beginning of the analysis, since no crack criterion is included. Due to the enormous increase in the number of degrees of freedom, the computation time is getting large. In addition, 3D lattice simulations with relatively fine meshes will be practically impossible with standard software in which the model has been implemented in a computing code for the parallel computing (Lilliu and van Mier 2003).

Rigid-Body-Spring Model (*RBSM*)

A spring network model has been developed by Kawai (1978) to study the crack propagation in RC structures. This approach is effective to implement the energy balance criterion for crack propagation, similar to those developed by Hillerborg et al. (1976) and Bažant and Oh (1983) for smeared cracking. A rigid-body-spring network is elastically uniform during uniform straining. The provided material domain is discretized by the Voronoi diagram and the nuclei of Voronoi cells are used to define the computational degrees of freedom. The Voronoi diagrams, based on a random distribution of nodal points, are used to model the materials into an assembly of rigid particles interconnected along their boundaries through flexible interfaces. The fracture initiation and propagation are modeled by either removing spring or completely degrading their elastic properties according to simple breaking rules. This approach is classified as a discrete element method, even though neighbor connectivity is defined and there is no special emphasis placed on contact modeling, in contrast to the distinct element method (Hakuno et al. 1993, Meguro et al. 1994) and the discontinuous deformation analysis method (Shi et al. 1989).

Bolander et al. (1998, 1999) have demonstrated the applicability of the rigid-body-spring network approach and the need for a fracture mechanics to model the cracking through analyses of scaled models of T-shape columns and RC beams. Although the local constituents may obey brittle fracture laws, a fine discretization of material disorder allows toughening mechanisms, such as a bridging at the crack face, to develop the quasi-brittle composite response. Saito et al. (1999) have also presented that the analyses of RC structures showed reasonable results in the load-displacement response and the crack propagation. The analytical application of RBSM to large-scale T-shape RC columns was demonstrated as shown in **Figure 1.4**. The model can predict not only flexural failure but also shear failure of RC beams/columns. Significant scatter in the numerically predicted peak loads indicated the mesh dependency problems. In the analysis, it is confirmed that the special attention must be given to the mesh design in the notch tip region.

(a) Specimen dimensions

(b) Numerical model of the column

(c) Crack patterns
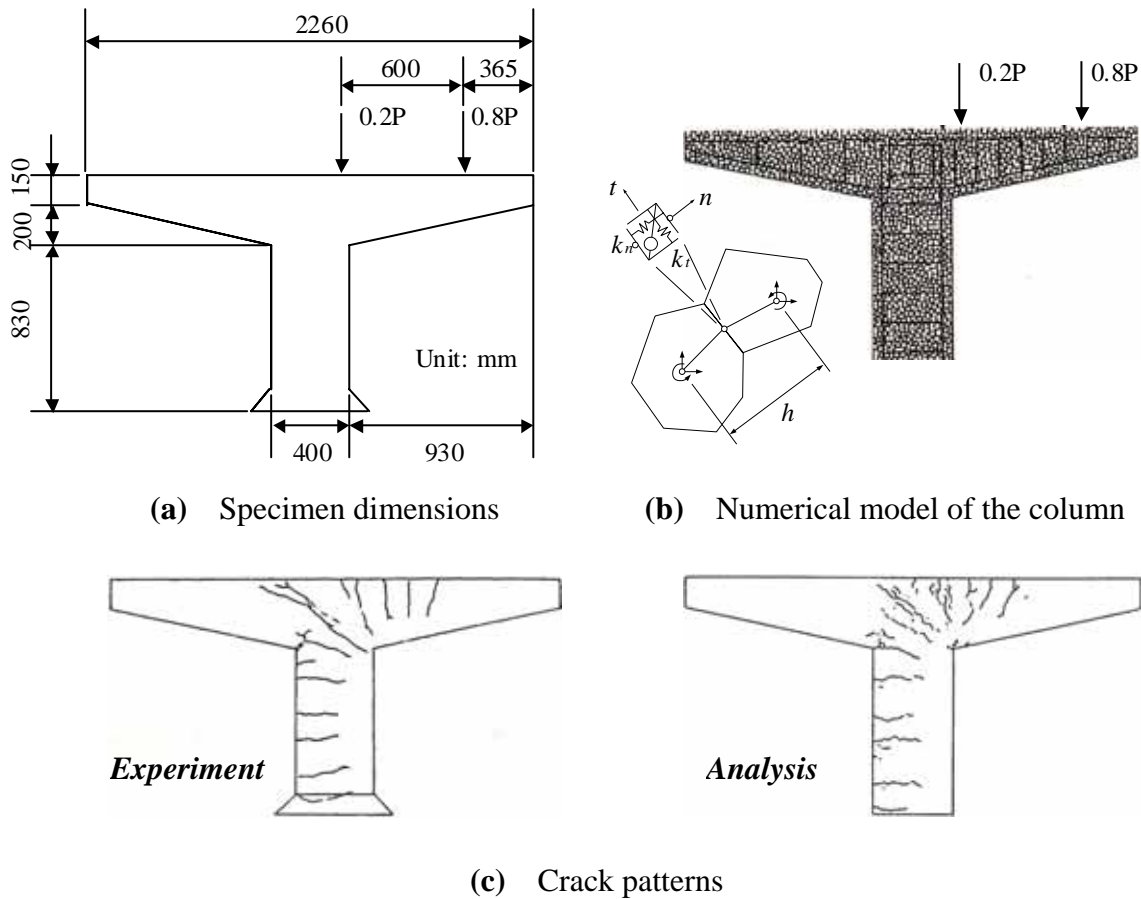
Figure 1.4 Applications of RBSM to T-shape RC columns subjected to eccentric loading (Saito and Hikosaka 1999)

In-plain constitutive law of RC with multi-directional cracks

Maekawa et al. (2001) have developed an in-plane spatially averaged constitutive model with up to four-way cracking. The compression, tension, and shear stress-strain relationships were applied on a couple of quasi-orthogonal cracks, using an active crack coordinate concept. In this concept, the crack that has the strongest nonlinearity due to the widely opened crack is selected as an active crack in which the compressive stress was carried across the crack surface. The other cracks are dormant that slightly contributes to the nonlinear stress-strain relationship. The active crack approach is easy to use and successfully applied to the quasi-orthogonal two-way cracking model. The similar concept can be applied to simulate the RC structural behavior with four-way cracking model. In a RC element, the average strain on global coordinates is converted to a local one based on the active coordinate. The stress transfers along these two active cracks are computed by the local constitutive models, including a coupled compression-tension model and a shear transfer model. To verify this

mode, the experiments for RC plates with multidirectional cracks were carried out. In this study, the dynamic nonlinear FE analysis was also carried out for seismic performance evaluation of RC structures with multi-directional cracks. From the analytical results, it was noticed that the modeling of spalling of cover concrete and buckling of longitudinal reinforcement was of importance to evaluate the deformation capacity of RC structures. For wall-type structures, the post-peak analysis showed the reasonable prediction with the softening compression modeling. Here, fixed crack approach was used in computation.

Lattice equivalent continuum model

Tanabe et al. (Tanabe and Ishtiaq 2001, Itoh and Tanabe 2001) have presented that reinforced concrete constitutive equations based on the concept of equivalent continua for a lattice system were formulated and investigated for their applicability to the development of more robust reinforced concrete constitutive equations. In the model, a RC member is discrete to the following three lattice systems; equivalent concrete lattice, equivalent reinforcement lattice, and equivalent concrete shear lattice. The derivation of constitutive equations is especially performed with respect to cracked concrete and reinforcement. The finite element for the continua of multi-directional cracked concrete can be represented by using the combination of uniaxial constitutive models. The analytical results showed the acceptable agreement with the experimental results of the UCSD columns under reversed cyclic loading (Itoh and Tanabe 2001).

Truss model and truss-arch actions

The truss model of Ritter (1899) and Mörsch (1903), also called as the strut-and-tie model, has been widely used in successively refined versions to analyze the failure of beams in diagonal shear (Schlaich et al. 1987). These models are proposed as a simple truss model to visualize the internal forces in a cracked beam. The trajectories of individual stress fields in a structure and the associated forces from the reinforcement are condensed. Their curvature is idealized to form the tension and compression members in a strut-and-tie model. Alternatively, the internal flow of forces can be traced and defined by the load path method. These methods are highly practical. However, the main target is the prediction of load carrying capacity or the clarification for the shear carrying mechanism of RC structural members. Consequently, the information about the deformation of the structural members cannot be predicted in the analysis.

1.2.2 3D analytical procedures

A few applications involving full 3D modeling of structural geometry, loading patterns, stress states, and strain distribution have emerged in the literature. In most of the analytical research, the model that is originally developed as a 2D model for simplicity is verified for structural performance evaluation of RC structures, in which a plane stress assumption is applicable. After the confirmation of its validity, the 2D model is extended into 3D analytical procedure. Here, 3D problems are classified into two large categories. One is a problem of structures consisting of the structural members that must be treated as 3D due to the geometrical shape and the loading condition, in which the plane stress assumption can be used with good justification. The other is a problem for 3D stress field that must to be expressed by means of full 3D solid elements. The research about 3D nonlinear analysis makes clear its advantages and disadvantages as follows.

Fiber model

Spacone et al. (1996a, 1996b) have presented the model by means of flexibility-based formulations that permitted a more accurate description of the force distribution within the element. The formulation of a fiber beam-column element for nonlinear static and dynamic analyses of RC frames has been proposed. In addition, the application of the proposed element to the simulation of hysteretic histories has been demonstrated. In the model, it is assumed that a plane section remains plane and normal to the longitudinal axis. In addition, the effects of shear and bond-slip are presently neglected. The difficulty with flexibility-based models is their implementation in a finite element program. The computing programs are developed based on the stiffness method of structural analysis and the subroutines derive the element forces and stiffness for given nodal displacement. The flexibility-based model offers a clear and reliable procedure for their implementation in a general purpose of finite element analysis. From this research, it has been confirmed that the results by the proposed fiber model show the good agreement with the experimental results of the pseudo-dynamic tests, especially for cyclic behavior inducing average damage in the structural members.

3D constitutive law of RC with multi-directional cracks

Hauke and Maekawa (2000) have presented a 3D constitutive model for nonlinear finite element analysis of RC member with special attention to cracking of concrete. In this research, post-cracking formulations derived from uniaxial tension tests are generalized into spatially arbitrarily inclined cracks in multiple directions. The anisotropic concrete tension

fracturing and reinforcement yield levels of the spatially averaged RC model in association with a 3D RC-zoning concept have been discussed. The proposed model was verified by numerically simulating inherently 3D shear failure of RC members subjected to torsion and RC short columns loaded in multi-directional shear. The proposed framework of 3D nonlinear analysis was successfully applied to the numerical response prediction of hollow and solid torsional members with low and high reinforcement relationships. For short RC columns under multi-axial loading, the 3D inclined variable shear plane and its associated shear failure were simulated. Using the Virtual Reality Modeling Language, Takahashi and Maekawa (1998) provided a new opportunity for looking inside cracked concrete. Consequently, the fully 3D inclined shear and crack planes can be clearly identified by post-processing works.

Finite element analysis with solid elements

Yonezawa and Noguchi (1995) have verified the newly developed connection of steel beam-RC concrete using the ABAQUS software and the user subroutines for constitutive model of concrete. The details of joints and the arrangement of reinforcement in RC columns were focused on. It is necessary to consider the internal stress transfer mechanisms based on the analytical study to investigate the shear resisting mechanism of joint. In the analysis, the stress transfer mechanisms should to be treated as a 3D problem. The damage evaluation of concrete and reinforcement to establish the rational design procedure for performance evaluation of RC structures has been expressed.

In addition, Noguchi et al. (2001, 2002) have conducted the 3D FE analysis for the performance verification of the steel beam-RC column joints. For the complexity of the joint region, the high-resolution numerical modeling will be required to complement experimental results and understand the joint behavior. These analyses were carried out using the DIANA. Since the development of computing technology has been achieved, the nonlinear 3D analysis using solid elements could be performed. Moreover, these analytical procedures have extended into the dynamic analysis. An example of FE mesh of RC shear wall on the shaking table tests (Noguchi et al. 2003) is shown in **Figure 1.5**.

Although these analyses can appropriately evaluate the 3D behavior of RC structural members at the structural and material levels, the computer to perform 3D FE analysis cannot be used in the practice because of the huge degrees of freedom. Hence, the lattice model (Niwa 1995, Miki et al. 2003a, 2003b) is used as an analytical model satisfying two requirements: the short computing time due to the decrease in the degrees of freedom and accurate prediction of RC structural behavior considering the material nonlinearity.
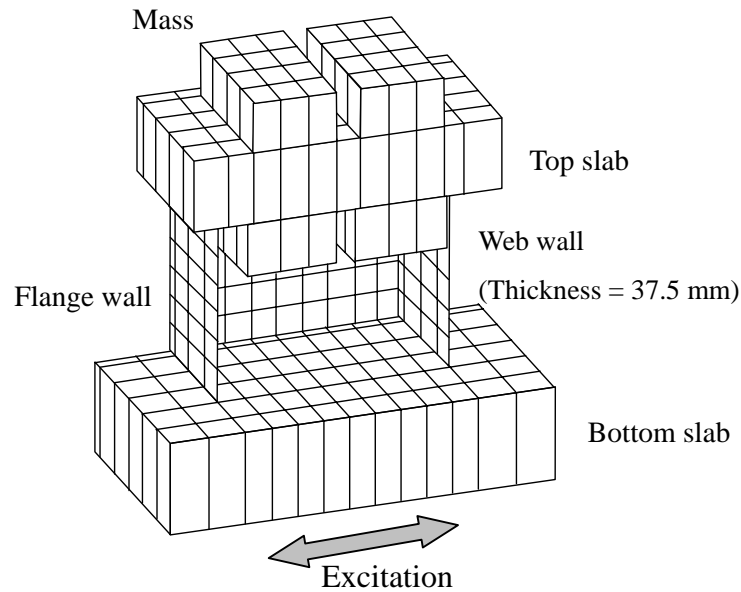
Figure 1.5   FE analytical mesh for RC shear wall (Noguchi et al. 2003)

1.2.3   Importance of taking post-peak behavior into consideration

Structures expected to be subjected to ground motion are designed according to the ductility design approach and for such structures, the post-peak behavior should be evaluated to understand its structural performance.   Moreover, RC columns subjected to large ground motion experience high deformation and the load-displacement relationship reaches the post-peak range.   Since the reliability of analytical prediction of post-peak behavior directly influences on the seismic performance of designed structures, the accurate prediction of the post-peak response is required.

In the experiments for RC columns conducted by Watanabe et al. (2001), the considerable softening phenomenon was observed in the load-displacement relationship at the large deformation region.   In addition, it has been realized (Suda et al. 1994) that this inelastic softening behavior was mainly due to the spalling of cover concrete and buckling of longitudinal reinforcement.   These mechanisms significantly influence on the deformation capacity of the structure.

Here, the effect of post-peak softening behavior on the evaluation of deformation capacity and ductility is discussed based on the ultimate displacement capacity definition of the JSCE specification (JSCE 2002).   As shown in **Figure 1.6**, the additional softening behavior due to
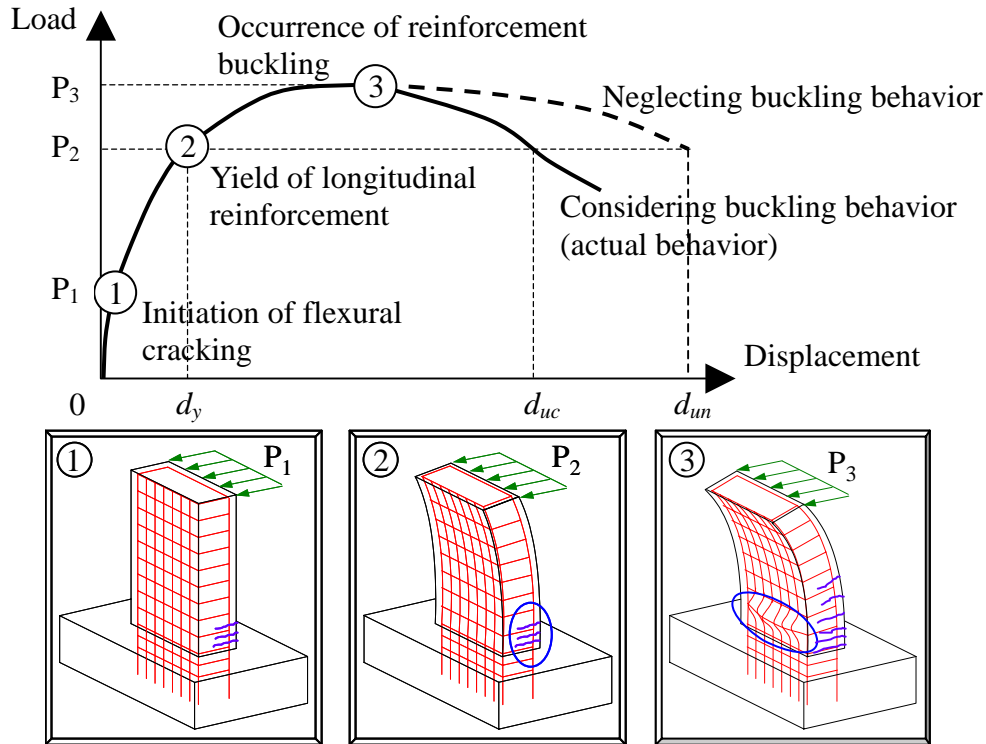
Figure 1.6   Load-displacement relationship of a RC column

the buckling of longitudinal reinforcement causes significant difference in the ultimate displacement.   Consequently, if these inelastic material mechanisms are overlooked in the analysis, the deformation capacity is overestimated and the designed structure cannot fulfill the performance requirement during the actual loading.   Hence, the significant attention for the buckling behavior of longitudinal reinforcement should be paid in the analysis.

1.2.4   Buckling model of reinforcement

Many experimental and numerical researches have been conducted.   Suda et al. (1994) experimentally verified the influence of buckling behavior of longitudinal reinforcement on the post-peak cyclic response of RC columns.   A special device, so called a small load cell for reinforcement, was developed to measure the post-yielding stress of longitudinal reinforcement.   Based on the experimental results, the empirical equations were proposed for the average stress-strain relationship of longitudinal reinforcement including buckling.   The approach seems suitable as the average response of reinforcement inside a RC member that included the effect of lateral ties and cover concrete.   However, the experiments covered few specimens with limited range of properties and arrangement of reinforcement.   Therefore, the empirical equations based on these limited data might not be general.

Most of the studies for the buckling of reinforcement were based on the experimental data with limited ranges of material properties, and in some cases, the boundary conditions were hardly reproduced. In the numerical investigation, Mau and El-Mabsout (1989) have performed a finite element analysis to study the average stress-strain behavior of reinforcement in compression including buckling. The analytical investigation was carried out for various length of reinforcement to its diameter ratios. It was found that the buckling took place after compression yielding in the cross section and the post-buckling response showed the softening of average stress. The averaged compressive response was found to depend on the slenderness ratio. It was also confirmed that the effect of buckling slightly recognized when the slenderness ratio was less than or equal to five. However, in their study, the average stress-strain relationship in compression was not formulated quantitatively.

Asazu et al. (2001) have formulated the relationship between the plastic hinge region and the buckling length based on the analytical results. The analysis was performed based on the individual longitudinal reinforcements modeled by a beam element with nonlinear springs of transverse reinforcement and cover concrete. The targets were circular RC columns with rectangular cross section. It was found that the plastic hinge was able to predict using the buckling length depending on the cross-sectional shape.

Dhakal et al. (2002a) have proposed a simple method to predict the buckling length of longitudinal reinforcement and the spalling of cover concrete in a RC member. The buckling behavior was proposed based on the microanalyses and verified for the several experimental tests on reinforcing bars subjected to monotonic and cyclic loading (Monti and Nuti 1992). In the analysis, the stability analysis was conducted giving due consideration to both geometrical and mechanical properties of the longitudinal reinforcement and the lateral ties. The analytical prediction considering spalling and buckling showed the good agreement with the experimental results. In addition, it was clarified that the average compressive stress-strain relationship including cyclic paths (Menegotto and Pinto 1973) and the softening in the post-buckling range could be described in terms of the product of square root of yield strength and the slenderness ratio of the reinforcement (Dhakal et al. 2002b).

Moreover, Tanoue et al. (2002) have presented the average stress-strain relationship based on their experimental and analytical observations. In the model, the stable shape is assumed for the straight rigid plastic column element having one plastic hinge. The simplified averaged stress-strain relationship considering the residual stress and the initial buckling stress was proposed. These methods are convenient to use in the model with somewhat large size elements because the spatially averaged stress-averaged strain relationship of buckling behavior of reinforcement is adopted.

1.3   Objectives and Research Significance

The damaging potential of strong earthquakes is accepted as an underlying premise by most design codes.   The standard specification of JSCE, for example, adopts the philosophy that structural damage such as the yielding of longitudinal reinforcement is acceptable during rare huge earthquakes but that collapse is not acceptable in any event.   Moreover, the subjective nature of observations of seismic performance should be immediately clear.   In order to obtain good performance of structures during earthquakes, it is necessary to analyze thoroughly the dynamic characteristics of the actual three-dimensional (3D) structural system.   In the analysis, designers must perform the verification using the dynamic analysis taking into account the material nonlinearity of concrete and reinforcement.

The response of RC columns obtained from the dynamic analysis is beneficial to estimate not only the behavior of RC columns during earthquake but also the state of deformation that includes the maximum displacement and the residual displacement.   In the practical design, the structural response is considered by analyzing along the principal axis of a structural system.   However, the actual ground motion will probably apply to actual 3D structures from different directions of its principal axis, and consequently the behavior of structures becomes more complex than one with uniaxial motion.   These loading conditions cannot be treated by 2D models in which the state of plane stress is assumed.   Therefore, 3D analysis is indispensable to verify the seismic performance of RC structures subjected to multi-directional ground motion.   In addition, the efficient and simple 3D numerical tool that must be objective is necessary to properly evaluate the seismic performance of RC structures.

The main objectives of this thesis are to enhance the capabilities of the 2D lattice model (Niwa et al. 1995) to the accurate 3D nonlinear analytical model.   In order to achieve these objectives, the thesis consists of two conceptual categories.   One is the development of the 3D lattice model and another is its application to the structural performance verification for RC structures.

The lattice model offers reasonable prediction of the shear carrying capacity of RC structural members, which is a significant advance from analytical methods based on fiber techniques. Moreover, since the lattice model discretized a RC structural member into truss elements, internal stress flows can easily be determined.   From an understanding of the internal resistance mechanism of RC structural members, the accuracy of analytical results can be evaluated.   In this study, the 3D dynamic lattice model analysis considering the buckling behavior of longitudinal reinforcement is carried out to predict the behavior of RC structures subjected to earthquake motion.

1.4   Contents of the Thesis

The flow of this thesis is shown in **Figure 1.7**.   The thesis conceptually consists of two parts. The first part is related to the development of 3D lattice model based on the concept of the 2D lattice model that is verified its performance through the comparisons with several experimental tests.   The second part explains the application of 3D lattice model analysis to the structural performance verification for RC structures.   The contents of the thesis are organized as follows.

Chapter 2 expresses the outlines of the 2D lattice model.   A brief review of the 2D lattice model in the literature is made and the determination of components of the 2D lattice model and the constitutive models of concrete and reinforcement are explained.   The models of buckling of longitudinal reinforcement and the pull-out of longitudinal reinforcement from the footing are newly introduced, of which features are explained.

The newly developed analytical method using the 3D lattice model is proposed in chapter 3. The determination for the location and the cross-sectional area of arch and truss members are explained.   The value of t representing a proportion of the arch part to the overall cross section of the member is updated to apply to the 3D lattice model.   In addition, the enhanced 3D lattice model is verified for uniaxial static cyclic loading.   The calibration of 3D lattice model analysis is conducted for ensuring its validity comparison with the results using the 2D lattice model analysis.

Chapter 4 discusses the applicability of 2D lattice model analysis.   The member level verification is performed for not only flexural dominated RC columns and but also shear dominated RC columns.   The buckling behavior of reinforcement and the pullout behavior of longitudinal reinforcement from the footing are considered in the analysis.   In addition, the 2D lattice model is used for the detailed analytical investigation of the RC columns strengthened by carbon fiber reinforced plastic sheet (CFS).   The applicability of 2D lattice model is confirmed by simulating the influence of transverse reinforcement and CFS on the seismic performance of RC columns.

Based on the applicability of the 2D lattice model, the 3D static lattice model is verified in chapter 5.   The performance of 3D static lattice model is confirmed by comparing the experimental results of RC columns subjected to uniaxial loading from diagonal direction of a section.   In addition, the 3D lattice model is verified for the results of pure torsional loading tests and tests under the combined loads of torsion and bending.

Moreover, in chapter 6, the applicability of 3D lattice model is extended to the dynamic analytical procedure.   The performance of 3D dynamic lattice model is confirmed by comparing with the experimental results of bilateral shaking table tests of large-scale RC columns.   The simulations for RC columns subjected to 3D multi-directional earthquake motion are also conducted.   In addition, the 3D lattice model is used for the seismic performance evaluation of RC columns regarding with the influence of characteristics of earthquake motions.   In the simulation, several strong motions recorded in Japan are used for the verification.

Chapter 7 presents the damage analysis for actual RC viaduct.   The earthquake damage evaluation for actual RC viaducts during Hyogo-ken Nanbu Earthquake is performed by the 3D dynamic lattice model analysis.   In addition, the comparison between the actual damage conditions and predictions is conducted.

Finally, chapter 8 includes the conclusions of the study and the recommendations for future research.

1.5   Targets of the Thesis

The targets of this thesis are summarized in **Table 1.1**.   The targets are including RC columns, RC beams, and RC viaducts with the rectangular or square cross section.   They are not including the circler cross sectional members.

Chapter 1   General Introduction
Background and objectives

DEVELOPMENT OF 3D LATTICE MODEL

Chapter 2
Analytical Model

➢ Outlines of 2D lattice model
➢ Modeling of each element
➢ Material models
➢ Nonlinear analytical procedure

Chapter 3
Development of 3D Lattice Model

➢ Configurations of 3D lattice model
➢ Determination of value of t
➢ Verification of 3D lattice model using results of 2D analysis

Chapter 4
Applications of 2D Lattice Model

➢ Shear analysis of RC columns
➢ Analysis considering buckling of reinforcement
➢ Analysis considering pull-out of reinforcement
➢ Dynamic analysis for shaking table tests

APPLICATION OF 3D LATTICE MODEL AT STRUCTURAL MEMBER LEVEL

Chapter 5
3D Static Lattice Model

➢ Static cyclic analysis for RC columns
➢ Torsional analysis for RC beams
➢ Analysis of RC columns subjected to combined loads of torsion and bending

Chapter 6
3D Dynamic Lattice Model

➢ Dynamic analysis for bilateral shaking table test
➢ Simulation of RC columns under 3D loading
➢ Dynamic analysis using several motions

APPLICATION OF 3D LATTICE MODEL AT STRUCTURE LEVEL

Chapter 7   Damage Analysis of Actual RC Viaducts

➢ Influence of vertical loads
➢ Influence of seismic bilateral loads

Chapter 8   General Conclusions

Figure 1.7   Flow of this thesis

17

Table 1.1 Targets of the thesis

ID	Cross section mm×mm	d mm	a mm	a/d	Grade	f_y MPa	p_s %	Grade	f_{wy} MPa	r_w %	f_c' MPa	Loading condition	Ref.
1	400 × 400	360	1245	3.5	SD295 D13	363	1.58	SD295 D6	368	0.23	35.7	Static	4.2
R–1 R–3 R–5	410 × 610	572	2440 2440 1830	4.3 4.3 3.2	Grade40	317 469 469	2.5	Grade60	360 324 324	0.06	37.9 34.1 32.7	Static	4.3
1, 2, 3 5, 6, 8	450 × 300	265	1500	5.7	SD345 D13	380 390	2.38	SD295 D6	360 340	0.05	27.0 32.0	Static Pseudo-dynamic	4.4
A series, K1 (A11)	400 × 400 (500 × 500)	360 (460)	1150	3.2 2.5	D13 D16 D19	358 ~ 397	1.27 ~ 2.87	D13	358 ~ 397	0.45 ~ 1.27	19.4 ~ 30.9	Static	4.5
A, B, C	800 × 400	350	2265	6.5	SD295A D13	357	0.87	SR235 φ9	319	0.08	27.6	Dynamic	4.6
r_w= 0.00 ~ 0.40	410 × 610	572	2574	4.5	Grade40	317	2.5	Grade60	360	0.00 ~ 0.40	37.9	Dynamic	4.7
A ~ F	450 × 300	265	1500	5.7	SD345 D13	380	2.38	SD295 D6	360	0.06	27.0	Dynamic actual motion	4.8
P–10 P–33 P–34	500 × 500	465	2500	5.4	SD295A D13	308	2.03	SR235 φ9	272	0.10	31.3 39.7 39.7	Static bilateral	5.2
B1~ 6	254 × 381	362	1346	3.7	# 4 ~ # 9	324	0.53 ~ 2.67	# 4	325	0.54 ~ 2.61	27.6 ~ 30.5	Static torsion	5.3
II–1~9	400 × 400 (Hollow section)	t = 60, 80, 120	1000	2.7	SD295 D10	369	0.35 ~ 1.39	SD295 D10	369	0.35 ~ 1.38	22.8 ~ 29.7	Static torsion	5.3
No.1 No.14	600 × 600 (Hollow section)	t = 100	3000	5.4	D6	320	2.04	D4	397	0.36	38.0 ~ 42.0	Static torsion bending	5.3
No.1 No.2	600 × 600	560	3000	5.4	SD295A D10	383	0.95	SD295A D6	350	0.14	34.1	Dynamic bilateral	6.2
$\theta = 0° ~ 90°$	450 × 300	265	1500	5.7	SD345 D13	380	2.38	SD295 D6	360	0.06	27.0	Dynamic diagonal	6.3
1	450 × 300	265	1500	5.7	SD345 D13	380	2.38	SD295 D6	360	0.06	27.0	Dynamic 3D motion	6.3
1 ~ 5	600 × 600	560	3000	5.4	SD295A D10	383	0.95	SD295A D6	350	0.14	34.1	Dynamic 3D actual motion	6.4
Shimokema R5	900 × 900 700 × 1100	840 1040	5250 4150 7100 4500	6.3 4.9 9.8 4.3	D32	349	2.16 2.16 2.01 2.58	D16 φ9	296	0.05 0.09 0.76 0.57	31.7	Dynamic actual motion	7.2
Hansui R5	900 × 900 700 × 1100	840 1040	5000 4000 7100 4500	6.0 4.9 9.8 4.3	D32	322	2.74 2.74 2.01 2.48	D16 φ9	263	0.05 0.09 0.76 0.57	29.1	Dynamic actual motion	7.2

Note; d: effective depth of cross section, a: shear span, f_y: yield strength of longitudinal reinforcement, p_s: longitudinal reinforcement ratio, f_{wy}: yield strength of transverse reinforcement, r_w: transverse reinforcement ratio, f_c': standard cylindrical compressive strength of concrete

$$p_s = \frac{\sum A_{sl}}{b \cdot h}, \quad r_w = \frac{A_{st}}{b \cdot s}$$

where, A_{sl}: cross-sectional area of a longitudinal reinforcement, A_{st}: cross-sectional area of a couple of transverse reinforcement, b: width of cross section, h: over all depth of cross section, s: spacing of transverse reinforcement

References in Chapter 1

[1]   Asazu, N., Unjoh, S., Hoshikuma, J., and Kondoh, M. (2001): Plastic Hinge Length of Reinforced Concrete Columns Based on the Buckling Characteristics of Longitudinal Reinforcement, *Journal of Materials, Concrete Structures and Pavements*, JSCE, No.682/I-56, pp.177-194, July. (in Japanese)

[2]   Bažant, Z. P. and Tabbara, M. R. (1990): Random Particle Model for Fracture of Aggregate or Fiber Composite, *Journal of Engineering Mechanics*, ASCE, Vol.116, No.8, pp.1686-1705, August.

[3]   Bažant, Z. P. and Oh, B. H. (1983): Crack Band Theory for Fracture of Concrete, *Materials and Structures*, RILEM, Vol.16, No.93, pp.155-177, May-June.

[4]   Bolander, J. E. and Saito, S. (1998): Fracture Analyses using Spring Networks with Random Geometry, *Engineering Fracture Mechanics*, Vol.61, Issues 5-6, pp. 569-591, November.

[5]   Bolander, J. E. and Le, B. D. (1999): Modeling Crack Development in Reinforced Concrete Structures under Service Loading, *Construction and Building Materials*, Vol. 13, Issues 1-2, pp. 23-31, March.

[6]   Dhakal, R. P. (2000): *Enhanced Fiber Model in Highly Inelastic Range and Seismic Performance Assessment of Reinforced Concrete*, Doctoral thesis, The University of Tokyo, September.

[7]   Dhakal, R. P. and Maekawa, K. (2002a): Modeling for Postyield Buckling of Reinforcement, *Journal of Structural Engineering*, ASCE, Vol.128, No.9, pp.1139-1147, September.

[8]   Dhakal, R. P. and Maekawa, K. (2002b): Reinforcement Stability and Fracture of Cover Concrete in Reinforced Concrete Members, *Journal of Structural Engineering*, ASCE, Vol.128, No.10, pp.1253-1262, October.

[9]   Maekawa, K., Fukuura, N., and An. X. (2001): 2D and 3D Multi-directional Cracked Concrete Model under Reversed Cyclic Stresses, *Modeling of Inelastic Behavior of RC Structures Under Seismic Loads*, ASCE, pp.56-78.

[10]   Hakuno, M. and Meguro, K. (1993): Simulation of Concrete-frame Collapse due to Dynamic Loading, *Journal of Engineering Mechanics*, ASCE, Vol.119, No.9, pp.1709-1723, September.

[11]   Hauke, B. and Maekawa, K. (2000): Three-Dimensional Modeling of Reinforced Concrete with Multi-Directional Cracking, *Concrete Library of JSCE*, No.36, pp.181-206, December.

[12]   Hillerborg, A., Modeer, M., and Petersson, P-E. (1976): Analysis of Crack Formation and Crack Growth in Concrete by means of Fracture Mechanics and Finite Elements, *Cement and Concrete Research*, Vol.6, pp.773-782.

[13] Ichinose, T., Imai, M., Okano, T., and Ohashi, K. (2001): Three-Dimensional Shear Failure of RC Columns after Cyclic Loading, *Modeling of Inelastic Behavior of RC Structures under Seismic Loads*, ASCE, pp.546-561.

[14] Itoh, A. and Tanabe, T. (2001): Analysis of RC Column Experiments at UCSD by an Equivalent Lattice Model, *Finite Element Analysis of Reinforced Concrete Structures*, ACI SP-205, pp.81-96.

[15] JSCE (2002): Standard Specifications for Concrete Structures-2002, *Seismic Performance Verification*, December.

[16] Kawai, T. (1978): New Discrete Models and their Application to Seismic Response Analysis of Structures, *Nuclear Engineering and Design*, Vol.48, Issue 1, pp.207-229, June.

[17] Kinugasa, H. and Nomura, S. (2000): Failure Mechanism of RC Beam under Reversed Cyclic Loading after Flexural Yielding Caused by Lateral Strain Accumulation in Plastic Hinge Region on Slip Region, *Journal of Structural and Construction Engineering*, AIJ, No.538, pp.147-153, December. (in Japanese)

[18] Lilliu, G. and van Mier, J. G. M. (2002): Effect of Particle Density on Tensile Fracture Properties of Model Concrete, *Proceeding of the third DIANA World Conference, Finite Elements in Civil Engineering Applications*, pp.69-77, Tokyo Japan, October.

[19] Lilliu, G. and van Mier, J. G. M. (2003): 3D Lattice Type Fracture Model for Concrete, *Engineering Fracture Mechanics*, Volume 70, Issues 7-8, pp927-941, May.

[20] Mau, S. T. and El-Mabsout, M. (1989): Inelastic Buckling of Reinforcing Bars, *Journal of Engineering Mechanics*, ASCE, Vol.115, No.1, pp.1-17, January.

[21] Meguro, K. and Hakuno, M. (1994): Application of the Extended Distinct Element Method for Collapse Simulation of a Double-deck Bridge, *Structural Engineering/ Earthquake Engineering*, Vol.10, No.4, pp.175s-185s, JSCE, January. (*Journal of Structural Mechanics and Earthquake Engineering*, No.483/I-26, pp.17-27)

[22] Menegotto, M. and Pinto, P. E. (1973): Method of Analysis for Cyclically Loaded R.C. Plane Frames Including Changes in Geometry and Non-elastic Behavior of Elements under Combined Normal Force and Bending, *Preliminary Report*, IABSE, No.13, pp.15-22, Lisbon.

[23] Miki, T., Niwa, J., and Lertsamattiyakul, M. (2003a): Earthquake Response Analysis for RC Bridge Piers Considering Reinforcement Buckling Behavior, *Journal of Materials, Concrete Structures and Pavements*, JSCE, No.732/V-59, pp.225-239, May. (in Japanese)

[24] Miki, T., Niwa, J., and Lertsamattiyakul, M. (2003b): Numerical Evaluation of Seismic Performance of Reinforced Concrete Bridge Piers Using Dynamic Lattice Model, *Concrete Library of JSCE*, Vol.41, pp.49-64, June.

[25]   Monti, G. and Nuti, C. (1992): Nonlinear Cyclic Behavior of Reinforcing Bars Including Buckling, *Journal of Structural Engineering*, ASCE, Vol.118, No.12, pp. 3268-3284, December.

[26]   Mörsch, E. (1909): Concrete-steel Construction (der Eisenbetonbau), *Transaction of the Third German Edition by E. P. Goodrich*, McGraw-Hill Book Co., New York.

[27]   Nakamura, H., Yamamoto, Y., Itoh, A., and Tanabe, T. (2003): Occurrence and Effects of Torsional Moment by Shifting of Shear Center of RC Cross Section, *Proceeding of Seminar on Simulation of Collapse of Concrete Structures; from Research to Practice*, Maui USA, November.

[28]   Niwa, J., Choi, I. C., and Tanabe, T. (1995): Analytical Study for Shear Resisting Mechanism Using Lattice Model, *Concrete Library of JSCE*, No.26, pp.95-109, December.

[29]   Noguchi, H., Kashiwazaki, T., Uchida, K., and Nozaki, Y. (2001): FEM Analysis for Structural Performance Design of Concrete Structures, *Modeling of Inelastic Behavior of RC Structures Under Seismic Loads*, ASCE, pp.257-275.

[30]   Noguchi, H., Zhang, D, and Kashiwazaki, T. (2002): Three-dimensional Finite Element Analysis of RC Beam-column Joints Reinforced by New Reinforcing Way, *Proceedings of the JCI*, Vol.24, No.2, pp.397-402. (in Japanese)

[31]   Noguchi, H., Zhang, D., and Kashiwazaki, T. (2003): Investigative Analysis for Improving the Precision of Dynamic FEM Analysis of RC Seismic Shear Walls, *Proceedings of the JCI*, Vol.25, No.2, pp.103-108. (in Japanese)

[32]   Ritter, W. (1899): The Hennebique Design Method (Die Bauweise Hennebique), *Schweizerische Bauzeittung (Zürich)*, Vol.33, No.7, pp.59-61.

[33]   Saito, S. and Hikosaka, H. (1999): Numerical Analyses of Concrete Structures Using Spring Network Models, *Journal of Materials, Concrete Structures and Pavements*, JSCE, No.627/V-44, pp.289-303, August.

[34]   Schlaich, J., Schafer, K., and Jannewein, M. (1987): Toward a Consistent Design for Structural Concrete, *Journal of PCI*, Vol.32, No.3, pp.75-150.

[35]   Shi, G. H. and Goodman, R. E. (1989): Generalization of Two-dimensional Discontinuous Deformation Analysis for Forward Modeling, *International Journal for Numerical and Analytical Methods in Geomechanics*, Vol.13, pp.359-380.

[36]   Spacone, E., Filippou, F. C., and Taucer, F. F. (1996 a): Fibre Beam-column Model for Non-linear Analysis of R/C Frames: Part I Formulation, *Earthquake Engineering and Structural Dynamics*, Vol.25, Issue 7, pp. 711-725, July.

[37]   Spacone, E., Filippou, F. C., and Taucer, F. F. (1996 b): Fibre Beam-column Model for Non-linear Analysis of R/C Frames: Part II Applications, *Earthquake Engineering and Structural Dynamics*, Vol.25, Issue 7, pp. 727-742, July.

[38] Suda, K., Murayama, Y., Ichinomiya, T., and Shinbo, H. (1994): Buckling Behavior of Longitudinal Reinforcements in RC Column Subjected to Cyclic Load, *Proceedings of the JCI*, Vol.16, No.2, pp.467-472. (in Japanese)

[39] Takahashi, T. and Maekawa, K. (1998): Visualization of Three Dimensional RC Crack Analysis using Immersive Multi-screen Display, *Proceedings of the JCI*, Vol.20, No.1, pp.149-154. (in Japanese)

[40] Takeda, T., Sozen, M. A., and Nielsen, N. N. (1970): Reinforced Concrete Response to Simulated Earthquakes, *Journal of the Structural Division*, ASCE, Vol.96, ST12, pp.2557-2573, December.

[41] Tanabe, T. and Ishtiaq, A. S. (2001): Development of Lattice Equivalent Continuum Model for Analysis of Cyclic Behavior of Reinforced Concrete, *Modeling of Inelastic Behavior of RC Structures under Seismic Loads*, ASCE, pp.297-314.

[42] Tanoue, K., Nakamura, h. Saito, S., and Higai, T. (2002): Modeling of Stress-Average Strain Relationship of Buckled Reinforcing Bars under Cyclic Loading, *Proceedings of the JCI*, Vol.24, No.2, pp.223-228. (in Japanese)

[43] Tsuchiya, S., Tsuno, K., and Maekawa, K. (2002): Three-dimensional FE Solid Response Analysis of RC Columns Subjected to A Combination of Permanent Eccentric Axial Force and Reversed Cyclic Torsion and Bending/Shear, *Concrete Library of JSCE*, Vol.39, pp.237-251, June.

[44] Yamamoto, Y., Bongochgetsakul, N., Nakamura, H., and Tanabe, T. (2003): Study on Movement of Shear Center and Mechanism of Torsional Moment Occurrence by Fiber Model, *Proceedings of the JCI*, Vol.25, No.2, pp.1075-1080. (in Japanese)

[45] Yonezawa, K. and Noguchi, H. (1995): Analytical Study on the Shear Strength of Beam-column Joints in Mixed Structure by Three-dimensional FEM, *Journal of Structural and Construction Engineering*, AIJ, No.471, pp.181-191, May. (in Japanese)

[46] Watanabe, T., Tanimura, Y., Takiguti, M., and Sato, T. (2001): Evaluation Method of Deformation Capacity Related to Damage Conditions for Reinforced Concrete Members, *Journal of Materials, Concrete Structures and Pavements*, JSCE, No.683/V-52, pp.31-45, August. (in Japanese)

2 ANALYTICAL MODEL

2.1 Introduction

An objective, simple, and accurate nonlinear analytical model is essential to simulate the structural performance of RC structures. In particular, the structural evaluation of a RC structure at its largely deformed state is necessary to clarify the seismic performance of structure subjected to huge earthquake motion. For flexural RC columns, material and geometrical nonlinearities such as the softening behavior of concrete in compression or the buckling of reinforcement should be considered. To meet such requirements for numerical analysis of a RC structure, the lattice model (Niwa et al. 1995) is focused in this study. This model is able to predict the shear carrying capacity of RC members with reasonable accuracy. Moreover, since the lattice model discretized a RC member into truss elements, internal stress flows can easily be determined. From an understanding of the internal resistance mechanism of RC members, the validity of analytical results can be confirmed. The expression about the 2D lattice model that is the basis of 3D model formulation is described in this chapter.

2.2 Outlines of Lattice Model

The lattice model consists of members representing both concrete and reinforcement, as schematically shown in **Figure 2.1**. The figure shows the lattice model of RC column. In the lattice model, the shear resisting mechanism of a structural member is considered as arch action and truss action. For the 2D lattice model, a RC member in 3D is regarded as the 2D model according to the plane stress condition. The concrete is modeled into flexural compression members, flexural tension members, diagonal compression members, diagonal tension members, vertical members, or arch members. For RC column, longitudinal and transverse reinforcement are modeled into horizontal and vertical member, respectively.

The diagonal compression members and the diagonal tension members represent the truss action of shear resistance mechanism in the lattice model. They are placed in a regular arrangement with inclination angles of 45° and 135° to the longitudinal axis of the model,
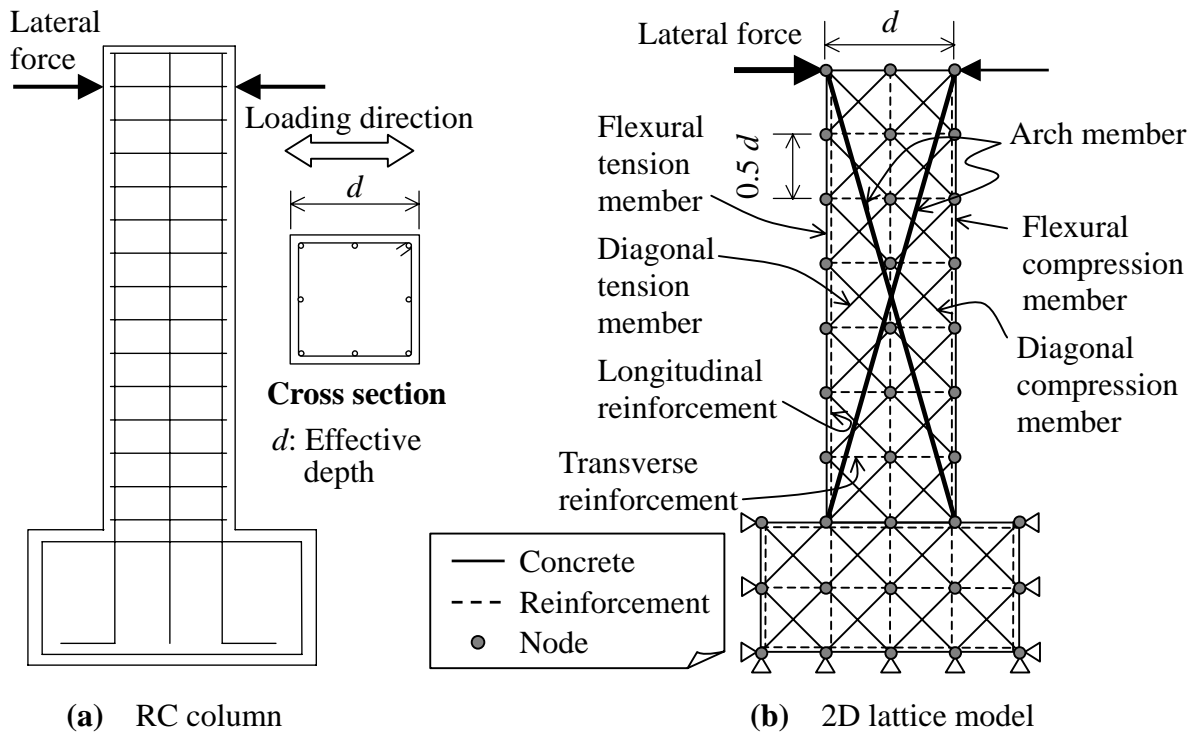
Figure 2.1   Outlines of the lattice model

respectively.   The lattice model seems to be categorized as a fixed angle truss model in which the diagonals are assuming as the 45° angle of inclination trusses.   Furthermore, this model does not directly take account for the components of the shear resisting mechanism, such as aggregate interlock and friction, dowel action of the longitudinal reinforcement, and direct shear across the uncracked plain concrete.   However, since the arch member considering the flow of internal forces is provided into the model with proper direction and location, the shear resisting mechanism of RC members can be represented appropriately. The example of configurations of arch members is shown in **section 2.4**.

By incorporating the arch member to represent the arch action, the lattice model can be used to estimate the changing direction of internal compressive stress flows after diagonal cracking. It should be noted that, for appropriate estimation of the shear resisting mechanism of RC members, the direction and the location of the arch member are important.   While the elastic finite element analysis may be used to determine the stresses in the concrete prior to cracking, this analysis method may not be appropriate for design, since considerable redistribution of stresses may occur after cracking.   Nonlinear finite element analysis is required to provide a capable tool of predicting the complete response of RC members.   For typical example of arch members of a cantilever RC column subjected to reversed cyclic loading, two arch members are modeled as a connection between the loading point and column-footing connection, as shown in **Figure 2.1**.
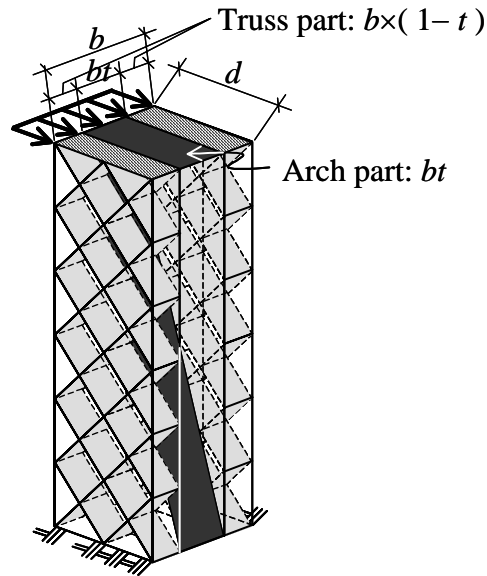
Figure 2.2   Cross section of RC column modeled
by the 2D lattice model

2.3   Modeling of Each Element

A schematic diagram of cross section of RC column in the 2D lattice model is shown in
Figure 2.2.   The concrete is divided into truss and arch members.   When the value of t is
defined as the ratio of the width of the arch part to the width of cross section b, the widths of
the arch part and the truss part are given by bt and $b (1 - t)$, respectively, where $0 < t < 1$.
The value of t is determined based on the theorem of the minimization of the total potential
energy for the 2D lattice model with the initial elastic stiffness.

Pre-analysis is carried out using the lattice model, with varying the value of t from 0.05 to
0.95 with an interval of 0.05.   The total potential energy can be calculated from the
difference between the sum of strain energy of each element and the external work.   The
strain energy is calculated from the stresses and strains of each lattice component produced
when the model is subjected to a small displacement at the loading point.   This small
displacement is fixed as 0.1% of the shear span in this study.   It is obvious that, when the
structure is subjected to large deformations, significant material nonlinearity is observed and
the value of t may vary as the deformation increases.   In this study, although the deformation
becomes large, the value of t as calculated from the initial stiffness is used.

Due to the existence of reinforcing bars, the bond effect between concrete and reinforcing
bars becomes significant in the post-peak behavior of concrete.   Furthermore, for flexural
tension members with reinforcing bars, the concrete still contributes to tensile resistance even

(a) Cantilever type column

Elastic elements

(b) Column fixed rotation at the top

(c) Slender beam (half span)

(d) Slender beam

(e) Deep beam
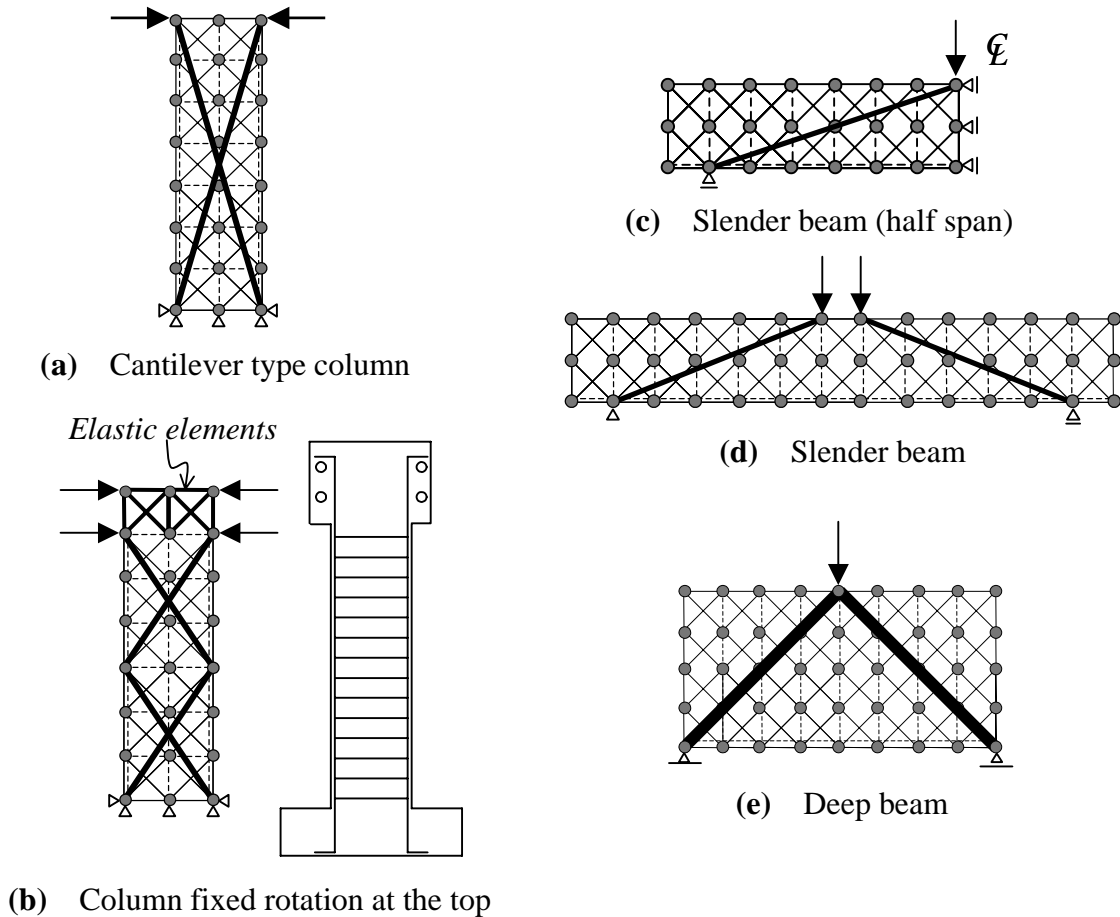
Figure 2.3   Configurations of arch members

after cracking.   Consequently, the cross-sectional area of concrete flexural members, for simplicity, is determined by considering the bond effect between concrete and reinforcing bars, and the cross-sectional area of the flexural tension or compression member is assumed to be the product of the double depth of cover concrete and the width of cross section.

2.4   Location and Direction of Arch Members

In the lattice model of RC members, it is important to design the location and direction of the arch members as mentioned previously.   In general, the location and direction of arch members are depending on the loading conditions and geometrical properties.   For the lattice modeling, the arch should be located along the compressive stress flows inside a RC member. In other words, the critical shear cracks relating to the load carrying capacity of entire member are referred to express the shear resisting mechanism.   Typical examples of modeling for RC columns/beams are illustrated in **Figure 2.3**.

In a cantilever-type RC column, the arch member is located to connect the loading point with

the bottom of the column. If s RC member is subjected to laterally cyclic loads, two arch members crossing each other are adopted as shown in **Figure 2.3 (a)**. On the other hand, when a RC column subjected to lateral cyclic loads at its top in condition of preventing the rotation, the arch members are installed according to a moment distribution as illustrated in **Figure 2.3 (b)**.

As for RC beams, the arch members are arranged to carry the internal force from the loading point to the support point as shown in **Figures 2.3 (c)** to **(e)**. It is noticed that a deep beam has the arch of which inclined angle to the longitudinal direction of a member is similar to that of truss members, while for a slender beam the angle is completely different from that of the truss members. Here, by incorporating an arch member to represent the arch action, the lattice model can be used to estimate the change of internal compressive stress flows after diagonal cracking. In addition, the arch members can appropriately represent the stress distribution in concrete members after the first yield of the transverse reinforcement, though the inclination angle of the diagonal compression member is fixed at 45 degrees.

2.5 Material Models

2.5.1 Compressive stress-strain relationships of concrete

It has been confirmed that, if a suitable amount of transverse reinforcement is used to confine the concrete, a significant increase in both compressive strength and ductility can be expected. In this study, in order to take into account this confinement effect by transverse reinforcement, the stress-strain relationship ($\sigma_c' - \varepsilon_c'$) proposed by Mander et al. (1998) as expressed by **Equation 2.1** and illustrated in **Figure 2.4**, is used as a material model for the diagonal compression members and the arch members.

$$\sigma_c' = \frac{f_{cc}' \cdot x \cdot r}{r - 1 + x^r} \tag{2.1}$$

where,

$$f_{cc}' = f_c' \left(2.254 \sqrt{1 + 7.94 f_l' / f_c'} - 2 f_l' / f_c' - 1.254 \right) \text{ (in N/mm}^2) \tag{2.2}$$

$$x = \varepsilon_c' / \varepsilon_{cc}' \tag{2.3}$$

$$\varepsilon_{cc}' = 0.002 \cdot \left\{ 1 + 5(f_{cc}' / f_c' - 1) \right\} \tag{2.4}$$
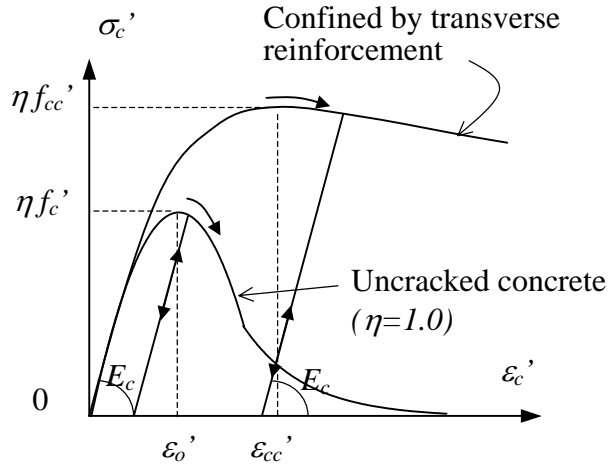
Figure 2.4 Compressive model of concrete
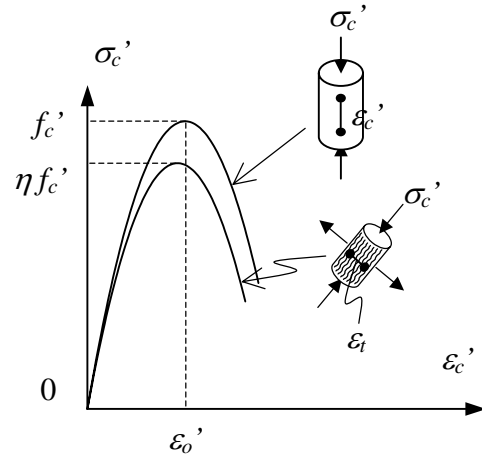
Figure 2.5 Reduction in compressive
strength of cracked concrete

$$r = E_c / (E_c - E_{sec}) \tag{2.5}$$

$$E_c = 5000\sqrt{f_c'} \ (f_c' \text{ is in N/mm}^2) \tag{2.6}$$

$$E_{sec} = f_{cc}' / \varepsilon_{cc}' \tag{2.7}$$

$$f_l' = 0.75 \cdot r_w f_{wy} \tag{2.8}$$

where, f_c' is the uniaxial compressive strength of the concrete, r_w is the transverse reinforcement ratio (= $A_w / b_w s$), A_w is the cross-sectional area of the transverse reinforcement, b_w is the width of web concrete of a RC member, s is the transverse reinforcement spacing, and f_{wy} is the yield strength of the transverse reinforcement.

Furthermore, Vecchio and Collins (1986) demonstrated that the compressive stress of diagonally cracked concrete decreases as the transverse tensile strain, ε_t, increases, as shown in **Figure 2.5**.   Therefore, the value of ε_t for the diagonal tension members, which are normal to the diagonal compression members, is used to determine the coefficient to express concrete compressive softening, η.   The behavior of the cracked concrete in compression is then characterized by **Equation 2.9**.   For the arch member, the transverse tensile strain of the diagonal tension member near the loading point is used.

$$\eta = 1.0 / \{0.8 - 0.34(\varepsilon_t / \varepsilon_0')\} \leq 1.0 \tag{2.9}$$

where, $\varepsilon_0' = -0.002$.

On the other hand, for flexural compression members including the cover concrete, the quadratic stress-strain relationship (**Equation 2.10**) proposed by Vecchio and Collins (1986) is adopted, as illustrated in **Figure 2.4**.

$$\sigma_c' = -\eta \cdot f_c' \left\{ 2(\varepsilon_c' / \varepsilon_0') - (\varepsilon_c' / \varepsilon_0')^2 \right\}$$ (2.10)

For flexural compression members, since the direction of compression stress is assumed to correspond to the direction of the principal tensile strain, the effect of compressive softening behavior represented by **Equation 2.10** is neglected, thus $\eta = 1.0$.

In the unloading path, stress is assumed to decrease with the initial stiffness. The reloading curve is assumed to follow the same path as the unloading one. In this study, decrease in the stiffness due to reversed cyclic loading is not taken into account the consideration for simplicity.

2.5.2   Tensile stress-strain relationships of concrete

Since the flexural tension members contain reinforcing bars, the previously mentioned bond action takes place between concrete and reinforcing bars, the concrete continues to sustain tension even after cracking. For the flexural tension members prior to cracking, a linear elastic relationship is applied, while the tension stiffening curve proposed by Okamura and Maekawa (1991) defined by **Equation 2.11** and illustrated in **Figure 2.6** is applied after cracking. The strain at crack initiation, ε_{cr}, is assumed to be 0.0001 (100 μ).

$$\sigma_t = f_t \left(\varepsilon_{cr} / \varepsilon_t \right)^{0.4}$$ (2.11)

where, f_t is the uniaxial tensile strength of concrete.

The diagonal tension members exhibit elastic behavior prior to cracking. However, once a crack occurs, concrete is assumed to exhibit tension softening behavior. In this study, softening behavior, expressed by the 1/4-model (Uchida et al. 1991) shown in **Figure 2.7** and **Equations 2.12** and **2.13**, is applied to the diagonal tension members.
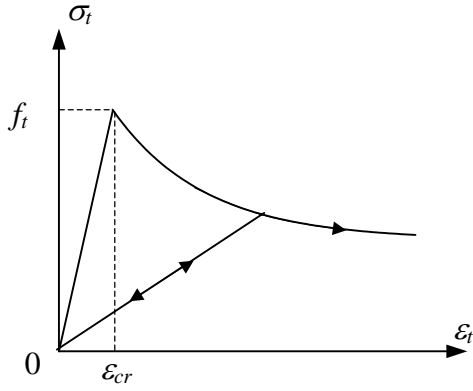
Figure 2.6 Tension stiffening model
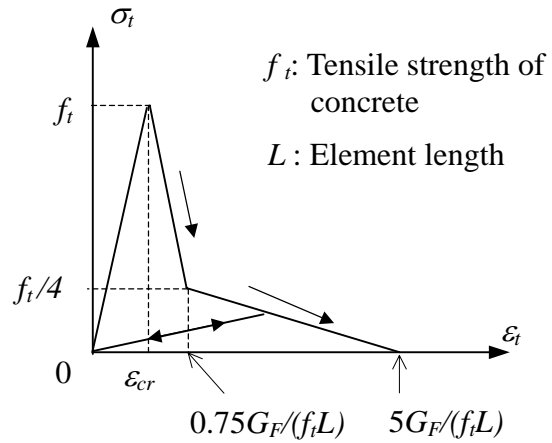
Figure 2.7 Tension softening model
(1/4 model)

$$\varepsilon_1 = \varepsilon_{cr} + 0.75 \, G_F / (f_t \cdot L) \tag{2.12}$$

$$\varepsilon_2 = \varepsilon_{cr} + 5.0 \, G_F / (f_t \cdot L) \tag{2.13}$$

where, f_t is the splitting tensile strength of concrete and L is the element length.   Here, the fracture energy of concrete, G_F, is assumed to be its standard value of 0.1 N/mm.

In each tensile model of concrete, the unloading path is assumed to fall directly to the origin and the reloading path is assumed to follow the unloading path.

2.5.3   Reinforcement model

The stress-strain relationship of the reinforcement is expressed as an elasto-plastic model under monotonic loading.   As shown in **Figure 2.8**, the stress-strain relationship of the reinforcement is bi-linear, having a tangential stiffness after yielding of $E_s /100$ (where E_s indicates the elastic modulus of reinforcement).   The unloading and reloading paths are also shown in **Figure 2.8**.   After yielding, the stiffness of the reinforcement decrease as the stress state moves from tension to compression, while similar behavior is observed when the stress changes from compression to tension.   This phenomenon, so-called the Bauschinger effect, is incorporated into the analysis using the model proposed by Fukuura et al. (1997).   This is an improved model developed for simplicity in numerical analysis, though it retains the same accuracy as Kato's model (Kato 1979).
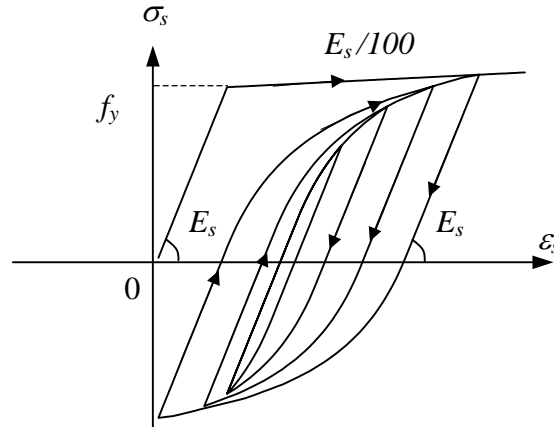
Figure 2.8   Stress-strain relationship of reinforcement under cyclic loading

2.6   Modeling for Buckling of Reinforcement and Pull-out Behavior

2.6.1   Buckling model of longitudinal reinforcement in concrete

In order to evaluate the buckling behavior of longitudinal reinforcing bars, the buckling model of reinforcing bars proposed by Dhakal (2000) is used.   This model is characterized as a spatially averaged material model that accurately takes into account the inelastic material mechanism of buckling.   In this model, the buckling behavior depends on both the ratio of buckling length, L that is an averaged region to the diameter of a reinforcing bar, D, L/D, and also the yield strength, f_y.   The buckling length must be determined prior to the analysis.

2.6.1.1   *Determination of buckling length*

One of the parameters that govern the averaged behavior of reinforcing bars in compression is the buckling length.   In compression tests of a bare bar, the effective buckling length is equal to the supported length of the test piece.   However, for reinforcing bars in concrete, this definition of effective buckling length cannot be applied.   The accurate method to predict the buckling length of longitudinal reinforcing bar based on the stability analysis is necessary to model the average compressive response of reinforcing bars in concrete.

In the determination of buckling length, first, the actual tie stiffness to influence on each of longitudinal reinforcing bar is calculated.   Next, the minimum spring stiffness required to hold the longitudinal reinforcing bars is determined.   Then, the required stiffness is compared with the actual tie stiffness to check the stability of the reinforcing bars in corresponding buckling modes.   The stable buckling mode is the smallest possible mode for

31
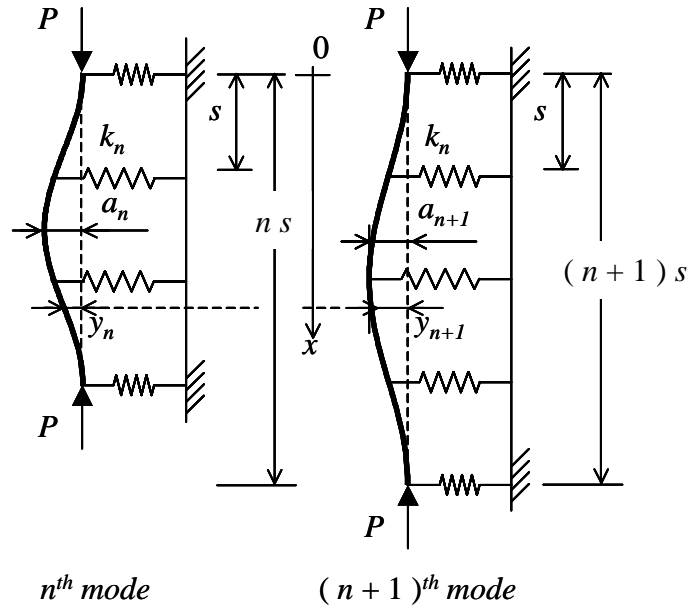
Figure 2.9   Determination of required spring stiffness for n-th buckling mode

which the required spring stiffness is less than the actual tie stiffness. The product of this stable buckling mode and the tie spacing gives the buckling length of the longitudinal reinforcement for given arrangement of lateral ties. Consequently, the buckling length is given by **Equation 2.14**.

$$k_t > k_n \;\Rightarrow\; L = n \times s; \;\; n = 1,\, 2,\, 3,\, \cdots \tag{2.14}$$

To define the buckling shape of the longitudinal reinforcing bar, a cosine curve is adopted. **Figure 2.9** represents the two possible modes of buckling (*n* and *n+1*) considered to derive the buckling length. The assumed lateral displacement profiles of the longitudinal reinforcing bar in these two modes are given by **Equations 2.15** and **2.16**.

$$y_n = \frac{a_n}{2}\left(1 - \cos\frac{2\pi x}{n \cdot s}\right) \tag{2.15}$$

$$y_{n+1} = \frac{a_{n+1}}{2}\left(1 - \cos\frac{2\pi x}{(n+1) \cdot s}\right) \tag{2.16}$$

The energy corresponding to each buckling mode includes the strain energy in the reinforcing bar, the energy stored in the elastic spring, and the energy due to shortening of the reinforcing bar. The total energy of the system, *U*, is calculated as the sum of energies associated with the two buckling modes, U_n and U_{n+1}. The energy associated with two consecutive buckling

modes and the total energy are given by the following equations:

$$U_n = \int_0^{ns} \frac{EI}{2}\left(\frac{d^2 y_n}{dx^2}\right)^2 dx + c_i \sum_{i=1}^{n} \frac{k_n}{2} y_n^{is\,2} - \int_0^{ns} \frac{P}{2}\left(\frac{dy_n}{dx}\right)^2 dx \qquad (2.17)$$

$$U_{n+1} = \int_0^{(n+1)s} \frac{EI}{2}\left(\frac{d^2 y_{n+1}}{dx^2}\right)^2 dx + c_i \sum_{i=1}^{n+1} \frac{k_n}{2} y_{n+1}^{is\,2} - \int_0^{(n+1)s} \frac{P}{2}\left(\frac{dy_{n+1}}{dx}\right)^2 dx \qquad (2.18)$$

$$U = U_n + U_{n+1} \qquad (2.19)$$

Here, the value of c_i is zero for springs in the central half of the buckling length for representing plasticity, and for the rest, it is 1. Similarly, EI is the averaged flexural stiffness of the reinforcing bar considering the plasticity along the axis of the bar and k_n and P are the critical spring stiffness and the axial load corresponding to the n-th mode, respectively.

When the total energy U is minimized with respect to each of the maximum amplitudes (a_n and a_{n+1}), the simultaneous equation can be obtained as the following equations:

$$\frac{\partial U}{\partial a_n} = 0 \qquad \Rightarrow \frac{2\pi^4 EI}{n^3 s^3} + \frac{c_i k_n}{4}\sum_{i=1}^{n}\left(1-\cos\frac{2i\pi}{n}\right)^2 - \frac{P\pi^2}{2ns} = 0 \qquad (2.20)$$

$$\frac{\partial U}{\partial a_{n+1}} = 0 \qquad \Rightarrow \frac{2\pi^4 EI}{(n+1)^3 s^3} + \frac{c_i k_n}{4}\sum_{i=1}^{n}\left(1-\cos\frac{2i\pi}{n+1}\right)^2 - \frac{P\pi^2}{2(n+1)s} = 0 \qquad (2.21)$$

The simultaneous equation is solved to obtain the required spring stiffness k_n and the corresponding load P.

For simplicity, the average flexural rigidity of reinforcing bars having normal strength is assumed to be half of the elastic flexural rigidity. The average flexural rigidity of reinforcing bar is also influenced by its yield strength. Hence, the average flexural rigidity of reinforcing bar throughout the buckling length EI is assumed to be a function of the elastic bending rigidity, $E_s I$ and the yield strength f_y as given in **Equation 2.22**.

$$EI = \frac{E_s I}{2}\sqrt{\frac{f_y}{400}}; \quad (f_y \text{ in MPa}) \qquad (2.22)$$
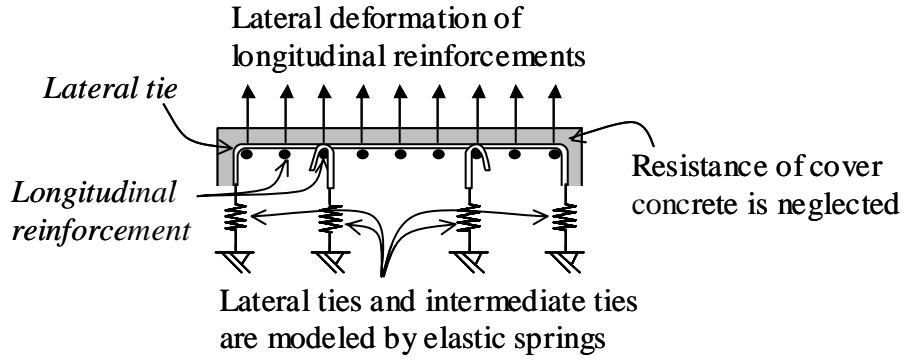
Figure 2.10 Modeling of lateral ties and intermediate ties

where, E_s and I are the elastic modulus and moment of inertia of a reinforcing bar.

In order to determine the stable buckling mode and buckling length, the actual effective stiffness of lateral tie having given strength and arrangement has to be evaluated in advance and it should be compared with the calculated required spring stiffness for different modes. The modeling of the lateral ties and the intermediate ties are illustrated in **Figure 2.10**. It is assumed that the resistance against the lateral deformation of longitudinal reinforcing bar is mainly governed by the axial stiffness of lateral tie. In addition, it is assumed that the total stiffness of both n_t lateral ties and n_{tin} intermediate ties equally contribute to n_l longitudinal reinforcing bars so that the buckling of these reinforcing bars occurs simultaneously. The restraining stiffness of the tie system against the buckling of one longitudinal reinforcing bar can be obtained using **Equation 2.23**.

$$k_t = \frac{1}{n_l} \cdot \frac{n_t E_t A_t + n_{tin} E_{tin} A_{tin}}{l_t} \tag{2.23}$$

where E_t, A_t, and l_t are elastic modulus, cross-sectional area, and the leg-length of transverse reinforcement, respectively. Similarly, E_{tin}, A_{tin}, and l_{tin} are elastic modulus, cross-sectional area, and the leg-length of intermediate ties, respectively. Here, n_l is the number of longitudinal reinforcing bars prone to simultaneous buckling; that is longitudinal bars at the flexural compressive side supported to remain uniformly equal compressive strain during any state of loading.

2.6.1.2 *Average stress-strain relationship of reinforcement*

As mentioned previously, the buckling model proposed by Dhakal (2000) depends on both the ratio of buckling length, L, to the diameter of reinforcing bar, D, L/D, and the yield strength f_y.

This model also depends on the local stress-strain relationship of reinforcement. The stress-strain relationship of reinforcement is usually modeled as bi-linear curve. After yielding, Bauschinger effect is considered by using the numerically improved model of reinforcing bars (Fukuura 1997). Hence, the following equations, relating to the absolute average compressive stress with the average compressive strain of reinforcing bars, can be used.

$$\sigma = \frac{\sigma^*}{\sigma_l^*}\left(\frac{\varepsilon_y + \varepsilon}{\varepsilon_y - \varepsilon^*}\right)\sigma_l; \qquad (-\varepsilon^* \leq \varepsilon < \varepsilon_y) \tag{2.24}$$

$$\sigma = -\sigma^* - 0.02E_s(\varepsilon + \varepsilon^*); \quad (\varepsilon < -\varepsilon^*) \tag{2.25}$$

where, σ_l and σ_l^* are the local stresses corresponding to ε (current strain) and ε^* (strain at the intermediate point), respectively. Similarly, ε_y is the yield strain of reinforcement. The coordinate of the intermediate point (ε^*, σ^*) is defined by **Equations 2.26** and **2.27**. In the following equations, L/D is called as the slenderness ratio (L: supported length, D: diameter of reinforcing bar) and f_y is the yield strength of reinforcement in MPa. The feature of this buckling model is shown in **Figure 2.11**.

$$\frac{\varepsilon^*}{\varepsilon_y} = 55 - 2.3\sqrt{\frac{f_y}{100}} \cdot \frac{L}{D}; \qquad \frac{\varepsilon^*}{\varepsilon_y} \geq 7 \tag{2.26}$$

$$\frac{\sigma^*}{\sigma_l^*} = \left(1.1 - 0.016\sqrt{\frac{f_y}{100}} \cdot \frac{L}{D}\right); \qquad \sigma^* \geq 0.2f_y \tag{2.27}$$
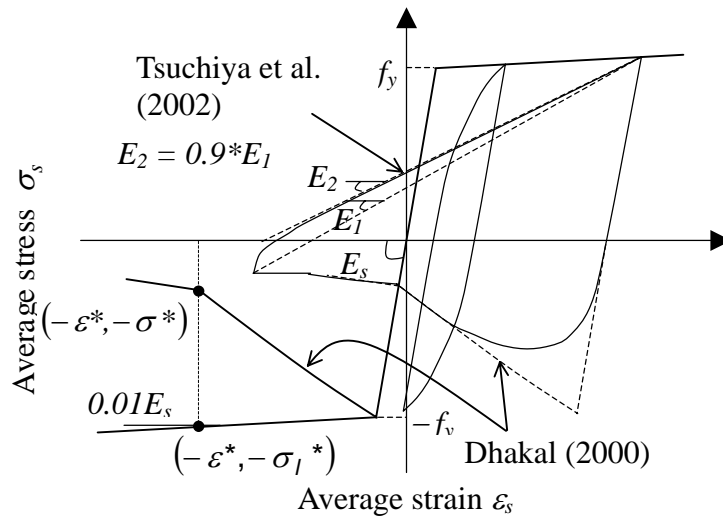
Figure 2.11 Buckling model of reinforcement

2.6.2   Pull-out model of longitudinal reinforcing bar from the footing

In column-footing joints or column-beam joints, additional deformation with respect to rotations caused by large slips in reinforcing bars is usually observed in test.   This is because of the sudden changes of cross section, that is geometry discontinuity.   The slip model of reinforcing bar considered in this study is based on the strain-slip models proposed by Mishima et al. (1992), of which the original model is proposed by Shima et al. (1987) and Shin et al. (1988).   The procedure for calculating the stress of reinforcing bar from the slip S out of the crack surface will be explained hereafter.

2.6.2.1   *Strain-slip model of reinforcing bar for monotonic loading*

The strain-slip model of reinforcing bar is formulated based on the normalized slip denoted by s, which is derived by normalizing the slip S, considering the influence of the diameter of reinforcing bar and compressive strength of concrete.

$$s = (S/D) \cdot K_{f_c} \tag{2.28}$$

where $K_{f_c} = (f_c'/20)^{2/3}$

$\quad\quad\quad S$: slip of reinforcing bar (mm)
$\quad\quad\quad D$: diameter of a reinforcing bar (mm)
$\quad\quad\quad f_c{}'$: compressive strength of concrete (MPa)

When reinforcing bar passes through a crack surface in concrete, bond deterioration near the crack surface is inevitable.   It is therefore necessary to consider its influence in modeling the strain-slip relationship for reinforcing steel.   Shin et al. (1988) defined a bond deterioration zones as 5D from the crack surface and assumed that the bond stress distribution in the zone is linear.   In the Shin's model, it is assumed that the length of bond deterioration zone remains constant regardless of strain in reinforcing bar.   The strain-slip model of reinforcing bar for monotonic loading is shown in **Figure 2.12**.

2.6.2.2   *Cyclic model for strain-slip of reinforcing bar*

Before yielding of reinforcing bar, the strain-slip relationship proposed by Shin et al. (1988) is used.   The cyclic model before yielding is illustrated in **Figure 2.13**.   As shown in the figure, the normalized slip, s is directly calculated from the strain of reinforcing bar, ε_s.
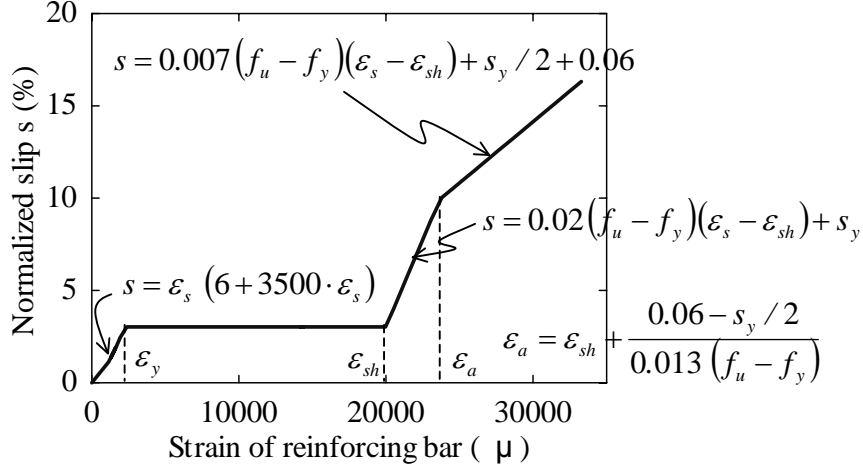
Figure 2.12   Strain-normalized slip relationship of reinforcing bar under monotonic loading

In contrast, it is observed that the strain distribution of reinforcing bar after yielding is discontinuous at the boundary between the yield and elastic regions as shown in **Figure 2.14**. In order to define the strain-slip relationship of reinforcing bar after yielding, it is reasonable to model the strain-slip relationship in the yield region and the elastic region separately. Here, strain of reinforcing bar at the flexural crack surface, strains of reinforcing at the boundary point in the yield region and the elastic region are defined as ε_s, ε_{sp}, and ε_{se}, respectively.   Similarly, the corresponding stresses of reinforcing bars are defined as σ_s, σ_{sp}, and σ_{se}.

It is assumed that the normalized slip s can be expressed as the sum of the slip in the yield region, s_{pl}, and the slip in the elastic region, s_e.   The slip s_{pl} and s_e are modeled separately as follows:

$$s = s_{pl} + s_e \tag{2.29}$$

Determination of slip s_{pl}

For modeling in the yield region, the slip s_{pl} can be defined as the strain of reinforcing bar integrated along the longitudinal reinforcing bar.   Here, the deformation of concrete is ignored.   If the strain distribution in the yield region is assumed to be linear as shown in **Figure 2.14**, the normalized slip s_{pl} of reinforcing bar can be expressed as follows:

$$O - A$$
$$s = \varepsilon_s \cdot \left(6 + 3500\,\varepsilon_s\right)$$

$$A - B$$
$$s = \varepsilon_{max} - \varepsilon_s{}' \left(6 + 3500\,\varepsilon_s{}'\right) \cdot 0.85, \quad \varepsilon_s{}' = \varepsilon_{max} - \varepsilon_s$$

$$B - C$$
$$s = 0.6\left(s_p - s_{min}\right) / \varepsilon_{min}{}^2 \cdot \left(\varepsilon_s - 4/3 \cdot \varepsilon_{min}\right)^2 + \left(16 s_{min} - s_p\right)/15$$

$$C - D$$
$$s = \varepsilon_s \cdot \left(6 - 3500\,\varepsilon_s\right)$$

$$D - E$$
$$s = \varepsilon_{min} - \varepsilon_s{}'' \left(6 - 3500\,\varepsilon_s{}''\right) \cdot 0.85, \quad \varepsilon_s{}'' = \varepsilon_{min} - \varepsilon_s$$

$$E - A$$
$$s = 0.6\left(s_p{}' - s_{max}\right) / \varepsilon_{max}{}^2 \cdot \left(\varepsilon_s - 4/3 \cdot \varepsilon_{max}\right)^2 + \left(16 s_{max} - s_p{}'\right)/15$$
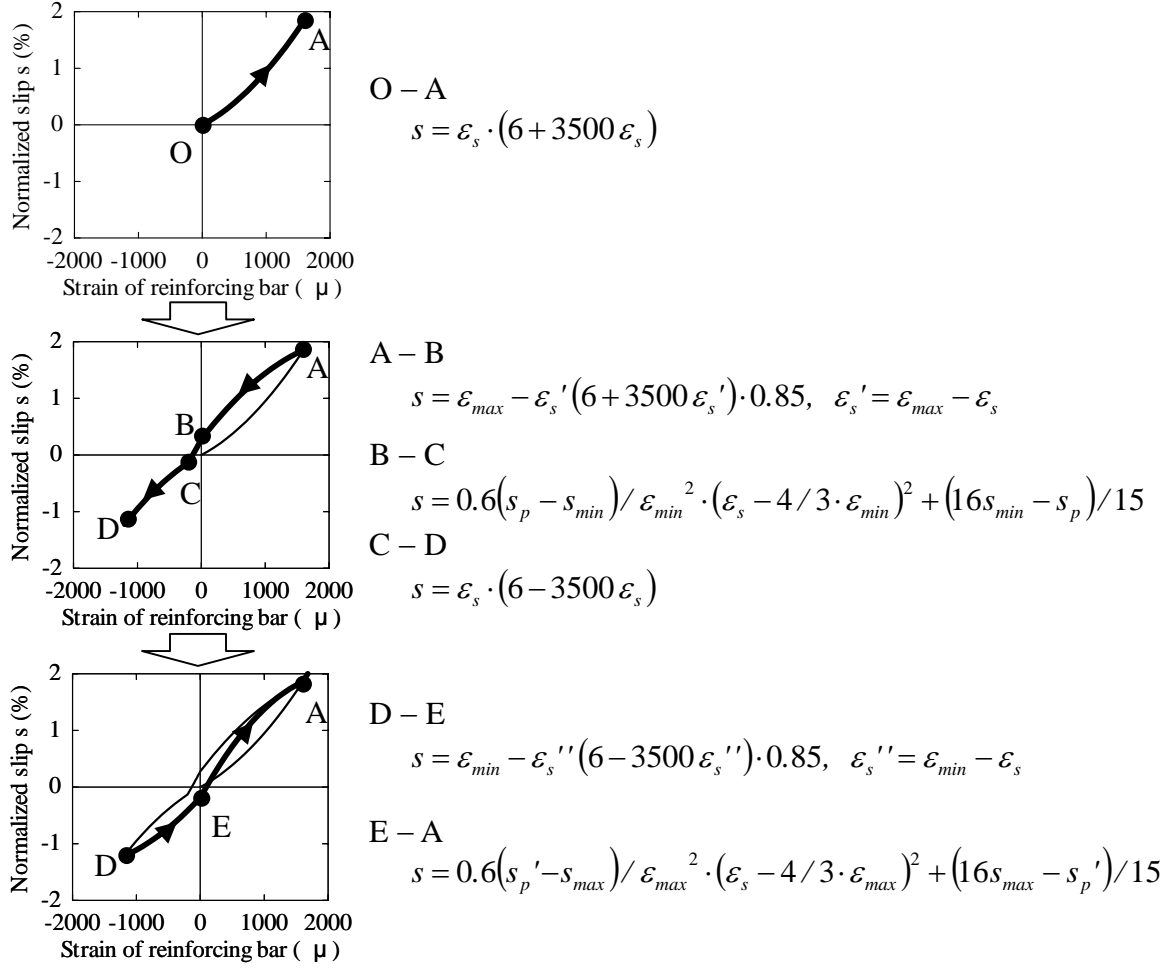
Figure 2.13   Strain-normalized slip relationship of reinforcing bar under cyclic loading (before yielding)

$$s_{pl} = \frac{\varepsilon_s + \varepsilon_{sh}}{2} \cdot l_y \cdot \left(K_{f_c} / D\right) \tag{2.30}$$

where, l_y is the length of the yield region from the flexural crack surface.   It is assumed that the yield region expands only when the strain of reinforcing bar exceeds the maximum strain experienced previously, and it does not change during unloading or reloading.

Ideguchi et al. (1988) experimentally proposed that the strain ε_s at the yield boundary point during unloading and reloading is almost related with the strain ε_{sp} at the crack surface (**Figure 2.14**).   In this study, this relationship is considered and the relationship between ε_s and ε_{sp} is assumed as follows:

$$\varepsilon_{sp} = \varepsilon_{sh} - \beta \cdot \left(\varepsilon_{max} - \varepsilon_s\right) \tag{2.31}$$

where β is an empirical parameter (Ideguchi et al. 1988), and assumed to be $\beta \approx 1.0$.   This
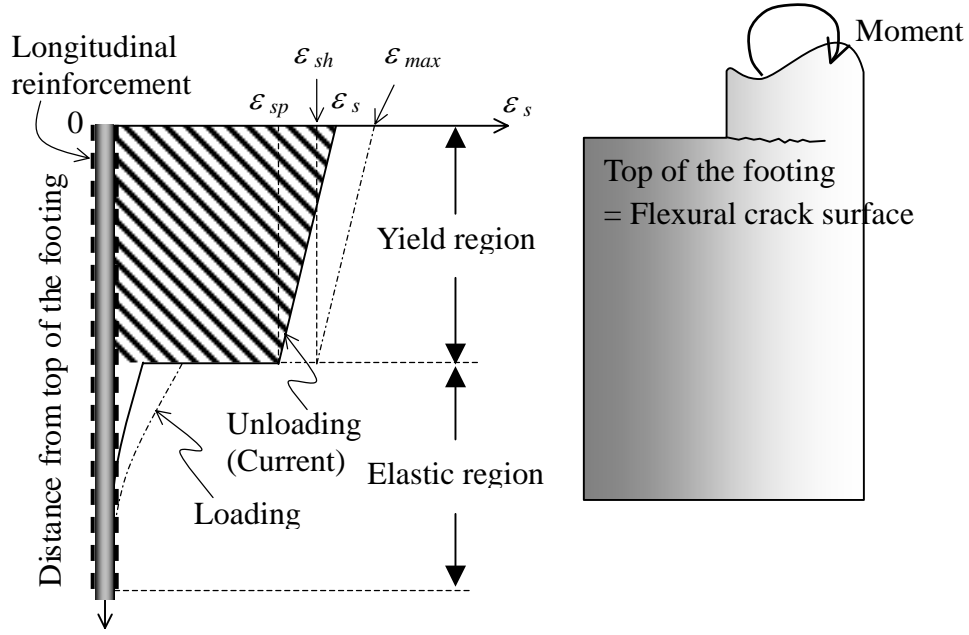
Figure 2.14 Distribution of strain of bar along longitudinal reinforcing bar

parameter is regarded as a material parameter. By substituting **Equation 2.29** into **Equation 2.28**, the following equation is obtained.

$$s_{pl} = \frac{(1+\beta)\varepsilon_s + \varepsilon_{sh} - \beta \cdot \varepsilon_{max}}{2} \cdot l_y \cdot \left(K_{f_c} / D\right)$$

(2.32)

Determination of slip s_e

For modeling in the elastic region, it is assumed that a hysteresis obtained by simplifying Shima's model (1987), as shown in **Figure 2.15**, is applied for the relationship between the strain ε_{se} and slip s_e of reinforcing bar in the elastic region. Since the elastic region of reinforcing bar is far away from the crack surface, it is assumed that the bond deterioration does not influence the behavior of reinforcing bar at the elastic region.

In general, although the strain distribution of reinforcing bar after yielding may be discontinuous, the stress distribution of reinforcing bar should be continuous. Considering the stress continuity of reinforcing bar that is $\sigma_{se} = \sigma_{sp}$, the strain at the boundary point in the elastic region is obtained as follows:

$$\varepsilon_{se} = \sigma_{sp} / E_s$$

(2.33)

O – A

$$s_e = \varepsilon_s \cdot \left(2 + 3500\,\varepsilon_s\right)$$

A – B

$$s_e = s_y^* - 0.85 \cdot \left(\varepsilon_y - \varepsilon_{se}\right)\!\left\{2 + 3500\!\left(\varepsilon_y - \varepsilon_{se}\right)\right\}$$

$$s_y^* = \varepsilon_y \cdot \left(2 + 3500\,\varepsilon_y\right)$$

B – C

$$s_e = 0.15\,s_y^* + \frac{1.15\,s_y^*}{\varepsilon_y} \cdot \varepsilon_{se}$$

C – D

$$s_e = s_{em} - 0.85 \cdot \left(\varepsilon_{se} - \varepsilon_{em}\right)\!\left\{2 + 3500\!\left(\varepsilon_{se} - \varepsilon_{em}\right)\right\}$$

D – A

$$s_e = s_{ep} + \frac{s_y^* - s_{ep}}{\varepsilon_y} \cdot \varepsilon_{se}$$
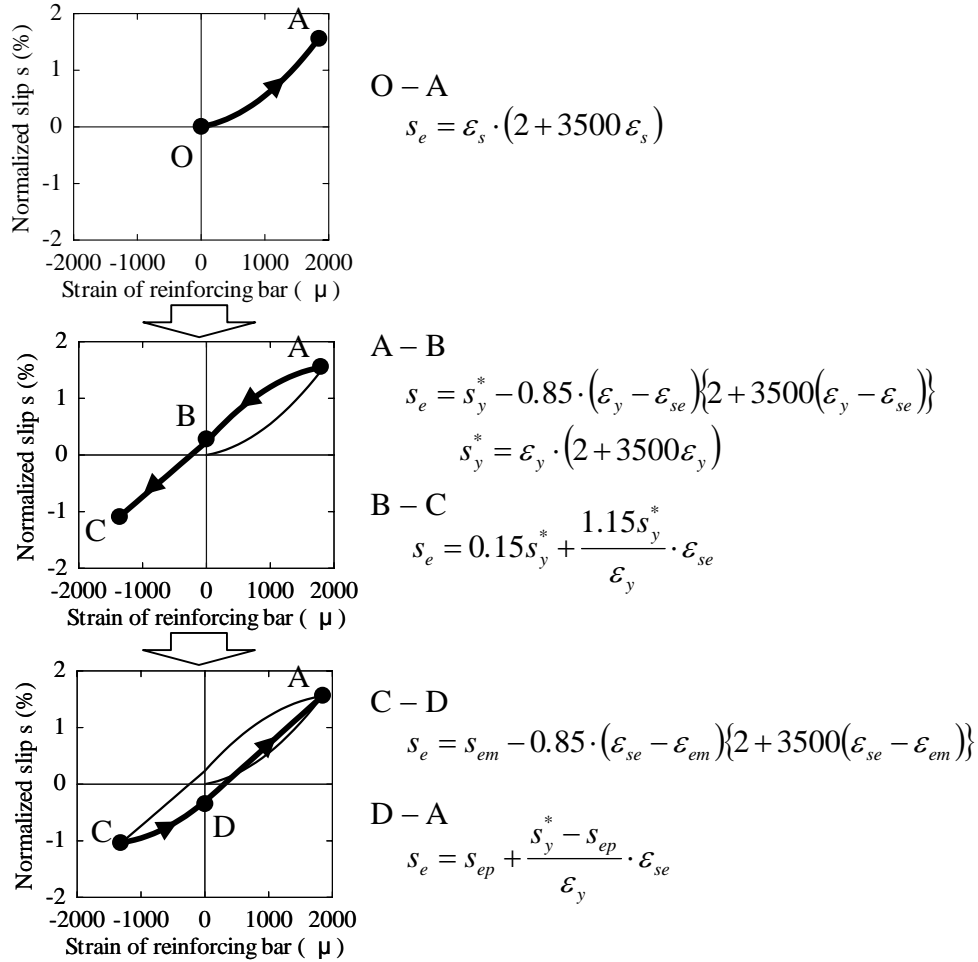
Figure 2.15   Strain-normalized slip relationship of reinforcing bar at the elastic region under cyclic loading

When Kato's model (1979) is applied to the stress-strain relationship of reinforcing bar at the boundary point in the yield region, the stress of reinforcing bar, σ_{sp} can be calculated from the strain of reinforcing bar, ε_{sp}.   Thus, ε_{se} can be calculated from ε_{sp}.   Consequently, by considering **Equation 2.31**, the steel slip s_e can be obtained as a function of the strain of reinforcing bar, ε_s at the crack surface.

Determination of length of the yield region l_y

As mentioned previously, the slips s_e and s_{pl} is calculated using strain of reinforcing ε_s.   In addition, the steel slip s is obtained by the summation of the slips s_e and s_{pl} using **Equation 2.29**.   In the formulation, the length of the yield region, l_y is necessary. l_y can be determined as follows.   It is assumed that the slip of longitudinal reinforcing bar occurs immediately after the reversal from loading to unloading and the slip is represented by s_u. By assuming $\varepsilon_s = \varepsilon_{max}$, the following equation is obtained using **Equations 2.29** and **2.32**.

$$s_u = \frac{(1+\beta)\varepsilon_{max} + \varepsilon_{sh} - \beta \cdot \varepsilon_{max}}{2} \cdot l_y \cdot \left(K_{f_c} / D\right) + s_y^*$$

$$= \frac{\varepsilon_{max} + \varepsilon_{sh}}{2} \cdot l_y \cdot \left(K_{f_c} / D\right) + s_y^* \qquad (2.34)$$

In order to consider the continuity of the model, the slip immediately after the load reversal to unloading must be equal to the maximum slip of reinforcing bar that is $s_u = s_{max}$. By solving **Equation 2.34** for l_y, the following equation is obtained.

$$l_y = 2\frac{s_{max} - s_y^*}{\varepsilon_{max} - \varepsilon_{sh}} \cdot \left(D / K_{f_c}\right) \qquad (2.35)$$

Since Shin's model gives s_{max} as a function of ε_{max}, the length l_y of the yield section can be calculated from ε_{max}. By substituting **Equation 2.35** into **Equation 2.32**, the slip in the yield region, s_{pl} can be given as follows:

$$s_{pl} = \frac{(1+\beta)\varepsilon_s + \varepsilon_{sh} - \beta \cdot \varepsilon_{max}}{\varepsilon_{max} + \varepsilon_{sh}} \cdot \left(s_{max} - s_y^*\right) \qquad (2.36)$$

Although β takes a value of about 1.0 as mentioned previously, it is a preferable method to treat β as a function of stress of reinforcing bar if a better agreement with the results of cyclic test of reinforced concrete panel is to be achieved. In this study, β is calculated using the following equation:
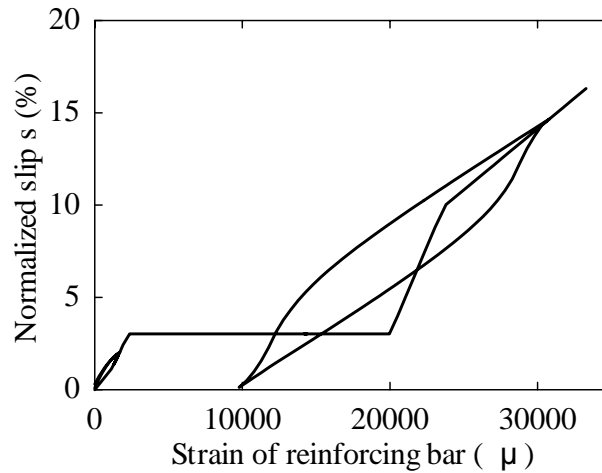
Figure 2.16　Strain-normalized slip relationship of reinforcing bar after yielding

$$\beta = \sigma_{max} / \sigma_y \tag{2.37}$$

where, σ_{max} is the maximum stress in reinforcing bar under tensile loads. Through above procedure, the relationship between the normalized slip s and the strain of reinforcing bar can be illustrated as **Figure 2.16**.

2.7 Nonlinear Dynamic Analysis Procedure

A computer program based on the dynamic lattice model has been newly developed by the authors (Miki et al.2003) to facilitate the nonlinear dynamic analysis of RC columns/beams. In the analysis, it is assumed that a mass equivalent to the self-weight of the structure is distributed over all the nodal points. It is also assumed that a concentrated mass having the weight of superstructure applies uniformly on the nodal points at the top of the structure.

The numerical procedure implemented in the computer program is explained below. The equations of motion are formulated to satisfy the equilibrium condition for the structure. Then, prior to time integration, nodal displacements of the lattice model are converted into those in the generalized coordinates by using the mode shape vector. The mode shape vector of vibration is obtained as the solution for the free vibration equations neglecting the damping. The mode of vibration can be obtained by solving the eigenproblem. In this study, the subspace iteration method is used to solve the eigenproblem.

The stiffness matrix, K can be obtained from the tangent stiffness considering the material nonlinearities of concrete and reinforcement. The damping matrix, C is generally given in the form of linear combination of the global stiffness matrix, K and the mass matrix, M. This is called the Rayleigh damping and expressed as the following equation:

$$C = a_0 M + a_1 K \tag{2.38}$$

where, a_0 and a_1 are the proportionality constants having units of 1/sec and sec, respectively.

By applying the orthogonality relationships using the vibration mode shapes (Clough and Penzien 1993), the Rayleigh damping expressed by **Equation (2.38)** leads to the following relationship between the viscous damping ratio h_n and frequency ω_n.

$$h_n = \frac{a_0}{2\omega_n} + \frac{a_1 \omega_n}{2} \tag{2.39}$$
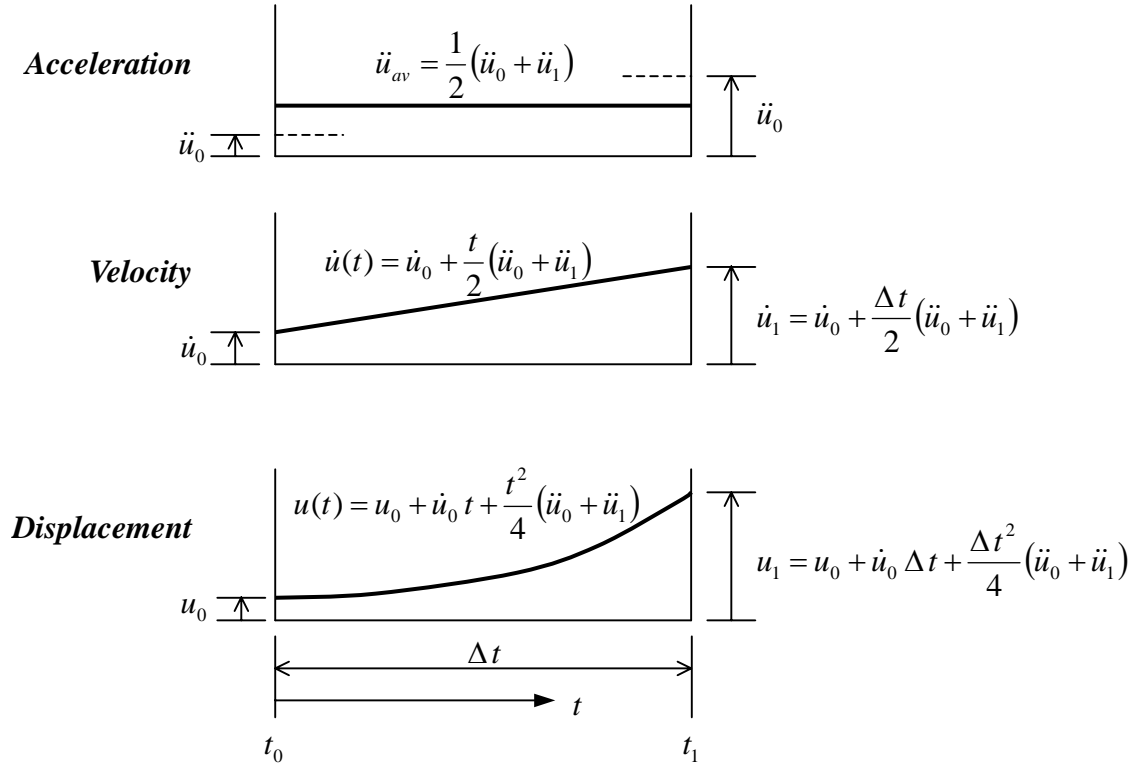
Figure 2.17　Motion based on the constant average acceleration

It is apparent that the two Rayleigh damping factors, a_0 and a_1, can be evaluated by the solution of a pair of simultaneous equations if the damping ratios h_m and h_n associated with two specific frequencies ω_m, ω_n are given. In general, it is assumed that the same damping ratio applies to both control frequencies; that is $h_m = h_n \equiv h$. In this case, the proportionality factors are given as follows:

$$\begin{Bmatrix} a_0 \\ a_1 \end{Bmatrix} = \frac{2h}{\omega_m + \omega_n} \begin{Bmatrix} \omega_m \omega_n \\ 1 \end{Bmatrix} \tag{2.40}$$

The use of the generalized coordinates serves to transform the equations of motion from a set of n simultaneous differential equations to a set of n independent normal coordinate equation. These equations can be solved using the direct time integration method. In this study, Newmark formulation is used as the time integration scheme. In the Newmark formulation, the basic integration equations for the final velocity and displacement of each time step are shown as follows:

Acceleration

$$\ddot{u}(t) = \ddot{u}_0 + \left(\frac{\ddot{u}_0 + \ddot{u}_1}{\Delta t}\right) \cdot t$$

$\ddot{u}_0$

$\ddot{u}_0$

Velocity

$$\dot{u}(t) = \dot{u}_0 + \ddot{u}_0 \cdot t + \left(\frac{\ddot{u}_0 + \ddot{u}_1}{\Delta t}\right) \cdot \frac{t^2}{2}$$

$\dot{u}_0$

$$\dot{u}_1 = \dot{u}_0 + \frac{\Delta t}{2}(\ddot{u}_0 + \ddot{u}_1)$$

Displacement

$$u(t) = u_0 + \dot{u}_0 \cdot t + \ddot{u}_0 \frac{t^2}{2} + \left(\frac{\ddot{u}_1 - \ddot{u}_0}{\Delta t}\right)\frac{t^3}{6}$$

u_0

$$u_1 = u_0 + \dot{u}_0 \Delta t + \ddot{u}_0 \frac{\Delta t^2}{3} + \ddot{u}_1 \frac{\Delta t^2}{6}$$

Δt

t

t_0 t_1
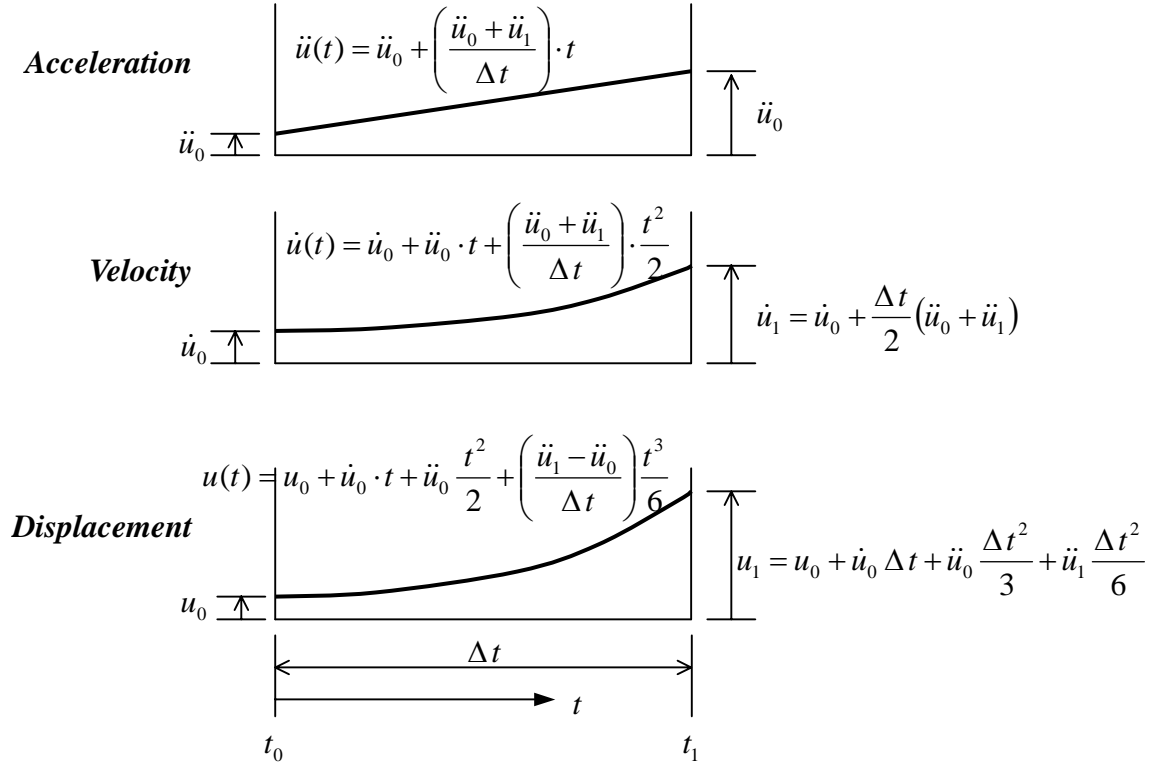
Figure 2.18   Motion based on the linear acceleration

$$\dot{u}_1 = \dot{u}_0 + (1 - \gamma)\Delta t\, \ddot{u}_0 + \gamma \Delta t\, \ddot{u}_1 \tag{2.41a}$$

$$u_1 = u_0 + \Delta t\, \dot{u}_0 + (\frac{1}{2} - \beta)\Delta t^2\, \ddot{u}_0 + \beta \Delta t^2\, \ddot{u}_1 \tag{2.41b}$$

where, $\dot{u}_1$, u_1 are the final velocity and displacement of each time step.   Similarly, $\dot{u}_0$, u_0 are the initial values velocity and displacement of each time step. Δt is the duration of time step.

It is evident in **Equation (2.41a)** that the factor γ provides a linear varying weighting between the influence of the initial and final accelerations on the change of the velocity.   Similarly, in **Equation (2.41b),** the factor β provides for weighting the contributions of these initial and final accelerations to the change of displacement.   When the factor is applied as $\gamma = 1/2$ in equations, the procedure is defined as Newmark β method.   Adopting this factor $\gamma = 1/2$ and setting $\beta = 1/4$ in **Equations (2. 41a)** and **(2. 41b)**, the Newmark formulation reduces linearly for the velocity as shown in **Figure 2.17**.   Thus, the Newmark $\beta = 1/4$ method is referred as the constant average acceleration method.   On the other hand, if β is taken to be 1/6 (with $\gamma = 1/2$), the acceleration varies linearly during the time step as shown in **Figure 2.18**.   These results also may be derived by the assumption of the linear acceleration method.   The constant average acceleration procedure is widely used in practice.   On the other hand, the

linear acceleration method is conditionally stable depending on the duration of time step, Δt. In the analysis, the constant average acceleration method is used.

However, this method for defining damping properties has no physical meaning and may lead to the damping for unexpected vibration mode shapes. From the study of the performance of this formulation (Hilber et al. 1977, Sing et al. 1991), it was noted that the factor γ controlled the amount of artificial damping induced by the step-by-step procedure; there was no artificial damping when $\gamma = 1/2$. In addition, if $\gamma > 1/2$, the numerical dissipation was present, and consequently it was possible to attain unconditionally stability and a favorable energy dissipation property if $\beta \geq 1/4 \, (\gamma + 0.5)^2$. In general, the Therefore, in the analysis of updated procedure, it is assumed that the viscous damping is neglected and the numerical damping of the Newmark method with factors $\beta = 0.36$ and $\gamma = 0.70$ is used as time integration (Committee 311 2002).

When RC structures are subjected to large ground motions, the nonlinear behavior may appear. Hence, it is necessary to iterate calculations until a sufficiently converged solution is obtained. In this study, the Newton-Raphson iteration method is used. The convergence criteria based on both force and energy criteria are used to detect the termination. The force criterion is determined from the out-of-balance force, which is equivalent to the difference between the external force and the summation of the inertial force, damping force and restoring force. In addition, the criterion for increments of the internal energy during the iteration is defined by the amount of work done by the out-of-balance force due to the displacement increment. In this study, the out-of-balance force and the energy increment are compared with their initial values during the iteration. Here, the convergence tolerances for the out-of-balance force and energy are set at 0.001 and 0.01, respectively.

References in Chapter 2

[1]   Clough, R. W. and Penzien, J. (1993): *Dynamics of Structures*, second edition, McGraw-Hill, Inc, Singapore.

[2]   Dhakal, R. P. (2000): *Enhanced Fiber Model in Highly Inelastic Range and Seismic Performance Assessment of Reinforced Concrete*, Doctoral thesis, The University of Tokyo, September.

[3]   Dhakal, R. P. and Maekawa, K. (2002a): Modeling for Postyield Buckling of Reinforcement, *Journal of Structural Engineering*, ASCE, Vol.128, No.9, pp.1139-1147, September.

[4]   Dhakal, R. P. and Maekawa, K. (2002b): Reinforcement Stability and Fracture of Cover Concrete in Reinforced Concrete Members, *Journal of Structural Engineering*, ASCE, Vol.128, No.10, pp.1253-1262, October.

[5]   Fukuura, N. and Maekawa, K. (1997): Computational Model of Reinforcing Bar under Reversed Cyclic Loading for RC Nonlinear Analysis, *Journal of Materials, Concrete Structures and Pavements*, JSCE, No.564/V-35, pp.291-295, May (in Japanese).

[6]   Hilber, H. M., Huges, T. J. R., and Taylor, R. L. (1977): Improved Numerical Dissipation for Time Integration Algorithms in Structural Dynamics, *Earthquake Engineering and Structural Dynamics*, Vol.5, pp.283-292.

[7]   Ideguchi, H., Matsumoto, S., and Maemura, M. (1988): Study on Distribution of Plastic Strain along a Steel Bar Subjected to Reversed Cyclic Loading and Calculating of the Steel Slip, *Proceeding of JSCE Annual Conference*, JSCE, Vol.431, No.5, pp.630-631 (in Japanese).

[8]   Kato, B. (1979): Mechanical Properties of Steel under Load Cycles Idealizing Seismic Action, *CEB Bulletin d'Information*, No. 131, pp.7-27, May.

[9]   Mander, J. B., Priestley, M. J. N., and Park, R. (1988): Theoretical Stress-Strain Model for Confined Concrete, *Journal of Structural Engineering*, ASCE, Vol.114, No.8, pp.1804-1826, August.

[10] Miki, T., Niwa, J., and Lertsamattiyakul, M. (2003): Numerical Evaluation of Seismic Performance of Reinforced Concrete Bridge Piers Using Dynamic Lattice Model, *Concrete Library of JSCE*, Vol.41, pp.49-64, June.

[11] Mishima, T., Bujadham, B., Maekawa, K., and Okamura, H. (1992): A Development of Constituent Material Models for a Reinforced Concrete Discrete Crack, *Journal of Materials, Concrete Structures and Pavements*, JSCE, No.422/V-16, pp.171-179, February.

[12] Niwa, J., Choi, I.C., and Tanabe, T. (1995): Analytical Study for Shear Resisting Mechanism Using Lattice Model, *Concrete Library of JSCE*, No.26, pp.95-109, December.

[13] Okamura, H. and Maekawa, K. (1991): *Nonlinear Analysis and Constitutive Models of Reinforced Concrete*, Gihodo-Shuppan, May.

[14] Shima, H., Chou, L., and Okamura, H. (1987): Micro and Macro Models for Bond Behavior in Reinforced Concrete, *Journal of the Faculty of Engineering*, The University of Tokyo (B), Vol.39, No.2, pp.133-194.

[15] Shin, H., Maekawa, K., and Okamura, H. (1988): Analytical Approach of RC Members Subjected to Reversed Cyclic In-plane Loadings, *Proceeding of the JCI Colloquium on Ductility of Concrete Structures and its Evaluation*, pp.(II-45)-(II-56), March (in Japanese).

[16] Shing, P. B., Vannan, M. T., and Cater, E. (1991): Impact Time Integration for Pseudo Dynamic Tests, *Earthquake Engineering and Structural Dynamics*, Vol.20, pp.551-576.

[17] Subcommittee for Damage Analysis of Concrete Structures Caused by Hanshin-Awaji Great Earthquake (Committee 311) (2002): *Verification of Procedures of Seismic Performance Evaluation based on Damage Analysis for Hanshin-Awaji Earthquake -Comparison of Analytical Procedures and its Application-*, Concrete Engineering Series No.49, December (in Japanese).

[18] Tsuchiya, S., Tsuno, K., and Maekawa, K. (2002): Three-dimensional FE Solid Response Analysis of RC Columns Subjected to A Combination of Permanent Eccentric Axial Force and Reversed Cyclic Torsion and Bending/Shear, *Concrete Library of JSCE*, Vol.39, pp.237-251, June.

[19] Uchida, U., Rokugo, K., and Koyanagi, W. (1991): Determination of Tension Softening Diagrams of Concrete by Means of Bending Tests, *Journal of Materials, Concrete Structures and Pavements*, JSCE, No.426/V-14, pp.203-212, February (in Japanese).

[20] Vecchio, F. J. and Collins, M. P. (1986): The Modified Compression Field Theory for Reinforced Concrete Elements Subjected to Shear, *ACI Journal*, Vol.83, No.2, pp.219-231, March/April.

3   DEVELOPMENT AND VERIFICATION OF 3D LATTICE MODEL

3.1   Introduction

The representation of a RC structure by the 3D model is necessary to treat the geometries and loading conditions that cannot be expressed by the 2D model.   The extension from the 2D lattice model to the 3D lattice model, which is an assembly of space trusses, is explained in this chapter.   In the previous study, it has been confirmed that the 2D lattice model analysis can appropriately predict the 2D response of RC structural members subjected to the monotonic or reversed cyclic loading (Niwa et al. 1995, Miki et al. 2003a, 2003b).   Hence, the enhancement of the lattice model to 3D analytical model is performed based on the concept of the conventional 2D lattice model.   In order to verify the performance of RC structures subjected to reversed cyclic loading, an appropriate configuration of 3D lattice components should be determined.   The schematic representation of the 3D lattice model is shown in **Figure 3.1**.   As for example of RC structure, a RC column is shown in the figure.

Assumption of plane stress

b: Width of cross section
d: Effective depth
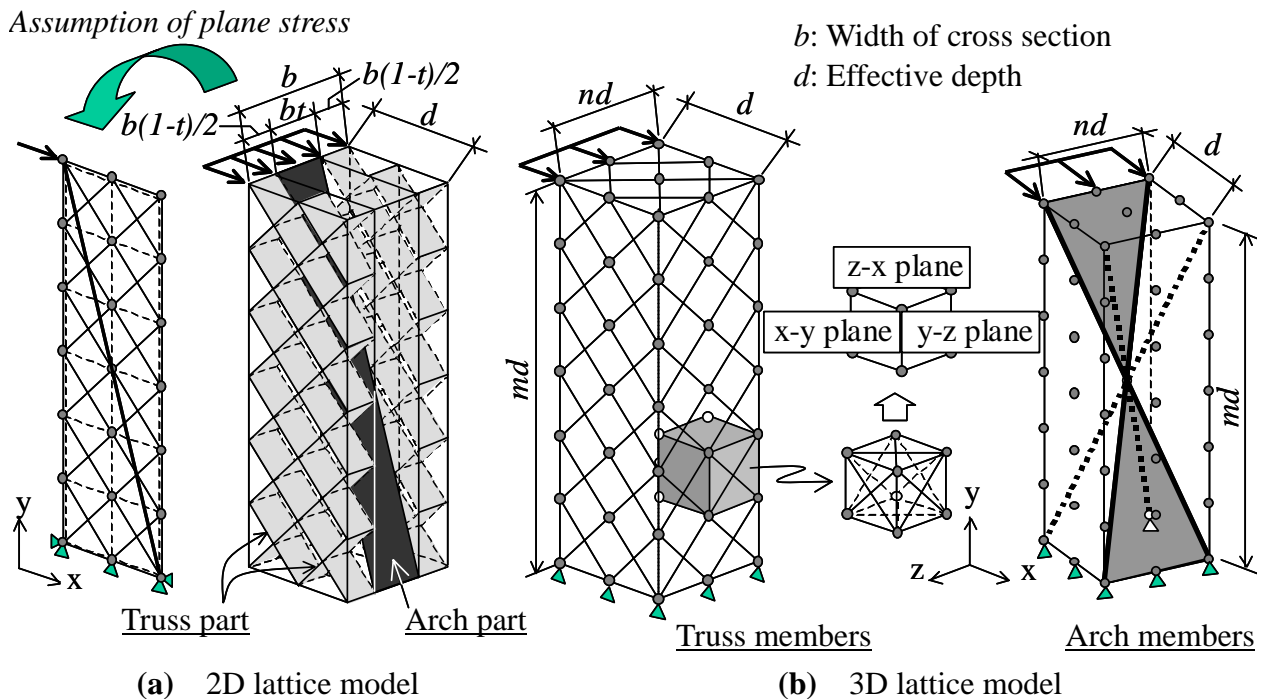
Figure 3.1   Discretization for the 2D and 3D lattice models

(a)   2D lattice model   (b)   3D lattice model

3.2 Configurations of Each Element in 3D Lattice Model

In the lattice model, the shear resisting mechanism is divided into arch action and truss action. As for the 2D lattice model, a RC member in 3D is modeled into 2D lattice model according to the plane stress condition as shown in **Figure 3.1 (a)**. Here, in the 3D lattice model, four arch members are arranged by connecting between the top and the bottom of the column at the opposite corners as illustrated in **Figure 3.1 (b)**. The resisting mechanism of a RC column subjected to one certain load consists of two arch members crossing each other. The stiffness of these arch members is assumed to be equivalent to one of two arch members in the 2D lattice model that is described later.

When lateral load is applied on the RC column from the diagonal direction of the section, it is assumed that the corner-to-corner arch action (from the loading point to the bottom of a column at opposite corner) inside the RC member is idealized as a compressive strut. That is represented by these arch members in the 3D lattice model. In addition, when the direction of lateral load is reversed, the direction of internal flow of compressive stresses is changed to intersect the former one as shown in **Figure 3.2**. Considering this situation, two couples of arch members are incorporated into the model symmetrically.

To represent the truss action, it is assumed that 3D space is comprised of an orthogonal coordinate system that is defined by three planes, such as x-y plane, y-z plane, and z-x plane. Two crossed truss members are located on each truss plane so that unit element consists of 12 truss members in six truss planes as shown in **Figure 3.1 (a)**. In each truss plane, the in-plane 2D constitutive law of concrete, with the consideration of the softening of compressive strength of diagonally cracked concrete depending on the transverse tensile
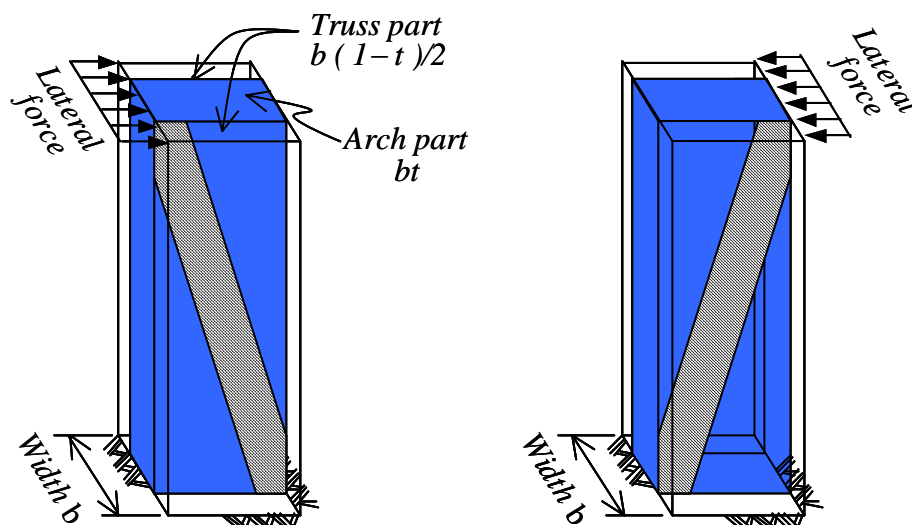
**Figure 3.2**   Idealization of internal flow of compressive stresses

strain (Vecchio and Collins 1986), can be used.   The validity of configuration for the 3D lattice model is verified by comparing with the results of the 2D lattice model.

3.3   Determination of Value of t

The value of t is defined by the ratio of the arch part width to the cross-sectional width of a RC member in the 2D lattice model as mentioned previously.   Assuming the global stiffness of 3D lattice model to be equivalent to that of 2D lattice model, the cross-sectional area of the arch member can be identified.   The schematic representation about the division of cross-section of the 3D lattice model is shown in **Figure 3.3**.   Here, the ratios of the arch part width to the width, b and the depth, d in the cross section of the column are defined by t_b and t_d, respectively.

With the determination of value of t in the 3D lattice model, both the cross-sectional width of the column and the cross-sectional depth of the column are evaluated in preliminary analysis. According to the 2D lattice model, the values of t_b and t_d in the 3D lattice model are determined based on the theorem of minimization of the total potential energy.   In the pre-analysis, the values of t_b and t_d are varied for each from 0.05 to 0.95 with an interval of 0.05.   Then the values of t_b and t_d are identified in which the total potential energy calculated in the pre-analysis is minimized.   The distribution of total potential energy obtained by the 3D lattice model with different values of t is shown in **Figure 3.4**.   From this figure, the values of t_b and t_d are determined to be 0.35 and 0.25, respectively.

The strain energy is calculated from stresses and strains of each lattice component when a small displacement is provided to the model at the loading point.   According to the procedure using in the 2D lattice model, the small provided displacement is fixed as 0.1% of
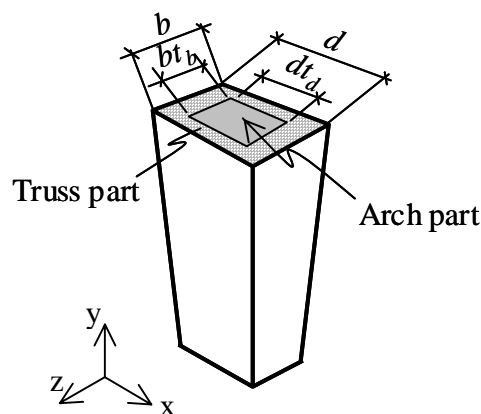
Figure 3.3   Partition of cross section in the 3D lattice model

Total potential energy (N-m)
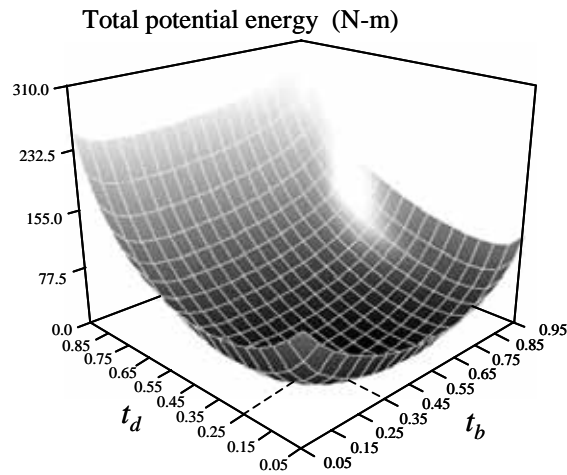
Figure 3.4   Total potential energy distribution calculated in the 3D lattice model

the shear span in this study.   It is obvious that, when a structure is subjected to large deformations, significant material nonlinearity is observed and the values of t may vary as the deformation increases.   In this study, even though the deformation becomes large, the values of t_b and t_d obtained with the initial stiffness are used as an approximation for simplicity, similar to the 2D lattice model analysis.

Here, it is assumed that the value of t calculated using the small displacement along the main loading direction is used to determine the cross-sectional area of an arch member in normal to the loading direction.   This assumption may not be suitable in the case that the depth and width of rectangular cross-section are comparatively different such as a wall-type RC column. In this study, however, this assumption is applied for simplicity and the values of t_b and t_d obtained by this method are used in the following analyses.

3.4   Modeling of Each Element

3.4.1   Concrete elements

In order to determine the configuration of the 3D lattice model, the cross-sectional area of arch members and truss members in the 3D lattice model will be derive as follows.

Arch members

The arch members assumed in the 2D lattice model and 3D lattice model are illustrated in **Figure 3.5**.   Now the global stiffnesses of 2D lattice model and 3D lattice model are

52

(a) 2D lattice model   **(b)** 3D lattice model
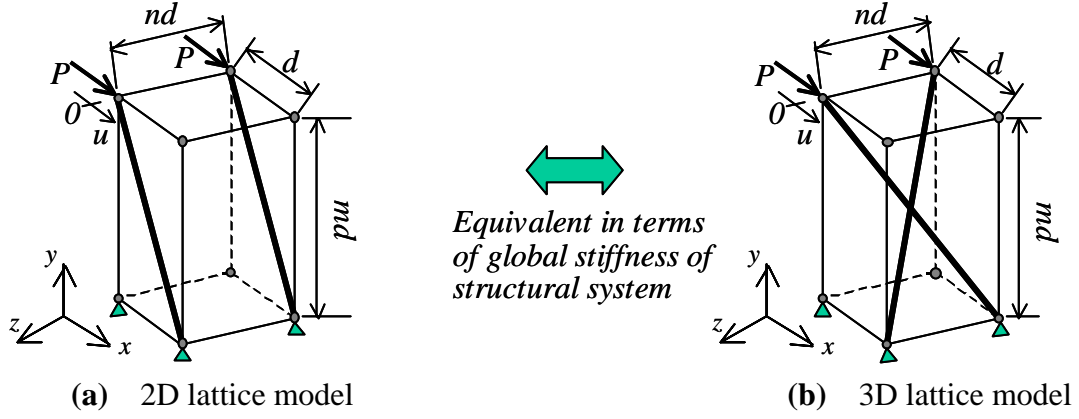
Fig. 3.5   Arch members in the 2D and 3D lattice model

compared with each other.   The equilibrium equation of local element is expressed as follows (Holzer 1985):

$$f = kd \tag{3.1}$$

$$k = \begin{bmatrix} k_{aa} & k_{ab} \\ k_{ba} & k_{bb} \end{bmatrix} = \gamma \begin{bmatrix} 1 & -1 \\ -1 & 1 \end{bmatrix} \tag{3.2}$$

where

$$\gamma = \frac{EA}{l} \tag{3.3}$$

in which k, d, and f are the stiffness matrix, the displacement vector, and the force vector of the local element, respectively. E, A, and l are the tangent stiffness, the cross-sectional area, and the length of element, respectively.

In the global coordinate system, the global element stiffness matrix, K can be obtained from the local element stiffness, k through the transformation as follows:

$$K = \Lambda^T k \Lambda \tag{3.4}$$

where

$$\Lambda = \begin{bmatrix} \lambda & 0 \\ 0 & \lambda \end{bmatrix} = \begin{bmatrix} c_1 & c_2 & c_3 & 0 & 0 & 0 \\ 0 & 0 & 0 & c_1 & c_2 & c_3 \end{bmatrix} \tag{3.5}$$

$$\lambda = \frac{\Delta X}{|\Delta X|} = \begin{bmatrix} c_1 & c_2 & c_3 \end{bmatrix} \tag{3.6}$$

$$\Delta X = X_k - X_j \tag{3.7}$$

Thus,

$$
K = \frac{EA}{l}
\begin{bmatrix}
c_1^2 & c_1 c_2 & c_1 c_3 & -c_1^2 & -c_1 c_2 & -c_1 c_3 \\
 & c_2^2 & c_2 c_3 & -c_1 c_2 & -c_2^2 & -c_2 c_3 \\
 & & c_3^2 & -c_1 c_3 & -c_2 c_3 & -c_3^2 \\
 & & & c_1^2 & c_1 c_2 & c_1 c_3 \\
 & \textit{sym.} & & & c_2^2 & c_2 c_3 \\
 & & & & & c_3^2
\end{bmatrix}
\tag{3.8}
$$

In **Equation 3.8**, c_i is a scalar value that is the direction cosine of the longitudinal axis of local element related to the global i axis. Similarly, X_j and X_k are the coordinate vectors at each end of the element, respectively and the difference vector ΔX coincides with the element axis.

For the arch members in the 2D lattice model illustrated in **Figure 3.5 (a)**,

$$
\Delta X_1 = \Delta X_2 = \begin{bmatrix} d & md & 0 \end{bmatrix}
\tag{3.9}
$$

$$
\therefore \lambda_1 = \lambda_2 = \frac{\Delta X_1}{|\Delta X_1|} = \frac{\Delta X_2}{|\Delta X_2|} = \begin{bmatrix} \dfrac{1}{\sqrt{1+m^2}} & \dfrac{m}{\sqrt{1+m^2}} & 0 \end{bmatrix}
\tag{3.10}
$$

Thus, the global stiffness matrix is obtained as follows:

$$
K_{2D} = 2\gamma_{2D}
\begin{bmatrix}
\dfrac{1}{1+m^2} & \dfrac{m}{1+m^2} & 0 & -\dfrac{1}{1+m^2} & -\dfrac{m}{1+m^2} & 0 \\
 & \dfrac{m^2}{1+m^2} & 0 & -\dfrac{m}{1+m^2} & -\dfrac{m^2}{1+m^2} & 0 \\
 & & 0 & 0 & 0 & 0 \\
 & & & \dfrac{1}{1+m^2} & \dfrac{m}{1+m^2} & 0 \\
 & & & & \dfrac{m^2}{1+m^2} & 0 \\
 & \textit{sym.} & & & & 0
\end{bmatrix}
\tag{3.11}
$$

where,

$$
\gamma_{2D} = \frac{EA_{arch-2D}}{l_{arch-2D}} = \frac{EA_{arch-2D}}{\sqrt{1+m^2}\,d}
\tag{3.12}
$$

in which $A_{arch\text{-}2D}$ is the cross-sectional area of arch members in the 2D lattice model. The values of m, n are determined in which md and nd correspond the width of cross section and the height of the column in the model, respectively. Here, d is the effective depth of cross section. For example, in the 3D lattice model as shown in **Figure 3.1 (b)**, m and n are equal to 1 and 3, respectively.

As for the arch members in 3D lattice model illustrated in **Figure 3.5 (b)**,

$$\Delta X_1 = \begin{bmatrix} d & md & nd \end{bmatrix} \tag{3.13}$$

$$\Delta X_2 = \begin{bmatrix} d & md & -nd \end{bmatrix} \tag{3.14}$$

$$\therefore \lambda_1 = \frac{\Delta X_1}{|\Delta X_1|} = \begin{bmatrix} \dfrac{1}{\sqrt{1+m^2+n^2}} & \dfrac{m}{\sqrt{1+m^2+n^2}} & \dfrac{n}{\sqrt{1+m^2+n^2}} \end{bmatrix} \tag{3.15}$$

$$\lambda_2 = \frac{\Delta X_2}{|\Delta X_2|} = \begin{bmatrix} \dfrac{1}{\sqrt{1+m^2+n^2}} & \dfrac{m}{\sqrt{1+m^2+n^2}} & \dfrac{-n}{\sqrt{1+m^2+n^2}} \end{bmatrix} \tag{3.16}$$

Hence, the global stiffness is obtained as follows:

$$K_{3D} =$$

$$2\gamma_{3D} \begin{bmatrix} \dfrac{1}{1+m^2+n^2} & \dfrac{m}{1+m^2+n^2} & 0 & -\dfrac{1}{1+m^2+n^2} & -\dfrac{m}{1+m^2+n^2} & 0 \\ & \dfrac{m^2}{1+m^2+n^2} & 0 & -\dfrac{m}{1+m^2+n^2} & -\dfrac{m^2}{1+m^2+n^2} & 0 \\ & & \dfrac{n^2}{1+m^2+n^2} & 0 & 0 & \dfrac{-n^2}{1+m^2+n^2} \\ & & & \dfrac{1}{1+m^2+n^2} & \dfrac{m}{1+m^2+n^2} & 0 \\ & & & & \dfrac{m^2}{1+m^2+n^2} & 0 \\ & \text{sym.} & & & & \dfrac{-n^2}{1+m^2+n^2} \end{bmatrix} \tag{3.17}$$

where

$$\gamma_{2D} = \frac{EA_{arch-3D}}{l_{arch-3D}} = \frac{EA_{arch-3D}}{\sqrt{1+m^2+n^2}\,d} \tag{3.18}$$

in which $A_{arch\text{-}3D}$ is the cross-sectional area of arch members in the 3D lattice model.

By assuming that the global stiffness of 3D lattice model is equal to that of 2D lattice model,

and that the displacement along z axis at the loading point is zero, the cross-sectional area of the arch member can be calculated from the **Equations 3.20** and **3.21**.

$$\frac{2\gamma_{2D}}{1+m^2} = \frac{2\gamma_{3D}}{1+m^2+n^2} \tag{3.19}$$

Thus,

$$A_{arch-3D} = \left(\frac{1+m^2+n^2}{1+m^2}\right)^{\frac{3}{2}} \cdot A_{arch-2D} \tag{3.20}$$

$$A_{arch-2D} = \frac{1}{2}bt_b \cdot dt_d \cdot \sin\theta \tag{3.21}$$

where, values of m and n indicate that md and nd are the cross-sectional width and the height of the column, respectively as mentioned previously.

In the modeling, the height of the lattice model is not always equal to the height of the column because the horizontal or vertical distance of two adjoining nodes is determined based on the half of the effective depth d. Hence, the height and the width of the 3D lattice model are set on the dimensions of the structure comparatively close to actual dimensions.
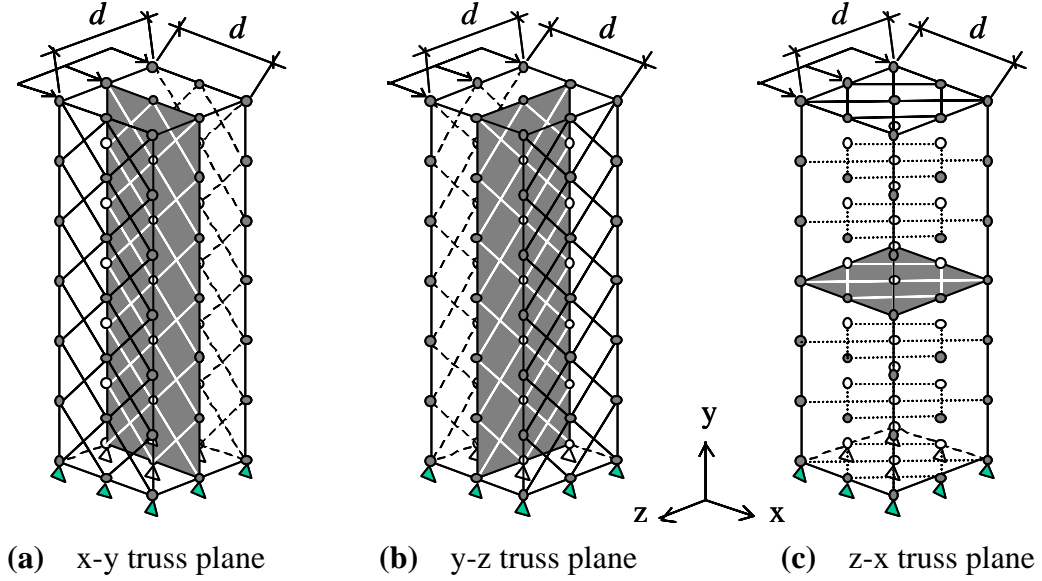
Truss members

Next, the determination for the cross-sectional area of truss members is described. In the 2D lattice model, the width of the lattice model is assumed to be the effective depth in the cross section of a column. Hence, the horizontal or vertical distance of two adjoining nodes is equal to $0.5d$, and then the thickness of the truss members on the side view of the column is equal to $0.5d\cdot\sin45°$. In order to represent the truss mechanism along the principal direction in 3D space, it is assumed that the cross-sectional area of truss members inside a RC column is a half of that at the surface of the column. The cross-sectional areas of truss members in x-y plane, y-z plane, and z-x plane illustrated in **Figure 3.6** by hatching are expressed as the following equations (**Equations 3.21** to **3.23**).

$$A_{truss-xy} = \frac{b(1-t_b)}{2m} \cdot \frac{d}{2}\sin45° \tag{3.21}$$

$$A_{truss-yz} = \frac{h(1-t_d)}{2} \cdot \frac{d}{2}\sin45° \tag{3.22}$$

$$A_{truss-zx} = \frac{a}{2n} \cdot \frac{d}{2}\sin45° \tag{3.23}$$

(a) x-y truss plane **(b)** y-z truss plane **(c)** z-x truss plane

Figure 3.6 Truss planes in the 3D lattice model

where, $A_{tsuss\text{-}xy}$, $A_{tsuss\text{-}yz}$, and $A_{tsuss\text{-}zx}$ are the cross-sectional areas of truss members in x-y plane, y-z plane, and z-x plane, respectively. b, h, and a represent the cross-sectional width, the cross-sectional height, and the shear span of the column, respectively.
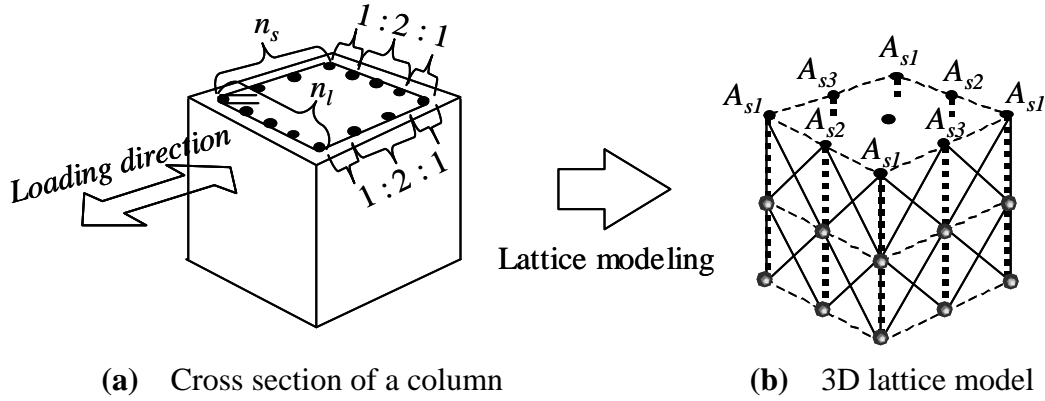
3.4.2 Reinforcement elements

For longitudinal reinforcement and transverse reinforcement, horizontal and vertical members are used. Of course, each reinforcement member is determined based on the actual cross section and actual location of reinforcements. **Figure 3.7** shows the example of the arrangements of longitudinal and transverse reinforcements at the single layer in which there is no intermediate ties. Here, the longitudinal reinforcement is divided into eight elements in one layer as illustrated in **Figure 3.7 (b)**. It is assumed that the cross-sectional areas of reinforcement along the side perpendicular or parallel to laterally loading direction are divided at a ratio of 1:2:1 (**Figure 3.7 (a)**). The cross-sectional areas of members of longitudinal reinforcement are expressed as the following equations (**Equations 3.24** to **3.26**).

$$A_{s1} = \left(\frac{n_l}{4} + \frac{n_s}{4} - 1 \right) \cdot A_l \qquad (3.24)$$

$$A_{s2} = \frac{n_l}{2} \cdot A_l \qquad (3.25)$$

$$A_{s3} = \frac{n_s}{2} \cdot A_l \qquad (3.26)$$

(a) Cross section of a column   **(b)** 3D lattice model

Figure 3.7   Arrangements of longitudinal and transverse reinforcements

where, A_{s1}, A_{s2}, and A_{s3} are the cross-sectional areas at the corner of section, at the middle of tension extreme fiber, and at the middle of the side parallel to laterally loading direction, respectively. Similarly, A_l is the cross-sectional area of longitudinal reinforcement. Here, n_l and n_s are the number of longitudinal reinforcement along with the side perpendicular and parallel to laterally loading direction, respectively.

As for transverse reinforcement, in the analysis, only the effect of the shear reinforcement ratio on the plastic deformation of the member is considered, while the intervals in reinforcement arrangement are not taken into account. In the lattice model, the transverse reinforcement is arranged at intervals of $0.5d$ throughout the model uniformly so that the actual transverse reinforcement ratio equals the model transverse reinforcement ratio. The transverse reinforcement ratio, r_w of an actual RC structural member is calculated by the following equation.

$$r_w = \frac{A_w}{b_w \cdot s}$$
(3.27)

where A_w is the cross-sectional area of a couple of transverse reinforcements, b_w is the width of the cross section of the RC member, and s is the transverse reinforcement spacing.

Hence, if the actual transverse reinforcement ratio equals the model transverse reinforcement ratio, the cross-sectional area of the transverse reinforcement members in the 3D lattice model, $A_{w\text{-}lattice}$ is obtained as follows:

$$A_{w-lattice} = \frac{0.5d}{s} \cdot A_w$$
(3.28)
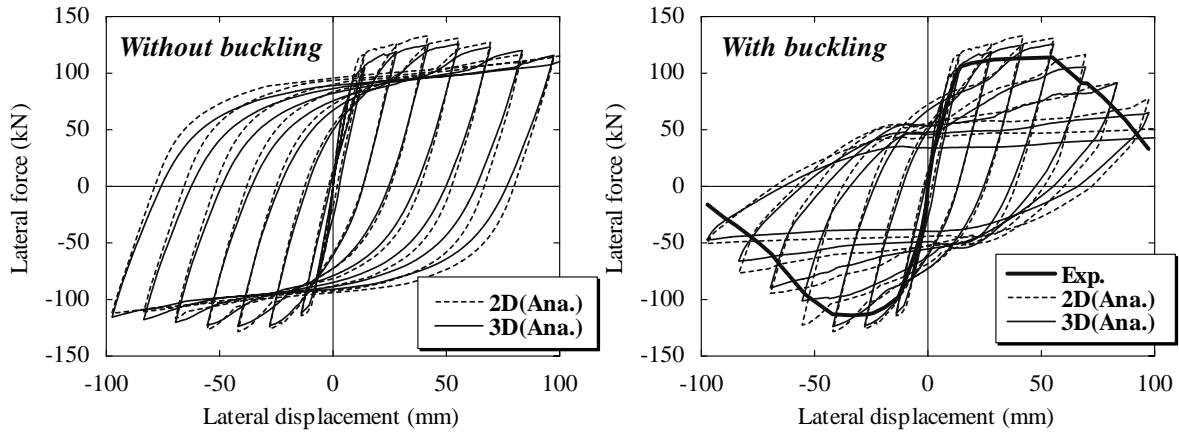
Figure 3.8　Lateral force-lateral displacement calculated from the 2D and 3D lattice model analyses

3.5　Verification of 3D Lattice Model by Using Results of 2D Analysis

To verify the accuracy of the 3D lattice model, the comparative analyses are performed using 2D and 3D lattice models. A rectangular column is considered with the following parameters: $f_c' = 27.0$ N/mm^2, $f_y = 380$ N/mm^2, $E_s = 172$ kN/mm^2, $f_{wy} = 360$ N/mm^2, and $E_{sw} = 175$ kN/mm^2. The longitudinal and transverse reinforcement ratios are set as 2.38 % and 0.056 %, respectively. The Constant compressive axial force of 79.7 kN is applied at the top of the column. The details of the specimen are descried in **section 4.4**. The relationships of lateral force-lateral displacement at the top of the column calculated from 2D and 3D lattice model analyses with and without considering the buckling of reinforcing bars are shown in **Figure 3.8**. In the figure, the experimental results are also shown as an envelope curve of lateral force-lateral displacement relationship. It can be observed from the figure that the results of 2D and 3D lattice model analyses are very close to each other in terms of the overall behavior of RC columns. The analysis can predict the post-peak behavior after the lateral displacement of around 50 mm. It is confirmed that the 3D lattice model analysis can predict the load carrying capacity and the post-peak behavior with similar accuracy of 2D analysis.

Strictly speaking, the load carrying capacity and energy dissipation capacity in the 3D lattice model analysis are slightly reduced as compared with those in the 2D analysis. This is due to the configuration of 3D lattice model. In the modeling of 3D lattice model, it is assumed that the cross-sectional area of truss members inside a RC column is half of that at the surface of the column. Because of this assumption, the truss members are not located uniformly along the depth direction even if the assumption of plane stress condition is possible.

According to the experimental results (Kinugasa and Nomura 2000, Itoh and Ichinose 1999), the discrepancy of the assumption of plane stress condition seems to be correct for the prediction of behavior at large deformation range. Consequently, the analysis by 3D lattice model can predict the load carrying capacity and the post-peak behavior accurately.

As observed in this figure, the 3D analysis can accurately predict the stiffness in the force-displacement curve, the force and the displacement at the peak, and the post-peak response as well. The softening behavior of lateral force in the post-peak region can also be evaluated appropriately. The comparison between the experimental and analytical results shows the good agreement between these two results. Conclusively, it is found that 3D lattice model analysis can appropriately predict the overall behavior of RC columns including the post-peak response.

3.6 Sensitivity Analysis

3.6.1 Introduction

The comparison between 2D and 3D analyses in the previous section has confirmed that the 3D lattice model had the similar accuracy to the 2D lattice model. Through the previous discussions, it can be recognized that the configurations of 3D lattice model can be appropriately conducted based on the concept of 2D lattice model. Herein, a quantitative interrelationship between several parameters and predictions by the 2D lattice model is analytically assessed. The parameters are including the mesh size, the value of t, and the numbers of iteration of the calculation. A rectangular RC column is used that is identical to that used in **section 3.5**. To investigate the influence of the parameters on the performance of the 2D lattice model, the buckling of reinforcement is neglected in the analysis.

3.6.2 Parametric study

Mesh size sensitivity

In order to verify the mesh size sensitivity in the 2D lattice model, two different meshes are investigated. In the analysis, a standard mesh as commonly used in the analysis, in which the adjusting nodal distance is fixed as $0.5d$, and a finer mesh fixed as $0.25d$ are considered. The analytical results as shown in **Figure 3.9** show that there is no significant difference between the standard and fine meshes. The analytical force at the initial cracking using the
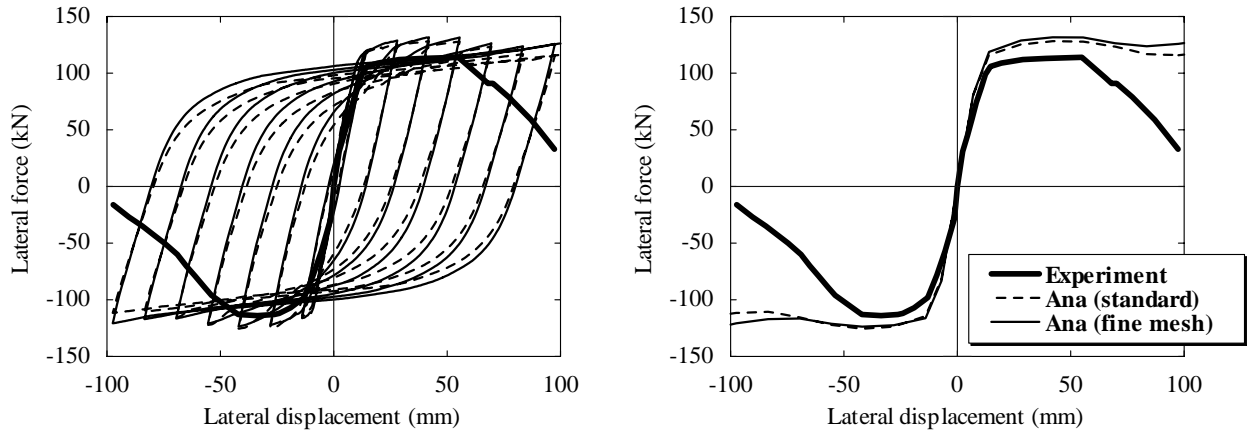
Figure 3.9   Mesh size sensitivity

finer mesh is also similar to the result using the standard mesh size.   The overall behavior with the standard size mesh is found to be close to the results with the finer mesh.

However, the computation time is significantly increasing because of the increase in the number of degrees of freedom.   The computing time is strongly depending on the analytical degrees of freedom.   Although the computing time is shorter than other commonly used FE analysis even if the finer mesh set as $0.25d$ is used, the standard mesh is better to use from the viewpoint of a practical use.   From the results, it is found that the accuracy is enough to predict the overall response of RC columns, though the mesh size fixed to the $0.5d$ seems rough meshing.

Effect of value of t

As mentioned previously, the analysis by the 2D lattice model is carried out using the value of t that is determined based on the principle of minimization of total potential energy.   In order to investigate the effect of the value of t on the analytical results, the cyclic analyses of the laterally loaded columns are carried out with several different values of t.   The results of lateral force-displacement relationships are illustrated in **Figure 3.10**.   For this column, it is confirmed in the pre-analysis that the value of t is obtained as 0.20.

In case of smaller value of t, it can be seen that higher energy dissipation capacity is predicted up to the large deformation range.   As the value of t increases, the maximum force increases slightly.   In the cases that the values of t are 0.20, 0.30, and 0.40, the stable lateral force-lateral displacement relationships are predicted.   The behavior shows the good agreement with the experimental observation.   In the case of large value of t, the deformation capacity decreases and the decrease in the force after diagonal cracks occurs in the analysis.

61
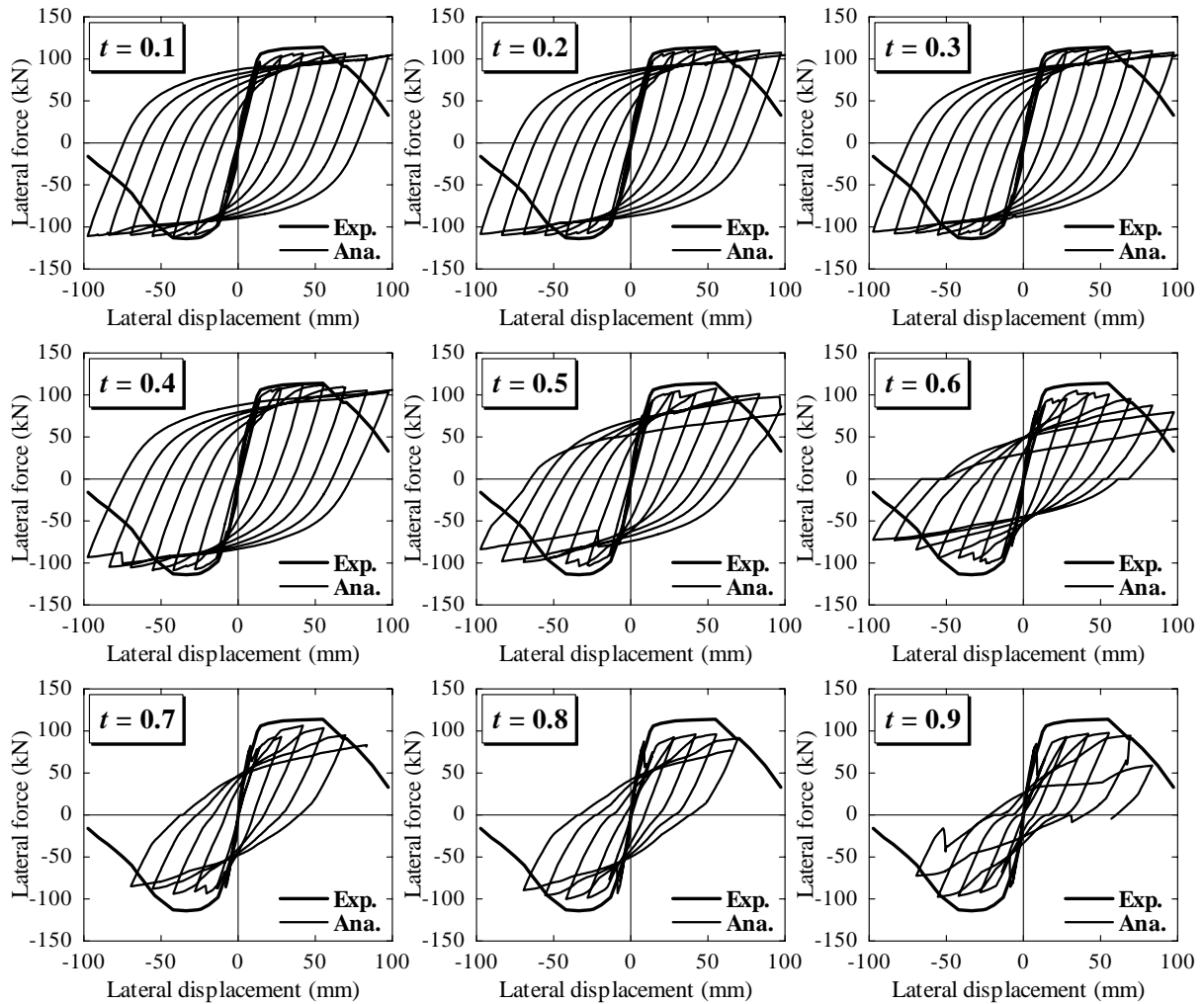
Figure 3.10   Effect of the value of t

By using the appropriate value of $t = 0.2$, which is determined from the principal of the minimization of total potential energy in this column, the analytical force-displacement curve is found to be show the good agreement with the experimental results before the buckling of reinforcement occurs.   From the results, it is recognized that the value of t determined from the principle of minimization of total potential energy is suitable for the modeling in terms of the prediction of load carrying capacity.   The analysis can predict reasonable behavior by considering the load resisting mechanism represented by both arch and truss actions and the appropriate proportion between arch and truss.

Here, in the experiment, the RC column failed in flexure after the yielding of longitudinal reinforcement and then the compressive crushing at the bottom of a column was observed. In this case, the localization of concrete crushing did not become significant.   If the localized failure takes place, the element length should be evaluated as compared with the localized failure zone observed in the experiment.   In addition, it is necessary to consider the

compressive localized failure zone of concrete in predicting the post-peak response if the compressive model of concrete using the average stress-average strain relationship includes the post-peak behavior. These matters should be studied in further research to improve the accuracy of the lattice model analysis for the post-peak prediction of the RC member that fails in the diagonal compressive failure.

Influence of iterative calculation number

Since the nonlinear responses appear when RC structures are subjected to large ground motions, it is necessary to iterate the calculation until a sufficiently converged solution is obtained. In the iteration, the convergence criteria based on both force and energy are used to detect the termination. In this study, the out-of-balance force and the energy increment are compared with initial values during the iteration. Here, the convergence tolerances for the out-of-balance force and energy are set as 0.001 and 0.01, respectively. However, the iteration does not always terminate by satisfying with these criteria. Hence, a limiting value of number of iteration is pre-determined. When the limiting value is inappropriate, the prediction cannot be performed completely.

The controlled displacement interval also may influence on the accuracy of calculation. In this section, the influence of the limiting number of iteration and the interval of controlled displacement on the analytical response is investigated. These analytical results are illustrated in **Figure 3.11**.

Figure 3.11 (a) shows the lateral force-lateral displacement relationships with varying the number of iteration of the calculation. From the figure, it is found that first branch depending on the number of iteration is the point at the initiation of flexural crackling. Similarly, second point is found to be at the yielding of longitudinal reinforcement. When the number of iteration is small such as 10 times, the convergence is insufficient and consequently, the lateral force- lateral displacement is found to be different from the experiment. The load gradually continues to increase after the longitudinal reinforcement yields. On the other hand, in the case with large number of iteration, the force-displacement curves are found to be close to the experimental result. Matching with the experimental observation, the load slightly increases after the longitudinal reinforcement yields. The tendency is observed in the case that the number of iteration exceeds 40 times. In this study, the number of iterative calculation is set to 50 as a sufficient value to detect the termination.

Figure 3.11 (b) shows the lateral force-lateral displacement relationships with various intervals of controlled displacement. It can be observed in the figure that in all cases the
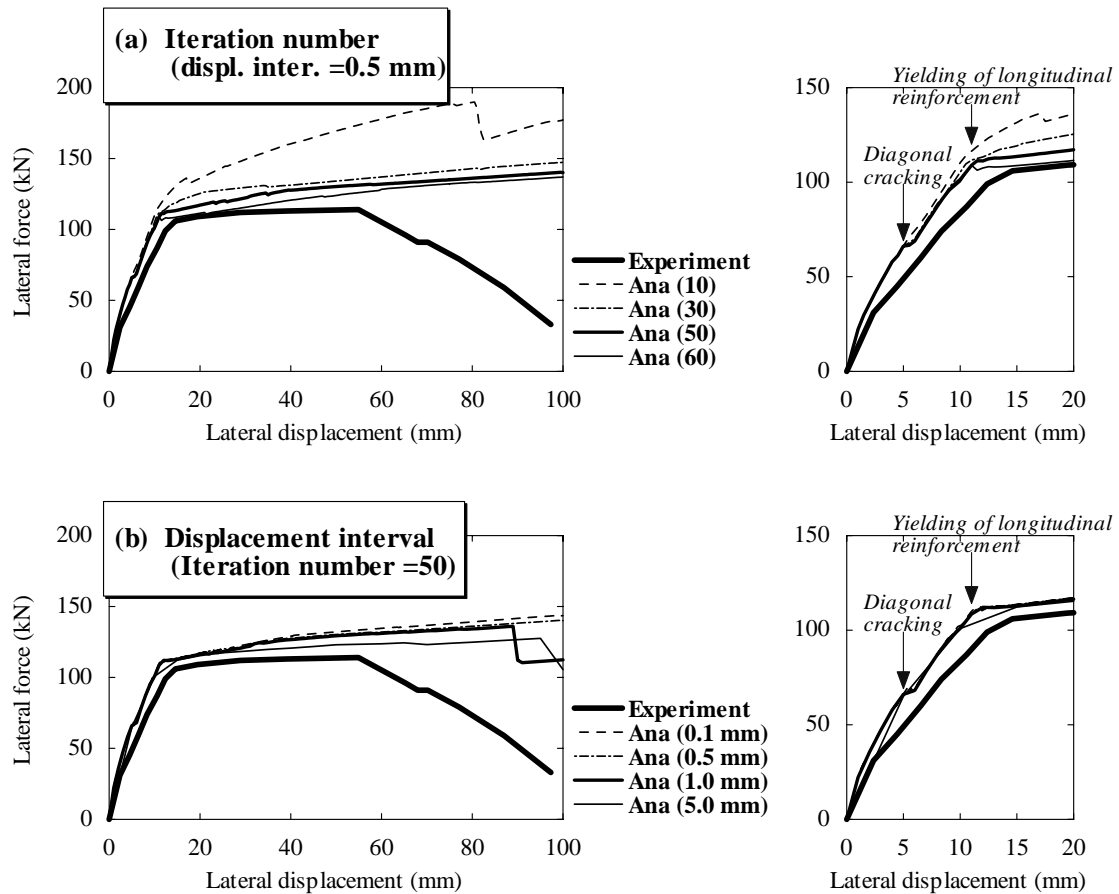
Figure 3.11   Influence of number of iteration and controlled displacement interval

slight difference is observed with each other.   Although the increase in the load is observed in case of 5.0 mm of displacement interval, the response before the longitudinal reinforcement yields is rough.   The interval of controlled displacement is set to 0.5 mm as a sufficient value to predict appropriate response in this study.   Although the verification is performed for laterally loaded RC column, the tendency is confirmed to be similar for other cases including both flexural or shear dominant RC columns and beams.

Longitudinal reinforcement parallel to loading direction

In the lattice model, the cross-sectional areas of reinforcement along the side perpendicular and parallel to laterally loading direction are divided into a ratio of 1:2:1 as shown in **Figure 3.12**.   In this section, the influence of the modeling method of longitudinal reinforcement at the side parallel to the loading direction is verified.   The analytical results are shown in **Figure 3.13**.   In this figure, the case of "0:0:0" is denoted the column neglected the side reinforcement.   In addition, in the case of "1:1:1", the cross-sectional areas of reinforcement at the side are divided into a ratio of 1:1:1.   Similarly, in the cases of "1:2:1" and "1:5:1", the cross-sectional areas of reinforcement at the side are divided into ratios of 1:2:1 and 1:5:1,

64

respectively.

In the case of "0:0:0", the load carrying capacity is lower than other cases, because the longitudinal reinforcement resisting to flexural tension is underestimated by neglecting the contribution of longitudinal reinforcement at the side of cross section. Other three cases show reasonable prediction for the load carrying capacity, though higher than the experimental results. In addition, a difference between these cases is not observed, in which the ratio of division of longitudinal reinforcements at the side for each is varied. It is recognized that the interval of controlled displacement of 0.5 mm is useful to obtain a sufficient value to perform the reasonable prediction.
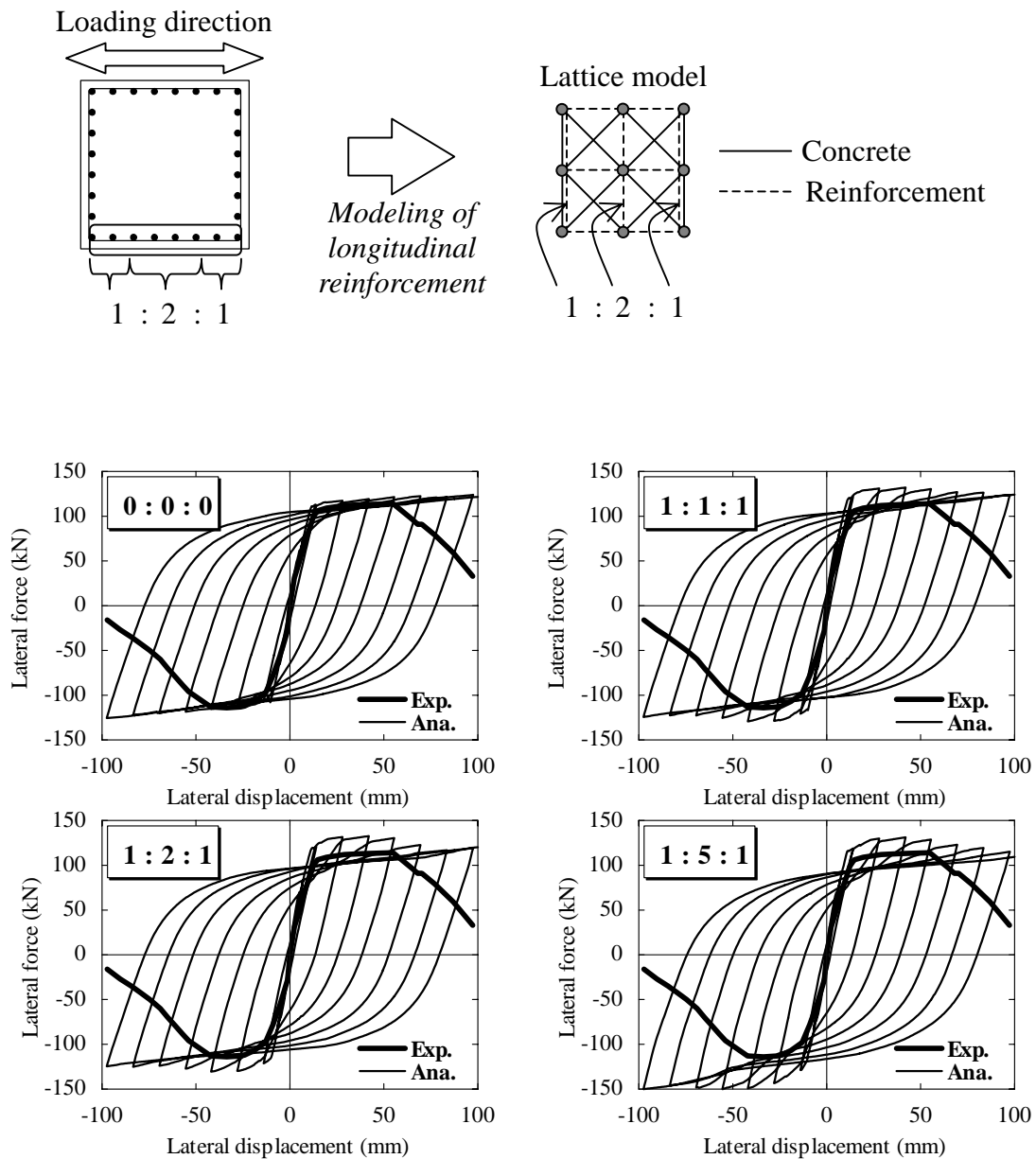

Figure 3.13 Influence of modeling method of side reinforcement

Axial force

In the previous section, the effect of the modeling procedures on the analytical response was investigated. To verify the fundamental performance of the lattice model, the quantitative relationship between the axial force and the post-peak response under cyclic loading is analytically investigated. The lateral force-displacement relationships of RC columns subjected to constant axial forces are illustrated in **Figure 3.14**. In the analysis, the buckling behavior of longitudinal reinforcement is neglected.

In the column subjected to 293 kN axial force, it can be seen that the response of the column shows higher initial stiffness and larger maximum lateral force as shown in **Figure 3.15**. On the other hand, when the axial force is reduced, the maximum lateral force decreases and the energy dissipation capacity increases. Regarding the post-peak response envelope as well, the comparison between these four cases provides a clear explanation. In the column subjected to the axial force of 293 kN, the sudden drop in the post-peak due to compressive crushing of concrete is predicted even if buckling behavior of longitudinal reinforcement is neglected. The column with no axial force shows higher energy dissipation capacity and the post-peak behavior in the lateral force-lateral displacement relationship disappears. From the analytical evaluation, it is found that the lattice model analysis can reasonably predict the effect of axial force on the analytical response including the post-peak behavior.
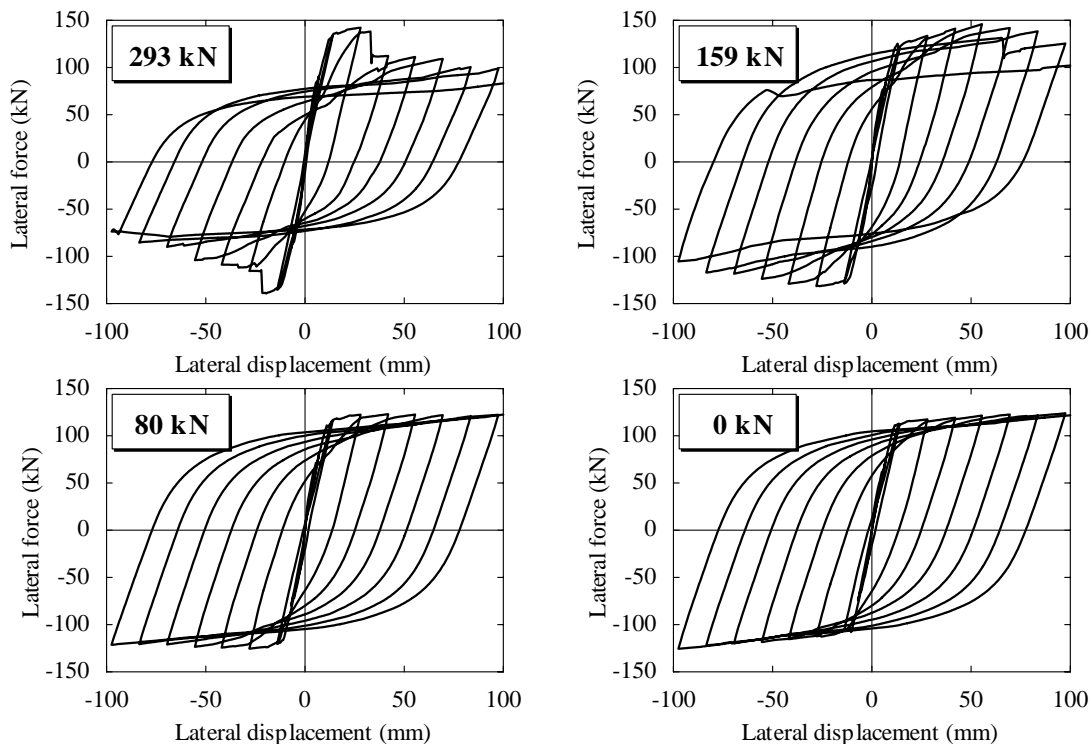
Figure 3.14   Influence of axial load (constant compression)
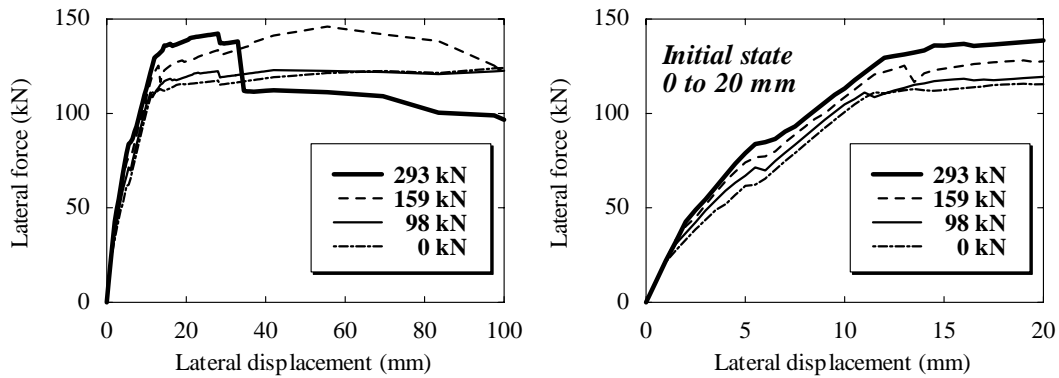
Figure 3.15　Envelope of force-displacement curves with various axial loads

3.7　Conclusions

The 3D lattice model, which is conceptually based on the 2D lattice model, is proposed and successfully used for the prediction of the cyclic response of RC columns.　In the 3D lattice model, a corner-to-corner arch action, from the top to the bottom of a column at opposite, is idealized as a compressive strut that is represented by arch members.　As for the truss action, it is assumed that 3D space comprised of an orthogonal coordinate system is defined by three planes.　In addition, the in-plane 2D constitutive law of concrete considering the softening of compressive stress of concrete depending on the transverse tensile strain (Vecchio and Collins 1986) is used.

These configurations of the 3D lattice model are verified for static cyclic analysis of the laterally loaded RC columns.　It is confirmed that the results of 2D and 3D lattice model analyses are close to each other in terms of the overall behavior of RC columns.　Moreover, from the comparison between the experimental and analytical results, it is found that 3D lattice model analysis can accurately predict the behavior of RC columns including the post-peak region with the same accuracy as the 2D analysis.

The parametric analyses are also conducted to quantitatively assess the relationship between several parameters and the predictions by the 2D lattice model.　From the analytical verifications, the mesh size sensitivities are confirmed and the appropriate method for the 3D lattice modeling is proposed.　Finally, it is found that the lattice model analysis can properly predict the influence of axial force on the analytical response including the post-peak response of RC columns.

References in Chapter 3

[1]   Holzer, S. M. (1985): *Computer Analysis of Structures, Matrix Structural Analysis and Structured Programming*, Elsevier Science Publishing, Co., Inc., New York.

[2]   Itoh, T. and Ichinose, T. (1999): Shear Strength and Three Dimensional Failure of RC Beam with Sufficient Shear Reinforcement, *Journal of Structural and Construction Engineering*, AIJ, No.526, pp.133-139, December (in Japanese).

[3]   Kinugasa, H. and Nomura, S. (2000): Failure Mechanism of RC Beam under Reversed Cyclic Loading after Flexural Yielding Caused by Lateral Strain Accumulation in Plastic Hinge Region on Slip Region, *Journal of Structural and Construction Engineering*, AIJ, No.538, pp.147-153, December (in Japanese).

[4]   Miki, T., Niwa, J., and Lertsamattiyakul, M. (2003a): Numerical Evaluation of Seismic Performance of Reinforced Concrete Bridge Piers Using Dynamic Lattice Model, *Concrete Library of JSCE*, No.41, pp.49-64, May.

[5]   Miki, T., Niwa, J., and Lertsamattiyakul, M. (2003b): Earthquake Response Analysis for RC Bridge Piers Considering Reinforcement Buckling Behavior, *Journal of Materials, Concrete Structures and Pavements*, JSCE, No.732/V-59, pp.225-239, May. (in Japanese)

[6]   Niwa, J., Choi, I. C., and Tanabe, T. (1995): Analytical Study for Shear Resisting Mechanism Using Lattice Model, *Concrete Library of JSCE*, No.26, pp.95-109, December.

[7]   Osada, K., Ohno, S., Yamaguchi, T., and Ikeda, S. (1997): Seismic Behavior of Reinforced Concrete Piers Strengthened with Carbon Fiber Sheets, *Concrete Library of JSCE*, No.30, pp.155-179, December.

[8]   Vecchio, F. J. and Collins, M. P. (1986): The Modified Compression Field Theory for Reinforced Concrete Elements Subjected to Shear, *ACI Journal*, Vol.83, No.2, pp.219-231, March/April.

4   APPLICATIONS OF 2D LATTICE MODEL IN POST-PEAK ANALYSIS OF RC COLUMNS

4.1   Introduction

The Hyogo-ken Nanbu Earthquake provided an opportunity for extensive revision of the standard specifications for the seismic design of concrete structures.   The updated standard specifications are based on the concept that considerable inelastic deformation can be permitted after the longitudinal reinforcement yields, rather than considering only elastic behavior, for concrete structures subjected to large ground motions.   A series of revisions for the standard specifications was carried out with respect to the design of reinforced concrete (RC) bridge columns for highway bridges, with the ductility design adopted to take into consideration the deformation capacity of structures.   It is also specified that designers must perform the verification using dynamic analysis taking into account the material nonlinearity of concrete and reinforcement.

At present, this dynamic analysis is generally used based on the frame model or the fiber model, which can simulate the mechanical behavior of RC columns in the nonlinear response region.   As for the frame model, the RC structure is modeled into individual RC members having restoring characteristics.   On the other hand, for the fiber model, a RC member is discretized longitudinally into several layers in which the layer is subdivided into some fiber element.   Each element consists of uniaxial fibers so that its stress-strain relationship can be properly incorporated.   These methods are recognized as a highly practical method to evaluate the plastic deformation of flexural RC structural members.   However, it is necessary to idealize the location and size of the plastic hinge region and incorporate the information about the plastic hinge region into the appropriate fiber element.   Moreover, one shortcoming of these models is the difficulty in estimating the behavior at the post-peak range, particularly when the failure mode of the RC member is shear.

In this study, these methods are replaced by the lattice model (Niwa et al. 1995, Miki et al. 2002, 2003a, 2003b).   This model offers reasonable prediction of the shear carrying capacity of RC members, making it a significant different approach from analytical methods based on fiber techniques.   Moreover, since the lattice model discretized an RC member into an

assembly of trusses, the internal stress flows can be easily determined. From an understanding of the internal resisting mechanism of RC members, the accuracy of analytical results can be confirmed.

The objective of this chapter is to develop a dynamic analysis procedure based on the 2D lattice model. The 3D analytical model whose development is main purpose of this thesis is based on the concept of the 2D lattice model. First, in order to verify the performance of 2D static lattice model under cyclic loading, the analytical predictions are compared with experimental results on laterally loaded RC columns that are expected to fail in either flexural or shear. Next, in order to confirm the applicability of the 2D lattice model to dynamic analysis, the experimental results from shaking table tests or pseudo-dynamic loading tests on RC columns are compared. Finally, the behavior of RC columns with different amount of transverse reinforcement and carbon fiber reinforced plastic sheet (CFS) is simulated.

4.2 Cyclic Analysis of RC Columns

4.2.1 Outlines of experiment

The experiments carried out by Takemura et al. (Takemura et al. 1997, Ductility Design Subcommittee 2001) on RC bridge piers subjected to static reversed cyclic loading are adopted as the analytical target. The specimen and arrangement of reinforcement are illustrated in **Figure 4.1**. The specimen is a cantilever RC bridge pier with a cross section of 400 mm by 400 mm. The reversed cyclic loading was applied by controlled horizontal displacement at a point 1,245 mm above the base of the pier. The material properties of the concrete and reinforcement are summarized in **Table 4.1**.

In the experiment, the displacement amplitude was increased stepwise in the increments of $n\delta_y$ (n = 1, 2, 3…) at each cyclic loading step. Here, δ_y is the lateral displacement at the initial yielding of longitudinal reinforcement at the bottom of the pier and is taken as $\delta_y = 6$ mm. The cyclic lateral displacement history used in the experiment is shown in **Figure 4.2**. The loading hysteresis identical to that in the experiment is provided in the analysis by using the displacement-controlled incremental calculation. During the test, a constant axial compressive load of 156.7 kN was applied at the top of the pier; this is equal to an applied axial compressive stress of 0.98 MPa.

In the discussion, the loading from the left hand side of a lattice model, as shown in **Figure 4.3**, is defined as the positive loading (with lateral force and lateral displacement expressed as
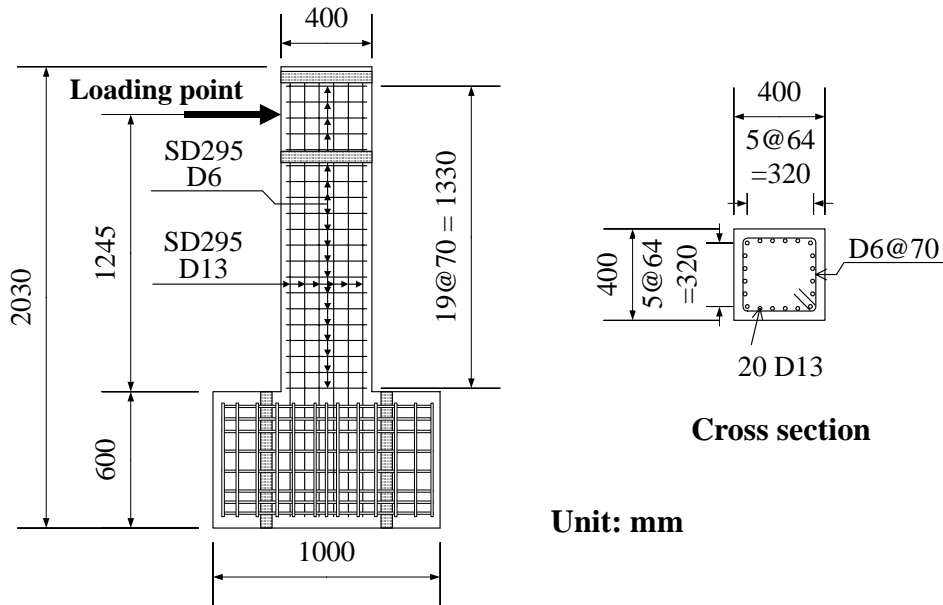
Figure 4.1   Specimen details and test setup

positive values).   In contrast, the loading from the right hand side is defined as the negative loading (with lateral force and lateral displacement given as negative values).

4.2.2   Lattice model of the specimen

The specimen shown in **Figure 4.1** is analyzed by the 2D static lattice model taking into account the cyclic loading condition (Ito et al. 2000), as depicted in **Figure 4.3**.   To simulate RC piers subjected to reversed cyclic loading, the flexural compression members and flexural tension members are assumed to have the same cross-sectional area.   In addition, since the specimen is a cantilever RC pier, two intersecting arch members connecting the loading points at the top of the pier and the opposite pier-footing connections are provided.   Here, from the results of pre-analysis already described, the value of t is obtained as 0.20.   The applied axial compressive load at the top of the pier is uniformly distributed over the top three nodes.
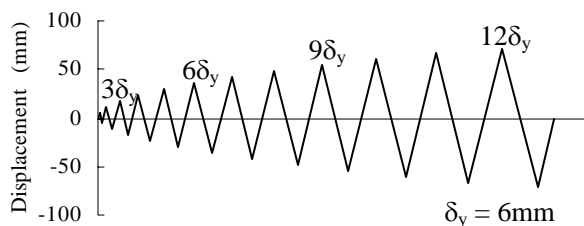
Figure 4.2   Cyclic lateral displacement history

**Table 4.1**   Material properties of
concrete and reinforcement

Uniaxial compressive strength of concrete, f_c' (MPa)		35.7
Yield strength of reinforcement, f_y (MPa)	SD295 D13	363
	SD295 D6	368

71
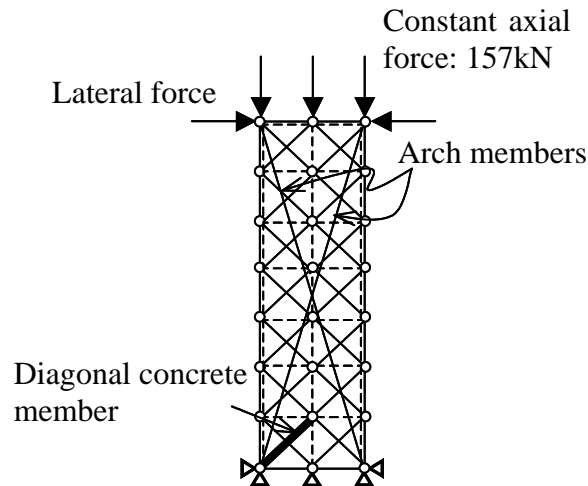
Figure 4.3   2D static lattice model

4.2.3   Hysteresis characteristic of RC piers

The lateral force-lateral displacement relationships obtained in the experiment and static lattice model analysis are shown in **Figure 4.4**.   The experimental result shows that the longitudinal reinforcement initially yields on the flexural tension side at the bottom of the RC bridge pier.   As the lateral displacement increases gradually after reversing the loading direction, the longitudinal reinforcement behaves plastically and deforms laterally outwards in a process referred to as buckling.   Ultimately, the lateral load-lateral displacement curve reaches the post-peak region accompanied by the buckling of longitudinal reinforcement and the spalling of cover concrete.   In the analytical result (shown in **Figure 4.4(b)**), the behavior of the RC bridge pier is found to be close to the experimental result.   The comparison of two results indicates that the analytical method is applicable to the prediction of the initial stiffness, the load carrying capacity, and the cyclic behavior of RC bridge piers after the yielding of longitudinal reinforcement.   The behavior can be successfully predicted

(a)   Experiment   **(b)**   Analysis
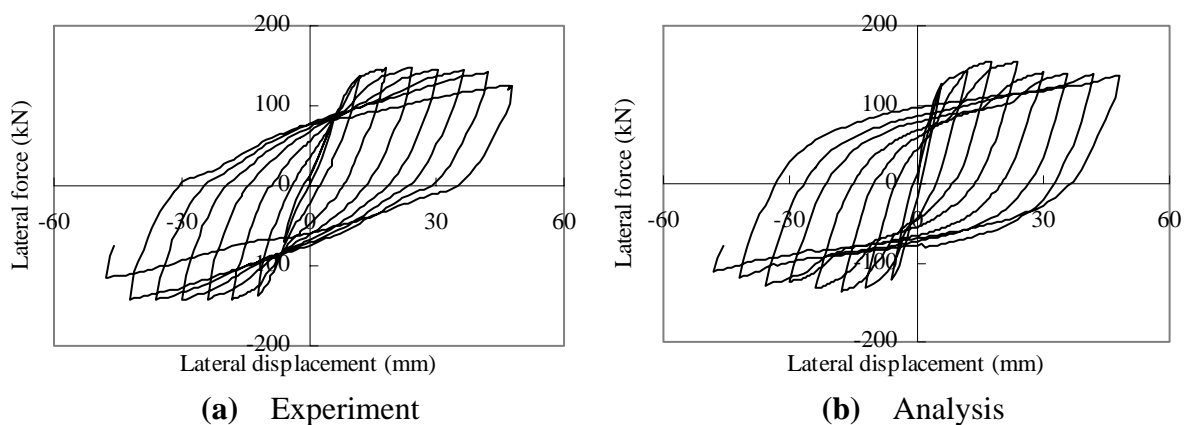
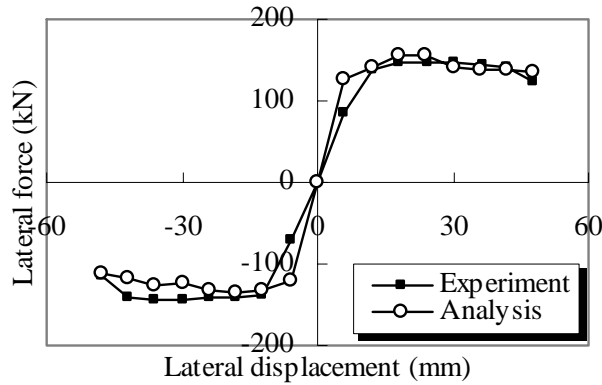**Figure 4.4**   Lateral force and lateral displacement relationships (experiment and analysis)

Table 4.2 Experimental and analytical results of lateral force and lateral displacement (static reversed cyclic loading test and static lattice model analysis)

	Experiment	Analysis
Yield strength (kN)	84.2	116.3
Yield displacement (mm)	6.0	5.0
Maximum lateral force (mm)	148.0	155.6
Ultimate displacement (mm)	42.0	48.0

until the load begins to decrease. However, it is also confirmed that further softening behavior in the post-peak region is not properly predicted by the analysis.

The experimental and analytical results of the lateral force and the lateral displacement at the yielding of longitudinal reinforcement, as well as the maximum lateral force and the ultimate displacement of the RC bridge pier are summarized in **Table 4.2**.   In the analysis, the point at which the longitudinal reinforcement yields is defined as when the longitudinal reinforcement strain at the bottom of the pier firstly reaches the yield strain of 2,000 μ.   On the other hand, the experimental yield displacement is obtained as the initial yield displacement in which the pull-out of longitudinal reinforcement from the footing is considered.   The ultimate displacement is obtained as the lateral displacement at the point when the lateral force corresponds to the load at the yielding of the longitudinal reinforcement in the pre-peak region.   In the analysis, after the longitudinal reinforcement yields, the compression softening behavior can be predicted in the diagonal concrete member at the base of the pier as the crack width increases perpendicular to the direction of the compressive stress.   These analytical results indicate that the local behavior causes the post-peak response of a RC bridge pier.   Therefore, the analytical responses of RC bridge piers are found to be in the good agreement with the experimental responses.

The experimental and analytical results shown in **Figure 4.4** can be expressed by the envelope curve as shown in **Figure 4.5**.   Although this analysis predicts the experimental results quite well until the ultimate displacement, some difference can be observed in the large deformation region.   This is caused by that the buckling of the longitudinal reinforcement and the spalling of concrete influence the behavior of RC bridge piers.   In order to correctly predict the behavior of RC bridge piers subjected to large lateral deformations, the consideration of the buckling of reinforcement would be necessary.   Nevertheless, the envelope curves and hysteresis loops for RC bridge piers can be predicted reasonably well up to the ultimate state by using the static lattice model.

Figure 4.5   Envelope curves of lateral force and lateral displacement (experiment and analysis)

4.2.4   Evaluation of failure mode and load resisting mechanism of RC piers

The load resisting mechanism is identified from the internal forces by focusing on the stress-strain relationship in one of the members in the lattice model, such as a diagonal concrete member at the bottom of the pier.   The stress-strain relationship of diagonal concrete member, which is marked by the bold line in **Figure 4.3**, is shown in **Figure 4.6**.   In the lattice model, the compression softening behavior of concrete proposed by Vecchio and Collins (1986) is applied.   With one pair of a diagonal compression member and a diagonal tension member, it is assumed that the compressive stress capacity of the diagonal members falls as the tensile strain on the members increases.   The dashed line in **Figure 4.6** represents the stress-strain curve of the uncracked concrete.   The figure shows that the compressive stress deteriorates rapidly as the diagonal cracks propagate from the pier-footing connection. During further loading, these cracks widely open while the compressive stress along with the diagonal crack decreases.   Consequently, in the analysis, the compression softening behavior of a diagonal concrete member governs the post-peak behavior in the load-displacement relationship and leads the RC bridge pier to the ultimate state.
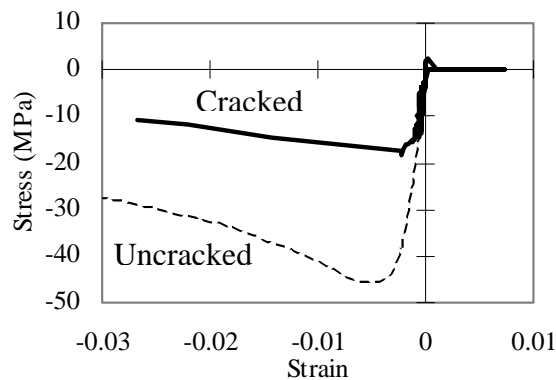

Figure 4.6   Stress-strain relationships of concrete in diagonal member

74

4.3   Shear Analysis of UC San Diego Columns

4.3.1   Experimental setup

A series of 1/3-scale models of RC bridge columns were tested by Xiao et al. (1993) at the University of California at San Diego.   Three tested columns had the different strength of longitudinal and transverse reinforcements and the shear span to effective depth ratio. Because of these conditions, all columns had relatively low shear carrying capacity.

Figure 4.7 shows the column R−1, which is the representative shape for all of the columns. The cross section of the column was 610 mm width and 410 mm depth.   All reinforcing bars had a minimum concrete covering of 25 mm.   The diameters of reinforcing bars were selected in which they would be in a scale consistent with that of the real columns.   The columns R−1 and R−3 had nearly identical configuration with the exception that the different strength of longitudinal and transverse reinforcements was used.   The longitudinal reinforcement in the column R−1 had yield strength of 317 N/mm^2, while in the column R−3 had yield strength of 469 N/mm^2.   The yield strength of transverse reinforcement in the R−1 was 360 N/mm^2, while in the column R−3 had yield strength of 324 N/mm^2.   On the other hand, the column R−5 had the identical details and arrangement as the column R−3 with the exception, in which the height from the top of a footing to the loading point was shorter. The columns R−1 and R−3 were 2440 mm height, while the column R−5 was 1830 mm height.   Concrete in the column R−1 was slightly stronger than that in the columns R−3 and R−5.   The material properties for three columns are shown in **Table 4.3**.
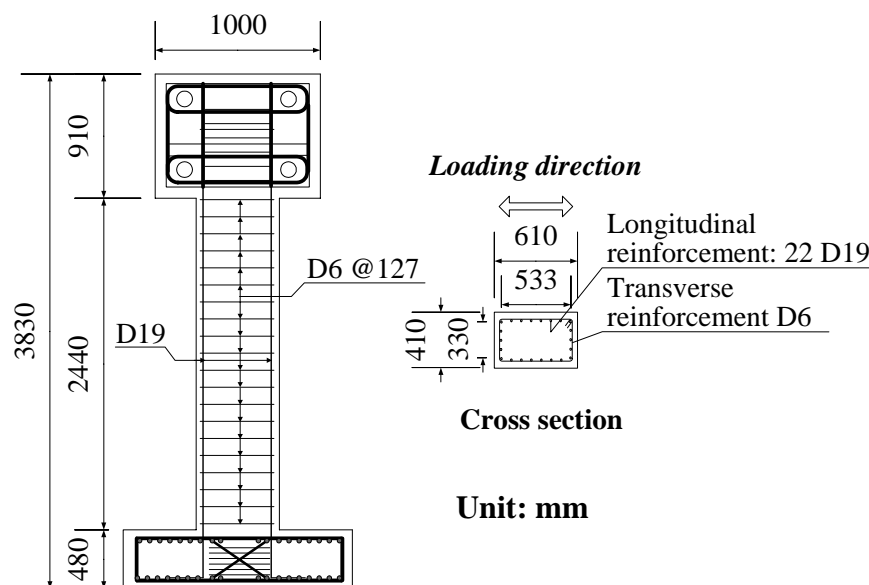

**Figure 4.7**   Details of the column R−1 and loading setup

Table 4.3 Material properties

Column	Concrete	Longitudinal reinforcement				Transverse reinforcement	
	f_c' (MPa)	Grade	f_y (MPa)	f_u (MPa)	Bar area (mm²)	f_{wy} (MPa)	Bar area (mm²)
R−1	37.9	Grade40	316.9	452.7	284.9 (Reinforcement ratio: 2.5%)	360.3	31.7 (@127mm, Reinforcement ratio: 0.12%)
R−3	34.1	Grade60	469.2	746.2		323.8	
R−5	32.7		469.2	746.2		323.8	

All of the columns were subjected to the same loading pattern. During the loading test, the footing of the column was fixed laterally against the slip and rotation. The laterally cyclic displacement is applied to the top of the column while the rotation is prevented by the double bending. The amplitude of the lateral displacement was increased stepwisely during the test. Throughout the test, a constant axial compressive load of 507 kN was applied to the top of the column to simulate the weight of a superstructure. For three columns, the column R−1 was designed to have the highest shear carrying capacity relative to its flexural capacity. Since the column R−3 had stronger longitudinal reinforcement, weaker transverse reinforcement, and weaker concrete than the column R−1, it experienced a more pronounced shear failure. The brittle shear failure was observed in the column R−5, which had essentially the same material properties as the column R−3, but was smaller shear span to depth ratio. **Figure 4.8** shows the crack patterns for three columns at or near their final loading stages. The major diagonal shear cracks formed near the top and bottom of the column in all cases.

(a) Column R−1   (b) Column R−3   (c) Column R−5
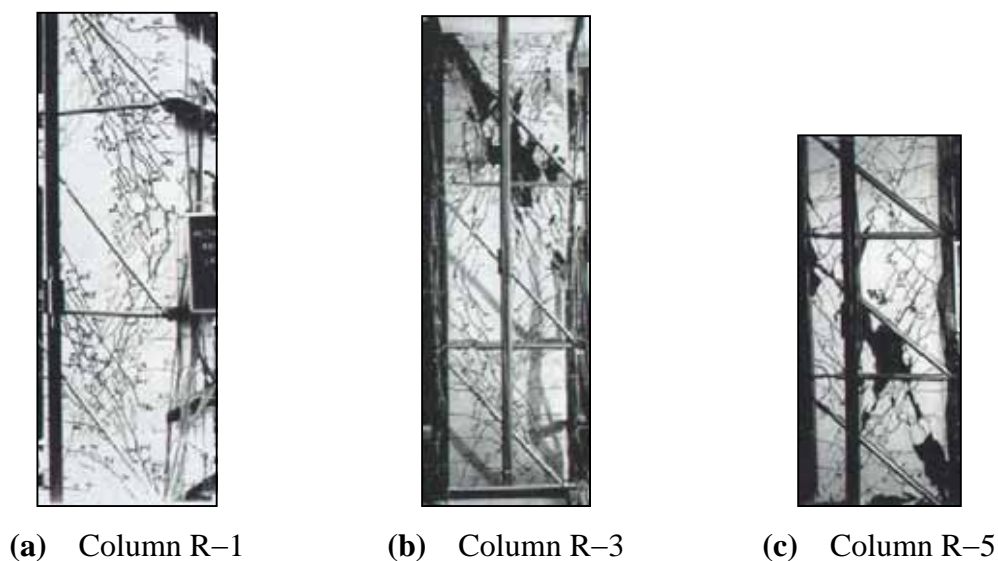
Figure 4.8 Crack patterns

(a)   Columns R−1 and R−3   (b)   Column R−5
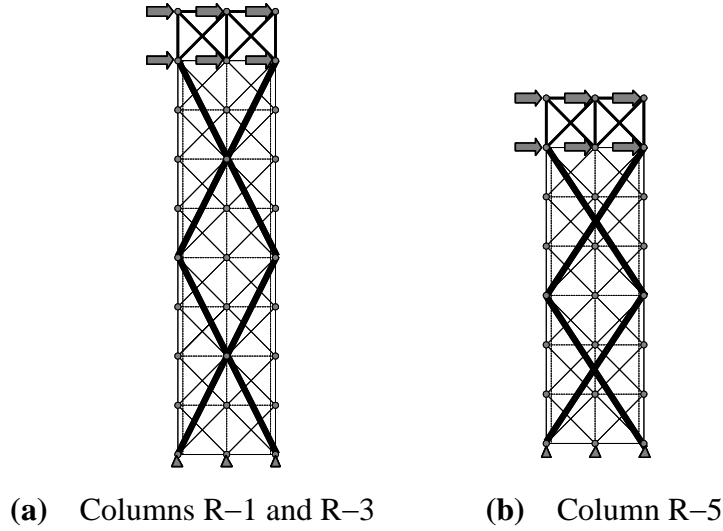
Figure 4.9   2D static lattice model

4.3.2   Configuration of lattice model

The 2D static lattice model and the boundary conditions used in the analyses are illustrated in **Figure 4.9**.   A constant axial compressive load is applied throughout the analysis to simulate the vertical load in the tests.   The lateral load is applied through controlled displacements as illustrated in the figure.   The displacements are provided only in the horizontal direction. To provide the controlled displacement with no rotation of the top of the column, the elastic elements are used as a loading stab in the analysis.   This loading condition prevents the rotation of the top of the column while allowing free vertical displacement.

4.3.3   Updated compressive model of concrete

In order to consider the cyclic behavior of concrete under both compression and tension, the cyclic stress-strain relationships proposed by Naganuma et al. (2000) are used in the lattice model.   In the model, the envelope curves used in the previous analysis of lattice model are applied as it is.

The features of the updated model proposed by Naganuma et al. (2000) are shown in **Figure 4.10**.   In this model, the plastic strain in compression, ε_{cp}', which is the strain corresponding to zero stress during unloading is used as represented by **Equation 4.1**.

$$\varepsilon_{cp}' = \left\{ 0.145 \left(\frac{\varepsilon_{cmax}'}{\varepsilon_{co}'} \right)^2 + 0.127 \left(\frac{\varepsilon_{cmax}'}{\varepsilon_{co}'} \right) \right\} \cdot \varepsilon_{co}' \qquad (4.1)$$

77
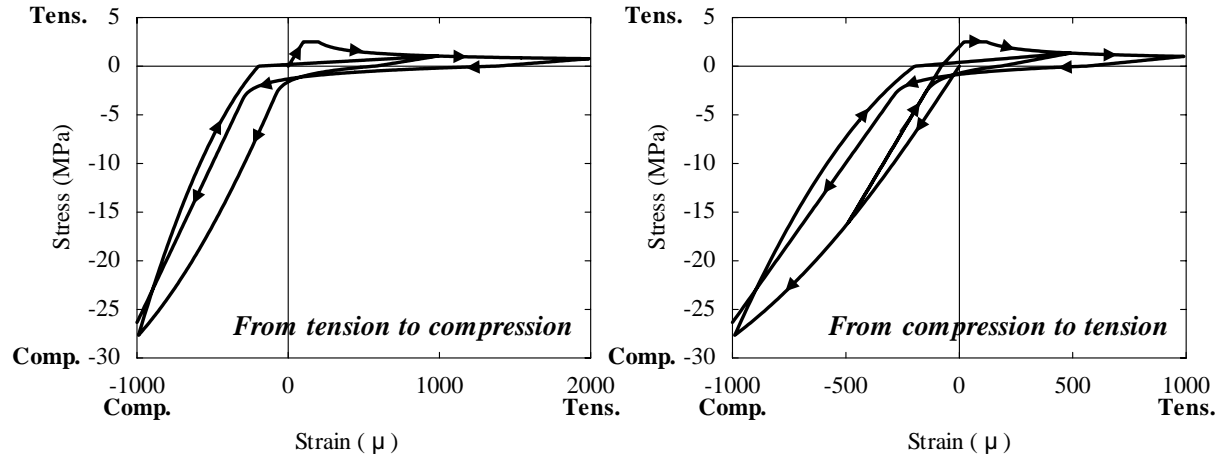
Figure 4.10   Stress-strain relationships of concrete (updated compressive model)

where, ε_{cp}' and ε_{cmax}' are the plastic strain and the maximum strain of concrete in compression during loading hysteresis, respectively.   Similarly, ε_{co}' is the strain corresponding to the compressive strength.

This model can evaluate the decrease in the stiffness of concrete during unloading and reloading as the maximum compressive strain increases.   However, in the large strain region, the plastic strain becomes unrealistic value since the plastic strain calculated from **Equation 4.1** is larger than the maximum strain.   Consequently, when the maximum strain of concrete becomes greater than $4\varepsilon_{co}'$, the plastic strain is obtained as follows:

$$\varepsilon_{cp}' = \left(\frac{\varepsilon_{cmax}'}{\varepsilon_{co}'} - 2.828 \right) \cdot \varepsilon_{co}'; \quad \varepsilon_{cmax}' \geq 4\varepsilon_{co}' \tag{4.2}$$

The unloading curve in the compressive model of concrete is obtained by the quadric curves that pass through the points at the maximum strain and the plastic strain and of which the stiffness immediately after the transition from loading to unloading is represented as the following equation.

$$E_{cmax} = 1.5 \cdot \frac{\sigma_{cmax}'}{\varepsilon_{cmax}' - \varepsilon_{cp}'} \tag{4.3}$$

where, E_{cmax} is the stiffness in the compressive stress-compressive strain relationship of concrete immediately after the transition from loading to unloading.   In addition, σ_{cmax}' is the stress when the strain becomes the maximum in the loading cycles.

In the reloading path, the stress is assumed to decrease in the direction to the point of stress σ_C

(a) Unloading before the stress reached σ_C (b) Unloading over the stress σ_C
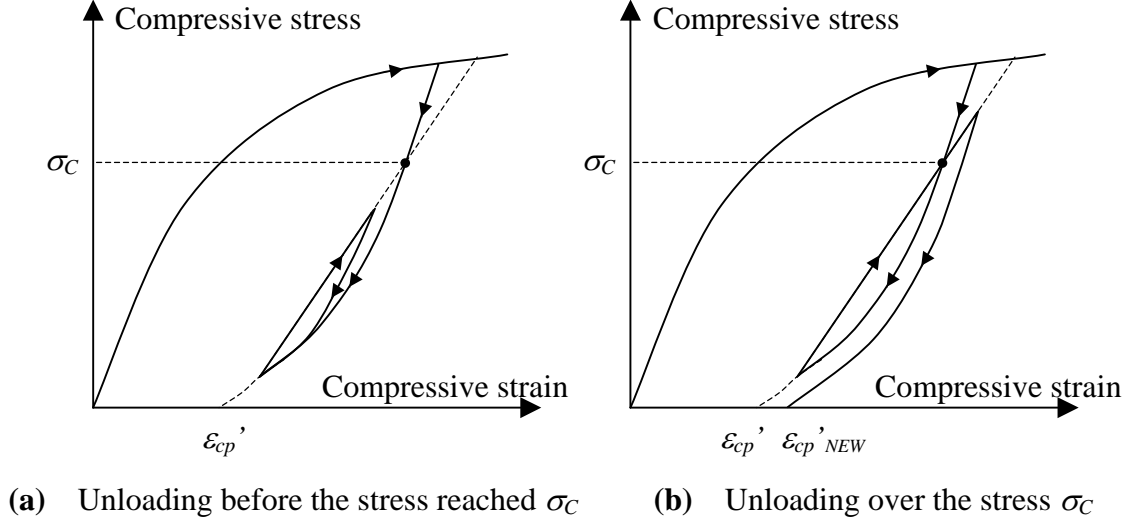
Figure 4.11   Detailed rules for internal loops of updated compressive model

on the unloading curve as represented by following equations.

$$\sigma_C = \frac{5}{6}\sigma_{cmax}'; \quad \varepsilon_{cmax}' \geq \varepsilon_{co}' \tag{4.4}$$

$$\sigma_C = min\left(\frac{2}{3}\sigma_{cmax}', \sigma_{cmax}' - \frac{1}{6}\sigma_{co}'\right); \quad \varepsilon_{cmax}' < \varepsilon_{co}' \tag{4.5}$$

The detailed scheme about the unloading and reloading hysteresis of internal curves is abstractly illustrated in **Figure 4.11**. In the unloading and reloading hysteresis, the pass is reset when the strain exceeds the point of stress σ_C calculated **Equations 4.4** or **4.5** and the plastic strain of concrete in compression, ε_{cp}' is calculated again (**Figure 4.11(a)**). On the other hand, during the internal state where the strain does not exceed the point of stress σ_C (**Figure 4.11(b)**), the unloading pass is assumed to proceed to the state of plastic strain calculated in the previous calculation step.

For the tensile model of concrete, the unloading path is assumed to fall according to the stiffness as represented by the following equation.

$$E_{tmax} = 1.5\frac{\varepsilon_{to}}{\varepsilon_{tmax}}E_{t0} \tag{4.6}$$

where, E_{tmax} is the stiffness in the tensile stress-tensile strain relationship of concrete immediately after the transition from loading to unloading. In addition, ε_{to} and E_{to} are the strain corresponding to the tensile strength of concrete and the initial stiffness in the tensile stress-tensile strain curve of concrete.

In the loading process from tension to compression, the closure of cracks is generated due to the loss of the load. On closing of cracks, the compressive stress is transmitted to the concrete across the crack surface. Since two crack surfaces start contacting with each other even though the strain of the concrete becomes zero. In this study, the strain beginning to transfer the compressive stress is given as 10,000 μ. It is obvious that the stiffness of the concrete during from the start contacting with two crack surfaces to the closure of cracks completely is smaller than that of uncracked concrete. The stress-strain model for the contact of crack surfaces is represented by the following logarithm curve.

$$\sigma = \left(log_e\left(\varepsilon+a\right)+b\right)\cdot c \tag{4.7}$$

where a, b, and c are constants. These constants are determined from the condition that the curve passes through the points at the plastic strain in tension and at the stress represented by **Equation 4.8**.

$$\sigma_J = -\left(1.0+0.02\left(\frac{\varepsilon_{t\,max}-\varepsilon_{to}}{\varepsilon_{to}}\right)\right)\cdot f_t \tag{4.8}$$

where, ε_{tmax} is the maximum tensile strain of concrete during loading hysteresis. Similarly, ε_{to} is the strain corresponding to the tensile strength of concrete, f_t.

When the tensile strain significantly increases, the stress of σ_J becomes larger. As a result, the compressive stress of concrete transmitted across the crack surfaces increases considerably. To avoid this unrealistic condition, the limit values for σ_J are set as -5 MPa for the flexural members and -5η MPa for the diagonal and the arch members, where η is the coefficient of concrete compressive softening obtained from **Equation 2.9**.

4.3.4   Analytical results and discussions

The nonlinear analyses by 2D static lattice model are carried out. **Figure 4.12** shows the load-displacement relationships of the column R−1 obtained by the experiment and the lattice model analysis. In the experiment, the column R−1 reached displacement ductility factor of three, where the shear failure occurred after the longitudinal reinforcement yielded. This is not regarded as a brittle shear failure since the column reached its flexural capacity and had some deformation with slight decrease in the load. The analytical results are found to be in the good agreement with the experimental results. The result of the analysis with updated model of concrete shows the higher energy dissipation capacity with slight pinching that
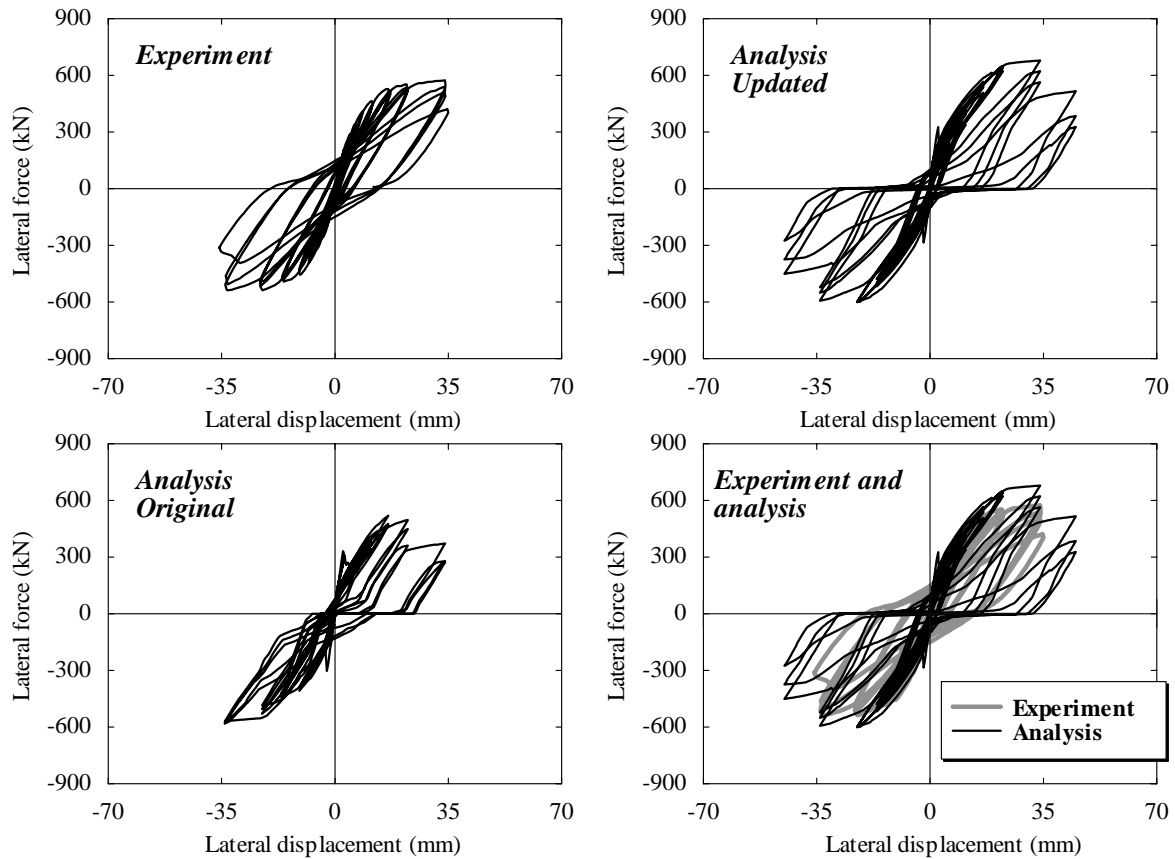
Figure 4.12   Load-displacement relationships of the column R−1

corresponding to the experimental observations.   On the other hand, the analytical result with the original model of concrete shows the significant pinching behavior in the cyclic load-displacement curve even if the decrease in the load is not seen in the analytical result. This is because that the compressive stress across the crack surface has been considered in the updated model.   Through the discussion, it is found that the compressive stress due to the premature contacts of crack surface influences on the cyclic loops in the load-displacement relationship.

To understand the behavior of the shear-dominated RC columns, the total horizontal displacement at the top of the column is separated into flexural and shear components.   This is obtained by separated displacements from the three portions of horizontal, vertical and diagonal measurements throughout the column height as previously shown in **Figure 4.8**. The experimental and analytical results of the flexural and shear deformations of the column R−1 are illustrated in **Figure 4.13**.   The experimental results cannot be obtained after the lateral displacement reached around 35 mm because some measurements reached their limit after the shear failure.   In the analysis, the scheme to separate into flexural and shear deformations performed by Ueda et al. (2002) is applied.   In this study, the horizontal

81
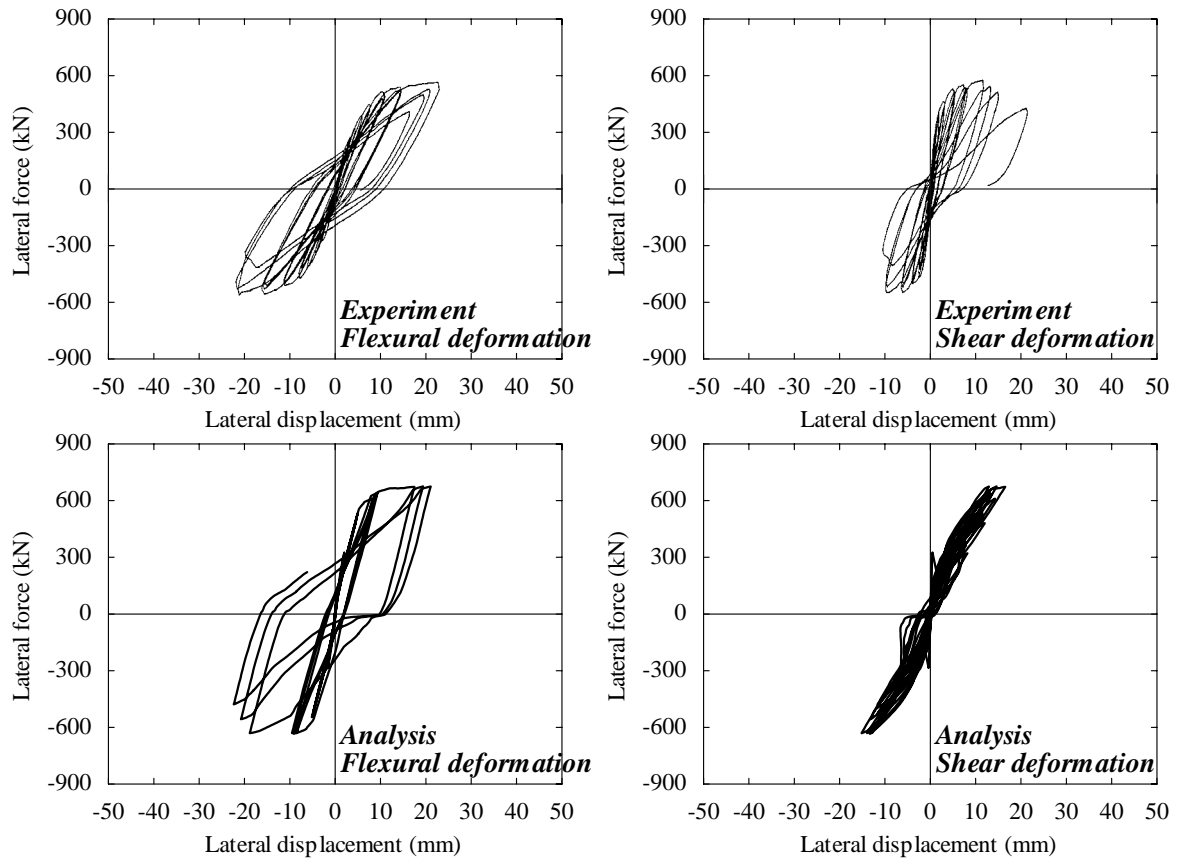
Figure 4.13   Decomposition of flexural and shear deformations for the column R−1

displacements of each layer in the 2D lattice model are calculated as schematically shown in **Figure 4.14**.   The shear deformation at the top of the column can be obtained by the integration throughout the column height.   On the other hand, the flexural deformation at the top of the column is calculated by the following equation.

$$\delta_f = \delta - \delta_s \tag{4.9}$$

where, δ, δ_f, and δ_s are the total displacement, the flexural deformation, and shear deformation at the top of the column.

Interestingly, in the experiment, the separated flexural and shear deformations show that when the lateral displacement was reached around 35 mm, the flexural deformation decreased as the shear deformation increased.   It is found from **Figure 4.13** that the analytical results of flexural deformation show the good agreement with the experimental results.   However, the shear deformation in the analysis is found to be smaller than that in the experiment. Consequently, the analysis cannot predict the shear failure at the lateral displacement of around 35 mm.   In order to understand the reason of this behavior, the stress-strain relationships in the lattice components are shown.
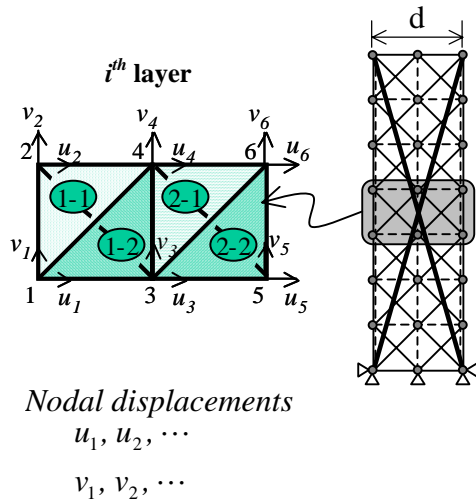
1. Calculation of shear strain of each element

$$\gamma_{xy}^{1-1i} = \frac{u_1 - u_2}{0.5\,d} + \frac{v_4 - v_2}{0.5\,d} \quad \gamma_{xy}^{2-1i} = \frac{u_3 - u_4}{0.5\,d} + \frac{v_6 - v_4}{0.5\,d}$$

$$\gamma_{xy}^{1-2i} = \frac{u_3 - u_4}{0.5\,d} + \frac{v_3 - v_1}{0.5\,d} \quad \gamma_{xy}^{2-2i} = \frac{u_5 - u_6}{0.5\,d} + \frac{v_5 - v_3}{0.5\,d}$$

2. Calculation of shear deformations in each element

$$\delta_s^{1i} = \frac{1}{2}\left(\gamma_{xy}^{1-1i} + \gamma_{xy}^{1-2i}\right)\cdot 0.5\,d \quad \delta_s^{2i} = \frac{1}{2}\left(\gamma_{xy}^{2-1i} + \gamma_{xy}^{2-2i}\right)\cdot 0.5\,d$$

3. Averaged shear deformations in a layer

$$\delta_s^i = \frac{1}{2}\left(\delta_s^{1i} + \delta_s^{2i}\right)$$

4. Shear deformation at the top of the columns

$$\delta_s = \sum_{i=1}^{n} \delta_s^i$$

Figure 4.14   Decomposition method of shear deformation from nodal displacement

Figure 4.15 shows the deformation of the 2D lattice model of the column R−1 at several stages characterized as the numbers in the load-displacement curve.   The displacements in the deformed shapes for all of the column analyses are magnified by a factor of ten.   It is found that the shape of a column in the 2D lattice model is visualized as the flexural prone deformation until the ultimate displacement is reached.   It is also found that the deformations of the column show the uniformly distributed throughout the column height.   It is found from **Figure 4.15** that the shear failure in the analysis takes place at the displacement ductility factor of four is reached, which is slightly later than in the experiment.   As a result, the ductility capacity of the column R−1 is overestimated in the analysis.   **Figure 4.16** shows the
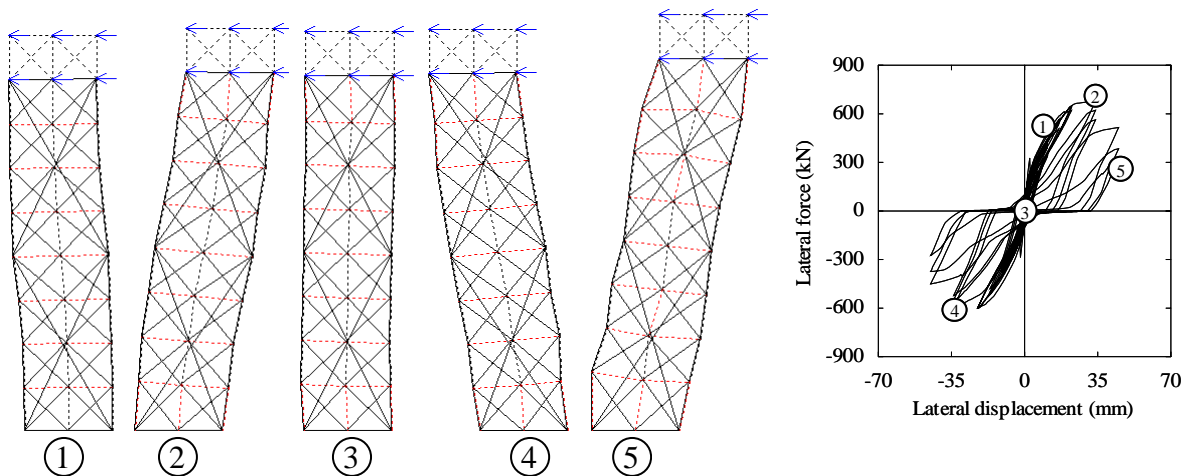
Figure 4.15   Deformed shape of lattice model for the column R−1
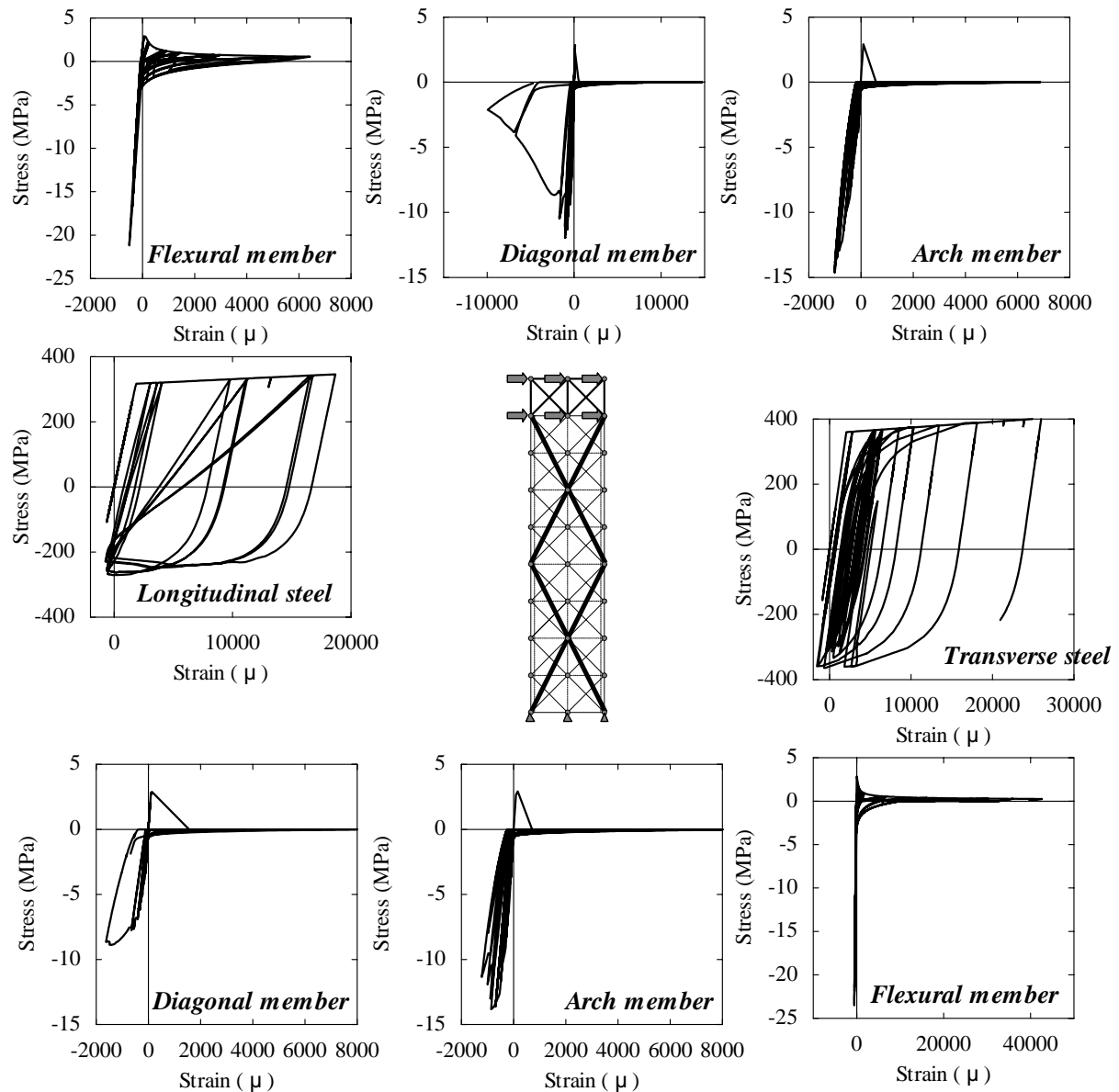
Figure 4.16   Stress-strain relationships in a representative element in the lattice mode for
the column R−1

stress-strain relationships of representative components in the model of the column R−1.
Here, in the lattice model, the shear resisting mechanism is considered by both truss and arch
mechanisms as mentioned previously.   The predicted shear failure is assumed to take place
when the stress in the arch or diagonal members decreases and the compressive softening
behavior of concrete is observed after the transverse reinforcement yields.   Here, it is
assumed that the compressive strength of arch or diagonal members decrease as the transverse
tensile strain perpendicular to the compressive direction increases.

Figure 4.17 shows the load-displacement relationships of the column R−3.   In the
experiment, the column R−3 was found to suffer a brittle shear failure at the displacement

ductility 1.5, followed by a severely pinched response. The higher yield strength of longitudinal reinforcement increased the flexural capacity than that of the column R−1, which reduced the displacement ductility capacity from 3 to 1.5, and changed the flexural shear failure of the column R−1 to a brittle shear failure. It is clear from **Figure 4.17** that the failure is attributed to shear, with a sudden increase in shear deformations while the stable flexural deformations remained small.

Figure 4.18 shows the flexural deformation and shear deformation of the column R−3 and **Figure 4.19** shows the deformed shape in the 2D lattice model of the column R−3. It is found from the analytical load-displacement curves and the predicted deformations that the analysis can appropriately predict the shear failure that occurred in the experiment. In the analysis, in addition, the shear deformation following the shear failure is found to increase more rapidly than the flexural deformation, similar to the experimental observation. It can be seen in **Figure 4.19** that some localization of deformation took place in the upper potion of the column. On the other hand, it is obvious in the experiment that the significant shear failure near the top of the column took place as demonstrated in **Figure 4.8**.

Figure 4.20 shows the stress-strain relationships of each component in the 2D lattice model of the column R−3. As mentioned previously, the shear failure in the analysis is assumed to occur when the compressive softening behavior of concrete in the arch or diagonal members appears. This is modeling to consider the shear failure in spite of the decrease in the shear stresses that are transferred across the inclined cracks by aggregate interlock. As a result, it is found that the analytical load-displacement relationship in the post-peak is milder than the experimental curve.

Figure 4.21 shows the experimental and analytical load-displacement relationships of the column R−5. The column R−5 had the highest shear demand for the column due to the high strength of longitudinal reinforcement and the reduced height of the column. In the experiment, the column R−5 showed the heaviest damage with a brittle shear failure prior to the displacement ductility of unity. The analytical load-displacement relationship with updated model of concrete is found to be close to the experimental curve. **Figure 4.22** shows the flexural and shear components of column R−5. The analysis can also predict the shear-dominated behavior of the column. Following shear failure, the analytical shear deformations significantly increase while the flexural deformations decrease within the same cycle. **Figure 4.23** shows the deformed shape of the 2D lattice model for the column R−5 and **Figure 4.24** shows the stress-strain relationships in the 2D lattice model. It is found in viewing **Figure 4.23** that the deformation is concentrated in the upper region of the column.
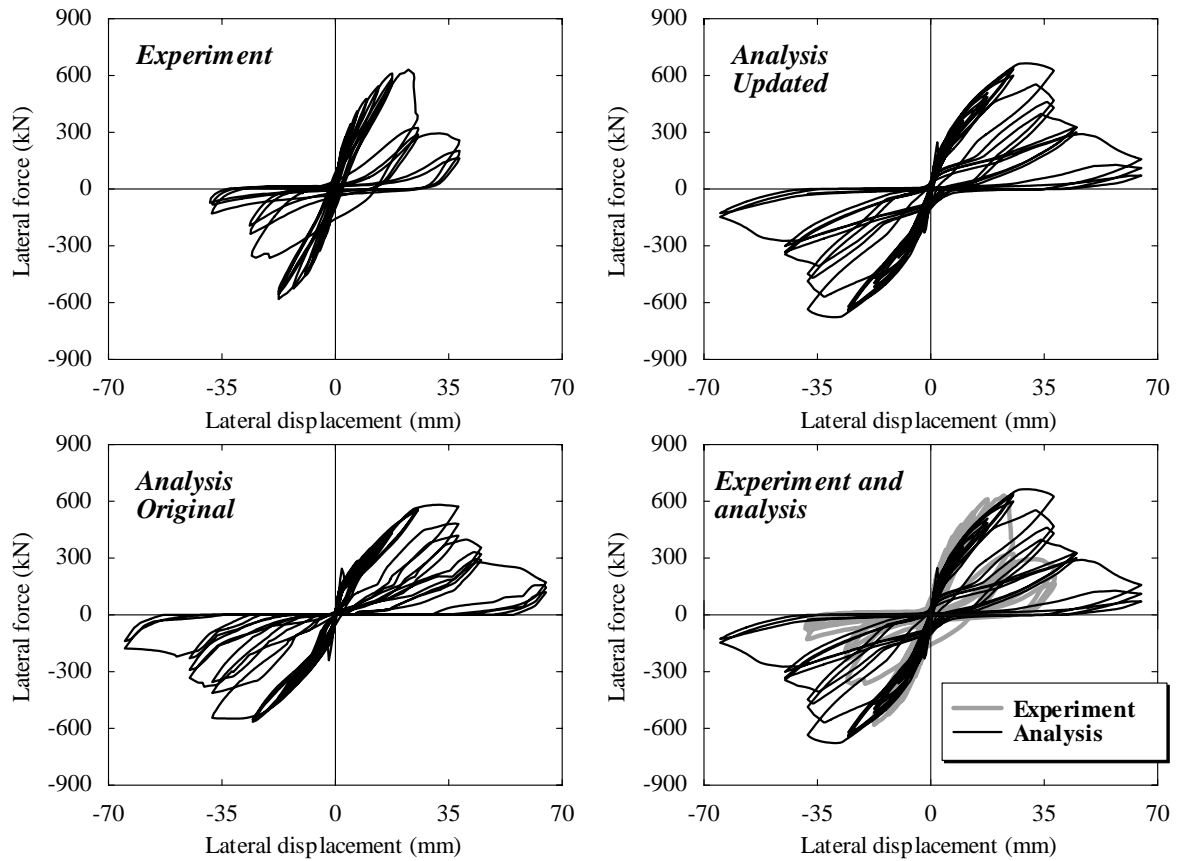
Figure 4.17   Load-displacement relationships of the column R−3
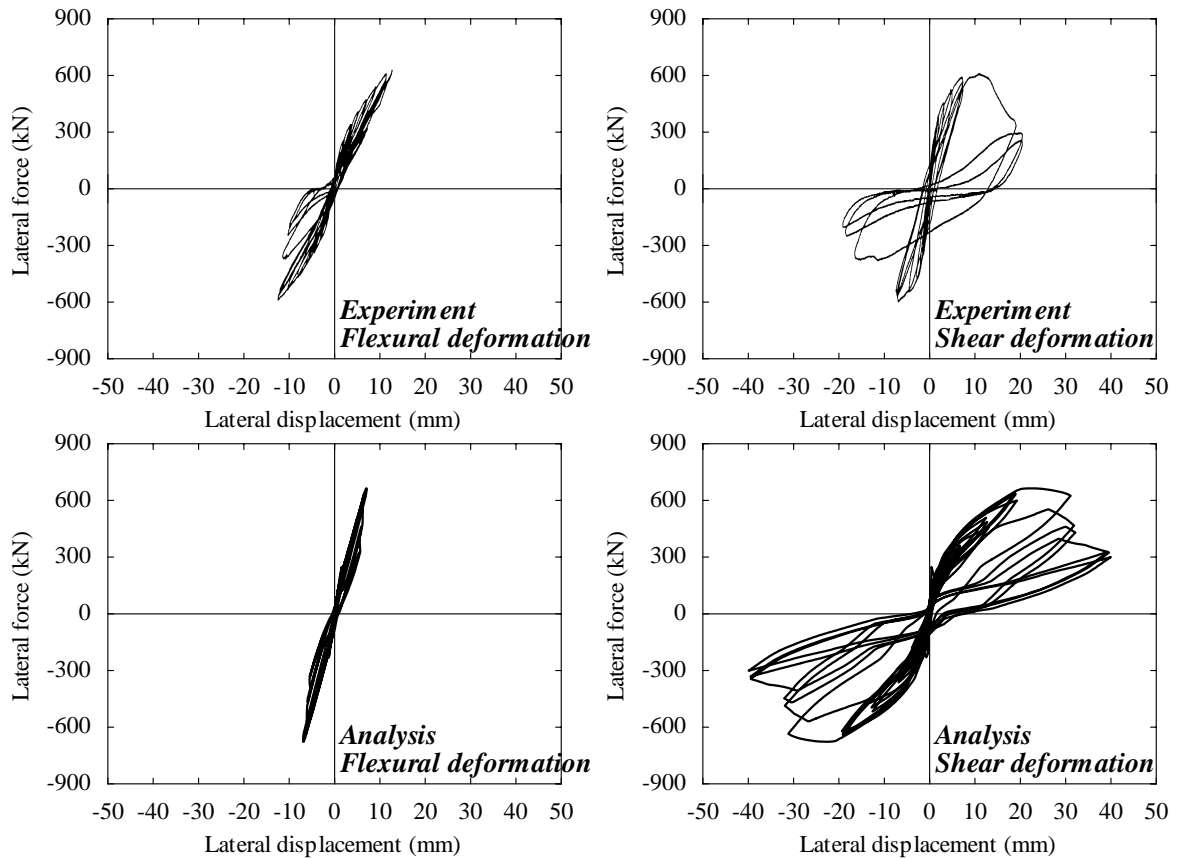
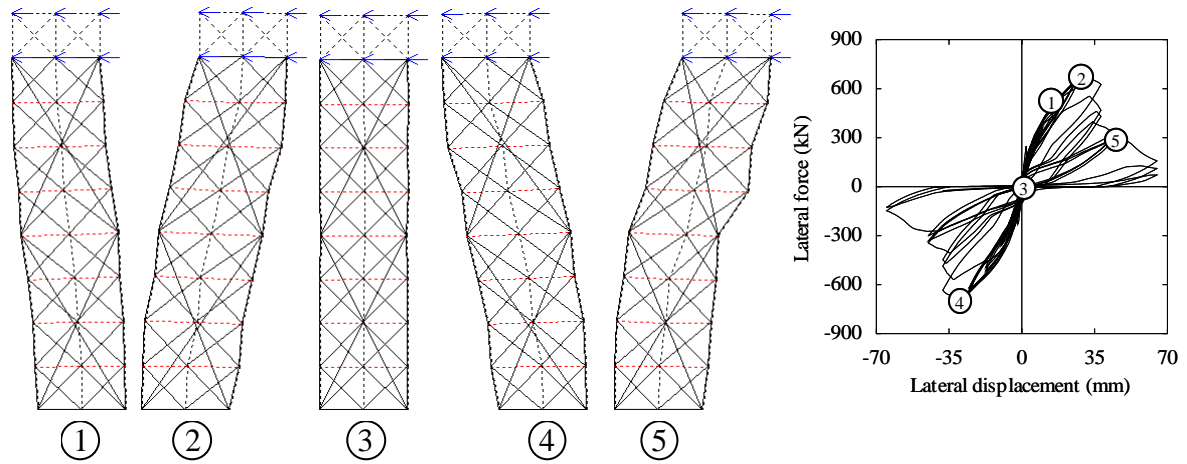**Figure 4.18**   Decomposition of flexural and shear deformations for the column R−3

86

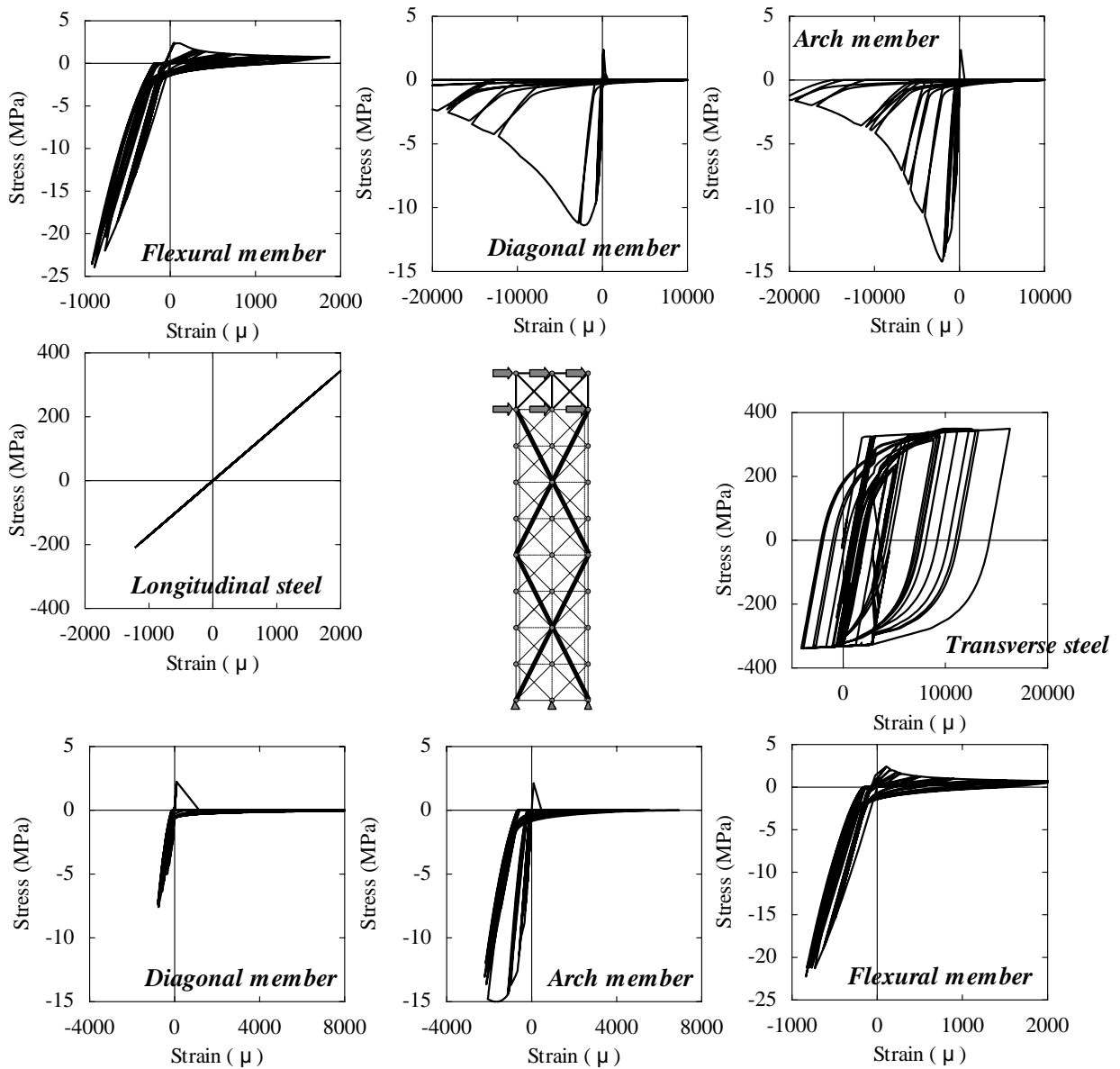**Figure 4.19** Deformed shape of lattice model for the column R–3
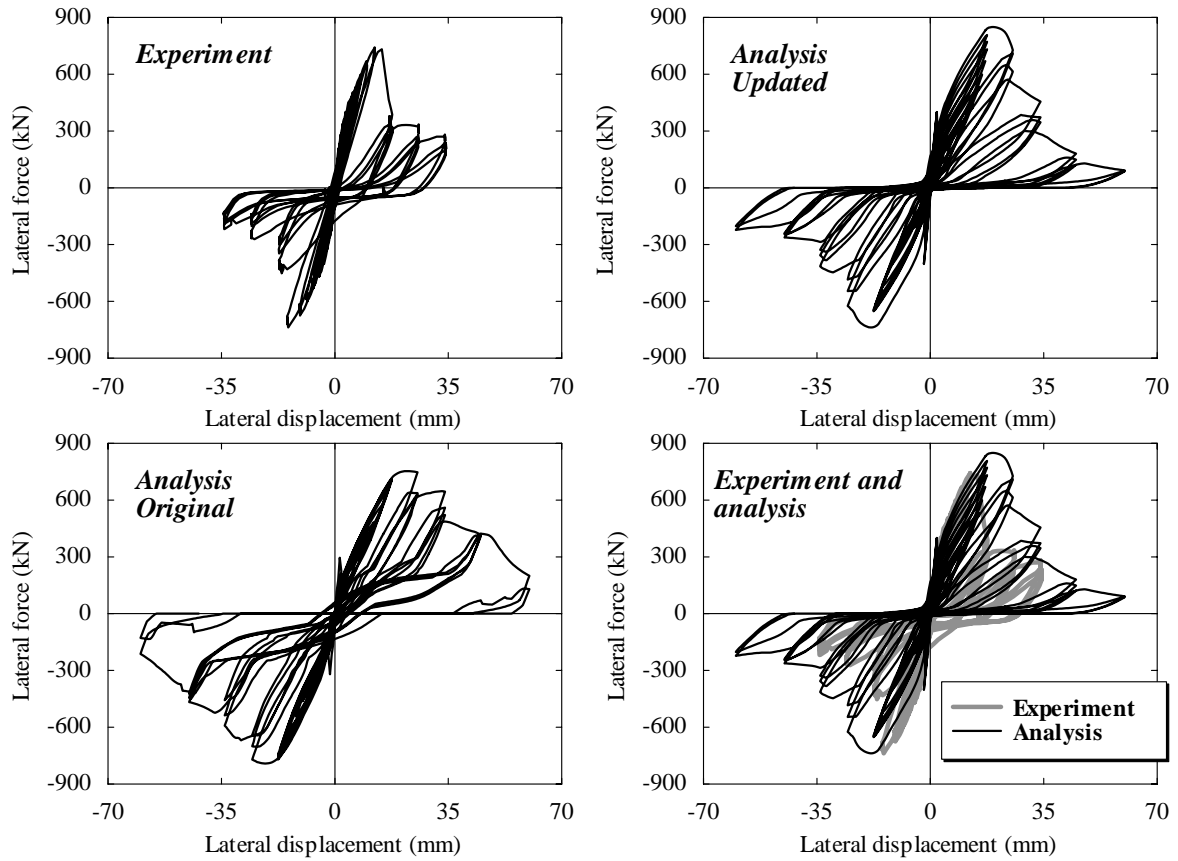

Figure 4.20 Stress-strain relationships in a representative element in the lattice mode for
the column R–3

87

Figure 4.21   Load-displacement relationships of the column R−5

Figure 4.22   Decomposition of flexural and shear deformations for the column R−5
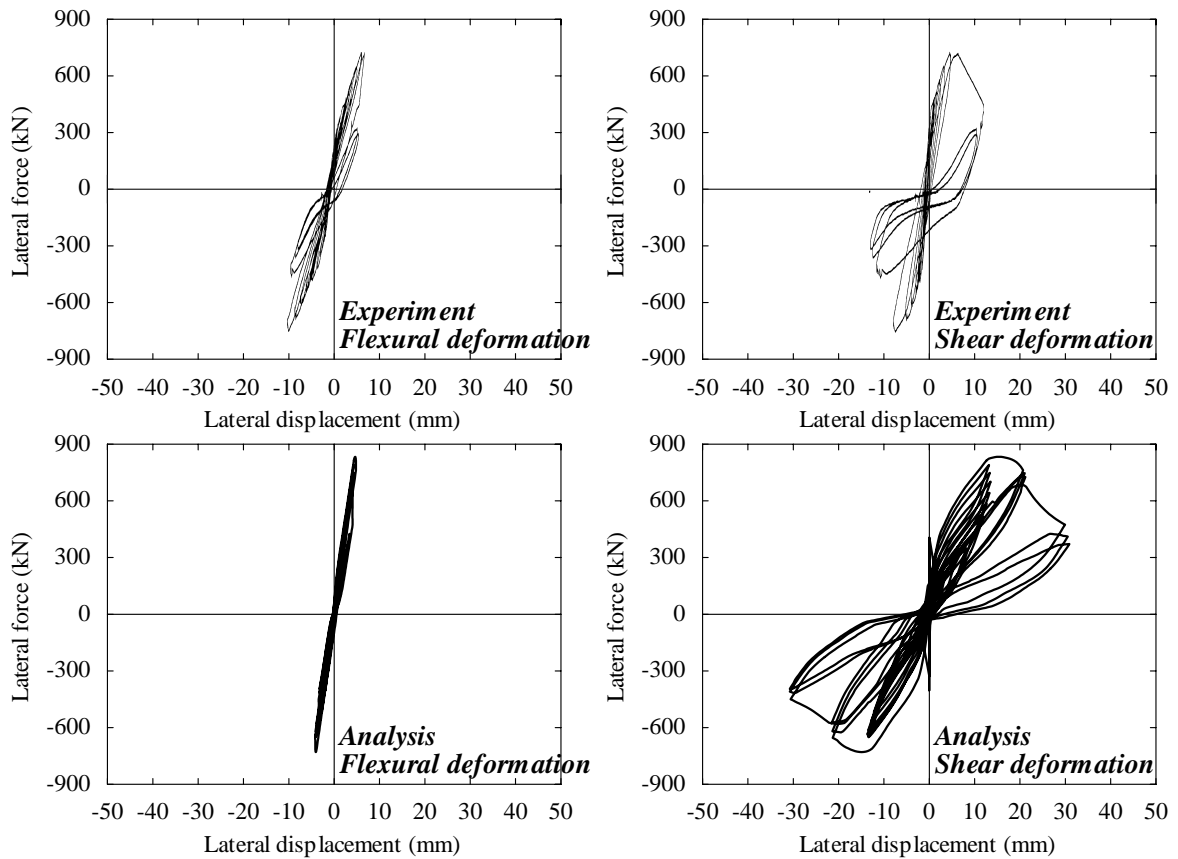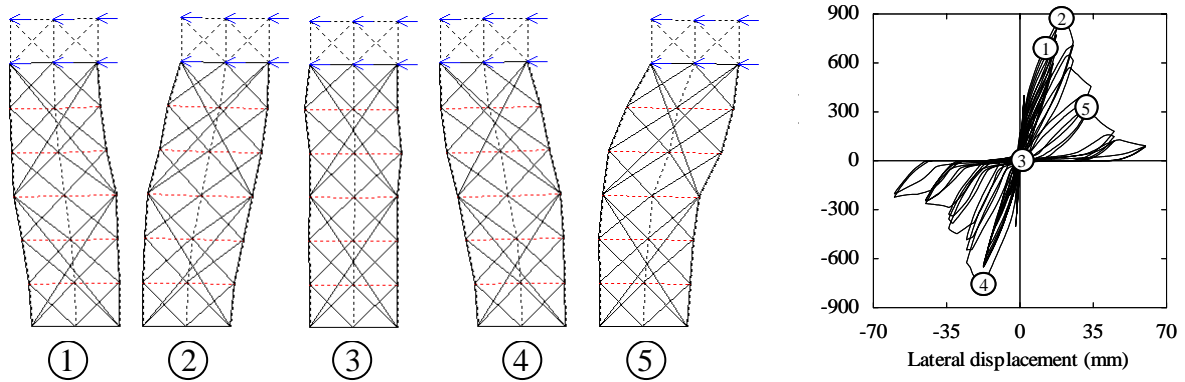
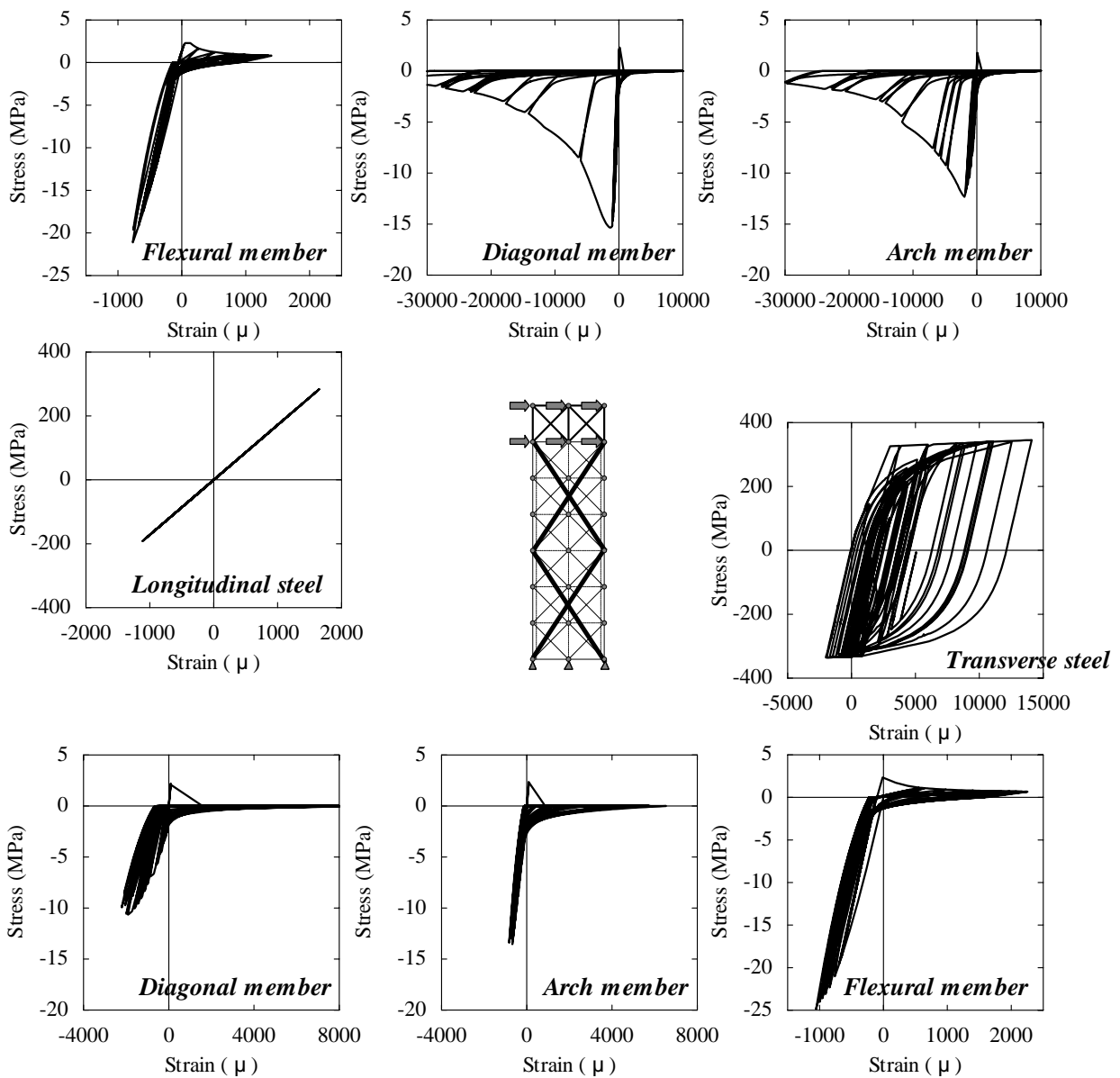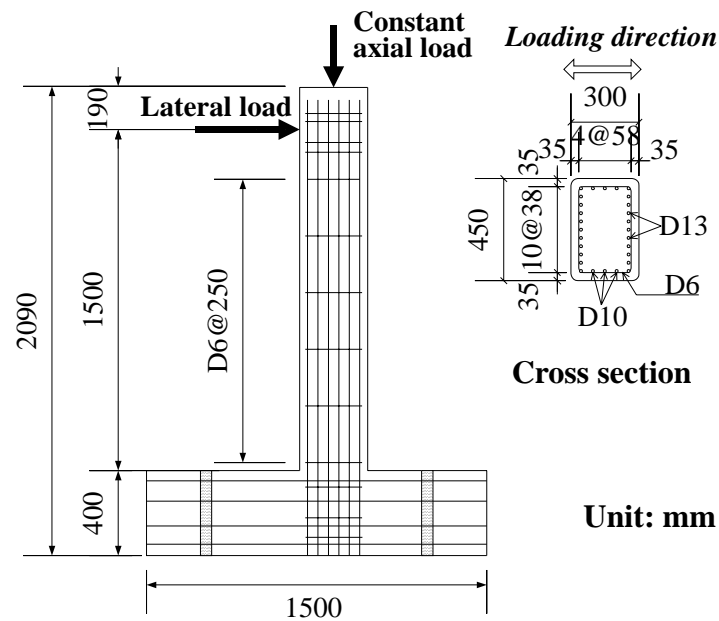**Figure 4.23**   Deformed shape of lattice model for the column R−5

Figure 4.24   Stress-strain relationships in a representative element in the lattice mode for the column R−5

Figure 4.25 Specimen and loading conditions

4.4 RC Columns Strengthened by CFS

4.4.1 Test conditions

The experiment on three RC bridge piers subjected to static reversed cyclic loading performed by Osada et al. (1997) is used to confirm the validity of the 2D static lattice model. The specimen is the cantilever RC pier with the rectangular cross section that is 300 mm depth and 450 mm width of cross section as shown in **Figure 4.25**. The arrangement of reinforcement

Table 4.4 Material properties

Specimen ID	Concrete f_c' (MPa)	Reinforcement				CFS		
		Grade	f_y (MPa)	f_u (MPa)	E_s (GPa)	Thickness (mm)	f_{CFS} (MPa)	E_{CFS} (GPa)
1, 2, 3, 6	27.0	SD295 D6	360	530	175	0.11	4220	243
		SD295 D10	350	500	172			
		SD345 D13	380	560	172			
5, 8	32.0	SD295 D6	340	560	187	0.11	4047	252
		SD295 D10	360	530	168			
		SD345 D13	390	570	172			

Note: specimens No.2, No.3, and No.8 are strengthened by the carbon fiber reinforced sheet (CFS).

Table 4.5 Experimental parameters

ID	Specimen	Number of layer(s) of CFS in transverse direction		Number of layer(s) of CFS in longitudinal direction	Loading condition
		0-300 (mm)	300-900 (mm)		
1	ST-N	–	–	–	Static cyclic
2	ST-CF	1	1	1/4	
3	ST-2CF	2	2	1/4	
5	APD40-N	–	–	–	Pseudo-dynamic
6	PD45-N	–	–	–	
8	APD40-CP	2	1	1/4	

*Note: 1/4 layer of CFS means that the bonded region between concrete surface and CFS was
reduced to one fourth part by using the unbond plastic sheet.*

and loading conditions are also illustrated in **Figure 4.25**.   The longitudinal and transverse reinforcement ratios were 2.38 % and 0.056 %, respectively.   The material properties of concrete and reinforcement are shown in **Table 4.4**.   The experimental cases are shown in **Table 4.5**.   The specimens No.1, No.2, and No.3 are used in the static cyclic test in which the specimen ID is identical to one used in the experiment.   The specimens No.2 and No.3 are strengthened by the carbon fiber reinforced plastic sheet (CFS).

The static reversed cyclic loading was provided by the controlled lateral displacement at the height 1,500 mm of the pier.   The displacement amplitude was stepwisely increased as the magnitude of $n \cdot \delta_y$, ($\delta_y = 13.9$ mm: the lateral displacement at the yielding of longitudinal reinforcement and $n = 1, 2, 3 \ldots$) with one time cycle in each step.   The lateral displacement at yielding was obtained from the calculation with fiber model in the pre-test.

In addition, in order to verify the performance of 2D dynamic lattice model, the experimental test also conducted by Osada et al. (1997) is adopted.   This experiment consists of pseudo-dynamic loading tests for RC bridge piers.   The specimens had the same dimensions as the piers used in the static cyclic loading test as previously described.   As for the calculation in the pseudo-dynamic test, the pier was modeled as a single-degree-of-freedom cantilever structure.   For a single degree-of-freedom structure, the equilibrium equation is expressed as follows:
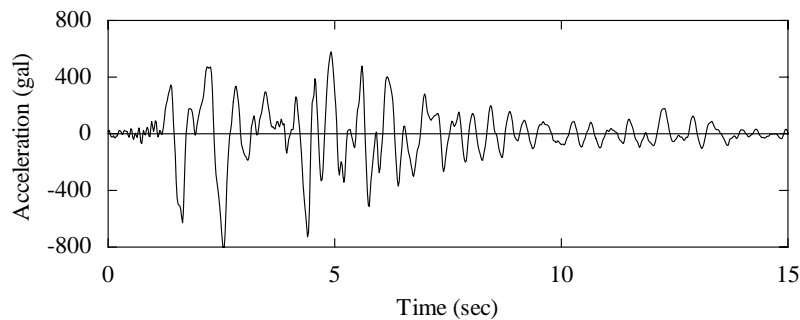
$$m \ddot{u}(t) + c \dot{u}(t) + k u(t) = r(t) \tag{4.1}$$

where m, c, and k are the mass, the damping constant, and the stiffness of the structure.

**Table 4.6** Initial conditions in pseudo-dynamic loading tests

ID	Specimen	Mass (ton)	Damping ratio, h	Yield displacement (mm)	Input maximum acceleration (gal)
5	PD40-N				146.
6	PD45-N	42.	0.03 (After yielding; $h=0$)	13.9	298.
8	PD40-CP				298.

Figure 4.26 NS component recorded at Marine Meteorological Observatory at 1995 Hyogo-ken Nanbu Earthquake (Maximum acceleration: 818 gal)

Similarly, $r(t)$ is the external force.   In a loading test, the iterative control was performed until difference between the estimated displacement applied to the piers and the measured displacement was within a certain convergence tolerance for proper solution.

To apply this scheme, the initial stiffness k used in the iteration should be higher than or equal to the actual tangent stiffness of the structures.   This condition can be satisfied easily for most structures that have a softening behavior.   For single-degree-of-freedom systems, the satisfaction of the above condition prevents the over shot of displacement, the unrealistic loading, and the unloading cycles during the iterative correction.   In the test, the displacement applied at the first iteration is estimated by using the initial stiffness of a pier. The factors and initial input data used in the experimental iteration are shown in **Table 4.6**. The integration time interval was 0.01 second for all tests with step-by-step solution using the central difference method.   For the input ground motion, the N-S element recorded at Kobe Marine Meteorological Observatory in Japan at Hyogo-ken Nanbu Earthquake (Kobe Earthquake, the maximum acceleration is 818 gal) was used.   In this test, the maximum amplitude of the input acceleration was modified to be 298 gal.   The input ground acceleration is shown in **Figure 4.26**.

For both the static cyclic and pseudo-dynamic loading tests, a constant axial compressive load of 79.7 kN (0.59 MPa in compressive stress) was maintained during the experiments.
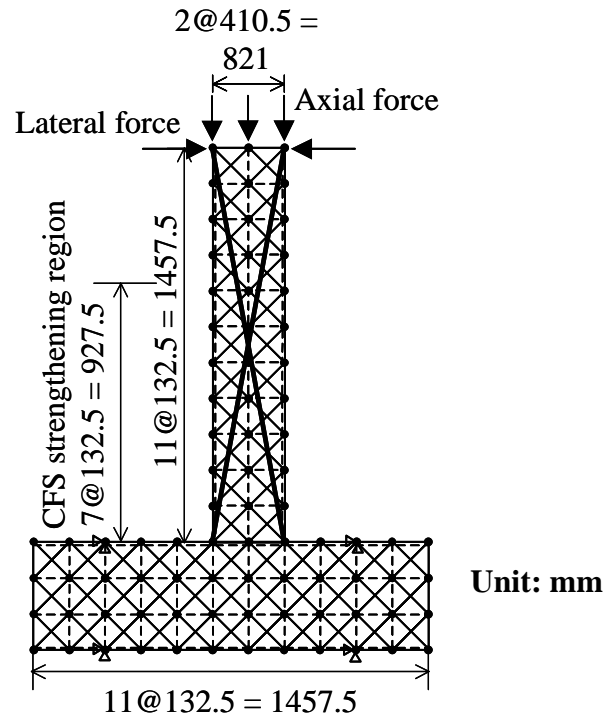
Figure 4.27 2D static lattice model

4.4.2 Static analysis

4.4.2.1 *Experimental and analytical results*

The 2D static lattice model is shown in **Figure 4.27**. The buckling of reinforcement is considered in all analytical cases. The stress-strain relationship considering confinement of concrete by both transverse reinforcement and CFS is applied to the strengthening region as shown in **Figure 4.27**. The stepwisely incremental displacement of 13.9 mm, which is corresponding to the yield displacement δ_y, is given in each cycle. Each cycle is one time. During the test, the constant compressive axial load of 79.7 kN is applied at the top three nodes in the lattice model so that the load of 26.5 kN is applied to each node.

The experimental and analytical results for the specimens No.1 to No.3 are shown in **Figure 4.28**. In the figure, the experimental results are shown as the envelope curves of load-displacement hysteresis. The analytical and experimental results of load and displacement at the first yield of the longitudinal reinforcement, the maximum load, the displacement at the maximum load, and the ultimate displacement are shown in **Table 4.7**. Here, the ultimate displacement is defined as the displacement corresponding to 80 % of the maximum load in the post-peak region.

93

Table 4.7 Results of static cyclic tests and 2D lattice model analysis

	No.1		No.2		No.3	
	Exp.	Ana.	Exp.	Ana.	Exp.	Ana.
Yield load (kN)	97.5	111.3	98.4	118.3	99.7	115.5
Yield displacement (mm)	13.9	12.0	13.9	13.5	13.9	13.5
Maximum load (kN)	110.0	132.6	115.0	138.3	116.0	140.3
Displacement at maximum lateral load (mm)	55.6	55.5	69.5	69.5	69.5	55.5
Ultimate displacement (mm)	55.6	55.5	83.4	83.5	97.3	111.0

In the experiment for the specimen No.1, which is not strengthened by CFS, it is observed that the diagonal crack propagates at the bottom of the pier during $-4\delta_y$. δ_y is the yield displacement. With the slight increase in the lateral displacement after reversing the loading direction, the longitudinal reinforcement behaves plastically and deforms laterally outwards in a process regarded as the buckling. The damage is distributed widely especially in $1h$ region (h: the overall depth of the cross section = 300 mm) from the top of a footing and the core concrete surrounded by the transverse reinforcement is deteriorated.

On the other hand, the analysis can predict appropriately the lateral load-lateral displacement curve until the displacement reaches the post-peak region. This displacement corresponds the initiation of the buckling of the longitudinal reinforcement and the spalling of cover concrete. However, it is found that analytical results slightly underestimate the displacement at the first yield of longitudinal reinforcement. Similarly, the analysis overestimates the lateral yield load. These results show a similar tendency to the conventional lattice model analysis (Miki 2002, 2003b). This tendency can be expressed by the following reasons.

It is necessary to consider the bond action between concrete and a reinforcing bar, for example to assess the constitutive law such as the average stress-average strain relationship of reinforcing bars embedded by concrete (Okamura and Maekawa 1991). Before the crack occurs, the average stress-average strain relationship shows similar to the stress-strain relationship of the bare bar. In this stage, the strain of a bar is uniformly distributed along its longitudinal axis. However, the strain distribution is changed after cracking, and then the strain concentrates at the portion of crack surfaces. The tensile force between adjacent cracks is transferred by concrete due to the bond stress between reinforcing bars and concrete. The local tensile force at a distinct cracked section is mainly carried by the reinforcing bars. The residual tensile force at crack sections is applied to the concrete. The effect of tension

softening is usually treated as a relationship between the average tensile stress and average tensile strain of concrete in the normal direction to crack surfaces. At the same time, the stress-strain relationship of reinforcing bar has to be treated based on its average behavior. Since the stress in reinforcing bar embedded by concrete varies along its longitudinal axis, the average stress-average strain relationship of reinforcing bar is significantly different from the behavior of a bare bar after cracking. Hence, the spatially averaged yield stress becomes lower than the yield stress of a bare bar as clearly pointed out by Okamura and Maekawa (1991). Consequently, it is recognized that the analytical result by the lattice model for the yield load and the load carrying capacity becomes the overestimated prediction. Moreover, it is found that there is a room of development for the constitutive model of reinforcing bar used in the analysis.

4.4.2.2 *Detailed investigation*

The analytical result of the specimen No.1 shows that the buckling of reinforcement took place during the loading cycle at $-4\delta_y$. The estimated buckling length is equal to $1d$, in which d is the effective depth, 265 mm, that is similar size of the experimental observation. As a result, the analytical and experimental results are in the good agreement with each other. The analytical result considering the buckling of reinforcement can appropriately predict the flexural behavior of a RC bridge pier. It is found that from **Figure 4.28**, the analytical load-displacement relationship showed the decrease in the lateral load after the lateral displacement of $5\delta_y$.

In the experiment for the specimen No.2, in which the pier is strengthened for $3h$ portion from the footing, the buckling of reinforcement occurred when the applied displacement reaches $-5\delta_y$. The buckling of reinforcement was observed at $1h$ height from the footing. h is the overall depth of the cross section of a pier. The gradual decrease in the lateral load was observed after the initiation of the buckling of reinforcement at the bottom of the pier. During the cycle of $-6\delta_y$, the fractures of CFS in transverse direction at the corner of cross-section was observed and CFS in the longitudinal direction simultaneously fractured. On the other hand, in the analysis, the buckling length of reinforcement is calculated as $0.5d$. It is smaller than the case of specimen No.1 without strengthening by CFS. This is caused by that CFS resists against the lateral deformation of longitudinal reinforcement. It is well known that the average behavior of reinforcing bar is very sensitive to its length, diameter, and the length to diameter ratio. Since the buckling length decreases due to the strengthening by CFS, the slight decrease in the stress is predicted after the buckling occurs. Consequently, it is found from the **Figure 4.28** that the buckling of reinforcement is delayed
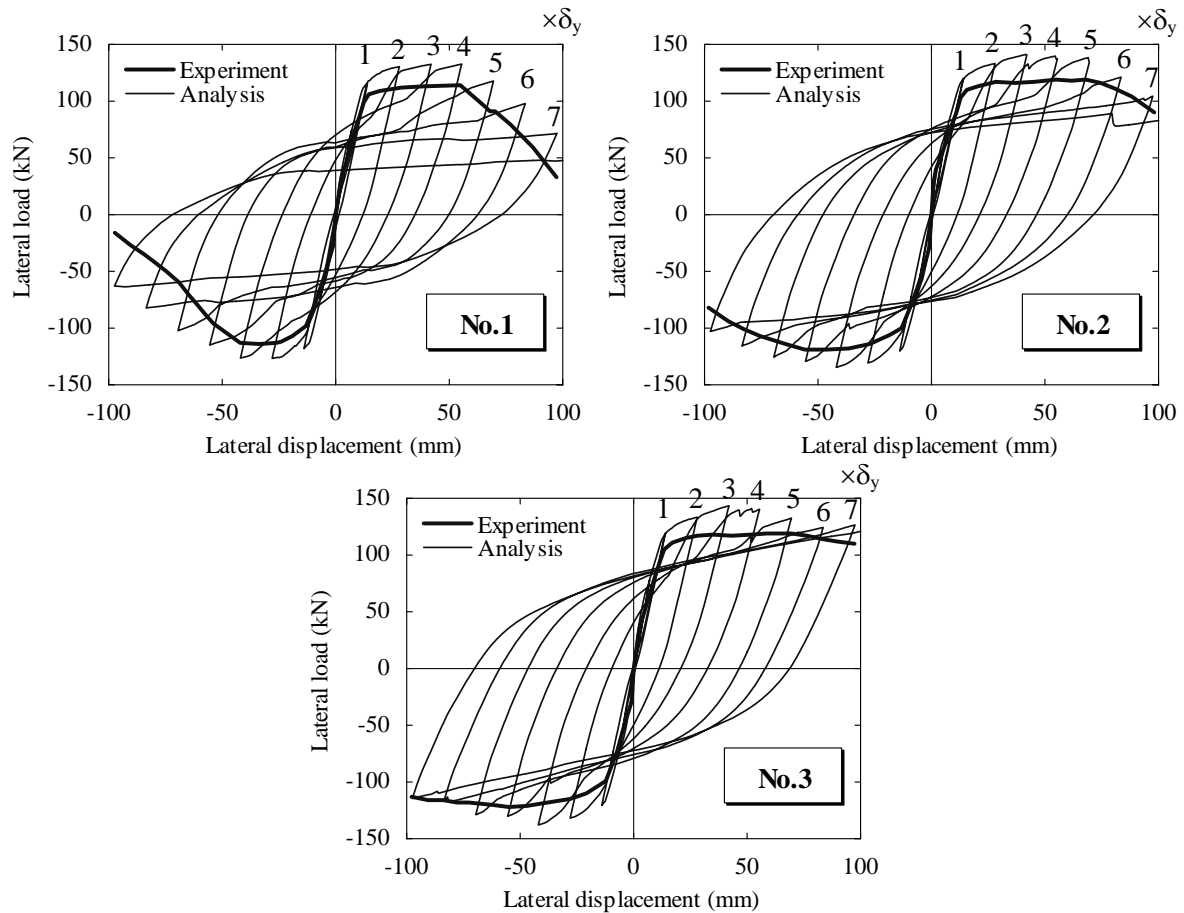
Figure 4.28 Effect of the amount of CFS on load-displacement relationships
(static cyclic test and 2D lattice model analysis)

and the load-displacement after the peak-load becomes milder. This is related to the post-buckling degradation of average behavior. The analytical behavior is found to show the good agreement with the experimental observation.

In the specimen No.3, in which the pier is strengthened by CFS of two layers at $3h$ region, the experimental result of load-displacement relationship showed stable post-peak behavior until $7\delta_y$. The damage was concentrated in $1h$ region and the buckling of reinforcement did not occur. This is a narrow region as compared with other results. In the analysis, the load-displacement relationship is found to be close to the experimental result. The buckling length is predicted as $0.5d$ that is similar to the analytical result on the specimen No.2. The load-displacement relationship is also similar to the curve as compared with the specimen No.2. The buckling behavior of reinforcement does not occur in the analysis because of the large amount of CFS for strengthening. This corresponds to the experimental result. The fracture of CFS at the corner of cross section was not observed in the experiment. In contrast, the analysis cannot predict the fracture of CFS, because of the geometrical disagreement of modeling in which the analytical model is in 2D.

4.4.3 Dynamic analysis

4.4.3.1 *Load carrying capacity and deformation capacity*

In this section, the nonlinear analysis using the 2D dynamic lattice model considering the buckling of reinforcement are carried out. The analytical procedure has been described in **section 2.7**. In this analysis, the Newmark $\beta = 1/4$ method is applied as the time integration. A time interval of 0.01 sec is used. In addition, the damping is introduced as the Rayleigh damping, $a_0 = 0.621$, $a_1 = 1.426 \times 10^{-3}$. Here, the damping ratio is assumed to be 3.0%.

Table 4.8 shows the results of the pseudo-dynamic loading test and the 2D lattice model analysis. In the table, the lateral load and lateral displacement when the longitudinal reinforcement yields at the base of the pier, the maximum lateral load and its corresponding displacement are shown. In the experiment, the yield displacement, δ_y is used that obtained from the static test (= 13.9 mm).

It is found that the analytical yield load and yield displacement are similar to the result of the static analysis. It is also found that the yield load is higher and the yield displacement is smaller than the experimental results. The analytical load-displacement curve of all piers is found to be slightly stiffer than the experimental one, especially with respect to the initial stiffness of the pier. As for the maximum load capacity, the analytical and experimental results are found to be in the good agreement with each other, but the analysis predicts slightly higher load than the experimental one that is also similar to the static analysis.

For the specimen No.5, the analytical maximum displacement is smaller than the

Table 4.8 Results of the pseudo-dynamic loading tests and the 2D dynamic lattice model analysis

|	No.5		No.6		No.8	
	Exp.	Ana.	Exp.	Ana.	Exp.	Ana.
Yield load (kN)	97.5	112.2	97.5	111.0	98.4	119.0
Yield displacement (mm)	13.9	12.7	13.9	12.5	13.9	13.4
Maximum load (kN)	108.6	117.3	116.5	130.1	128.3	138.7
Maximum displacement (mm)	23.6	19.8	66.3	71.5	70.9	71.9
Residual displacement (mm)	3.0	4.2	6.8	17.6	15.3	36.5

experimental one, while for the specimens No.6 and No.8 the analytical maximum displacement is larger than the experimental prediction. In the pseudo-dynamic loading test, the damping ratio, h is given zero after the yielding of longitudinal reinforcement to consider the hysteresis damping due to material nonlinearity of concrete and reinforcement. In contrast, the analysis incorporates the viscous damping and the damping ratio is set as $h = 0.03$ (3.0 %) during loading. The hysteresis damping for material nonlinearity can be considered as well. In the specimen No.5, in which the input ground motion is regarded as low level, the analytical response becomes smaller than the experimental one because of the higher initial stiffness of the pier. The specimens No.6 and No.8 subjected to large ground motion show larger lateral deformation in the analysis in spite of the consideration both the viscous damping and hysteresis damping. Through the discussion, it is found that the analytical stiffness of a RC pier after yielding of longitudinal reinforcement is slightly underestimated.

4.4.3.2 *Hysteretic performance*

Figure 4.29 shows the experimental and analytical relationships between the lateral force and the lateral displacement at the top of the specimens No.5, No.6, and No.8. The results of experiment and analysis for the displacement time histories at the top of the piers are illustrated in **Figure 4.30**. The residual displacements are defined as the displacements at around 15 seconds as shown in **Figure 4.30**. The residual displacement obtained by the pseudo-dynamic loading tests and the 2D dynamic lattice model considering the buckling of reinforcement is tabulated in **Table 4.8**.

It is found that the analytical results of the specimen No.5 show the linear response. The analytical behavior is very close to the experimental one. In the experiment, slight increase in the lateral load was observed and the fine flexural crack took place at the bottom of the pier. In this level of ground motion, the diagonal cracks and the crushing of concrete did not occur. The residual displacement is found to be around zero in both the experiment and analysis.

In the specimen No.6, in which the amplitude of ground motion is twice the case of the specimen No.5, the large deformation is predicted after the longitudinal reinforcement yields. It corresponds to the experimental results. It can be observed that the analytical load-displacement relationship of the pier shows higher energy dissipation capacity. After the buckling of reinforcement took place, the pinching behavior is dominant as shown in **Figure 4.29**. This behavior is also observed in the experiment. From the displacement history as shown in **Figure 4.30**, the residual displacement remaining in one direction is predicted after around 2.7 seconds, at which the maximum displacement is reached.

(a) Experiment   **(b)** Analysis
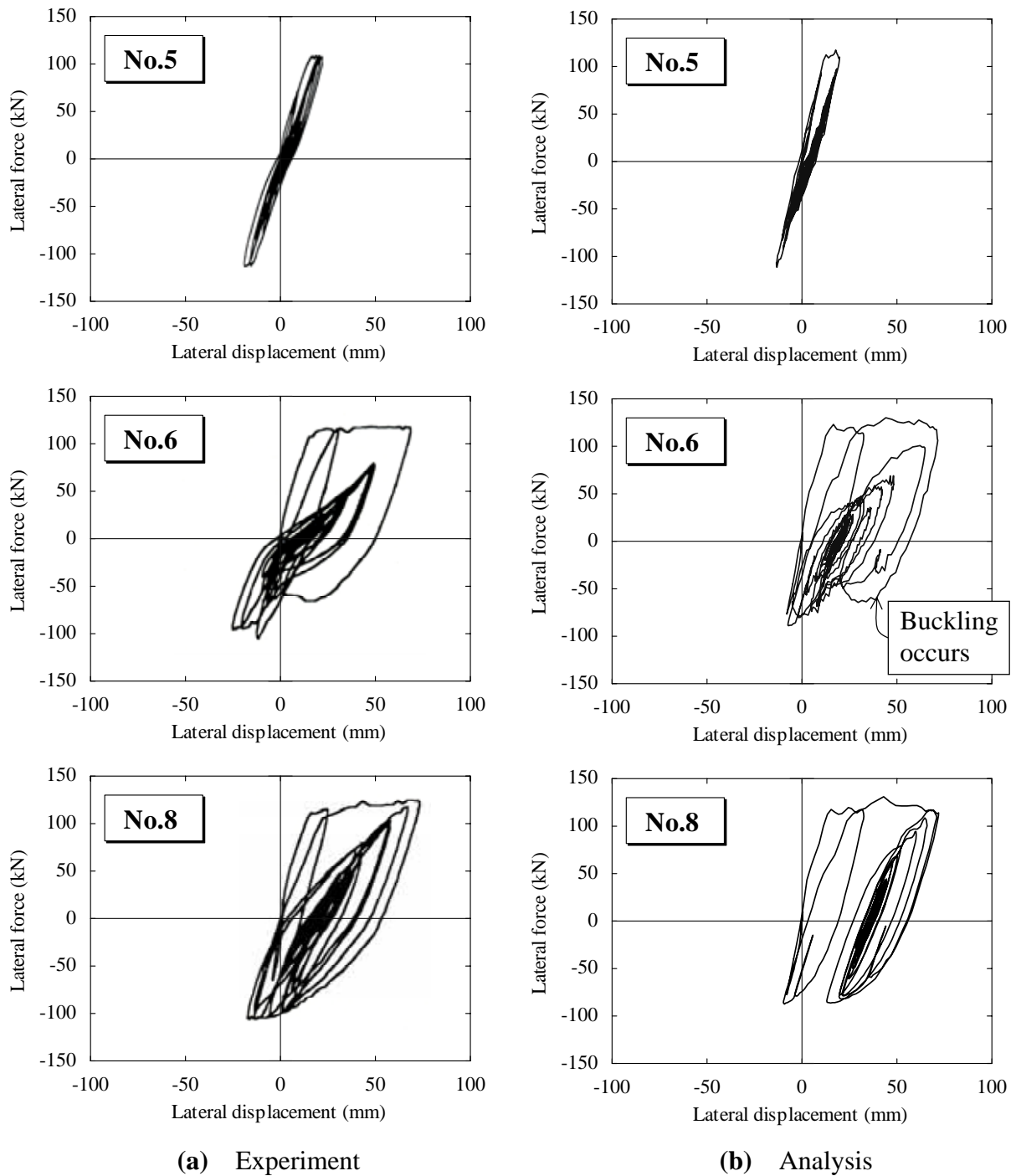
Figure 4.29   Hysteresis loops obtained from the pseudo-dynamic loading tests and the 2D
dynamic lattice model

Similarly, the analytical load-displacement relationship of the specimen No.8 is found to be
close to the experimental one.   The hysteresis relationships, in both the experiment and
analysis, indicate the higher energy dissipation capacity after yielding of longitudinal
reinforcement.   With the damage condition in the experiment, the spalling of cover concrete
and the fracture of CFS were not observed.   In the analysis, the buckling behavior of
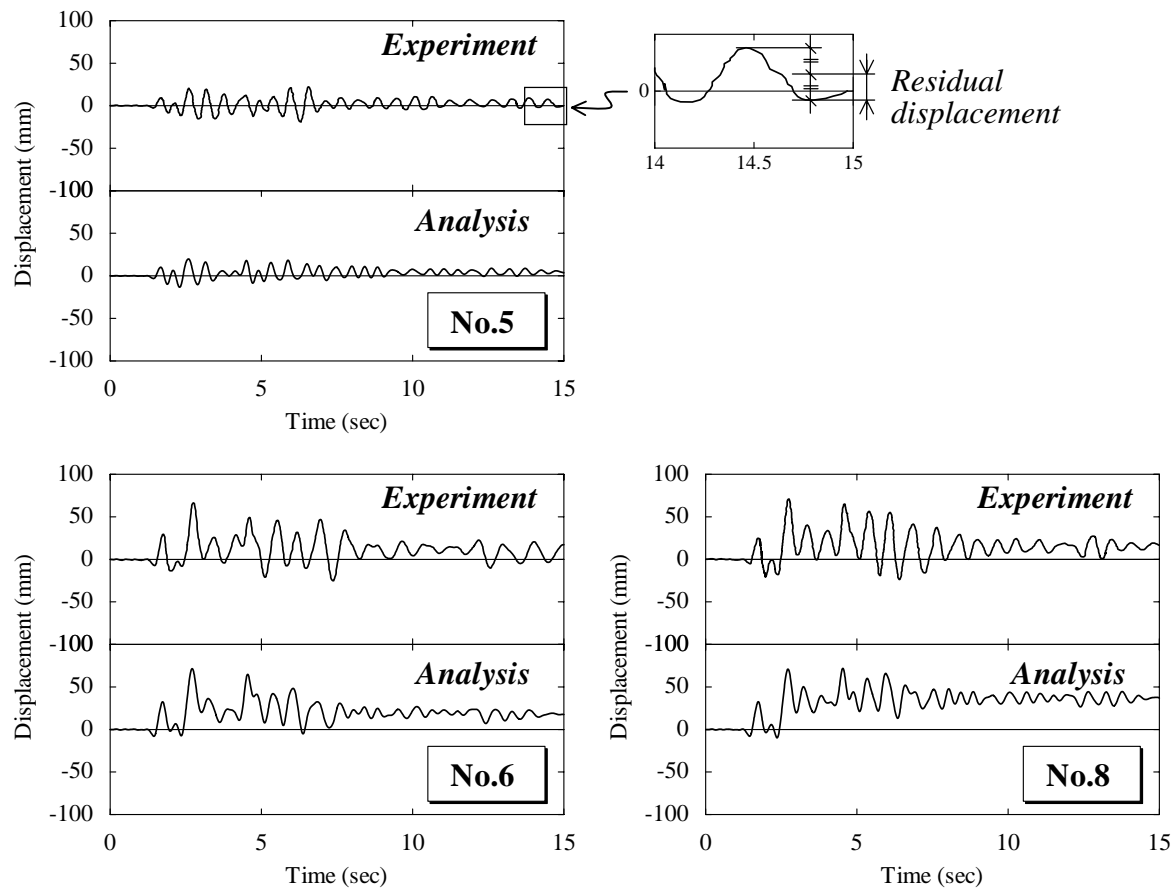
Figure 4.30 Displacement histories obtained from the pseudo-dynamic loading tests and the 2D dynamic lattice model

reinforcement cannot be predicted and the RC pier shows stable behavior during shaking even if the large deformation range is reached. However, the analytical tangent stiffness during unloading and reloading is stiffer than the experimental one. As a result, the frequencies of the specimen No.8 after first seven seconds become higher. This is caused by that the stiffness of concrete under compressive cyclic loading is evaluated higher than the reality, in which the stiffness is assumed as the initial stiffness of concrete in compression. Therefore, the improvement for the constitutive model of concrete under cyclic loading in compression and tension is necessary to predict by the lattice model with high accuracy.

Through previous discussions, although there are some rooms to improve the model, it is confirmed that the analysis using 2D dynamic lattice model considering the buckling behavior of longitudinal reinforcement can predict the seismic response of RC bridge piers with appropriate accuracy. In addition, the analysis can reasonably capture the seismic performance of RC bridge piers strengthened by CFS with respect to the load-displacement curves, the maximum displacements, and the residual displacements.

## 4.5   2D Analysis Considering Pull-out of Longitudinal Reinforcement

4.5.1   Experimental setup

The target is the experimental tests of RC columns subjected to reversed cyclic loadings performed by Ishibashi el al. (2000).   The deformation capacity of a RC column is evaluated to simulate the behavior of the column at large deformation range, especially in terms of the bond-slip behavior.   In the experiment, the direct measurement system of bond-slip of longitudinal reinforcement from a footing was developed.   Pre-cast box cavity was provided to set the displacement measurement in the footing with stainless steel pipe, silicon tube, and wire.   The wire was connected to a longitudinal reinforcing bar at the bottom of the column. The dimension of the column and arrangement of reinforcement are shown in **Figure 4.31**. The material properties of concrete and reinforcement are tabled in **Table 4.9**.

For loading pattern, the displacement amplitude was stepwisely increased in increments of $n \cdot \delta_y$ (n = 1, 2, 3…) during each loading step.   Each cycle of same amplitude is one time.   Here, δ_y is the lateral displacement at the initial yielding of the longitudinal reinforcement ($\delta_y = 5.8$ mm) at the bottom end of the column.   The identical loading hysteresis to experiment is used in the analysis by a displacement-controlled incremental calculation.   During the test, a constant axial compressive load of 156.7 kN (0.59 MPa in compression) was applied at the top of the pier.
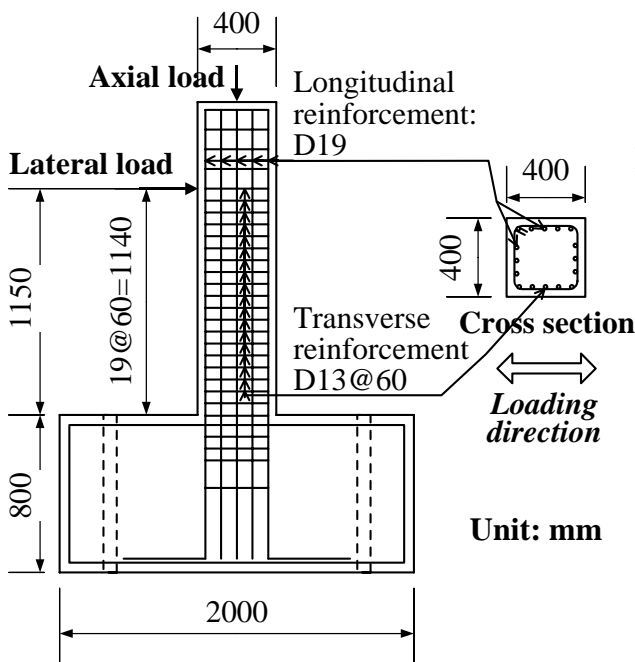
Figure 4.31   Details of the specimen
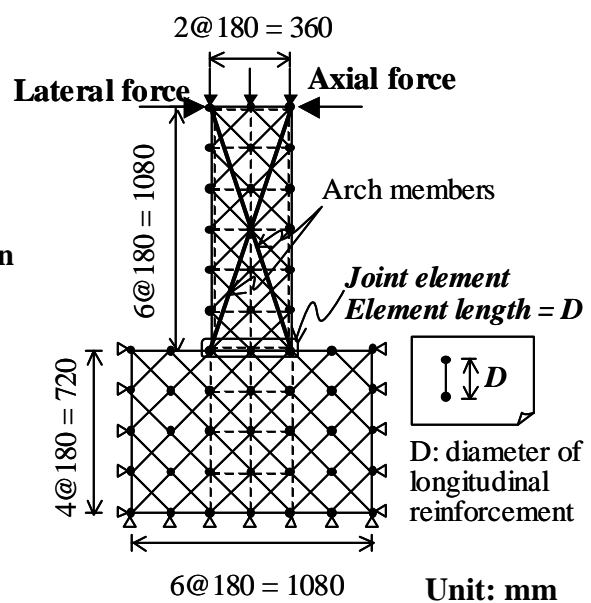
Figure 4.32   2D static lattice model

101

Table 4.9   Specimen and material properties

Specimen No.	Cross section (mm × mm)	Concrete f_c' (MPa)	Longitudinal reinforcement				Transverse reinforcement		Axial compressive stress (MPa)
			Diameter	f_y (MPa)	E_s (GPa)	Diameter	Spacing (mm)	
A1		26.4	D19	378.4	183		80	0.98
A2		23.3		378.4	183		60	
A3		26.8	D16	397.2	184	D13	70	0.49
A5	400 × 400	29.1	D13	358.3	181		140	
A6		30.9	D19	378.4	183		50	
A8		23.8	D16	397.2	184		120	0.98
A9		21.7		378.4	183	D16		
A11	500 × 500	24.6	D19	378.4	183	D13	60	
K1	400 × 400	19.4		375.1	182			

4.5.2   Construction of lattice model and joint elements

The 2D lattice model to discretize the RC column with a rigid footing is illustrated in **Figure 4.32**.   In the model, the joint element is provided to connect between the column and the footing.   The strain-slip relationship of longitudinal reinforcement discussed in **section 2.6.2** is incorporated into the joint elements.   In the model of the joint elements, the tensile behavior is mainly governed by the bond action between concrete and reinforcement, while the compressive stress is carried by concrete at the bottom of the column.

When the joint element is treated as a truss element, the element length must be important. Here, the axial force-deformation relationship in the local element model is presented as follows:

$$\boldsymbol{f} \;=\; \boldsymbol{kd} \tag{4.2}$$

where

$$\boldsymbol{k} = \begin{bmatrix} k_{aa} & k_{ab} \\ k_{ba} & k_{bb} \end{bmatrix} = \gamma \begin{bmatrix} 1 & -1 \\ -1 & 1 \end{bmatrix} \tag{4.2}$$

$$\gamma = \frac{EA}{l} \tag{4.3}$$

in which $\boldsymbol{k}$ is the stiffness matrix, $\boldsymbol{d}$ is the displacement vector, and $\boldsymbol{f}$ is the force vector. Similarly, E, A, and l are the tangent stiffness, the cross-sectional area, and the length of an

element, respectively. If the length of a joint element l is extremely smaller than that of other longitudinal reinforcement members, the axial stiffness of an element becomes greatly larger. It cannot provide the reasonable results. To determine the length of a joint element, the previous study presented by Murayama et al. (2001) is referred in this study. They proposed a stress-slip relationship of longitudinal reinforcement based on the experimental observation. In their study, the analysis was conducted by using the model of stress-slip relationship of longitudinal reinforcement in which they recommended to make the element length equal to the diameter of a reinforcing bar.

4.5.3   Verification for slip of longitudinal reinforcement from the footing

In the experiment for the specimen K1, the slip of longitudinal reinforcement at the joint between the column and the footing was directly measured as mentioned previously. The experimental result for the relationship between the strain and slip of longitudinal reinforcement at the bottom of the column is shown in **Figure 4.33**. It can be observed in the figure that the stable behavior for the slip of longitudinal reinforcement is measured until the ultimate state in the experiment. The analytical cyclic history of strain-slip relationship of the joint element is also shown in the figure. From **Figure 4.33**, it is found that the pull-out behavior of a longitudinal reinforcement can be captured by the joint elements incorporating the strain-slip relationship of longitudinal reinforcement. Hence, it is confirmed that the joint element considering the bond action between concrete and reinforcement inside the footing can predict the pull-out behavior of longitudinal reinforcements.

(a)   Cyclic response   **(b)**   Maximum response during each cycle
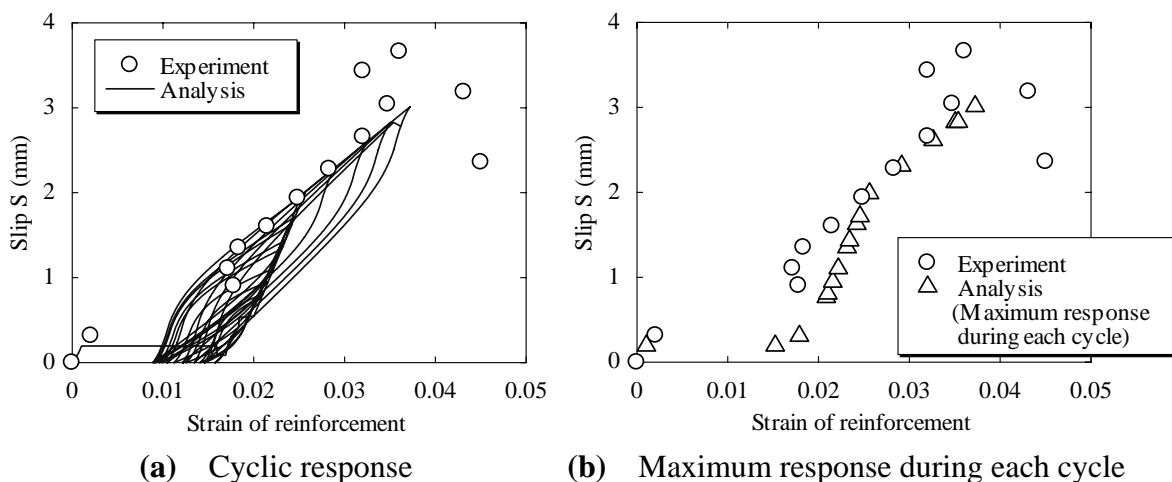
**Figure 4.33**   Strain-slip relationship of longitudinal reinforcement at the bottom of the column
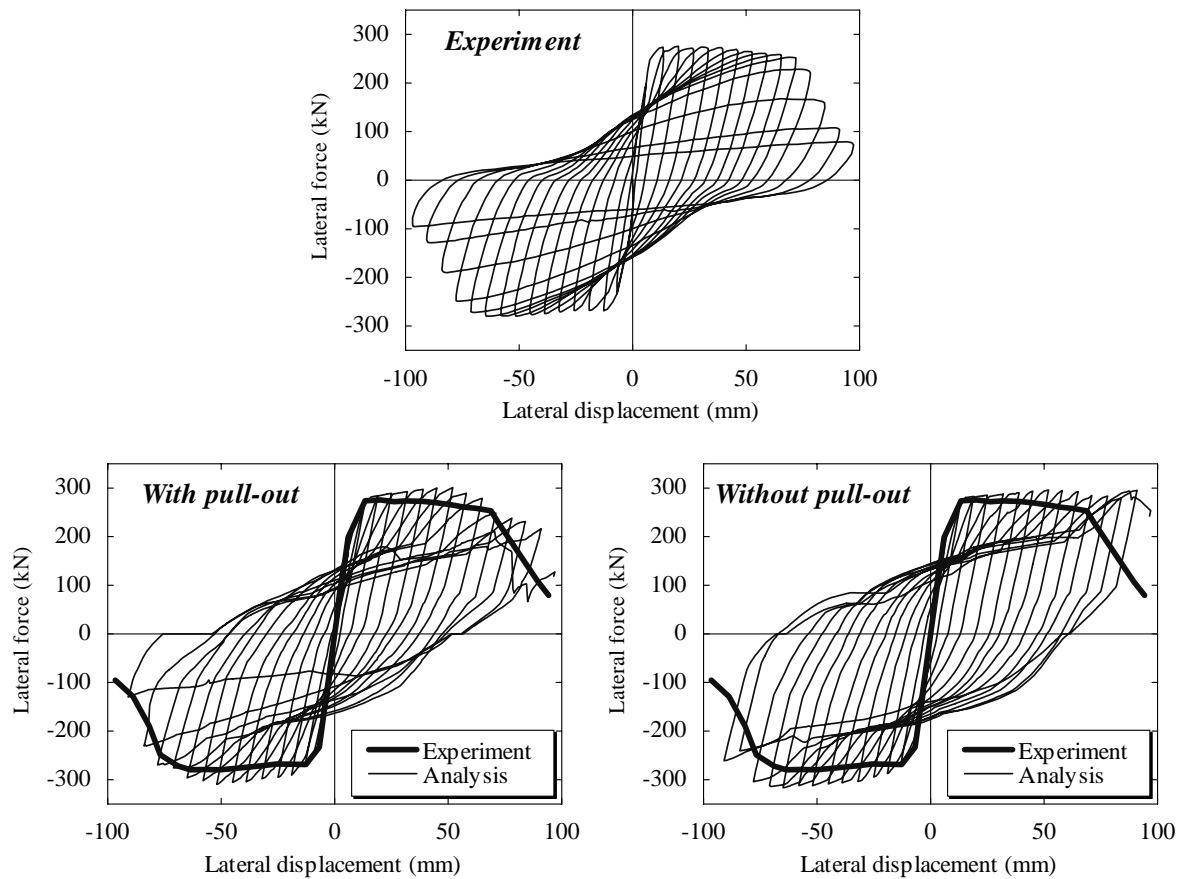
Figure 4.34 Lateral load-lateral displacement relationships of the specimen K1 (experiment and analysis)

4.5.4 Hysteretic characteristics

The experimental and analytical results are illustrated in **Figure 4.34**. The reversed cyclic loading tests and the 2D lattice model analysis are conducted for the specimen K1. In the analysis, the results both considering and neglecting the pull-out behavior of longitudinal reinforcement are shown. Here, the buckling behavior of longitudinal reinforcement is ignored in the analysis. This is because that the main objective in this analysis is to investigate the individual effect of the pull-out behavior of longitudinal reinforcement on the overall cyclic behavior of RC columns. As expected, it is difficult to take place the buckling of reinforcement at the bottom of the column since the RC column is sufficiently reinforced by the transverse reinforcement. However, it is believed that the analytical interaction between the buckling of longitudinal reinforcement and the pull-out of longitudinal reinforcement at the bottom of the column should be investigated in future.

By comparing between two analyses, the analytical initial stiffness considering pull-out behavior is higher and the analytical displacement the peak load is smaller than the results
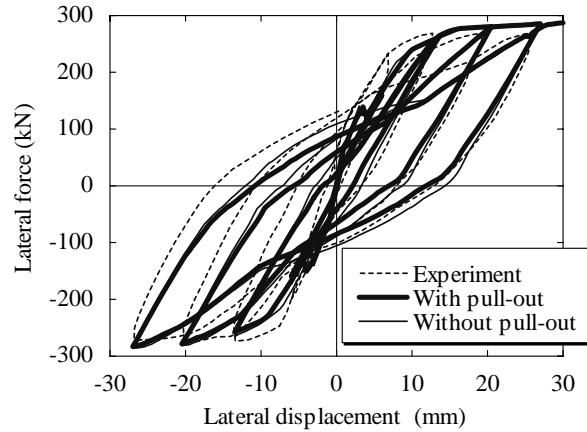
Figure 4.35   Hysteresis loops of the specimen K1during initial 4 d_y range

neglecting the pull-out behavior.   It can be observed that the analysis considering pull-out behavior predicts the slightly larger energy dissipation capacity than that neglecting pull-out behavior.   Similarly, in the analysis considering pull-out behavior, the tangent stiffness during cyclic loading is smaller than that neglecting pull-out behavior.

The relationship between lateral displacement and accumulative energy dissipation for the specimen K1 is shown in **Figure 4.36**.   The accumulated value of energy dissipation is calculated as the area surrounded by one cycle of the hysteresis loops.   The figure demonstrates that the decrease in the dissipated energy by the RC column after lateral displacement reaches to 80 mm can be predicted by the static lattice model analysis considering the pull-out behavior of longitudinal reinforcement.   It corresponds to the experimental observation.   The pull-out behavior significantly influence on the prediction of both the energy dissipation and the residual displacement.   Therefore, the consideration of the pull-out of longitudinal reinforcement from the footing range is required in the analysis to
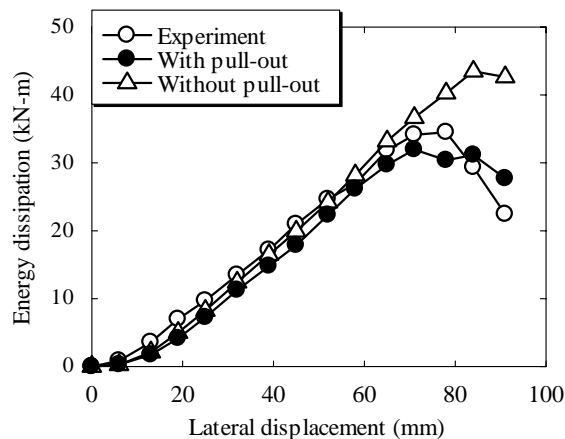

Figure 4.36   Accumulative energy dissipation for the specimen K1

predict the residual displacement with appropriate accuracy.

In order to understand the effect of pull-out behavior of longitudinal reinforcement on the post-peak behavior of a RC column, the detailed investigation is carried out.　In the analysis, this post-peak behavior can be explained by the softening behavior of an arch member of concrete.　The stress-strain relationships of concrete in compression obtained from the analysis with and without the pull-out behavior are shown in **Figure 4.37**.　The remarkable element is set as one arch member of concrete as also shown in **Figure 4.37**.

Here, the case in which the pull-out model is provided at the connection between the column and the footing is focused on.　When the RC column is reached at the large deformation region, the tensile strain of longitudinal reinforcement at the column-footing connection significantly increases due to the locally large flexural tensile stress at the flexural crack surface.　As a result, the stress is beyond the stress corresponding to the strain hardening. This tensile strain is larger than the prediction neglecting the pull-out behavior.

Consequently, the compressive stress in the arch member connecting between the loading point and the bottom of the column increases.　It causes the larger strain of concrete in the arch member.　This behavior results in the post-peak softening of the load-displacement relationship of the RC column.　It shows the good agreement with the experimental results. However, it should be noted that this analysis considers the pull-out behavior of longitudinal reinforcement while the buckling of reinforcement is ignored.　When the buckling behavior of reinforcement actually takes place at the flexural compressive extreme fiber, this softening behavior may change due to the interaction effect between the pull-out and the buckling of longitudinal reinforcement.
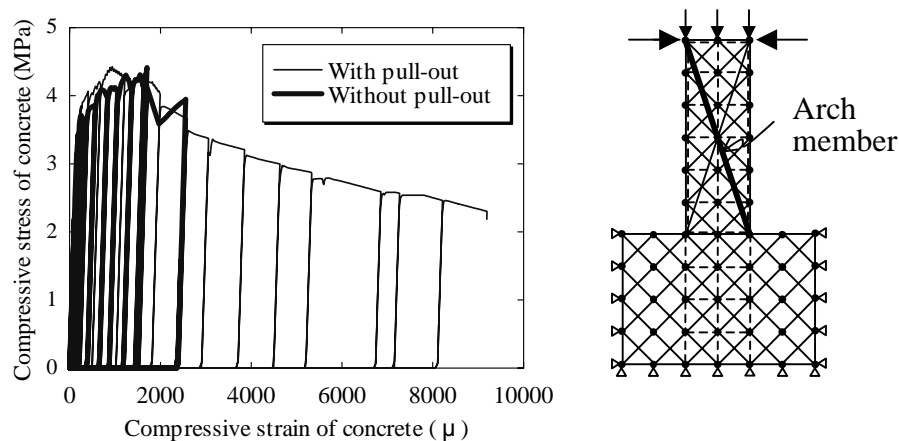
Figure 4.37　Compressive stress-strain relationships of arch member of concrete

**Table 4.10** Response of RC column calculated from 2D static lattice model

Specimen No.	Yield displacement (mm)		Ultimate displacement (mm)		Displacement ductility factor		Yield load (kN)		Maximum load (kN)	
	Exp.	Ana.	Exp.	Ana.	Exp.	Ana.	Exp.	Ana.	Exp.	Ana.
A1	8.13	9.5	73.41	69.30	9.03	7.29	218.9	230.7	282.9	283.1
A2	7.66	9.0	82.05	80.10	10.71	8.90	214.6	258.9	278.3	291.8
A3	6.18	8.0	76.78	69.40	12.42	8.68	143.5	187.9	203.9	237.1
A5	5.41	6.5	90.17	46.10	8.85	7.09	114.1	141.9	145.3	150.4
A6	6.92	9.0	61.27	85.50	13.03	9.50	222.4	225.6	307.3	290.4
A8	6.54	8.5	61.27	56.10	9.37	6.60	175.1	214.8	222.9	241.0
A9	6.80	9.0	90.66	82.90	13.33	9.21	208.0	210.6	292.3	290.7
A11	5.80	6.0	71.62	78.60	12.35	13.10	265.8	232.7	366.4	322.6
K1	5.80	6.0	78.10	76.04	13.47	12.67	208.7	241.4	274.4	287.0

4.5.5   Parametric study

The analyses by using 2D static lattice model considering the pull-out behavior of longitudinal reinforcement are conducted.   In the analyses, the parameters are the amounts of longitudinal and transverse reinforcements and the axial load those may affect the post-peak response and the deformation capacity of RC columns.   The results of experiment and analysis are tabulated in **Table 4.10**.   The experimental results normalized by the analytical responses are shown in **Figure 4.38**.   Herein, the ultimate displacement is defined as the lateral displacement at the point when the lateral force corresponds to the yield load of longitudinal reinforcement in the post-peak region.   Similarly, the displacement ductility factor is defined as a quotient of the ultimate displacement and the yield displacement.

In the previous study (Miki et al. 2002), the analysis by using the conventional lattice model has been predicted the higher initial stiffness and the smaller yield displacement than the results of experiment.   In contrast, the enhanced lattice model with a footing part can predict reasonable response of the RC columns in which the pull-out behavior of longitudinal reinforcing bars is considered.   Since the prediction of yield displacement is smaller, the displacement ductility factor is evaluated larger than the experimental observation. Nevertheless, the analysis can predict the maximum load and the ultimate displacement appropriately.
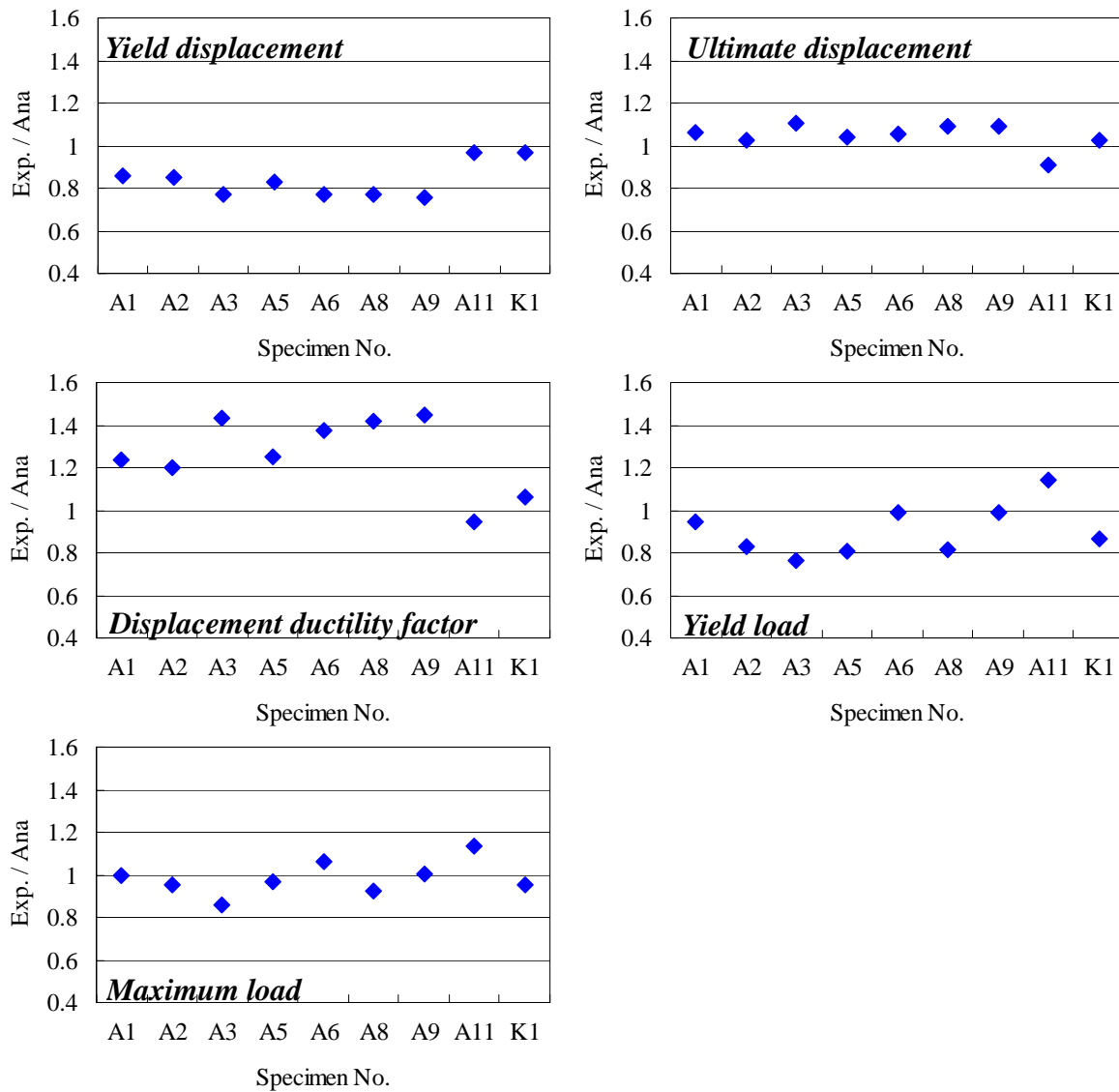
Figure 4.38   Analytical responses obtained by the 2D static lattice model

4.6   Dynamic Analysis for Shaking Table Tests of RC Bridge Piers

4.6.1   Outlines of target structures

The analytical target selected for the dynamic lattice model analysis is a series of shaking table tests (Kawashima and Hasegawa 1994) on RC bridge piers, as explained below.

The experiment was carried out on a structural system in which the pier supports a superstructure component consisting of a beam.   Here, the weight of the beam was 393.2 kN. The external lateral force acting on the RC bridge pier was the inertial force provided by the

beam.   The specimen was a cantilever RC bridge pier of rectangular cross-section with a rigid footing.   The details and dimensions of the tested pier are shown in **Figure 4.39**.   The input ground motion was the EW component recorded at Lake Hachiro-gata in Japan during Nihonkai-Chubu Earthquake of 1983 as shown in **Figure 4.40**.   The maximum acceleration in the ground motion was 144 gal.   In order to make the predominant period of the ground motion close to the natural period based on the initial stiffness of the RC bridge pier, the time axis of motion was condensed by 50 %.

The main significant characteristics of this ground motion are the long duration of the principal motion and the acceleration peaks that occur at 20 seconds and 50 seconds after the start.   A verification based on long-duration ground motion is very beneficial because it provides different insight than the verification based on comparatively large ground motion over a short period, such as experienced during Hyogo-ken Nanbu Earthquake.

The experiments were carried out on three specimens with different maximum accelerations: 275 gal, 360 gal, and 402 gal.   These are denoted as Case-A, Case-B, and Case-C, respectively.   As regards the material properties of the specimens, the averaged compressive strength of concrete in three specimens was 29.2 MPa.   The yield strength of the longitudinal was 357 MPa, while that of the transverse reinforcement was 319 MPa.
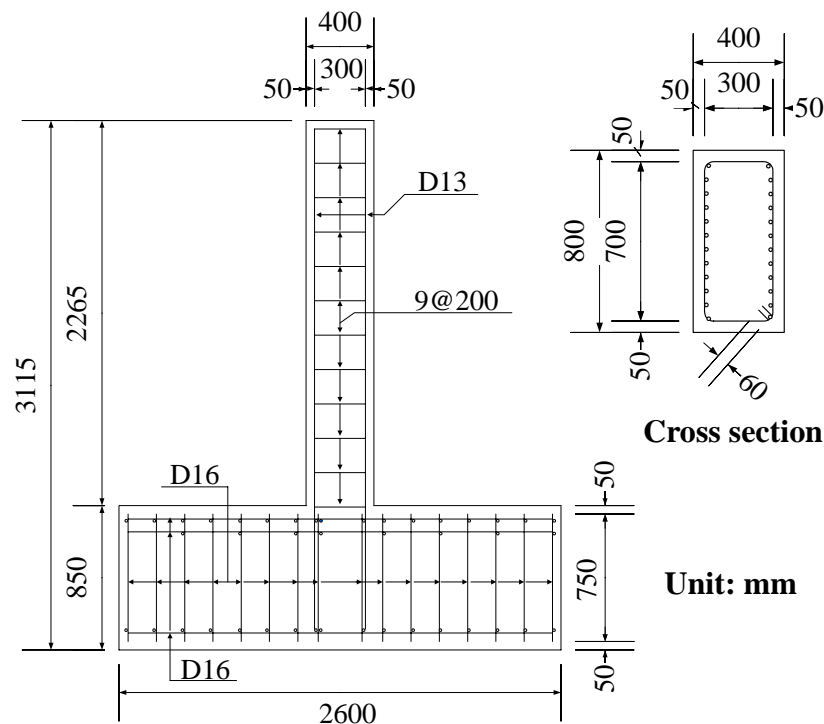
Figure 4.39   Specimen details and test setup (shaking table test)
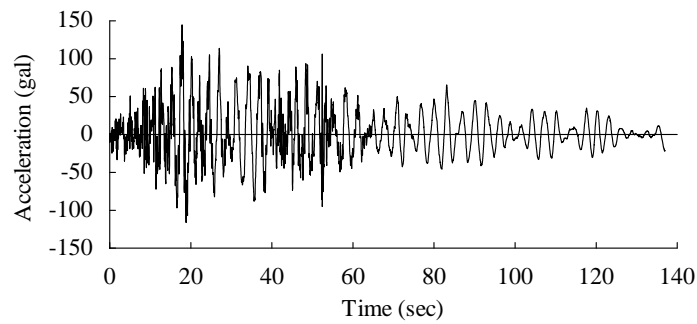
Figure 4.40   EW component wave recorded at Lake Hachiro-gata in Japan at Nihonkai-Chubu Earthquake in 1983 (Maximum acceleration: 144 gal)
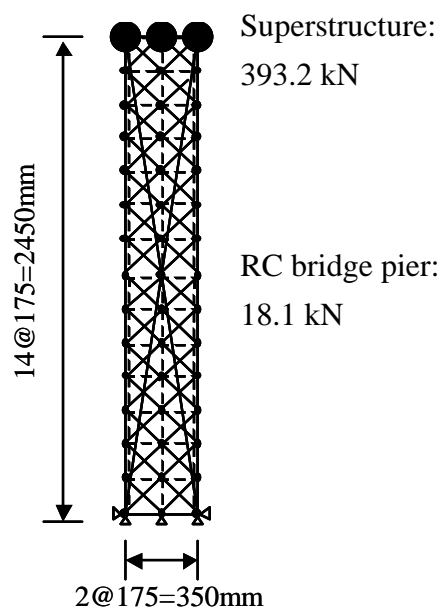
Figure 4.41   2D dynamic lattice model of RC bridge pier

4.6.2   Analytical model

The RC bridge pier in the experiment is modeled into the 2D dynamic lattice model as shown in **Figure 4.41**.   The difference between this model and another dynamic lattice model used in a previous study (Ito et al. 2002) is to consider the confinement effect due to the transverse reinforcement, which is incorporated by applying the stress-strain model proposed by Mander et al. (1988).   Moreover, Fukuura's model of reinforcement (1997) considering Bauschinger effect (Kato 1979), which is known as premature yielding of the reinforcement upon reversal of the strain direction, is also used.   The considerations made in applying the constitutive model of each material are also newly improved in this study.   The value of *t* is fixed at 0.10 based on the results of pre-analysis.

In the dynamic lattice model, the masses of the RC bridge pier and the superstructure are uniformly distributed over all nodal points and over the top three nodes, respectively, using the lumped-mass idealization. In this analysis, the Newmark $\beta = 1/4$ method (constant average acceleration procedure) is applied as the time integration. A time interval is set as 0.005 sec. The damping is introduced into the analysis in the form of the viscous forces as the Rayleigh damping, $a_0 = 0.426$, $a_1 = 9.243 \times 10^{-5}$. Here, a_0 and a_1 are the Rayleigh damping factors as described in **section 2.7**. The damping ratio is assumed to be 1.0%.

4.6.3   Nonlinear dynamic analysis for RC bridge piers

To verify the performance of the 2D lattice model in the nonlinear dynamic analysis, the experimental results from shaking table tests are adopted for comparison. Furthermore, the seismic behavior of RC bridge piers is evaluated using the dynamic lattice model.

The hysteresis loops for Case-A, Case-B, and Case-C piers are illustrated in **Figure 4.42**, with both experimental results and analytical ones from the dynamic lattice model. In the case of experimental results, the hysteresis loop is defined as the relationship between the inertial force and the horizontal displacement of the top of the pier. The inertial force can be calculated as the product of the mass of the beam, that is 393.2 kN, and the acceleration of the beam. On the other hand, in the case of the analytical results, the relationships between the sum of the restoring forces and the damping forces at the top three nodes and the displacement response at the top of the pier are shown in the figure. The experimental and analytical displacement time histories at the top of the pier are shown in **Figure 4.43**. Moreover, the experimental and analytical responses of the RC bridge pier (the yield lateral force, the yield lateral displacement, the maximum lateral force and the maximum lateral displacement) are tabulated in **Table 4.11**. In the experiment and analysis, the yield load and yield displacement are defined as the force and displacement at the initial yielding of longitudinal reinforcement as observed at the bottom of a pier in which the tensile strain of reinforcement reaches 2,010 μ.

As can be seen in **Figure 4.42**, in all the experimental cases, the longitudinal reinforcement yielded first. In Case-B, and Case-C, where the input ground acceleration is larger than in Case-A, greater plastic deformation was observed after the yielding of the reinforcement. The analytical results demonstrate that these characteristics of RC bridge piers can be predicted using the dynamic lattice model. Furthermore, the dynamic response, such as the maximum lateral force and lateral displacement at the top of RC bridge piers, is evaluated by the 2D dynamic lattice model appropriately.
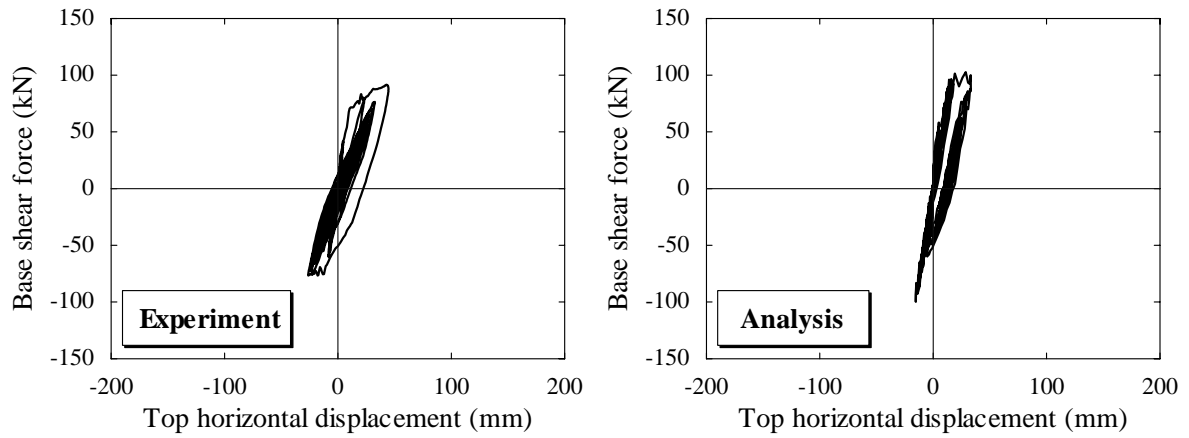
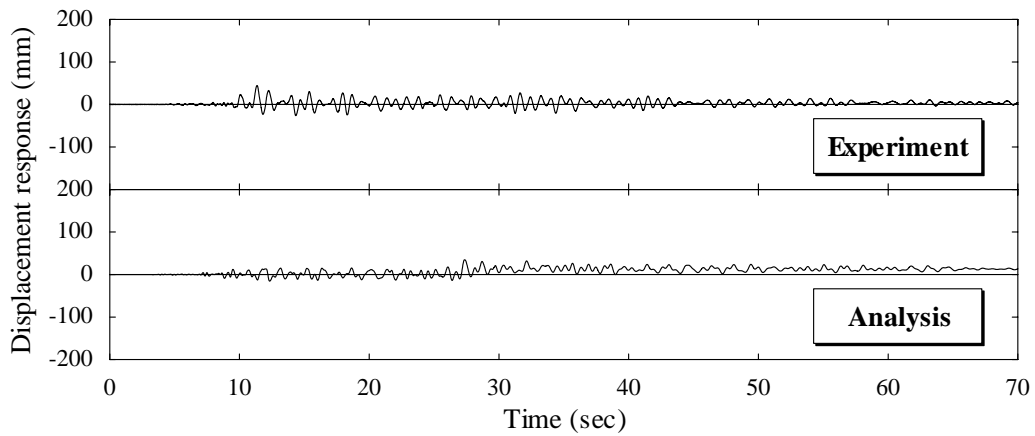**(a)** Case-A (275 gal)
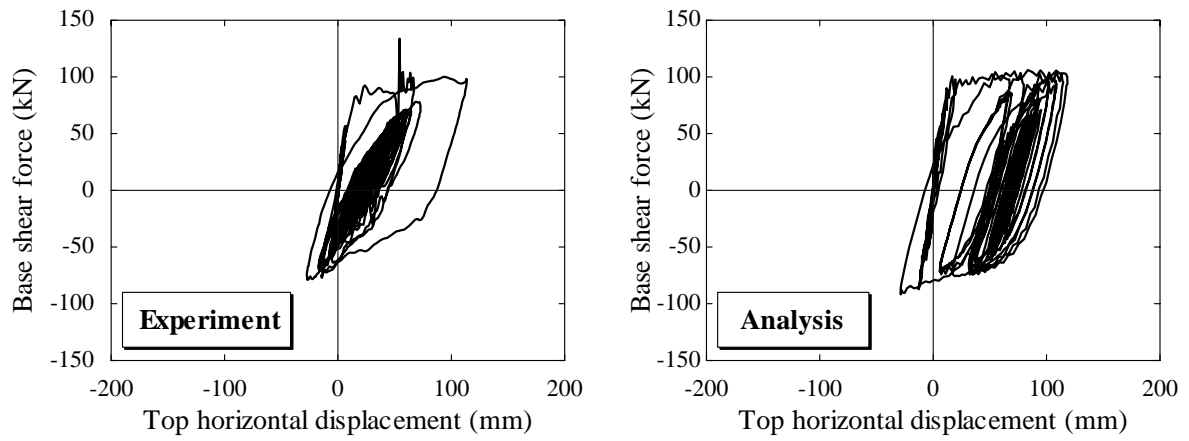
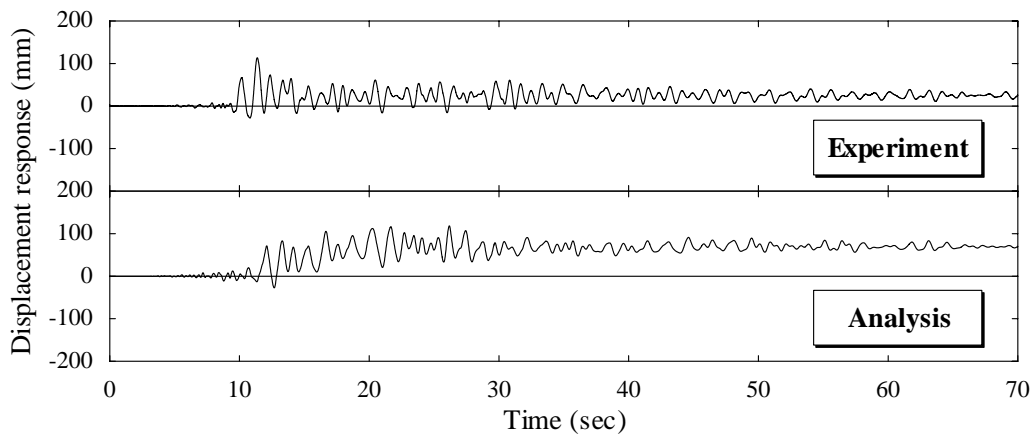**(b)** Case-B (360 gal)
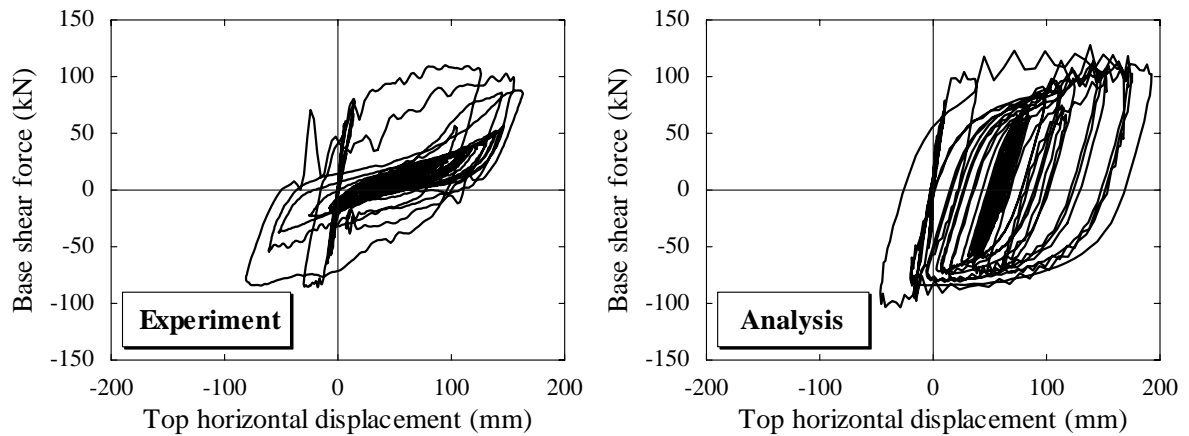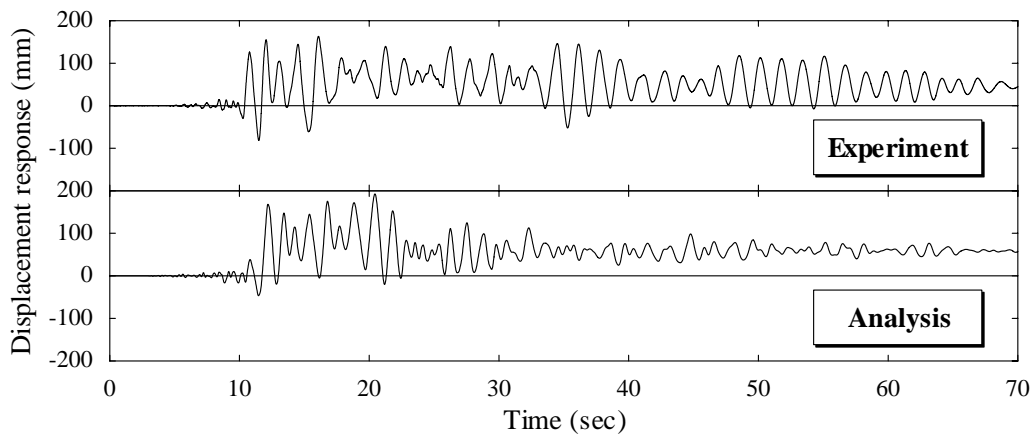

(c) Case-C (402 gal)

Figure 4.42 Hysteresis loops of RC bridge piers (the shaking table test and the 2D dynamic lattice model)

(a) Case-A (275 gal)

(b) Case-B (360 gal)

(c) Case-C (402 gal)

Figure 4.43 Displacement time histories of RC bridge piers subjected to three magnitudes of ground motion (the shaking table test and the 2D dynamic lattice model)

Table 4.11   Experimental and analytical results obtained form the shaking table test and the 2D dynamic lattice model

|	Case-A		Case-B		Case-C	
	Exp.	Ana.	Exp.	Ana.	Exp.	Ana.
Yield lateral force kN	72.7	90.4	76.1	93.4	79.2	98.5
Yield lateral displacement (mm)	14.1	14.8	15.5	15.5	13.5	15.9
Maximum lateral force (mm)	91.6	99.4	104.3	104.1	110.2	128.8
Maximum lateral displacement (mm)	44.4	34.8	113.6	118.4	163.1	192.6

There is, however, a difference between the experimental and analytical results beyond the maximum displacement.   In **Figure 4.42**, the internal cyclic loop in the experimental results for Case-B indicates a behavior with larger vibration amplitude and lower stiffness than the initial stiffness.   A comparison of the experimental and analytical results indicates that, beyond the maximum response, the dynamic lattice model predicts stiffer behavior and greater amplitude than the experiment.

The experimental hysteresis loops for Case-C indicate the low stiffness and comparatively less energy dissipation with slight pinching, as shown in **Figure 4.42 (c)**.   On the other hand, the analysis predicts the high capacity for energy dissipation, which contradicts the experimental observation.   In particular, it is found that the displacement response amplitude computed after 30 seconds is less than the experimental measurements, as shown in **Figure 4.43 (c)**.   This means that the longitudinal reinforcement continues to sustain the large flexural compressive stress because the local buckling is disregarded.   Moreover, this difference arises from assumptions regarding the stiffness of concrete in compression under unloading and reloading conditions.   Since the deterioration of stiffness at large displacement is disregarded, the analytical value may become large.   Despite this shortcoming, the dynamic lattice model can predict the response of RC bridge piers in the region between the yielding of the longitudinal reinforcement and the maximum response very well, though the effects of buckling of reinforcement are not taken into consideration.

4.7 Parametric Analysis on Effect of Transverse Reinforcement

4.7.1 Outlines of analytical cases

The dynamic lattice analysis is used to model six RC bridge piers with different transverse reinforcement ratios to quantify the influence of transverse reinforcement on the seismic performance.   The analytical targets are cantilever RC piers of rectangular cross section with a height of 2,440 mm.   These are identical to UC San Diego piers mentioned in **section 4.2**. The shape and dimensions of these piers are shown in **Figure 4.44**.   The material properties are tabulated in **Table 4.12**.   In the table, the transverse reinforcement ratio, r_w, varies from 0.00% (no transverse reinforcement) to 0.40%.   The superstructure is modeled as three concentrated masses of 2,000 ton at each of the top three nodes of the pier.   The input ground motion is Nihonkai-Chubu Earthquake motion described earlier and shown in **Figure 4.40**. The maximum amplitude of the ground motion is adjusted to 450 gal.
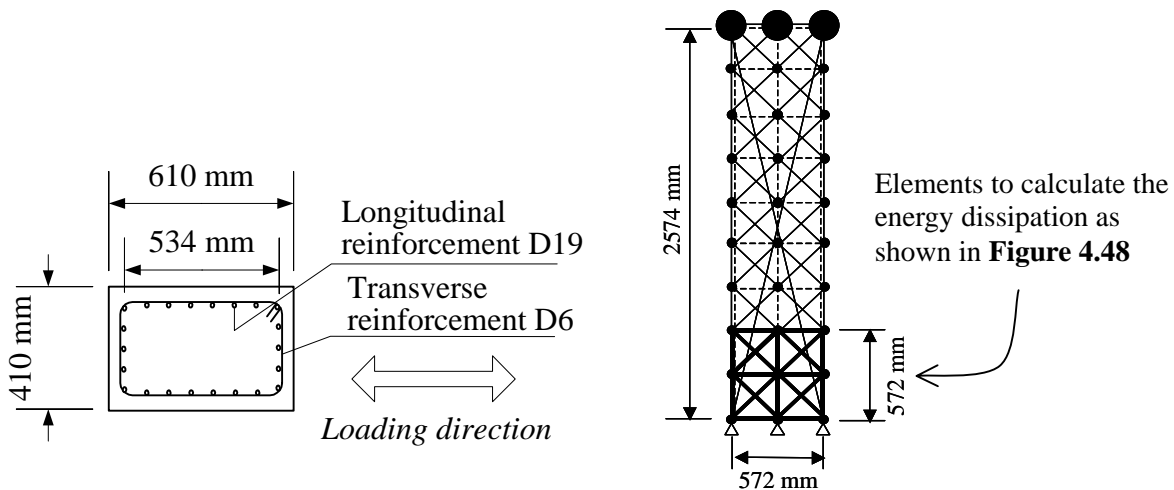
Figure 4.44   Cross section of the column

Figure 4.45   2D dynamic lattice model

Table 4.12   Material properties and transverse reinforcement ratio

Compressive strength of concrete, f_c' (MPa)		38.0					
Yield strength of reinforcement, f_y (MPa)	Longitudinal reinforcement D19	317					
	Transverse reinforcement D6	360					
Transverse reinforcement ratio, r_w (%)		0.00	0.04	0.08	0.12	0.20	0.40

Table 4.13 Maximum response of RC bridge piers obtained from the 2D dynamic
lattice model analysis

Transverse reinforcement ratio, r_w (%)	0.00%	0.04%	0.08%	0.12%	0.20%	0.40%
Maximum base shear force (kN)	366.2 (1.00)	398.5 (1.09)	417.4 (1.14)	419.0 (1.14)	461.7 (1.26)	477.4 (1.30)
Maximum lateral displacement (mm)	142.8 (1.00)	150.9 (1.06)	180.3 (1.26)	162.0 (1.13)	165.3 (1.16)	162.0 (1.13)

Note: The values in parenthesis indicate the normalized ratio of the responses of each pier to that
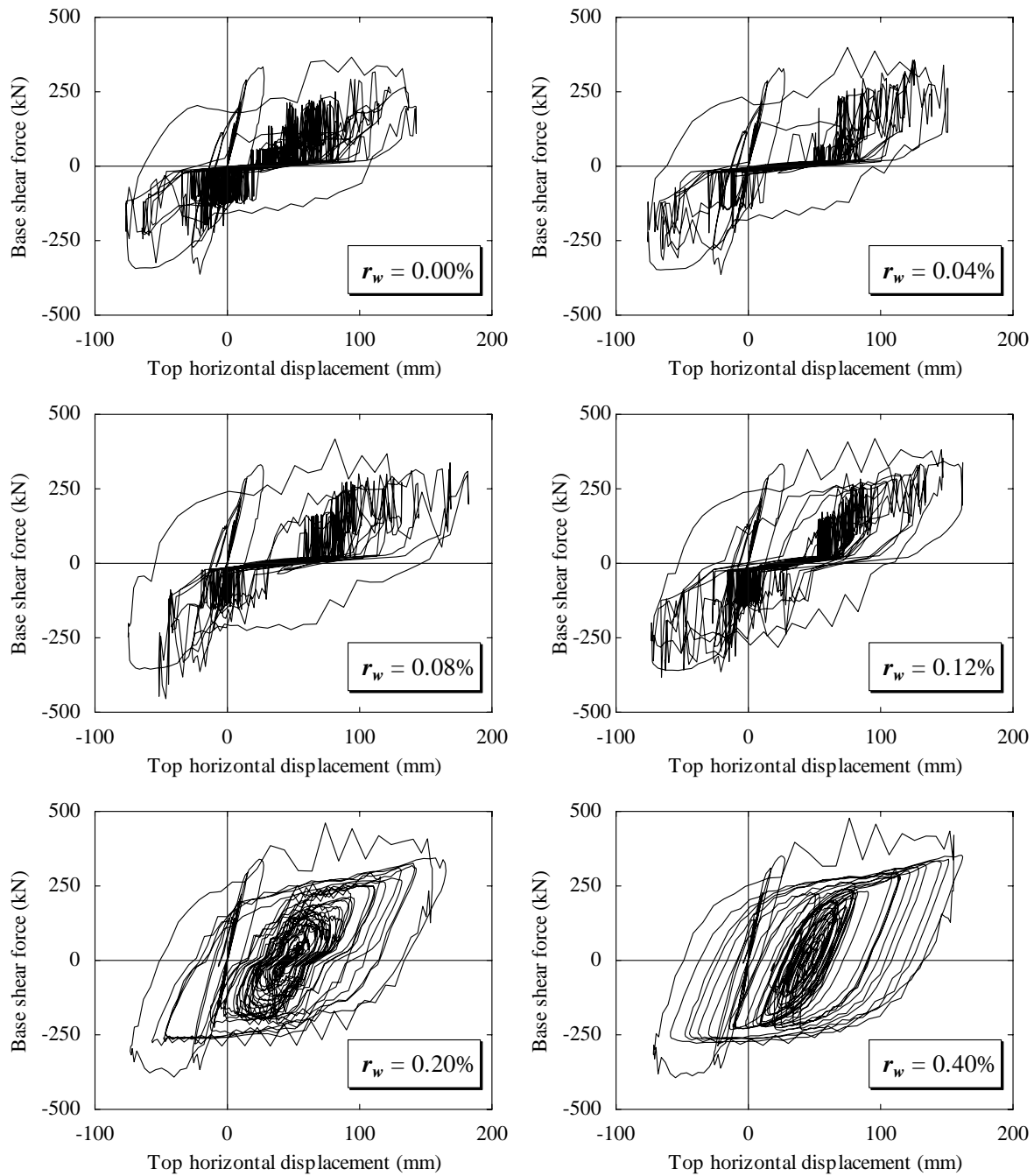*of the pier with no transverse reinforcement (r_w = 0.00 %).*

In the dynamic analysis, the Newmark $\beta = 1/4$ method is applied for the time integration. A time interval of 0.02 sec is used. The damping is introduced into the analysis as the Rayleigh damping $a_0 = 0.621$, $a_1 = 1.426 \times 10^{-3}$. Here, the damping ratio is assumed to be 3.0%.

The idealization of the 2D dynamic lattice model is shown in **Figure 4.45**. Here, according to pre-analysis, the values of t for the six RC bridge piers are determined between 0.10 and 0.15. In general, the value of t increases with the increase in the transverse reinforcement ratio. This tendency corresponds to observations made in a previous study (Ito et al. 2000).

4.7.2 RC bridge piers with varying transverse reinforcement ratios

The maximum response of each pier and the normalized ratio of the response of each pier to that of the pier with no transverse reinforcement ($r_w = 0.00\%$) are shown in **Table 4.13**. The relationship between the base shear force and the top horizontal displacement obtained from the 2D dynamic lattice model are shown in **Figure 4.46**. These analytical results confirm that the maximum base shear force increases as the transverse reinforcement ratio is increased. On the other hand, it is also found that the transverse reinforcement ratio has little influence on the maximum displacement response within the range of transverse reinforcement ratios investigated in this study.

In **Figure 4.46**, however, it is clear that the energy dissipation capacity rises as the amount of transverse reinforcement is increased. This influence of transverse reinforcement ratio on the energy dissipation capacity will be discussed in the following section.

Figure 4.46   Hysteresis loops of RC bridge piers with different transverse reinforcement
ratios calculated by the 2D dynamic lattice model

4.7.3   Energy dissipation capacity of RC bridge piers

The analytical time histories of cumulative energy dissipation for the six RC bridge piers are
shown in **Figure 4.47**.   This accumulated value of energy dissipation is obtained as the area
surrounded by one cycle of the hysteresis loop (in the base shear force versus top horizontal
displacement relationship) during the shaking table test.   The figure demonstrates that higher
cumulative energy dissipation with the increase in the transverse reinforcement ratio is
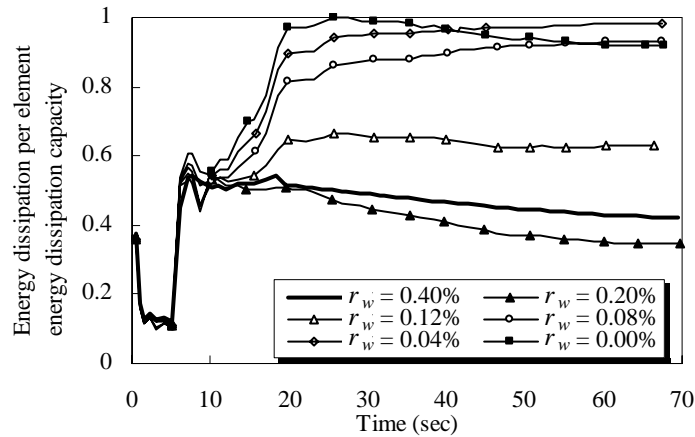
117
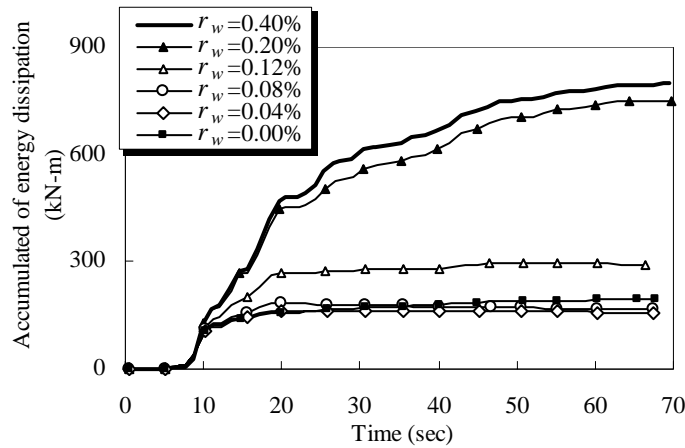
Figure 4.47 Accumulated energy dissipation of RC bridge piers with different transverse reinforcement ratios calculated by the 2D dynamic lattice model

predicted by the dynamic lattice model. Because of their greater energy dissipation capacity, RC bridge piers with sufficient transverse reinforcement (r_w = 0.40% and 0.20%) can be expected to dissipate energy as they are subjected to further seismic loading. On the other hand, RC bridge piers with little or no transverse reinforcement (r_w = 0.00%, 0.04%, and 0.08%) cannot be expected to dissipate the energy of subsequent loading because of their limited dissipation capacity.

Next, the distribution of energy dissipation within the pier is verified in terms of the energy dissipated by each element of the lattice model. In this regard, the lattice model comprises several truss elements in which an average stress and average strain relationship is assumed to govern each element. Because of this assumption, the energy dissipated by each element can be easily calculated from the product of the energy dissipated and the element volume, where the energy dissipated in the element is defined as the area closed by the stress-strain relationship for the unloading and reloading curves. The ratio of summed energy dissipation in the elements (one area of focus) to the total energy dissipation capacity of the pier is shown in **Figure 4.48** for the six piers. Here, the elements focused on are in the region of two layers from the bottom of the pier (or 1d from the bottom of the pier) as shown by the thick lines in **Figure 4.45**.

Note that as the value of the ratio in **Figure 4.48** approaches 1.0, the greater the energy dissipation in elements in the focused region. In the case of piers with r_w = 0.40% and 0.20%, around 40% of totally absorbed energy is dissipated in the region at the bottom of the piers. Similarly, around 60% is dissipated for the pier with a transverse reinforcement ratio r_w = 0.12%. Furthermore, almost all energy is consumed within the 1d region of piers with little or no transverse reinforcement (r_w = 0.00%, 0.04%, and 0.08%). The hysteresis energy

Figure 4.48   Ratio of summed energy dissipation in several elements to energy dissipation capacity of RC bridge piers

is dissipated in a zone above the bottom of the pier that becomes larger as the transverse reinforcement ratio is increased.   This expansion of the damage zone is confirmed in the analysis.   Hence, by taking into the consideration of the energy dissipation in individual elements, the distribution of energy dissipation in a RC bridge pier can be evaluated by the dynamic lattice model.   Moreover, this analysis confirms that the damage zone of a RC bridge pier during an earthquake can be quantitatively predicted by evaluating the distribution of energy dissipation.

4.8   Seismic Evaluation Using Several Earthquake Motions

4.8.1   Analytical cases

A rectangular column, geometrically similar to the one used in **section 4.4**, is considered with the following properties: $f_c^{'}$ = 27.0 MPa, f_y = 380 MPa, and E_s = 172 GPa.   For the reference column (Column A), the longitudinal and transverse reinforcement ratios are 2.38 % and 0.056 %, respectively.   The axial compression of 250 kN is applied at the top the of column. The details and dimensions of the tested columns are shown in **Figure 4.25**.   In the analysis, six columns are used for investigation of the effect of the retrofitting method on the seismic performance of a RC column.   The columns of B and C are transversely strengthened by CFS at 1h and 3h regions from the top of the footing, respectively, where h (= 300 mm) is the cross-sectional height of the column.   The column D is strengthened by CFS at 1h region longitudinally and transversely.   The analytical cases are shown in **Table 4.14**.

For the columns A to D, NS component of Hyogo-ken Nanbu Earthquake (the maximum

Table 4.14 Analytical cases

Column	Number of layer(s) of CFS in transverse direction		Number of layer(s) of CFS in longitudinal direction	Input maximum acceleration (gal)
	0 – 300 (mm)	300 – 900 (mm)		
A	–	–	–	450 (Near-field motion)
B	2	1	1/4	
C	2	2	1/4	
D	2	1	1	
E	2	1	1/4	200 (Far-field motion)
F	2	1	1/4	450 (Far-field motion)

Note: 1/4 layer of CFS means that the bonded region between concrete surface and CFS was reduced to one fourth part by using the unbond plastic sheet.

acceleration: 818 gal) is used as the input ground motion.   It is important to evaluate the seismic performance of RC structural members subjected to the near-field earthquake ground motion since the occurrence of huge earthquakes in urban areas is inevitable such as Kobe earthquake.   During these large earthquakes, the large-amplitude ground motions can be recorded by special sensors, so-called accelerometers.   The seismic performance of RC structural members subjected to strong motion of possible large earthquakes in future is beneficial to design earthquake-resistant structures.   In the analysis, the maximum amplitude of the motion is modified to be 450 gal.   The input ground acceleration is previously shown in **Figure 4.26**.

Other two columns have same details and arrangement as column B.   The input ground acceleration is EW component recorded at Lake Hachiro-gata in Japan during Nihonkai-Chubu Earthquake of 1983, as previously shown in **Figure 4.40**.   Here, the maximum ground acceleration, of which the original is 144 gal, is enlarged to 200gal (column E), and 400gal (column F).   The analytical cases are summarized in **Table 4.14**.

In the dynamic analysis, the superstructure is modeled as three concentrated masses of 40 ton at each of the top three nodes of the column.   The Newmark $\beta = 1/4$ method is applied as the time integration.   A time interval of 0.01 sec is used.   In addition, the damping is introduced as the Rayleigh damping, $a_0 = 0.621$, $a_1 = 1.426 \times 10^{-3}$. a_0 and a_1 are the Rayleigh damping factors as expressed in **section 2.7**.   Here, the damping ratio is assumed to be 3.0%.
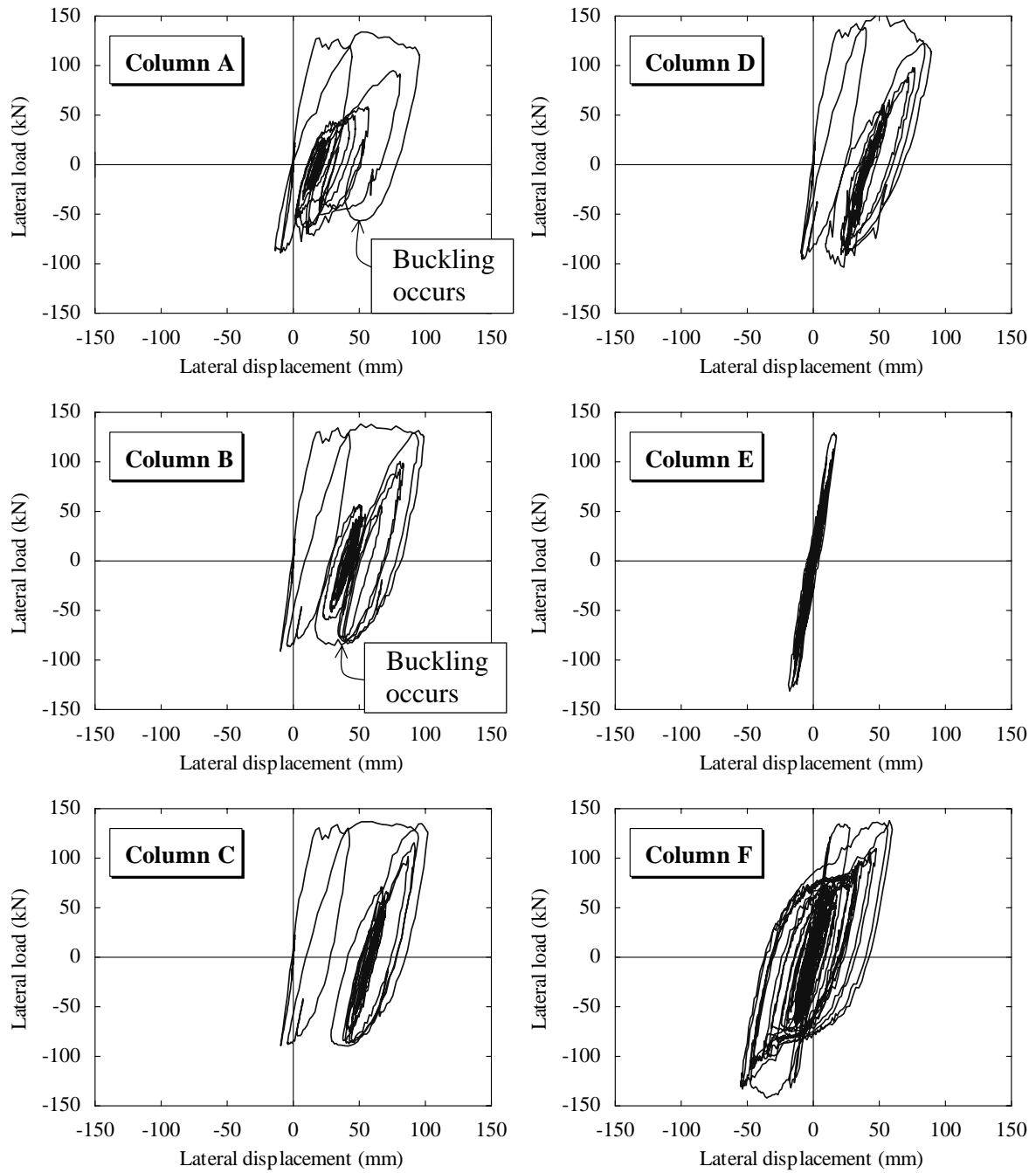
Figure 4.49   Hysteresis loops calculated by the 2D dynamic lattice model

4.8.2   Verifications using near-field earthquake motion

Figure 4.49 shows the analytical results of 2D lattice model considering the buckling of longitudinal reinforcement.   The displacement time histories at the top of the column are shown in **Figure 4.50**.   The analytical results of the columns A to D subjected to the motion of Hyogo-ken Nanbu Earthquake are shown in the figure.   The results of the columns E and F are shown later.   The analytical lateral load and lateral displacement when longitudinal

121
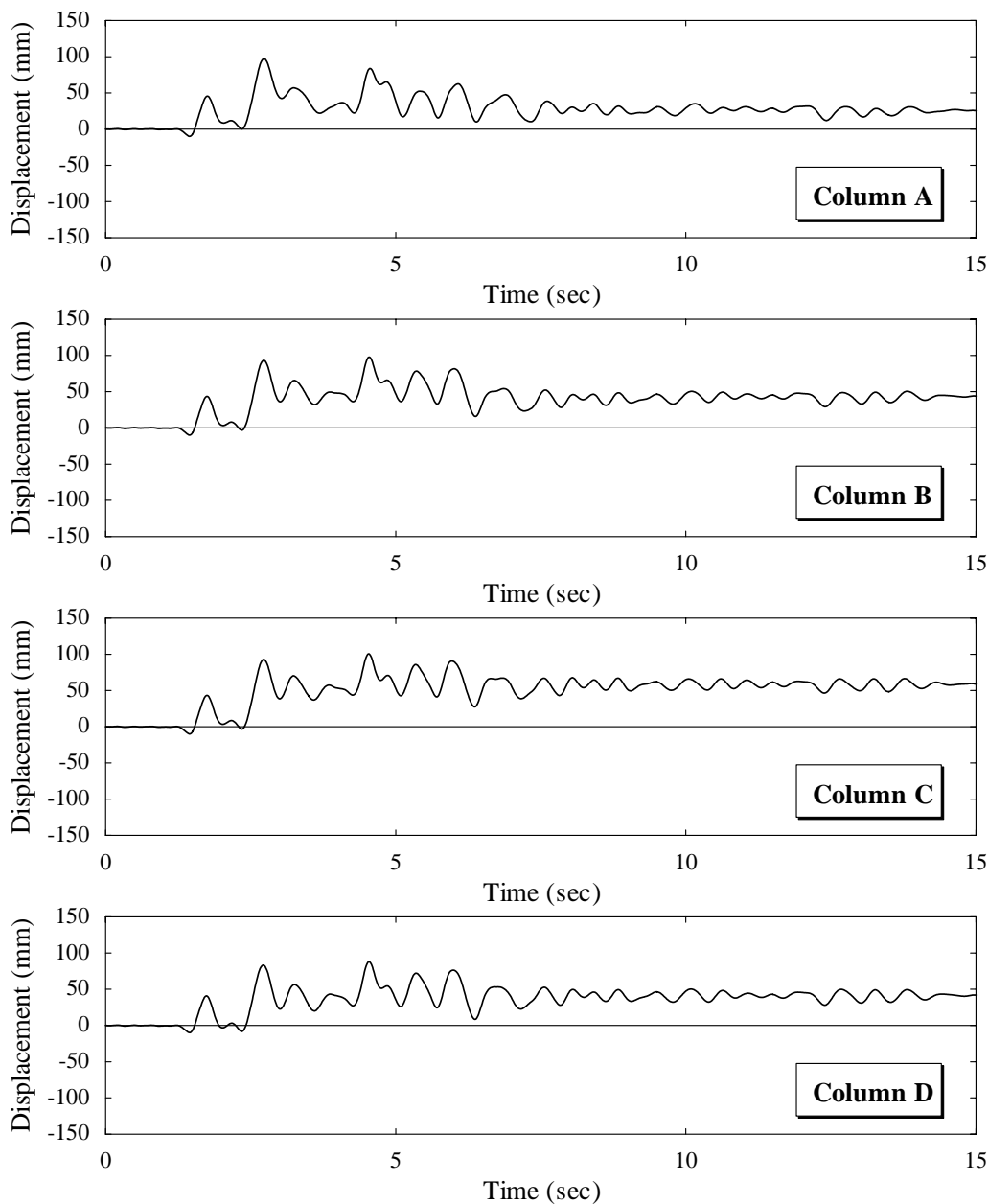
Figure 4.50   Displacement time histories obtained by the 2D dynamic lattice model
analysis (Hyogo-ken Nanbu Earthquake)

reinforcement yields, the maximum lateral load, and the maximum lateral displacement are
tabulated in the **Table 4.15**.   Here, the columns A and B are geometrically identical to the
specimens No.6 and No.8 in **section 4.4**.   The maximum accelerations of input motion are
296 gal in the case of the columns A and B, while 450 gal for the case of the specimens No.6
and No.8.

To verify the effect of the intensity of earthquake motion on the seismic response of RC
columns, the analytical results in this section are compared with the result in **section 4.4** that

Table 4.15   Responses of RC columns calculated from the 2D dynamic lattice model

Column	A	B	C	D	E	F
Lateral yield load (kN)	98.8	102.7	103.1	107.4	109.0	101.9
Lateral yield displacement (mm)	12.1	12.1	12.1	12.2	12.6	12.1
Maximum lateral load (kN)	133.3	138.2	138.4	152.4	118.3	127.2
Maximum lateral displacement (mm)	97.4	97.8	100.5	88.1	18.8	59.8
Ultimate lateral displacement (mm)	25.6	43.4	58.5	41.3	1.5	0.6

has been previously shown in **Table 4.8**.   In the cases that same strengthening method is provided, there is small influence of the intensity of earthquake motion on the lateral yield load, lateral yield displacement, and maximum lateral load.   The specimens No.5, No.6, and the column A are the columns without strengthening, while the specimen No.8 and the column B are the columns strengthened by CFS at 1*h* region.

There exist slight differences in the lateral yield load even in the case that the amount of longitudinal reinforcement is similar.   This is also observed in the results of between the columns B and C, or the columns E and F.   In the analysis, the lateral yield load is defined as the load when the longitudinal reinforcement firstly yields at the base of the column.   Since the interval of time integration is 0.01 seconds, the strain at the first yielding of longitudinal reinforcement is not necessarily in the agreement with the actual yield strain of longitudinal reinforcement.   Consequently, the slight difference of the lateral yield load exists even for the columns having the same amount of longitudinal reinforcement.

It is found that the maximum lateral displacement significantly increases with the increase in the intensity of input ground motion as compared with other responses, such as the lateral yield load, the lateral yield displacement, and the maximum lateral load.   This indicates that the energy of earthquake motion is absorbed mainly due to the lateral plastic deformations, while the lateral load after the yielding of longitudinal reinforcement slightly increases.   For the columns A to D, after the column is subjected to first large ground motion, the maximum displacement is predicted and then the residual displacement remains in the direction of the maximum displacement.   In addition, it is found from the **Figure 4.49** that the stable cyclic behavior of the columns is observed even if the buckling of longitudinal reinforcement is predicted as shown in the columns A and B.

It can be observed in the **Table 4.15** that the lateral yield load increases with the increase in

the amount of CFS though each column has slight difference in the lateral yield displacement. The largest lateral yield load is predicted in the column D.　 The column D is strengthened by CFS longitudinally and transversely.　 Similarly, the maximum lateral load of the column D is largest in all cases.　 However, the lateral load-lateral displacement curve of the column D shows the post-peak softening since the compression softening of concrete becomes more dominant due to the contribution of flexural strengthening by longitudinal CFS.

For the maximum lateral displacement, the column C strengthened by CFS at the wider range shows the large deformation.　 The buckling behavior is not significant in the column C though the buckling behavior of longitudinal reinforcement is observed in the columns A and B as shown in **Figure 4.49**.　 Hence, it is found that the effect of the retrofitting method on the seismic response is confirmed in the results of 2D lattice model analysis.

The results of the columns B and C are compared in which the amount of CFS in transverse direction is different from each other.　 In the column B, the significant buckling behavior of longitudinal reinforcement is observed after the displacement is reached the maximum.　 The stiffness of the column during vibration decreases than the initial one.　 In addition, the column B shows the higher energy dissipation with slight pinching and hence the residual displacement becomes small.　 On the other hand, for the column C, the buckling of reinforcement does not take place.　 The stiffness remained high even after the maximum displacement is reached.　 The significant energy dissipation capacity is prominent. Consequently, the residual displacement of the column B is smaller than that of the column C as shown in **Figure 4.50**.

4.8.3　 Verifications using far-field earthquake motion

The analytical results of the columns E and F by 2D dynamic lattice model considering the buckling of reinforcement have been shown in **Figure 4.49**.　 The displacement time histories at the top of the columns E and F are illustrated in **Figure 4.51**.　 In this figure, the result of the column B is also shown in which the duration time of input ground motion is 70 seconds. The analytical lateral load and lateral displacement when the longitudinal reinforcement yields, the maximum lateral load and the maximum lateral displacement response are shown in the **Table 4.15**.

It can be observed in the **Figure 4.49** that the column E subjected to the ground motion of 200 gal shows the linear response.　 In the analysis, the flexural cracks occur in the element at the bottom end of the column.　 On the other hand, the analytical deformation of the column F
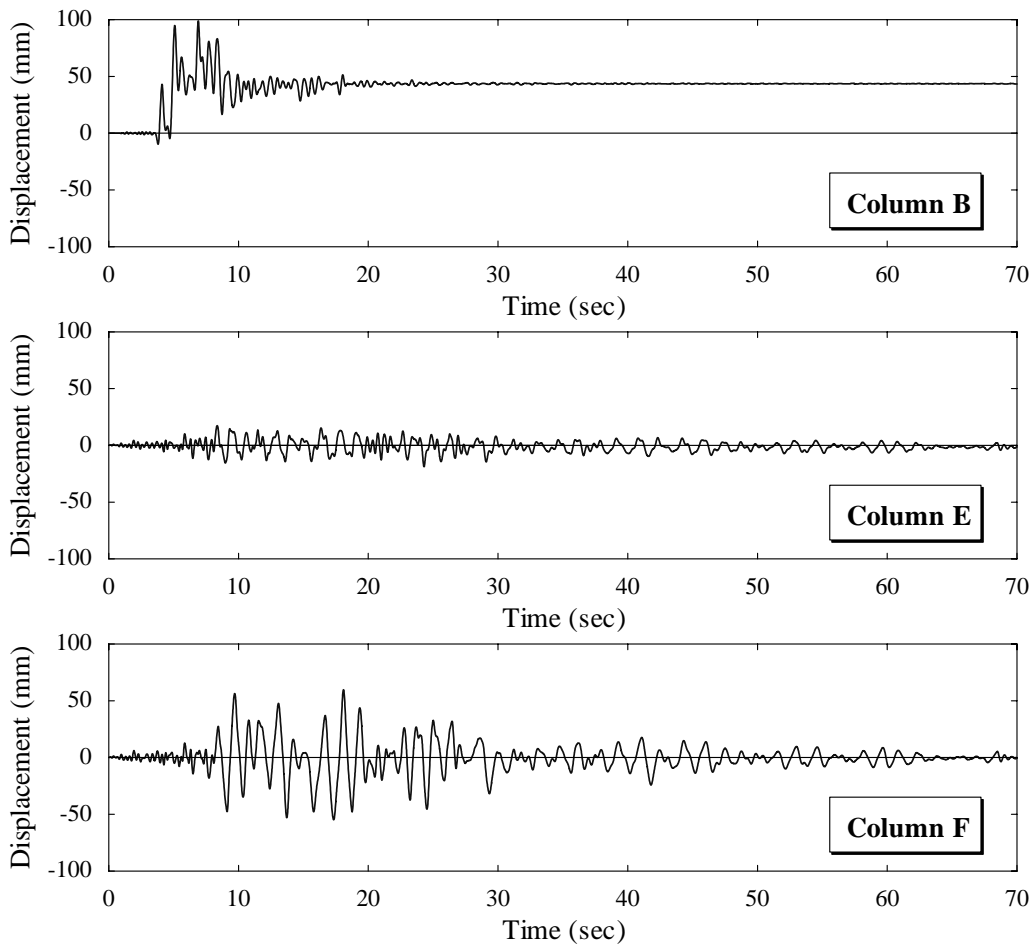
Figure 4.51 Displacement time histories obtained by the 2D dynamic lattice model analysis (Nihonkai-Chubu Earthquake)

(input ground motion is 400 gal) becomes significantly larger than results of the column E. Here, the input ground motion used in this analysis is symmetrical to the time axis that means similar amplitudes in the positive and negative accelerations as illustrated in **Figure 4.40**.

The residual displacement is different from the response of the column B subjected to Kobe Earthquake motion. Near-fault impulse type ground motion results in a sudden rupture of energy into the structure that must be dissipated inputted energy immediately. This motion is usually characterized by a single unidirectional large excursion. On the other hand, the sinusoidal type ground motion with longer duration requires a more steady dissipation of energy over a longer period with numerous reversals of loading. As a result, the residual displacement in the column F becomes smaller than the result of the column B though the behavior of both columns is in inelastic range. In addition, for the column F, the duration of vibration is considerably longer than the column B subjected to the pulse type motion with the short duration and the high acceleration, such as Kobe Earthquake motion.

4.9   Conclusions

This chapter involves the analyses of RC columns under the cyclic loading by the 2D static lattice model.   The analysis is also carried out for three shear shear-dominated RC columns tested at University of California, San Diego.   In addition, the analytical results using the 2D dynamic lattice model are compared with the results obtained by the shaking table tests.   The seismic performance verifications are conducted for RC columns with different amount of transverse reinforcement and CFS.   Finally, the seismic performance verifications using two different earthquake motions are carried out.

The significant improvement in predicting the post-peak response can be achieved by considering the buckling behavior of longitudinal reinforcement.   In the model, the buckling behavior is treated as the spatially averaged stress-strain model of reinforcement.   It is found that the 2D lattice model analysis considering the buckling of longitudinal reinforcement can reliably predict the post-peak response and cyclic loops representing the energy dissipation capacity of RC columns with sufficient accuracy.   The accuracy of prediction is also improved considering the pull-out behavior of longitudinal reinforcement at the column-footing connection by using the joint element having the strain-slip relationship of reinforcement.   The pull-out behavior of longitudinal reinforcement is found to influence on the stiffness and the energy dissipation capacity of RC columns.   The consideration of the pull-out behavior makes the analytical results close to the experimental results, and consequently, the accuracy is improved.

The simulation of RC columns with different amount of transverse reinforcement clarifies that the maximum lateral load increases with the increase in the amount of transverse reinforcement.   By looking at the energy absorbed in individual elements, the distribution of the energy dissipated in RC columns can be evaluated by the 2D dynamic lattice model. Moreover, it is confirmed that the damage zone in RC columns during an earthquake can be quantitatively predicted by evaluating the distribution of energy dissipation.   Through the simulation of RC columns with different strengthening procedure, the influence of the strengthening by CFS on the seismic performance of RC columns is clarified.

From the simulation using two different earthquake motions, it is found that the hysteresis loops and the displacement time histories are completely different.   The influence of the kind of ground motion on the seismic response of the RC columns can be evaluated.   It is also found that the 2D dynamic lattice model analysis can appropriately predict the seismic response of RC columns subjected to large ground motion.   In order to perform a proper prediction, the consideration for the buckling of longitudinal reinforcement is necessary.

References in Chapter 4

[1] Dhakal, R. P. (2000): *Enhanced Fiber Model in Highly Inelastic Range and Seismic Performance Assessment of Reinforced Concrete*, Doctoral thesis, The University of Tokyo, September.

[2] Dowell, R. K. and Seible, F. (2001): UCSD Shear Column Benchmark Tests, *Finite Element Analysis of Reinforced Concrete Structures*, ACI SP-205, pp.15-39.

[3] Ductility Design Subcommittee (2001): *Cyclic Loading Test Data of Reinforced Concrete Bridge Piers*, Earthquake Engineering Committee, JSCE, pp.12-22, March.

[4] Fukuura, N. and Maekawa, K. (1997): Computational Model of Reinforcing Bar under Reversed Cyclic Loading for RC Nonlinear Analysis, *Journal of Materials, Concrete Structures and Pavements*, JSCE, No.564/V-35, pp.291-295, May. (in Japanese)

[5] Ishibashi, T, Kobayashi, K., and Umihara, T. (2000): Study on Quantity Evaluation of Pull Out of Longitudinal Bar from Footing of RC Piers Reversed Cyclic Loading of Large Deformation Range *Journal of Materials, Concrete Structures and Pavements*, JSCE, No.648/V-47, pp.43-54, May. (in Japanese)

[6] Ito, A., Niwa, J., and Tanabe, T. (2000): Evaluation by Lattice Model of Ultimate Deformation of RC Columns Subjected to Cyclic Loading, *Concrete Library of JSCE*, No.36, pp.295-307, December.

[7] Ito, A., Niwa, J., and Tanabe, T. (2002): Non-Linear Dynamic Analysis of Reinforced Concrete Piers Based on the Lattice Model, *Journal of Materials, Concrete Structures and Pavement*s, JSCE, No.676/V-51, pp.27-39, May. (in Japanese)

[8] Kato, B. (1979): Mechanical Properties of Steel under Load Cycles Idealizing Seismic Action, *CEB Bulletin d'Information*, No. 131, pp.7-27, May.

[9] Kawashima, K. and Hasegawa, K. (1994): Experimental Investigation on Nonlinear Seismic Response of Bridge Columns and Accuracy of Equal Energy Assumption, *Journal of Structural Mechanics and Earthquake Engineering*, JSCE, No.483/I-26, pp.137-146, January. (in Japanese)

[10] Mander, J. B., Priestley, M. J. N., and Park, R. (1988): Theoretical Stress-Strain Model for Confined Concrete, *Journal of Structural Engineering*, ASCE, Vol. 114, No.8, pp.1804-1826, August.

[11] Miki, T., Niwa, J., and Lertsamattiyakul, M. (2002): Numerical Evaluation for Seismic Performance of Reinforced Concrete Bridge Piers Using Dynamic Lattice Model, *Journal of Materials, Concrete Structures and Pavements*, JSCE, No.704/V-55, pp.151-161, May. (in Japanese)

[12] Miki, T., Niwa, J., and Lertsamattiyakul, M. (2003a): Earthquake Response Analysis for RC Bridge Piers Considering Reinforcement Buckling Behavior, *Journal of Materials, Concrete Structures and Pavement*s, JSCE, No.732/V-59, pp.225-239, May. (in Japanese)

[13] Miki, T., Niwa, J., and Lertsamattiyakul, M. (2003b): Numerical Evaluation of Seismic Performance of Reinforced Concrete Bridge Piers Using Dynamic Lattice Model, *Concrete Library of JSCE*, Vol.41, May.

[14] Mishima, T., Bujadham, B., Maekawa, K., and Okamura, H. (1992): A Development of Constituent Material Models for a Reinforced Concrete Discrete Crack, *Journal of Materials, Concrete Structures and Pavements*, JSCE, No.422/V-16, pp.171-179, February. (in Japanese)

[15] Murayama, Y., Ichinomiya, T., and Suda, K. (2001): Stress-pullout hysteresis model for Reinforcing Bars Anchored in Massive Concrete, *Journal of Structural Engineering*, JSCE, Vol.47A, pp.673-684, March. (in Japanese)

[16] Naganuma, K. and Ohkubo, M. (2000): An Analytical Model for Reinforced Concrete Panels under Cyclic Stresses, *Journal of Structural and Construction Engineering*, AIJ, No.536, pp.135-142, October. (in Japanese)

[17] Niwa, J., Choi, I. C., and Tanabe, T. (1995): Analytical Study for Shear Resisting Mechanism Using Lattice Model, *Concrete Library of JSCE*, No.26, pp.95-109, December.

[18] Okamura, H. and Maekawa, K. (1991): *Nonlinear Analysis and Constitutive Models of Reinforced Concrete*, Gihodo-Shuppan, May.

[19] Osada, K., Ohno, S., Yamaguchi, T., and Ikeda, S. (1997): Seismic Behavior of Reinforced Concrete Piers Strengthened with Carbon Fiber Sheets, *Concrete Library of JSCE*, No.30, pp.155-179, December.

[20] Takeda, T., Sozen, M. A., and Nielsen, N. N. (1970): Reinforced Concrete Response to Simulated Earthquakes, *Journal of the Structural Division*, ASCE, Vol.96, ST12, pp.2557-2573, December.

[21] Takemura, K. and Kawashima, K. (1997): Effect of Loading Hysteresis on Ductility Capacity of Reinforced Concrete Bridge Piers, *Journal of Structural Engineering*, JSCE, Vol.43A, pp.849-858, March. (in Japanese)

[22] Ueda, T., Sato, Y., Ito, T., and Nishizono, K. (2002): Shear Deformation of Reinforced Concrete Beam, *Journal of Materials, Concrete Structures and Pavements*, JSCE, No.711/V-56, pp.202-215, August.

[23] Vecchio, F. J. and Collins, M. P. (1986): The Modified Compression Field Theory for Reinforced Concrete Elements Subjected to Shear, *ACI Journal*, Vol.83, No.2, pp.219-231, March/April.

[24] Xiao, Y., Priestly, M. J. N., and Seible, F. (1993): Steel Jacket Retrofit for Enhancing Shear Strength of Short Rectangular Columns, Report No.SSRP-92/07, Department of Applied Mechanics and Engineering Sciences, University of California, San Diego, 192pp., July.

5   3D STATIC LATTICE MODEL ANALYSIS

5.1 Introduction

In the previous chapter, the performance of 2D lattice model has been confirmed in predicting the behavior of RC structural members that indicated the shear dominated or flexural dominated response.   One of the primary advantages of the 2D lattice model is to estimate the changing direction of internal compressive stress flows after diagonal cracking. However, the analytical target is limited within the structural member in which the assumption of plane stress is given.

As for the load resisting mechanisms of actual structures, various loading conditions under flexural, shear, axial force, and torsion should be considered.   Herein, the 3D problem, such as the condition under torsion or bilateral loading will be discussed.   Since the structural behavior of RC members under torsion or bilateral loading has been experimentally well investigated, it can be used as a good analytical target for improving and verifying the 3D analytical concept.

Hence, the application of 3D lattice model to RC structures under arbitrary loading conditions including bilateral loading and combinations of torsion, bending, and shear will be presented in this chapter.

## 5.2 RC Columns Subjected to Bilateral Loading

5.2.1 Experimental setup

The experiments carried out by Kawashima et al. (1991, 1993) on RC bridge piers subjected to static reversed cyclic loading are used as the analytical target.   To investigate the effect of biaxial loading, the test was conducted for RC bridge piers subjected to bending from the diagonal direction of the section.   The tests were for the square sectional piers.

The piers were three RC bridge cantilevers with a square cross section of 500 mm × 500 mm. All reinforcing bars had a minimum of 35 mm of concrete cover. The diameter of longitudinal reinforcing bars was 13 mm, and consequently the longitudinal reinforcement ratio was 2.03 %. The transverse reinforcements were 9 mm diameter round bars with 250 mm spacing. Hence, the transverse reinforcement ratio was 0.10 %. The dimensions and reinforcement arrangement of the specimen are illustrated in **Figure 5.1**. The longitudinal reinforcement in all piers had the nominal yield strength of 295 N/mm^2, while the transverse reinforcement had nominal yield strength of 235 N/mm^2. The average compressive strength of concrete was 31.3 N/mm^2 in the column P–10 and 39.8 N/mm^2 in columns P–33 and P–34. The material properties of the concrete and reinforcement are summarized in **Table 5.1**.

The piers had an identical dimension and arrangement of reinforcement, while the loading direction is different each other. In the column P–10, the lateral load was provided along the principal axis, while in the columns P–33 and P–34, the load was provided in the direction of a diagonal of the pier cross section. For the specimens of P–33 and P–34, the loading stub at the top portion of the pier was inclined from the principal axis as were 30° and 45°, respectively. The loading conditions on the test specimen are shown in **Figure 5.2**.
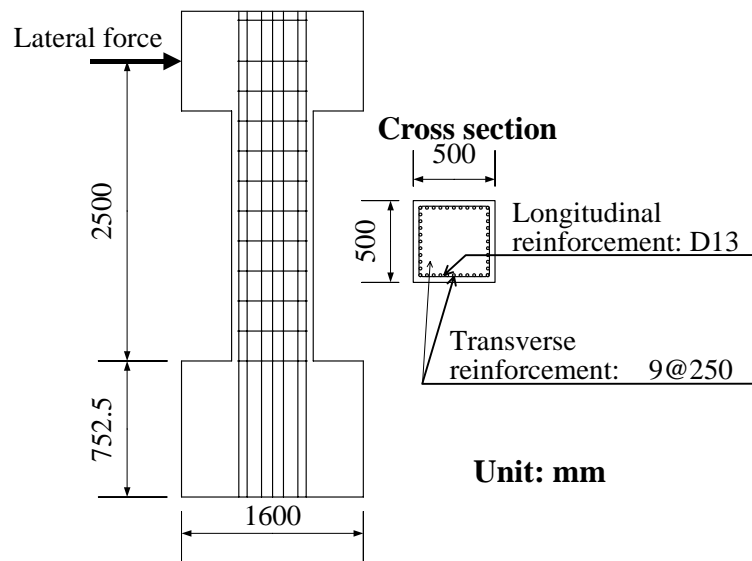
Figure 5.1   Details of specimen and arrangement of reinforcement
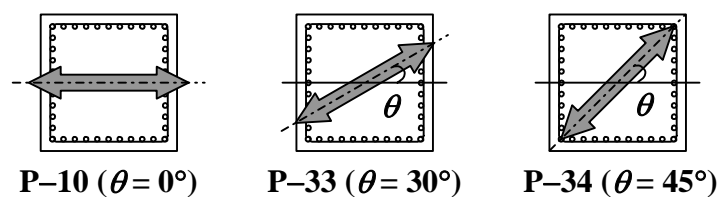
Figure 5.2   Loading conditions

Table 5.1 Specimen and material properties

Specimen No.	Cross section (mm × mm)	Concrete f_c' (MPa)	Longitudinal reinforcement			Transverse reinforcement		
			Grade	f_y (MPa)	p_s (%)	Grade	f_y (MPa)	r_w (%)
P–10		31.3						
P–33	500 × 500		SD295A D13	308	2.03	SR235 φ9	272	0.10
P–34		39.7						

In the experiment, the displacement amplitude was increased stepwisely in increments of $n \cdot \delta_y$ (n = 1, 2, 3…) at each loading step.   Here, δ_y was determined as the lateral displacement when the measured strain of the longitudinal reinforcement at the bottom of the pier firstly reached the yield strain of $1{,}800\mu$, and was taken as δ_y = 13 mm in the column P–10.   The yield displacement was used to control the displacement in both columns P–33 and P–34. The loading cycles were controlled of ten each cycle at the same amplitude.   In the test, the axial load was not applied because of the limitation of loading apparatus.   The loading hysteresis identical to that in the experiment is applied in the analysis by using a displacement-controlled incremental calculation.

5.2.2   Effect of loading direction on cyclic behavior of the piers

The experimental lateral load-lateral displacement relationships at the top of the pier for each specimen are shown in **Figure 5.3**.   In all specimens, similar behavior was observed while the development of damage was significantly different.   The experimental observations for all specimens during each loading cycle are shown in **Table 5.2**.

In the experiment, the results of the specimen P–10 showed that uniform flexural cracks gradually appeared and the behavior was governed by the crack nearest to the footing until the displacement reached $3\delta_y$.   During further loading, the spalling of cover concrete developed near the column-footing joint.   Moreover, the buckling of reinforcement could be slightly observed after scratching the spalled cover concrete out in the experiment.   When the displacement reached $6\delta_y$, the fracture of longitudinal reinforcement was observed due to a low-cycle fatigue.   This is caused by that the longitudinal reinforcement is subjected to large cyclic deformation including bending and stretching.
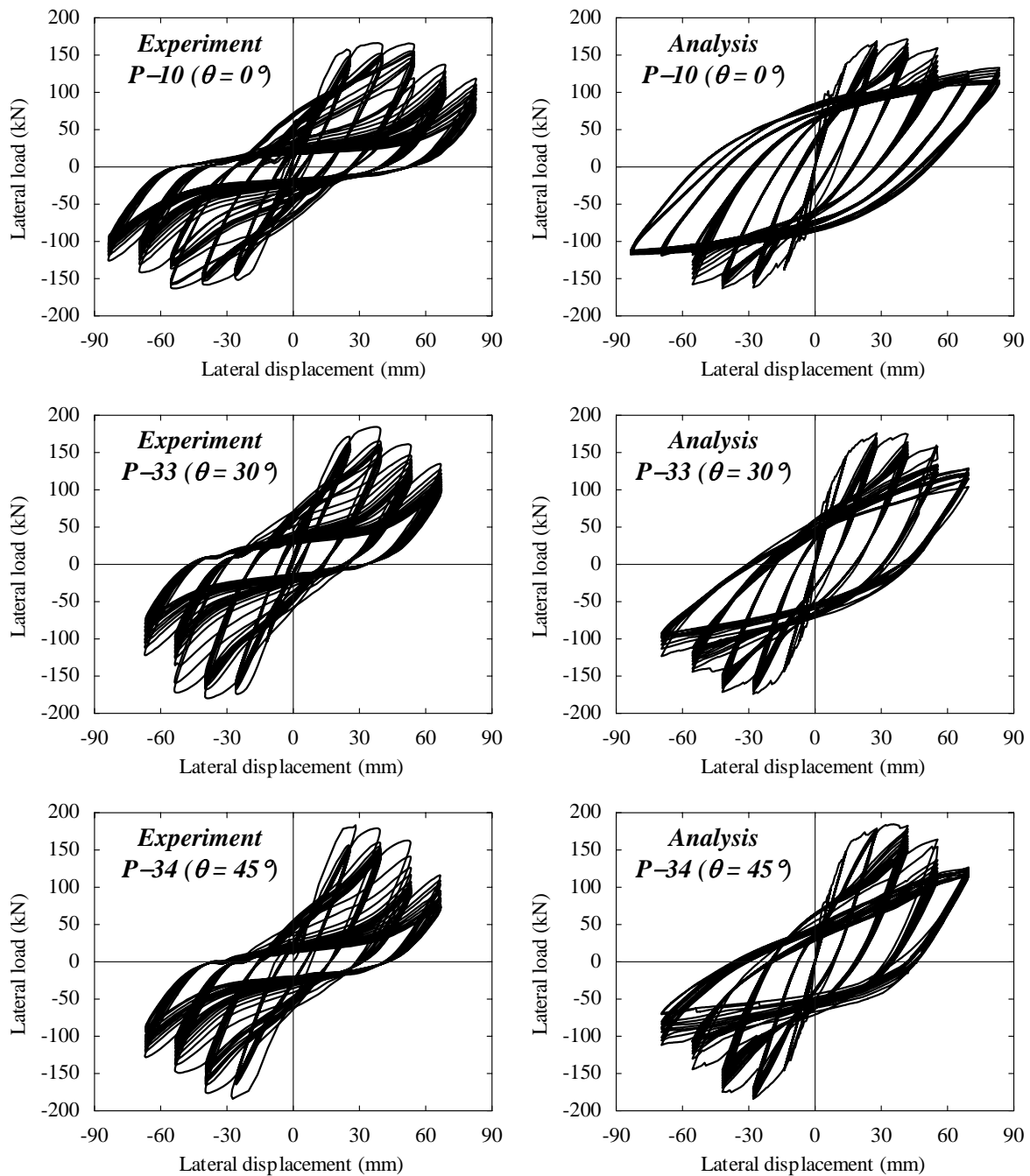
Figure 5.3 Lateral load-lateral displacement relationships obtained by the cyclic loading test and the 3D static lattice model

On the other hand, it is found that the deterioration in the specimen P−33 was faster than that in the specimen P−10.   The spalling of cover concrete at the corner of section appeared at the bottom of the pier when the displacement reached around $3\delta_y$.   After the spalling of cover concrete, the gradual decrease in the lateral load was observed in the post-peak region of load-displacement curve and the ductility reduced.   This rapid decrease in the lateral load was caused by the fracture of longitudinal reinforcement due to the low-cycle fatigue.   In the specimen P−34, the behavior at each loading cycle was similar to the specimen P−33.

Table 5.2 Progress of failure during loading cycles

ID	$1\delta_y$	$2\delta_y$	$3\delta_y$	$4\delta_y$	$5\delta_y$	$6\delta_y$	$7\delta_y$	$8\delta_y$
P−10	Initiation of flexural cracks			Spalling of cover concrete during around 50 cm range	Fully spalled out and buckling of longitudinal reinforcement	Fracture of longitudinal reinforcement at 1 bar	3 bars	7 bars
P−33	Initiation of flexural cracks		Spalling of cover concrete during 20 cm range	Fully spalled out during 40-60 cm range and buckling of longitudinal reinforcement	Fracture of longitudinal reinforcement at 2 bars	8 bars	5 bars	3 bars
P−34	Initiation of flexural cracks		Spalling of cover concrete	Fully spalled out and buckling of longitudinal reinforcement	Fracture of longitudinal reinforcement at 4 bars	4 bars	2 bars	6 bars

Next, the analyses using 3D static lattice model are carried out for these three piers.   The analytical lateral load-lateral displacement relationships at the top of the pier for each specimen are illustrated in **Figure 5.3**.   The envelope curves of the experimental and analytical load-displacement relationships are illustrated in **Figure 5.4**.   In the figure, the envelope curves indicate the relationships connecting the points corresponding to the maximum displacement of each step at the first and the tenth cycles.

For the specimen P−10, the analytical and experimental results are found to show the good agreement with each other.   Matching with experimental observation, the buckling behavior of longitudinal reinforcement is predicted at the lateral displacement of more than 55 mm.   However, the divergence of analytical results from the experimental results is observed at the large deformation range.   This is because that the fracture of longitudinal reinforcing bars due to the low-cycle fatigue is not incorporated in the analysis.

In the specimen P−33, the analytical load-displacement relationship is also found to be close to the experimental result.   It is found that the flexural ductility of these square piers subjected to bending from the direction of section diagonal is almost similar to that for bending from the direction of a principal axis of the section.   In both the experiment and analysis, the slight increase in the load carrying capacity is observed.   After the analytical displacement exceeded around 40 mm, the gradual decrease in the lateral force can be observed in the post-peak region of load-displacement relationship.   That is similar to the

(a) First cycle

(b) Tenth cycle



(c) Comparison between first and tenth cycles
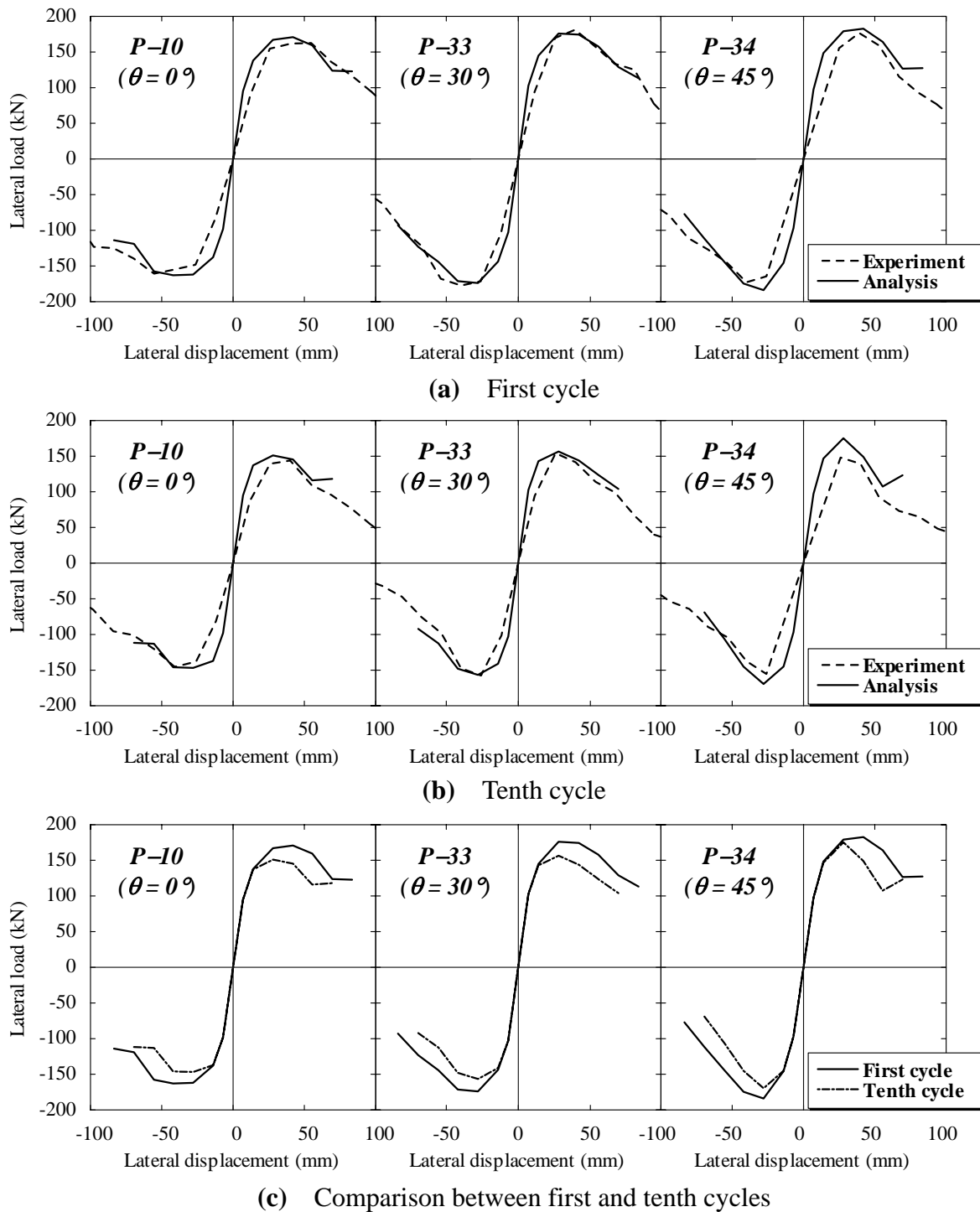
Figure 5.4 Analytical envelope curves of lateral load and lateral displacement

experimental observation. This point is corresponding to the compressive softening of concrete at the base of the pier and the initiation of the buckling of longitudinal reinforcement. However, it can be observed in **Figure 5.4** that the difference between analytical and experimental results is recognized at the large deformation range. It may be caused by that the spalling of cover concrete at the corner of section is disregard in the analysis.

134

For specimen P−34, it can be observed that the experimental and analytical load-displacement curves and its envelope curves are very close to each other, as shown in **Figures 5.3** and **5.4**. The analytical and experimental comparison of the load carrying capacity of RC piers indicates that there is slight difference with the load carrying capacity if the lateral load is applied from the direction of a principal axis of the section. The tenth cycle for the same displacement produced nearly the same response and the degradation of stiffness cannot be observed until the lateral displacement reached at 50 mm. In this region, the analytical response shows higher energy dissipation capacity with slight pinching during unloading and reloading. However, in the post-peak region, the significant degradation of load carrying capacity during same displacement in each cycle can be observed. This is caused by the simultaneous degradation between the compressive softening of concrete and the buckling of reinforcement at the base of the pier.

In order to investigate the effect of only the compressive softening of concrete on the analytical results, the analysis neglecting the buckling of reinforcement is carried out. **Figure 5.5** shows the analytical load-displacement relationships of all cases of the piers obtained from the 3D lattice model analysis neglecting the buckling behavior of reinforcement. It can be seen in the figure that the gradual decrease in the load after the lateral displacement reaches around 42 mm. The degree of decrease in the load is larger as the angle to the principal axis of the section becomes larger. Consequently, the post-peak softening of the load-displacement relationship of the specimen P−34, in which the angle to the principal axis $\theta = 45°$, is steepest in these three piers. Although the decrease in the load carrying capacity can be predicted, the higher energy dissipation capacity is prominent.
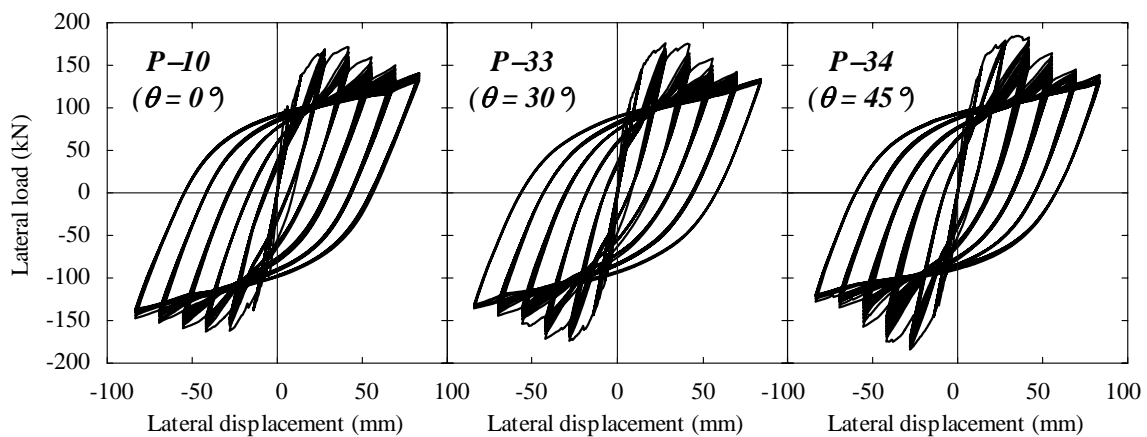

Figure 5.5   Analytical hysteresis loops obtained from the 3D lattice model neglecting buckling behavior of longitudinal reinforcement

135

However, it is found that the significant decrease in the load, which can be predicted in the analysis considering the buckling behavior of reinforcement, cannot be observed. This is also different from the experimental load-displacement curves.

5.2.3 Detailed analytical investigation

The quantitative relationships between the loading direction and the cyclic behavior of the piers are verified by the 3D lattice model analysis. The analytical results of stress-strain relationships of concrete at the bottom of the pier are illustrated in **Figure 5.6**. For three specimens, the flexural members of concrete, which is located at flexural extreme fibers in compression and tension at the bottom of the pier, are focused on and shown as the elements A and B in the figure.

(a) Element A
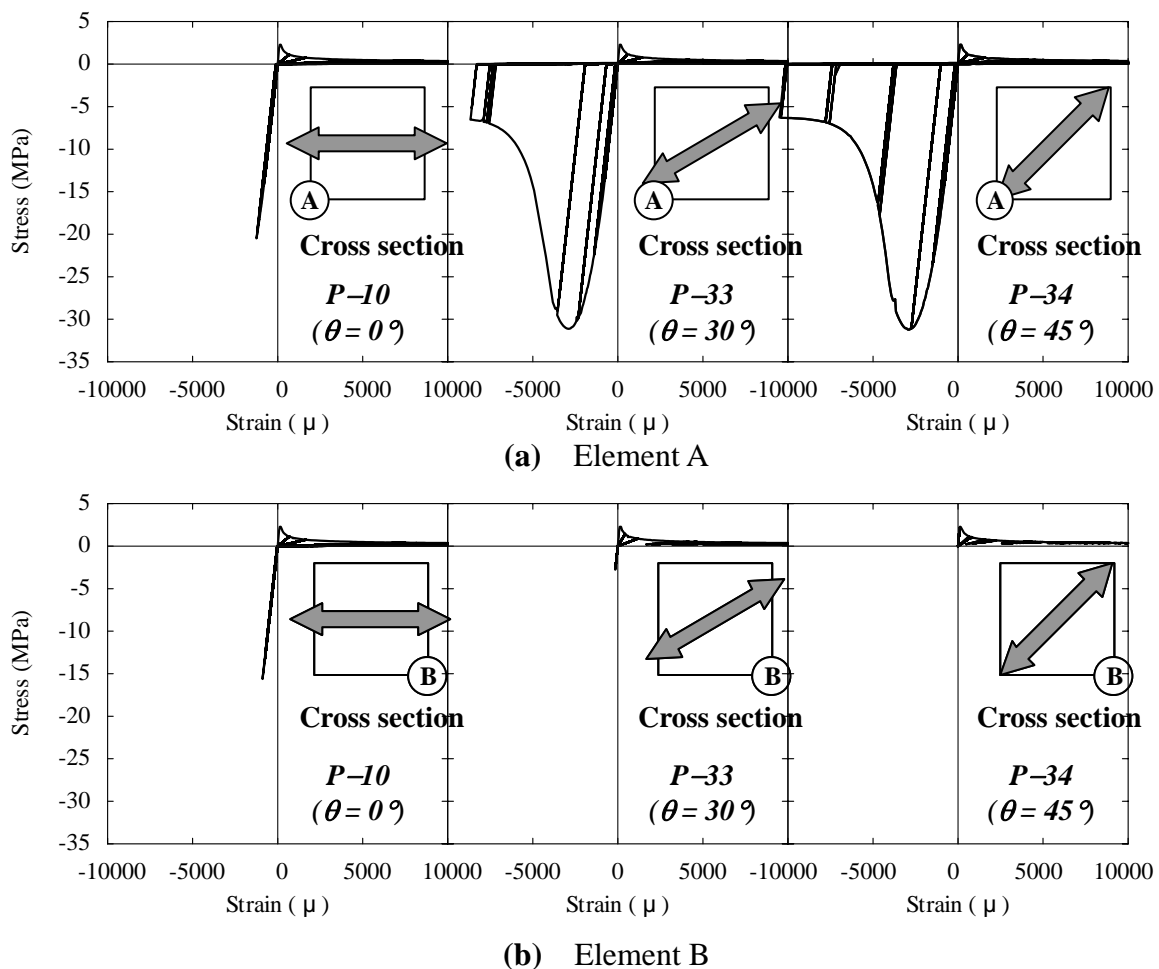
(b) Element B

Figure 5.6 Stress-strain relationships of concrete in the longitudinal direction at the bottom of the pier (The elements A and B are flexural members of concrete.)

As shown in the figure, for the specimen P−10, the stress-strain relationship indicates almost elastic behavior throughout the loading, though the buckling behavior of longitudinal reinforcement takes place. This is because that the large plastic strain of longitudinal reinforcement in tension provides the compressive stress even if the compressive stress is produced in the longitudinal reinforcement after the load reversal.   For the specimen P−33, it is observed that larger compressive strain occurs in the element A at the corner of section in the bottom of the pier. This is matching with the experimental observation in which the spalling of cover concrete is initiated at the corner of section at the bottom of the pier. Consequently, it is found that the analysis can predict the severe post-peak softening behavior in the stress-strain curve of concrete at the element A. Similarly, the element A in the specimen P−34 shows larger compressive strain during the loading cycles.   It is found that the more severe deterioration of the flexural members of concrete is observed at the element A, while the element B remains in tension.

Through the these analytical discussions, it is found that the 3D lattice model analysis can explain the influence of the loading direction on the cyclic behavior of RC bridge piers quantitatively in terms of the stress-strain relationships of each member.

5.3   Torsional Analysis of RC Beams

5.3.1   Introduction

When RC structures such as RC high piers or multi-deck RC frames are subjected to seismic loads, the structural members are resisting against the load combinations including significant torsion and shear.   The 3D complex load carrying mechanisms of RC structures are observed here.   As a result, the response of the structure during loading becomes complex.   These problems should be treated as 3D.

Here, 3D analytical modeling is necessary to treat the case that the response of RC structures subjected to bending, shear, seismic bilateral loading, or torsion and their combinations is predicted.   Since the torsional behavior of structural concrete members has been experimentally well investigated, it becomes a good analytical target for verifying and improving the 3D analysis concept.   In this section, the analyses by 3D static lattice model are carried out for RC beams with solid or hollow section subjected to pure torsion.

5.3.2   Tested specimens and experimental setup

To verify the performance of 3D lattice model, the experiment of pure torsional loading tests for RC beams performed by Hsu (1968) and Nagataki et al. (1986) are used for comparison. The dimensions of specimen and arrangements of reinforcement are illustrated in **Figure 5.7**. The experimental parameters are listed in **Table 5.3**.

In the experiment of Hsu (1968), six RC beams with rectangular cross section were tested. The specimen was reinforced by various amounts of torsional reinforcement, 0.53 % to 2.67 %, including equal volumes of longitudinal and transverse reinforcements.   The torsional reinforcement ratio is obtained from **Equations 5.1** and **5.2**.

$$p_l = \frac{\sum A_{sl}}{b \cdot h} \tag{5.1}$$

$$p_t = \frac{A_{st} \cdot 2(h_o + b_o)}{b \cdot h \cdot s} \tag{5.2}$$

where, p_l and p_t are longitudinal and transverse reinforcement ratios, respectively.   Similarly, A_{sl} and A_w are the cross-sectional area of one longitudinal and one transverse reinforcing bar, respectively.   Here, b and h represent the width and height of the beam and b_o and h_o indicate the length of transverse reinforcing bar along the width and the height of cross section. s is the spacing of each transverse reinforcement.

(a)   Solid sectional RC beam
(Hsu 1968)

(b)   Hollow sectional BC beam
(Nagataki et al. 1986)
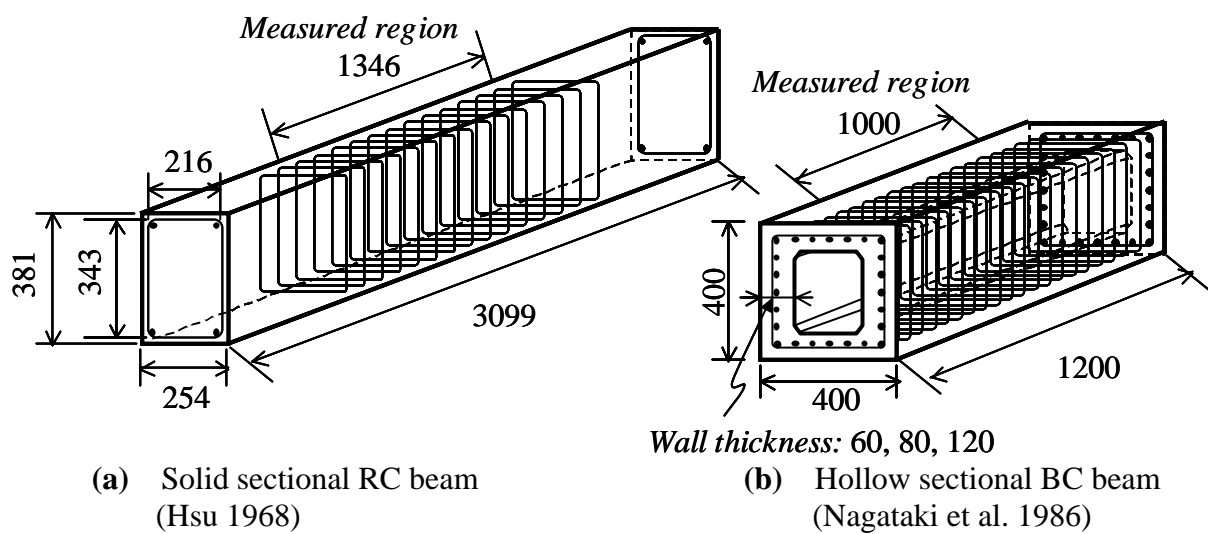
Figure 5.7   RC beams for pure torsional tests

Table 5.3 Material properties of concrete and reinforcement

| Tested by	ID	Concrete			Longitudinal reinforcement			Transverse reinforcement			Cross sectional shape
		$f_c{}'$ (MPa)	f_t (MPa)	E_c (GPa)	f_{ly} (MPa)	E_s (GPa)	p_s (%)	f_{ty} (MPa)	E_s (GPa)	r_w (%)	
Hsu 1968	B1	27.6	3.25	27.6	323.6	196.5	0.534	324.8	196.5	0.537	Solid
	B2	28.6	3.13				0.827			0.823	
	B3	28.1	2.82				1.17			1.17	
	B4	30.5	3.14				1.60			1.61	
	B5	29.0	2.99				2.11			2.13	
	B6	28.8	3.50				2.67			2.61	
Nagataki 1986	II–1	22.8	1.51	–	368.5	212.7	1.39	368.5	212.7	1.38	Hollow
	II–2	23.0	1.51				1.05			1.04	
	II–3	26.2	1.69				0.697			0.689	
	II–4	25.6	1.66				0.348			0.350	
	II–5	26.7	1.75				1.05			0.350	
	II–6	27.3	1.72				0.348			1.04	
	II–7	28.7	1.84				1.05			1.04	
	II–8	29.7	1.90				1.05			1.04	
	II–9	29.7	1.90				1.05			1.04	Solid

The cross-section was 254 mm × 381 mm. The length of all beams was 3,099 mm and the length over which the angle of twist was measured is 1,346 mm at the center of a beam. The compressive strength of concrete was from 27.6 N/mm^2 to 30.5 N/mm^2. The averaged yield strength of longitudinal and transverse reinforcements was around 324 N/mm^2 and the elastic modulus was around 197 kN/mm^2.

Nagataki et al. (1986) performed the pure torsional loading tests for RC hollow sectional beams in which the wall thickness was varied as 60 mm, 80 mm, and 120 mm. The length of all beams was 1,200 mm and the length over which the angle of twist was measured was 1,000 mm at the center of a beam. The cross section was 400 mm × 400 mm.

The longitudinal and transverse reinforcements were arranged as one layer for each as illustrated in **Figure 5.7**. The ratios of longitudinal and transverse reinforcements varied from 0.35 % to 1.39 % and from 0.35 % to 1.38 %, respectively. The compressive strength of concrete used in the test ranged from 22.8 N/mm^2 to 29.7 N/mm^2. The longitudinal and transverse reinforcements were D10 with the yield strength of around 369 N/mm^2 and the elastic modulus of around 213 kN/mm^2.
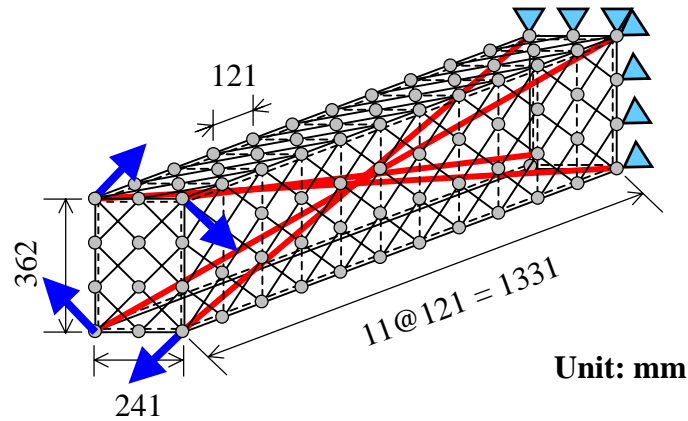
Figure 5.8   3D lattice model for solid sectional beams

5.3.3   Torsional analysis of solid sectional RC beams

The 3D static lattice model used for torsional analysis is shown in **Figure 5.8**.   The specimen has the rectangular cross section in which the width and the depth are different from each other.   In the modeling, the horizontal or vertical distance of two adjacent nodes is determined based on one-third of the effective depth d of 362 mm.   Consequently, the number of division in the cross section of the lattice model is set as 2×3.   For simplicity, the length where the angle of twist is measured in the test is modeled here.

The distributions of the total potential energy with various amounts of reinforcement obtained by the 3D static lattice model are shown in **Figure 5.9**.   It is found that the value of t_b increases as the ratios of longitudinal and transverse reinforcements increases.   On the other hand, the amount of reinforcement is not influential on the value of t_d, and the value of t_d remains 0.30.   For the specimen B1 in which the amount of reinforcement is small, the values of t become $t_b = 0.35$ and $t_d = 0.30$, respectively.   In contrast, the specimen B6 with large amount of reinforcement shows larger value of t_b,: $t_b = 0.50$ and $t_d = 0.30$.   In this case, the width of an arch part becomes larger than that of other specimens, and consequently the arch action is found to be dominant in the load carrying mechanism.   Hence, from the results obtained by the 3D lattice model, it is found that the ratio of an arch part to the cross-sectional width of the beam increases with the increase in the ratio of the longitudinal and transverse reinforcements.

The analysis using the 3D lattice model with the values of t_b and t_d is carried out.   The experimental and analytical results are shown in **Figure 5.10**.   These results show the torque and the angle of twist relationships of solid sectional RC beams with various amount of reinforcement.   In the figure, the values of t_b and t_d using in the analysis are also shown.   It
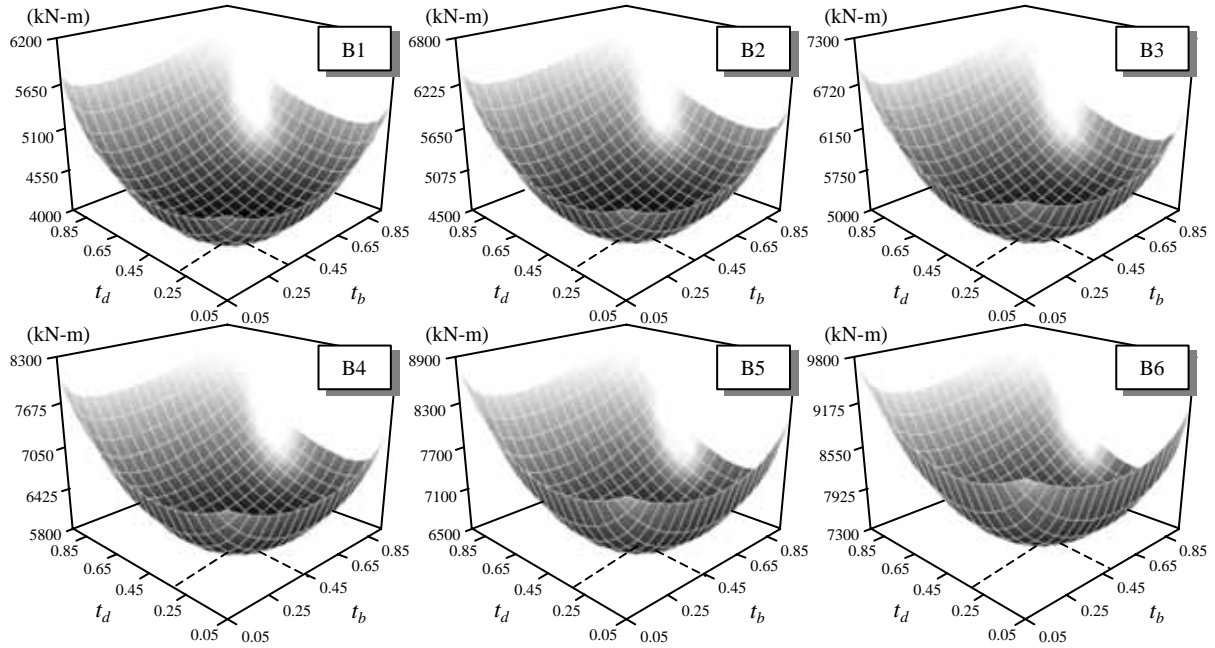
Figure 5.9 Distributions of total potential energy with various amount of reinforcement

is found from the figure that the results of experiment and analysis are in good agreement with each other.

From **Figure 5.10**, it is observed that the analytical results of the specimen B1 with small amount of reinforcement show that the torque does not increase after diagonal cracking. This is caused by that the transverse reinforcement yields right after the diagonal cracks occur and then the longitudinal reinforcement yields. Consequently, the torque is almost constant after the yielding of longitudinal reinforcement. In this case, the yielding of the transverse reinforcement takes place at not the shorter surface of the cross section but the longer surface. These phenomena correspond to the experimental observations.

With the increase in the amount of longitudinal and transverse reinforcements, the analytical torque increases after the diagonal cracking. The degree of increase in the torque is depending on the amount of longitudinal and transverse reinforcements. It is found that the deterioration of stiffness after the diagonal cracking becomes mild in case of RC beams with the large amount of reinforcement. For the specimens B2, B3, and B4, though the torque increases after diagonal cracks occur, the longitudinal reinforcement yields in the large twist region and then the maximum torque is reached due to the compressive softening of diagonal concrete members. On the other hand, for the specimens B5 and B6, as the amount of reinforcement increases, the compression softening behavior of concrete becomes more dominant so that the diagonal compressive failure of concrete occurs before the reinforcement yields. The behavior predicted in the analysis is also observed in the experiment.
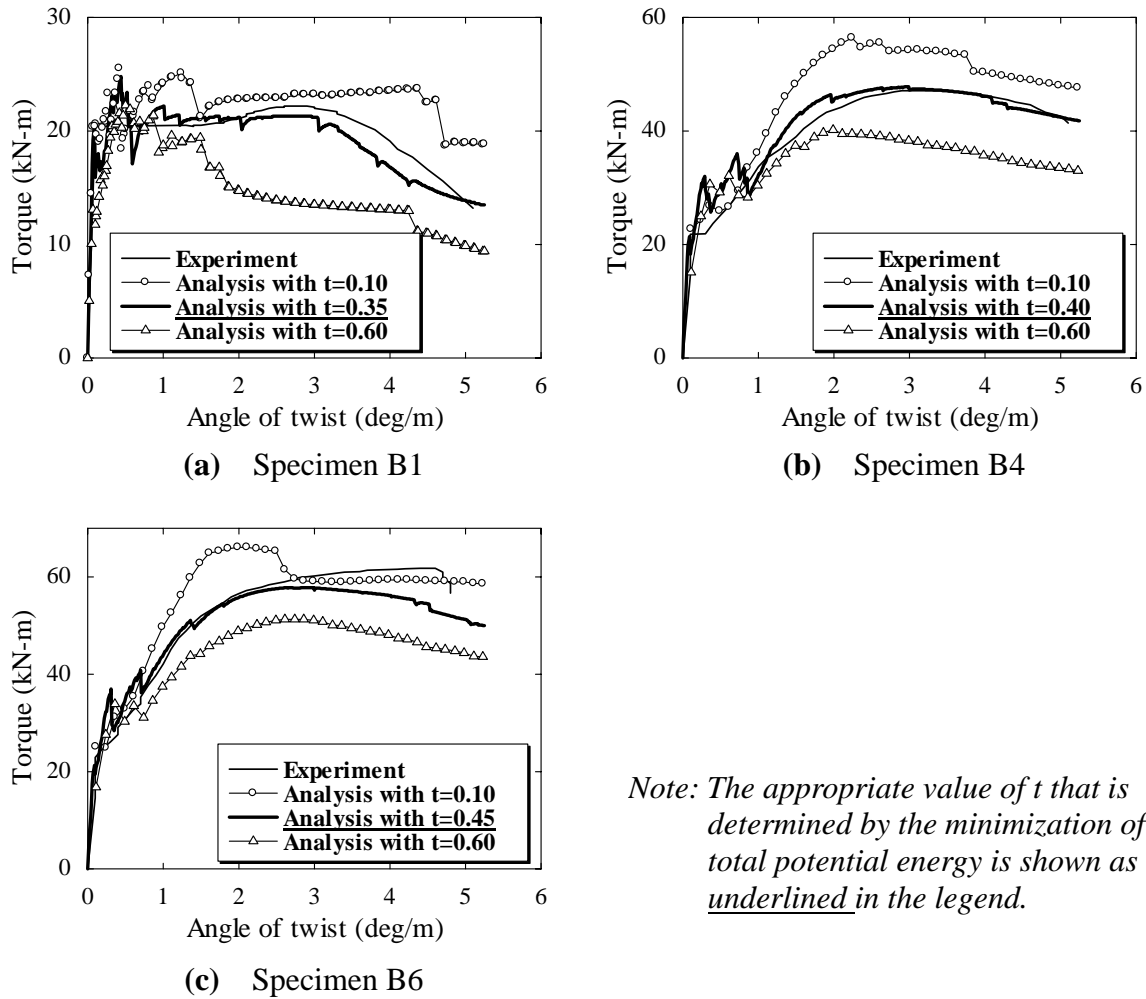
141
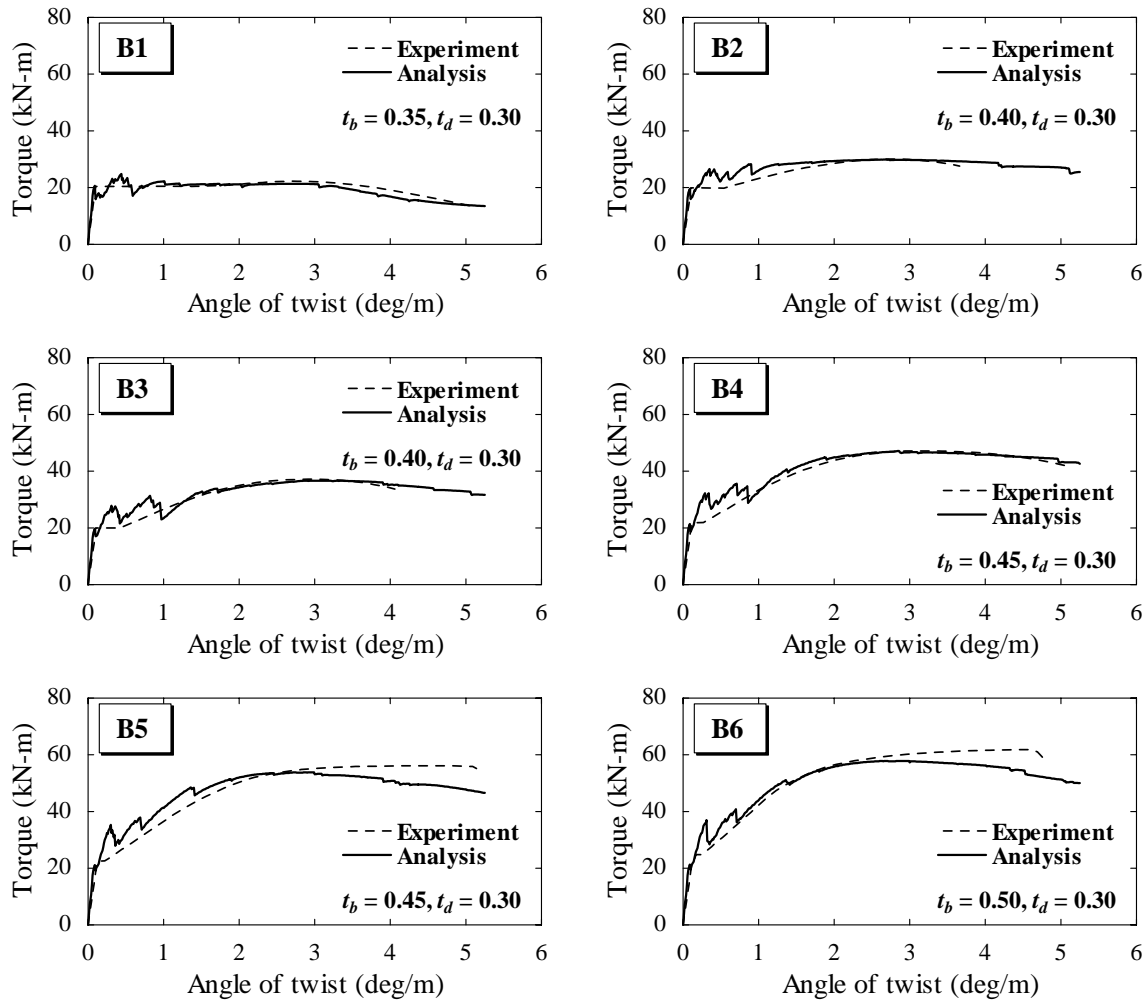
Figure 5.10 Torque-angle of twist relationships obtained by torsional test and the 3D static lattice model analysis

Therefore, it is found that the torsional analysis based on the 3D lattice model can predict the reasonable torque-twist relationships of solid sectional RC beams including the estimation of the failure mode with the various amounts of reinforcement.

5.3.4 Effect of value of t on analytical response

As mentioned previously, the analysis by the 3D lattice model is performed using the value of t that is determined based on the principle for the minimization of total potential energy. Hereafter, in order to investigate the effect of the value of t on analytical response, the torsional analyses are carried out with several different values of t. The experimental and analytical results of the specimens B1, B4, and B6 are illustrated in **Figure 5.11**. In the figure, the results using appropriate value of t that is determined by the minimization of total potential energy are also shown as underlined in the legend. Since the value of t_d is not

Figure 5.11   Influence of value of *t* on the analytical response

affected by the amount of reinforcement, the value of t_b is focused on in the parametric analysis.

For the specimen B1 in which the smallest amount of reinforcement is arranged, it is observed that the behavior of a RC beam is linear before the diagonal crack initiates.   That is not influenced by the value of *t*.   After the torsional crack occurs, the maximum torque with small value of *t* ($t_b = 0.10$) is larger than that with an appropriate value of *t* ($t_b = 0.35$).   The results of these two cases indicate the similar behavior in the plastic plateau of the torque-angle of twist curve after the reinforcement yields.   On the other hand, in case of beams with large value of *t* ($t_b = 0.60$), though the maximum torque is almost the same to the one with the appropriate value of *t* ($t_b = 0.35$), the torque decreases more steeply after the angle of twist reaches at around 1.5 deg/m.   This is due to the softening of concrete in compression that occurs in the diagonal concrete member.   From these results, it is found that for RC beams with small amount of reinforcement, in which the reinforcement yields just

143

after the diagonal cracks occur, the maximum torque analyzed using the small value of t is larger than that with the appropriate value of t. It is also found that the deformation capacity decreases in case of beams with the large value of t as compared with the analytical result with the appropriate value of t.

In the specimen B4, the torsional behavior of the beam before the diagonal cracks initiate is not affected by the value of t. However, after the diagonal cracks occur, there are some differences in each case. The stiffness that is represented as the inclination of the torque-angle of twist relationship with small value of t ($t_b = 0.10$) is larger than that with an appropriate value of t ($t_b = 0.40$). The maximum torque is also larger than that with an appropriate value. The angle of twist corresponding to the maximum torque is similar to the results with an appropriate value of t ($t_b = 0.40$). On the other hand, it is found from **Figure 5.11** that the stiffness after diagonal cracking with large value of t ($t_b = 0.60$) is smaller than that with an appropriate value of t ($t_b = 0.40$). In this case, the maximum torque decreases and reaches at the twist angle of around 2.0 deg/m, which is smaller than the case with an appropriate value of t ($t_b = 0.40$).

For the specimen B6 having large amount of reinforcement, the stiffness with small value of t ($t_b = 0.10$) is larger than that with an appropriate value of t ($t_b = 0.40$). It is similar to the behavior of the specimen B4. Consequently, the maximum torque is considerably reduced in comparison with the experimental results. However, when the angle of twist is reached at around 3.0 deg/m, the torque decreases abruptly. This post-peak softening in the torque-angle of twist relationship corresponds to the post-peak behavior of the diagonal concrete members. Therefore, it is found that the value of t influences the torsional response of RC beams with large amount of the reinforcement, especially the stiffness after the diagonal cracking, the maximum torque, and the torsional deformation capacity.

Through previous discussion, it is recognized that the appropriate value of t is necessary to model RC structural members properly. In addition, these analytical results also suggest that the value of t determined based on the principle of the minimization of total potential energy is suitable in the 3D lattice model to predict the torsional behavior, the maximum torque, and deformation capacity. By considering the load resisting mechanism represented by arch and truss actions with the appropriate proportion of each part, the analysis can predict reasonable behavior after the diagonal cracks occur. Moreover, the compressive stresses along the diagonal cracks can be evaluated considering the compressive softening behavior of concrete depending on the transverse tensile strain. Consequently, it is found that the reasonable response of RC beams under pure torsional loads can be predicted adequately.
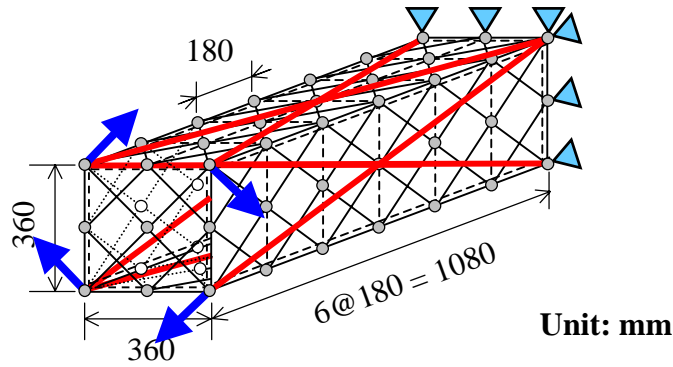
Figure 5.12 3D lattice model for hollow sectional beams

5.3.5 Torsional analysis of hollow sectional RC beams

When the hollow sectional beams are analyzed, it is unrealistic to assume the corner-to-corner arch action inside RC beams in the same way as the solid sectional beams. The stress flow in the beam subjected to torsional load is limited inside the wall. In the analysis, it is assumed that the arch and truss actions are individually formed in each of four walls of hollow sectional RC beams. In the 3D lattice model, four couples of arch members crossing each other are located in the four walls as illustrated in **Figure 5.12**. In order to model the hollow sectional beam, the value of *t* is newly defined as the ratio of the width of an arch part to the wall-thickness.

The analytical results by the 3D lattice model of the torque and angle of twist relationships for the hollow RC beams are shown in **Figure 5.13**. The experimental results are also shown in the figure as a solid line. From these figures, it can be confirmed that the experimental and analytical results show the good agreement with each other. It is also found that 3D lattice model analysis can predict the torsional behavior and the failure mode including the maximum torque and the deformation capacity accurately.

In the specimens II−1 to II−4, the longitudinal and transverse reinforcement ratios are identical. The analyses for specimens II−1, II−2, and II−3, in which the sufficient reinforcement is arranged, show that the compressive softening of concrete in the diagonal member is predicted prior to the yielding of longitudinal reinforcement. As a result, the torque decreases gradually after the maximum torque is reached. This post-peak softening behavior cannot be captured in the experimental result of the specimen II−1. The experimental and analytical results of the torque-angle of twist relationships are found to show the good agreement with each other. On the other hand, in the specimen II−4, the
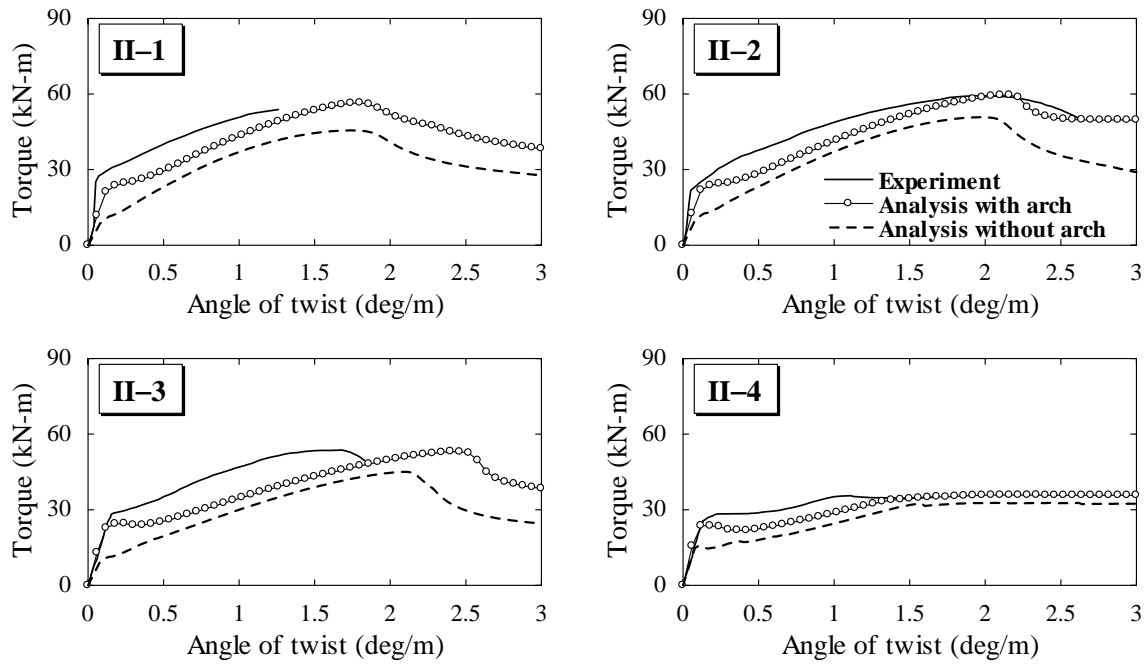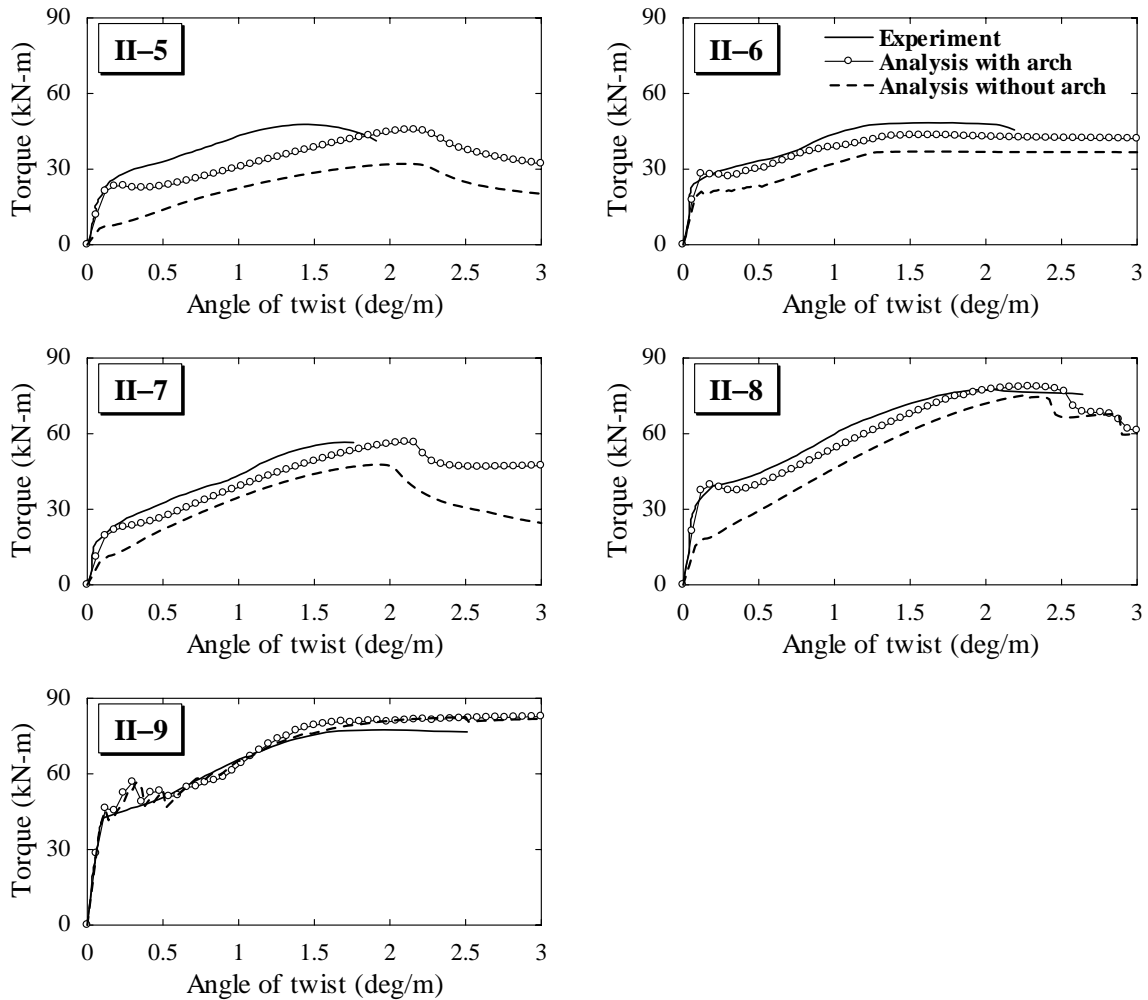
145

Figure 5.13 Torque-angle of twist relationships obtained by torsional test and the 3D static lattice model analysis

torque becomes constant after the longitudinal and transverse reinforcements yield. Consequently, the softening in the torque-angle of twist curve is not observed even in the high deformation range.   This response corresponds to the experimental result.

For the specimens II−5 and II−6, in which the reinforcement ratios are completely different, the analytical torque-angle of twist curves are found to be close to the experimental curves. For the specimen II−5 with relative large amount of longitudinal reinforcement, the softening of concrete in compression is predicted in the diagonal member before the longitudinal reinforcement yields.   In contrast, it can be observed that the specimen II−6 with relative large amount of transverse reinforcement does not exhibit the softening response in the analytical result even when the torsional deformation becomes large.

Here, since the transverse reinforcement is arranged as a single layer, the confined effect of concrete with both longitudinal and transverse reinforcements cannot be expected in the wall of hollow section.   In the experiment, it is also observed that the spalling of cover concrete of the wall easily occurs not only outside but also inside of the hollow section.   Hence, the stress-strain relationship of unconfined concrete in compression that shows inductile behavior such as plain concrete is used in the analysis for diagonal and arch members of concrete.

The specimens II−7 and II−8 are RC beams with different wall thickness.   In the analysis, the specimen II−7 with thin walls shows the softening response in the torque-twist angle

Figure 5.13 Torque-angle of twist relationships obtained by torsional test and the 3D static lattice model analysis (continued)

curve due to the compressive softening of concrete in the diagonal member prior to the yielding of reinforcement. It is predicted in the specimen II–8 with thick wall that the transverse reinforcement yields and then the post-peak softening in the torque-twist angle curve appears, which is observed in the experiment as well.

5.3.6   Influence of value of *t* in hollow sectional RC beams

In order to investigate the effect of arch members on analytical response, the analyses by the 3D lattice model with no arch members are carried out.   The analytical results are shown in the **Figure 5.13**.   In the analysis, truss members are determined based on the value of *t* that is used in the previous analysis, while only arch members is neglected.

As mentioned previously, RC beams with large amount of reinforcement such as the

specimens II–1, II–2, II–3, II–5, and II–7 show the compressive softening of concrete prior to the yielding of reinforcement. In these beams, it is found that the analytical results neglecting arch members shows that the cracking and the maximum torques are considerably reduced in comparison with the analytical results considering arch members, as well as experimental results. Here, the tangent stiffness from the initiation of cracks to the maximum torque is found to be almost same as each other.

On the other hand, the specimens II–4, II–6 and II–8, in which the amount of reinforcement is relatively small and the yielding of reinforcement is observed, provide no difference in the maximum torque and the post-cracking stiffness while the cracking torque decreases in the case that the arch members are not provided.

These results lead the understanding of the proportion of arch and truss components depending on the loading level. For beams of which the maximum torque is governed by the compressive softening of concrete, it is found that the angle of twist corresponding to the maximum torque is similar because of the existence of arch members. This fact can be mainly attributed to the reason that the arch and truss members of concrete in tension are able to resist the torsional forces before the diagonal cracks occur. On the other hand, after cracking, the truss members govern the torsional response of hollow sectional RC beams.

In the solid beam of the specimen II–9, it is found that the existence of arch members does not influence the analytical results. This is because of the assumption that the corner-to-corner arch action inside the RC beam is idealized as a compressive strut. In this case, arch members may not contribute toward the resisting mechanism of torsional loads.

5.4   RC Columns Subjected to Combined Loads of Torsion and Bending

5.4.1   Introduction

In **section 5.3**, it has been confirmed that the 3D lattice model analysis can predict the behavior of RC beams subjected to pure torsion with adequate accuracy. However, even in the previous research (Niwa et al. 1990, Rahal and Collins 1995), it has been confirmed that the analysis by 2D model can predict the pure torsional behavior by considering the in-plane RC constitutive models. The models are including the compressive stress-strain relationship of diagonally cracked concrete, the softening in compression and tension, and the tension stiffening. These models are based on the thin-wall theory in which the solid sectional beam is treated as an equivalent hollow sectional beam and the equivalent shear stress flow in the
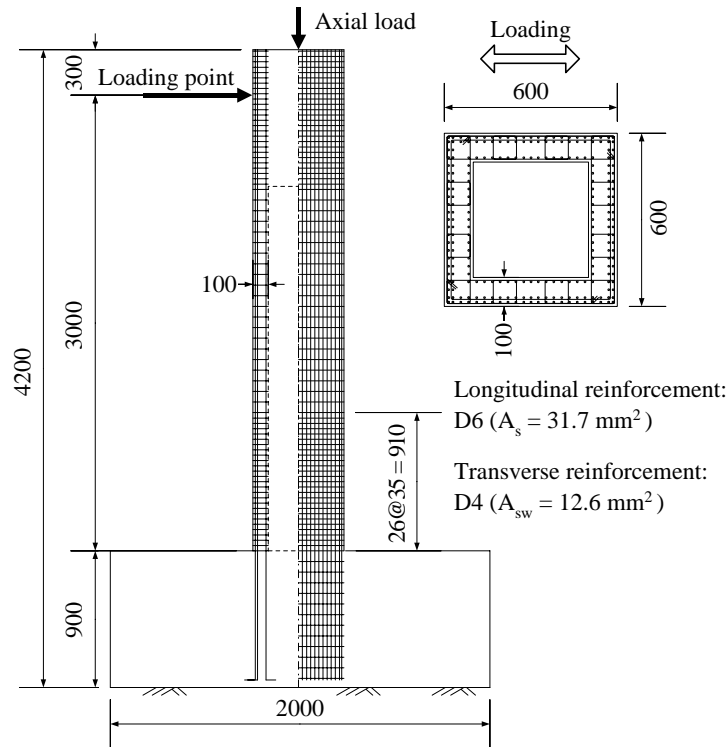
Figure 5.14 Specimen for test under cyclic combined loading of torsion and bending

wall is assumed.   Therefore, the validity of 3D lattice model has not been clearly verified by dealing with only a problem of pure torsion.   Herein, to verify the performance of 3D lattice model, the simulation of RC beams subjected to the combined cyclic loading of torsion and bending will be carried out.

5.4.2   Test specimens and loading condition

The analytical target is a 1/10-scale model of a hollow sectional RC high bridge pier (Yukawa et al. 1999).   The dimensions and arrangements of reinforcement are shown in **Figure 5.14**. The cross-section used in the test was a square of 600 mm × 600 mm and the wall thickness was 100 mm.   The height of the pier from the footing was 3,000 mm.   The compressive strength and elastic modulus of concrete ranged from 38 N/mm^2 to 42 N/mm^2 and 25 kN/mm^2 to 29 kN/mm^2, respectively.   The strength properties of longitudinal reinforcement of D6 were 320 N/mm^2 of the yield strength and 496 N/mm^2 of the tensile strength.   The transverse reinforcement of D4 had 397 N/mm^2 of the yield strength and 573 N/mm^2 of the tensile strength.   The diameter of longitudinal and transverse reinforcements was adjusted by scale-down so that it corresponds to the size of an actual bridge pier.

In the experiment, two loading cycles were applied to the identical two specimens.   The

149

specimen No.1 was the pier subjected to uniaxial reversed cyclic loading and the specimen No.14 was the pier subjected to combined cyclic loading of torsion and bending.

The loading sequence consisted of lateral pushing and pulling cycles was controlled by the lateral displacement after the first yielding of longitudinal reinforcement, which corresponded to the horizontal displacement $\delta_y = 11.3$ mm. The displacement at the first yield was determined by the measured displacement at designed yield force ($= 178.4$ kN). The lateral displacement was applied with three complete pushing and pulling cycles. In addition, vertical actuator was provided to apply the axial load of 588 kN during lateral loading cycles.

In series of torsion and bending combinations, two actuators were provided to apply the lateral forces and torque simultaneously. The lateral force was obtained from the sum of forces in two actuators and the torque was calculated by multiplying the difference of forces in two actuators by the distance between these two. Here, the axial load of 588 kN was provided by un-bond high-strength strands at the top of the pier. Here, the theoretical load carrying capacity decreases with the increase in the lateral displacement because of $P-\Delta$ effect resulting from the axial load. The additional moment of $P-\Delta$ effect with increasing lateral displacement was taken into account in both experiment and analysis.

The torsional loading was provided by assuming the compatibility of proportional torsional deformation to flexural deformation. Before the torsional cracks occur, the combined loading of torsion and bending produced the cycles that were initially conducted in the force control following that the ratio of torque to flexural moment was constant to 15 %. After torsional cracking, the loading cycles were switched to the displacement control followed that the ratio of the torsional deformation to the flexural deformation before the cracks occur was ensured to be constant. Consequently, the relationship between the angle of twist and the lateral displacement at the loading point is expressed by the following equation.

$$\frac{\theta_{twist}/H}{d_{lateral}} = 7.33 \times 10^3 \ (rad/mm^2) \tag{5.3}$$

where, θ_{twist} and $d_{lateral}$ are the angle of twist and the lateral displacement at the loading point, respectively. H is the distance from the top of the footing to the loading point in the pier.

5.4.3   Analytical results and discussions

The experimental and analytical results of the specimens No.1 and No.14 are shown in **Figure 5.15**.

For the specimen No.1, the experimental result showed that the longitudinal reinforcement yields initially on the flexural tension side at the bottom of the column. With further loading, the lateral force reached the maximum at the displacement of $3\delta_y$, then the lateral force was maintained up to displacement $9\delta_y$. Ultimately, the lateral force-lateral displacement curve reached the post-peak region accompanied with the buckling of longitudinal reinforcement and the spalling of the cover concrete. It was observed in the experiment that the spalling of cover concrete and the buckling of reinforcement took place during the loading cycle at displacement $8\delta_y$. The longitudinal reinforcement initiated to deform laterally, as a result, the hook of intermediate ties opened during the cyclic loading at displacement $11\delta_y$. In addition, the buckling of reinforcement showed more pronounced, and eventually those longitudinal reinforcements were fractured by low-cycle fatigue as the consequence of successive buckling and straightening. Consequently, the lateral force severely decreased to 45% of the maximum force.

On the other hand, in the analysis of the specimen No.1, the behavior of a RC column is found to be similar to the experimental result. The comparison of two results indicates that the analysis can predict the stiffness, the load carrying capacity, and the cyclic behavior of a RC column after the yielding of the longitudinal reinforcement. These predictions are successfully performed up to the lateral displacement of $8\delta_y$. The analytical hysteresis loop shows higher energy dissipation capacity and the pinching is not observed. It corresponds to the experimental observation.

The analytical results of load-displacement relationships neglecting the buckling of reinforcement are also illustrated in **Figure 5.15**. The comparison between these cases indicates that the buckling of reinforcement does not much affect the overall behavior of the column. This is caused by that the sufficient amount of transverse reinforcements is provided in the wall of hollow section. Consequently, the analysis by 3D lattice model can appropriately predict the cyclic behavior until the large deformed region is reached.

However, the hysteresis loops in the load-displacement curve are found to be slightly larger in the analysis than in the experiment. It is also confirmed that further softening behavior in the post-peak region is not properly predicted by the analysis. This is because that the fracture of longitudinal reinforcement due to the low-cycle fatigue is disregarded. This phenomenon shall influence predictions of the ultimate failure condition of RC columns. Hence, the consideration of low-cycle fatigue of reinforcement must be required to properly predict the behavior of RC columns subjected to a significant large deformation.

When the cover concrete of the column spalls off, a continuous support of core concrete along
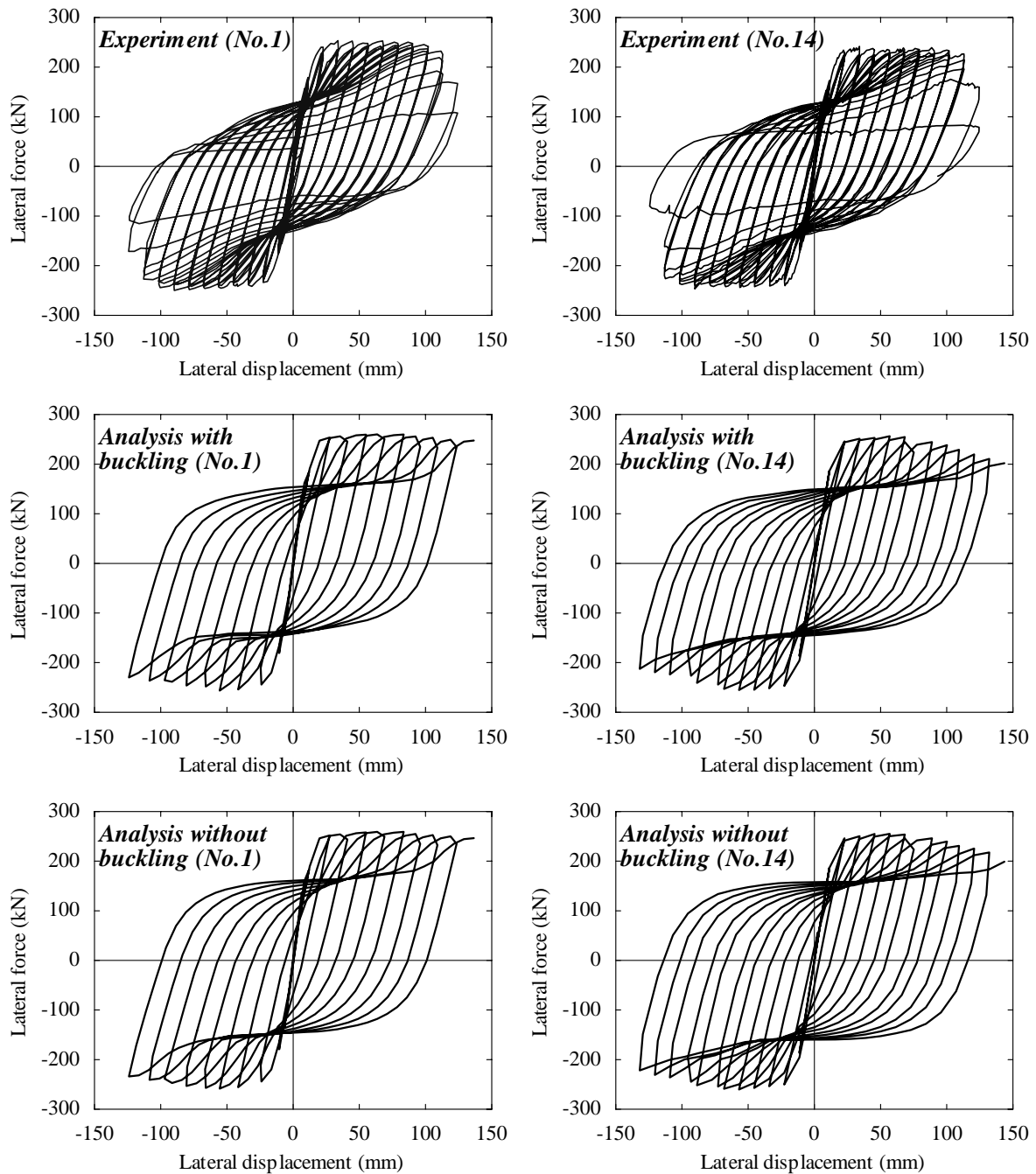
Figure 5.15   Lateral force-lateral displacement relationships of RC columns subjected to uniaxial cyclic loading or combined loading of torsion and bending

one side, which prevents the buckling towards the inside, is observed in the solid sectional beams.   On the other hand, for the hollow sectional beam, it is also observed that the spalling of cover concrete in the wall easily occurs not only outward but also inward of the section in the experiment.   Although the behavior of the buckling towards the inside in the hollow section should be considered in the analysis, the influence of the buckling of reinforcement is not significant in this case due to the sufficient amount of transverse reinforcement as mentioned previously.

In the experiment of the specimen No.14, combined loading of torsion and bending caused the localized compressive failure due to the stress concentration at the corner of cross section at displacement $8\delta_y$. As a result, the buckling of longitudinal reinforcement and the spalling of cover concrete was locally observed at the corner of cross section. When the column was subjected to further loading, the longitudinal reinforcement started buckling, and consequently, the hook of intermediate ties opened during the cyclic loading at displacement $10\delta_y$.

It is found that the analysis can predict the stiffness, the load carrying capacity, and the cyclic behavior of a RC column after the yielding of longitudinal reinforcement until the lateral load begins to decrease at the displacement of $10\delta_y$. The analytical hysteresis loop shows higher energy dissipation capacity. Here, the pinching behavior is not observed. It is same as the experimental observations. However, the hysteresis loops in the load-displacement curve are found to be slightly larger in the analysis than in the experiment. This is because that the effect of low-cycle fatigue of longitudinal reinforcement is disregarded in the analysis.

When RC columns have the sufficient amount of transverse reinforcements, the buckling length becomes shorter since the transverse reinforcement prevents the buckling of longitudinal reinforcement. Although the low-cycle fatigue is rarely observed in actual earthquake damages, the consideration for the low-cycle fatigue of longitudinal reinforcement is necessary to predict the seismic response of RC structures with higher accuracy.

5.4.4　Effect of torsional behavior on load carrying capacity

In the experiment, to consider the compatibility of proportional torsional deformation to flexural deformation, the combination of torsion and bending is maintained with the control following that the ratio of torsional torque to flexural moment is constant to 15 %. The simulations, in which the ratio of torsional torque to flexural moment varies from 20 % to 50 %, are carried out. In the simulations, the interaction between torsional behavior and flexural behavior of RC columns is investigated by 3D lattice model analysis. The analytical envelope curves of load-displacement relationships for each case are shown in **Figure 5.16**.

As observed in the experiment, the behavior of RC columns subjected to combined loads of torsion and bending can be treated as the behavior under uniaxial cyclic loading when the ratio of torsional torque to flexural moment is 15 %. It is also found that the flexural behavior does not influence until the ratio becomes at least 30 %. Within this range, the behavior shows similar to the one of 15 %, though the maximum load is slightly reduced. On the other hand, when the ratio of torsional torque to flexural moment becomes over 40 %,
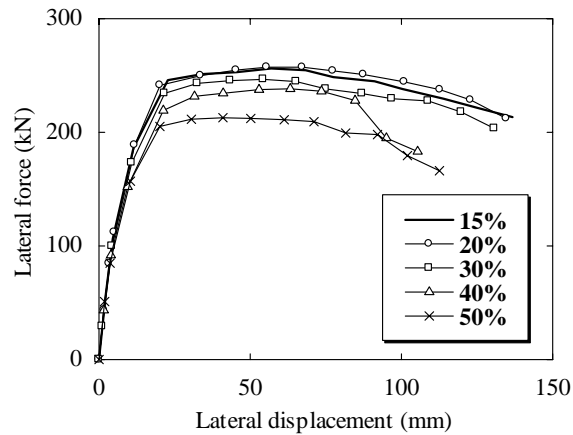
Figure 5.16   Influence of torsional behavior on bending behavior

not only the maximum force but also the deformation capacity decreases even if the RC column is reinforced by the sufficient amount of transverse reinforcement.   The maximum force in the case of 50% is reduced to around 80 % in the case of the uniaxial cyclic loading.

From the comparison between each case, it is found that the lateral force at the same lateral displacement is influenced by torsional deformation.   The remarkable effect on the maximum force and deformation capacity is observed with the increase in the ratio of torsional torque to flexural moment.   This is because of the deterioration of compressive stresses due to both torsion and bending.   It is also found that the interaction between torsion and flexural tension is closely related to the decrease in the yield force and the load carrying capacity with the increase in the torque.

From the analytical discussion, it can be confirmed that the 3D lattice model analysis can appropriately predict the 3D response of RC columns subjected to the combined loading of torsion and bending.   In addition, the combined effect of torsional and flexural deformations on the load carrying capacity and the deformation capacity can be assessed by the simulation.

5.5   Conclusions

In this chapter, the nonlinear analyses of RC beams are performed by using the 3D static lattice model.   As proposed in the previous chapter, in the 3D lattice model, the original shear resisting mechanism is divided into arch and truss actions.

The 3D static lattice model is verified by the experimental results of RC columns subjected to lateral forces from diagonal direction of a section.   The comparison between the

experimental and analytical results shows that the 3D lattice model analysis can successfully predict the behavior of RC columns under bilateral loading.   The analysis is found to be able to predict the severe deterioration in terms of the strain in each element.   In addition, the analysis can explain the influence of loading direction on the cyclic behavior of RC columns quantitatively.   However, the divergence of analytical results from experimental results is observed at large deformation range because of unconsidered matter on the fracture of longitudinal reinforcement due to the low-cycle fatigue.

The analyses by the 3D static lattice model are carried out for RC beams with solid or hollow section subjected to pure torsion and the applicability of the model to the prediction of torsional behavior is confirmed.   In the pre-analysis, it is found that the ratio of an arch part to the cross-sectional width of the beam increases with the increase in the amount of reinforcement.   With appropriate values of t_b and t_d, it is found that the torsional analysis based on 3D lattice model can predict the reasonable torque-twist relationships of solid sectional RC beams including the estimation of the failure mode with the various amount of reinforcement.   By considering the load resisting mechanism represented by arch and truss actions, the analysis can predict reasonable behavior such as the direction of internal flow of forces after the diagonal cracking.   Moreover, the compressive stresses along the diagonal cracks can be evaluated by considering the softening behavior of compressive strength of concrete depending on the transverse tensile strain.

To verify the performance of the 3D lattice model under more general loading condition, the analytical simulation of hollow sectional RC columns subjected to the combined cyclic loading of torsion and bending is carried out.   It is confirmed that the 3D lattice model analysis can appropriately predict the 3D response of RC column subjected to the combined cyclic loads of torsion and bending.   In addition, the effect of combination of torsional and flexural deformation on the load carrying capacity and the deformation capacity can be assessed by the analytical simulation.

References in Chapter 5

[1]   Hsu, T. T. C. (1968): Torsion of Structural Concrete -Behavior of Reinforced Concrete Rectangular Members, *Torsion of Structural Concrete*, ACI SP-18, pp.261-306.

[2]   Kawashima, K. (1991): Effect of Oblique Excitation on Dynamic Strength and Ductility of Reinforced Concrete Bridge Piers, *Civil Engineering Journal*, Public Works Research Center (PWRC), No.33, Vol.8, pp.27-33. (in Japanese)

[3]   Kawashima, K., Hasegawa, K., Nagashima, H., Koyama, H., and Yoshida, T. (1993): Seismic Design Method of Reinforced Concrete Bridge Piers Based on Dynamic Strength and Ductility, *Journal of Research PWRI*, No.190, pp.51-57, May. (in Japanese)

[4]   Nagataki, S., Okamoto, T., Lee, S., and Yamaoka, S. (1986): A Study on Torsional Properties of Reinforced Concrete Members, *Journal of Materials, Concrete Structures and Pavements*, JSCE, No.372/V-5, pp.157-166, August. (in Japanese)

[5]   Niwa, J., Higai, T., and Moriya, N. (1991): Analytical Studies on Reinforced Concrete Linear Members Subjected to Torsion, *Concrete Library of JSCE*, No.18, pp.31-47, December.

[6]   Rahal, K. N. and Collins, M. P. (1995): Analysis of Sections Subjected to Combined Shear and Torsion -A Theoretical Model, *ACI Structural Journal*, Vol.92, No.4, pp.459-469, July/August.

[7]   Takiguchi, K., Kimura, M., Kokusho, S., and Kobayashi, K. (1980): Study on the Restoring Characteristics of Reinforced Concrete Columns to Bi-directional Displacements -Part II Experiments and Analysis-, *Journal of Structural and Construction Engineering*, AIJ, No.296, pp.77-87, October. (in Japanese)

[8]   Yoshimura, M., Aoyama, H., and Kawamura, M. (1980): Analysis of Reinforced Concrete Structure Subjected to Two-dimensional Forces -Part I Analysis of RC Columns Subjected to Biaxial Bending-, *Journal of Structural and Construction Engineering*, AIJ, No.298, pp.31-41, December. (in Japanese)

[9]   Yukawa, Y., Ogata, T., Suda, K., and Saito, H. (1999): Seismic Performance of Reinforced Concrete High Pier with Hollow Section, *Concrete Library of JSCE*, No.34, pp.103-120, December.

6   APPLICATION OF 3D DYNAMIC LATTICE MODEL

6.1   Introduction

In recent years, several significant progresses of the analytical technology for concrete structures have been achieved.   The developments of numerical methods based on concrete mechanics and its application to nonlinear analytical procedure have been also contributed to improve the prediction of RC structural behavior.   Based on the developments of both structural engineering and seismic engineering, the nonlinear dynamic analysis using the strong ground motions of actual earthquakes can be performed even in the practical design. The response of RC columns obtained from the dynamic analysis is rather beneficial from a viewpoint of the restoration or rehabilitation after earthquakes to estimate the state of deformation including the maximum and residual displacements.

In a practice, the structural response is considered by analyzing along the principal axes of structural system.   However, the actual ground motion will generally apply to actual three-dimensional (3D) structures from different directions of their principal axes.   As a result, the behavior of structures along each principal axis might be underestimated.   In these loading conditions, the structure is subjected to combined loads of bilateral bending, shear, and torsion.   Consequently, the behavior becomes more complex than that under the uniaxial motion.   The 3D analysis is indispensable to clarify the seismic performance of RC columns subjected to the multi-directional ground motion.   In addition, the efficient and simple 3D numerical tool with the objective outcomes is required to evaluate the seismic performance of RC columns properly.

In general, the dynamic analysis is performed based on the frame model or the models using the fiber technique.   As for the frame model, the RC structure is modeled into some individual RC beams/columns that incorporate their restoring characteristics.   On the other hand, as for the fiber model, the RC structural member is discretized longitudinally into several layers and each of which is subdivided into some fiber elements.   In these models, the shear failure of the RC structural members cannot directly be predicted because of the limitation of each modeling.   Hence, the 3D analytical method that can predict the shear failure of RC structural members is extremely required.

In this chapter, the 3D lattice model analysis, which has been proposed and verified on the RC structural members in the static analysis, will be extended to the dynamic analysis.

## 6.2 RC Columns Subjected to Seismic Bilateral Loading

6.2.1 Outlines of target RC columns and loading condition

The targets selected for the dynamic lattice model analysis is a series of bilateral shaking table tests (Unjoh et al. 2002) on the large-scale RC columns, as explained below. The experiment was carried out with the specimen, which was a cantilever RC column of square cross-section with 600 mm × 600 mm, the height of 3,000 mm and with a rigid footing. The external bilateral loads acting on the RC column was the inertia force developed by the weight at the top of the column. The details and dimensions of the tested column are shown in **Figure 6.1**. For the material properties of the specimens, the standard cylindrical compressive strength of concrete was 34.1 N/mm^2. The yield strength of longitudinal and transverse reinforcements was 383 N/mm^2 and 350 N/mm^2, respectively. The Young's modulus of both longitudinal and transverse reinforcements was 185kN/mm^2.

The input ground motions were NS and EW components recorded at Takatori Station in Japan during Hyogo-ken Nanbu Earthquake 1995 (**Figure 6.2**). The input ground motion of EW
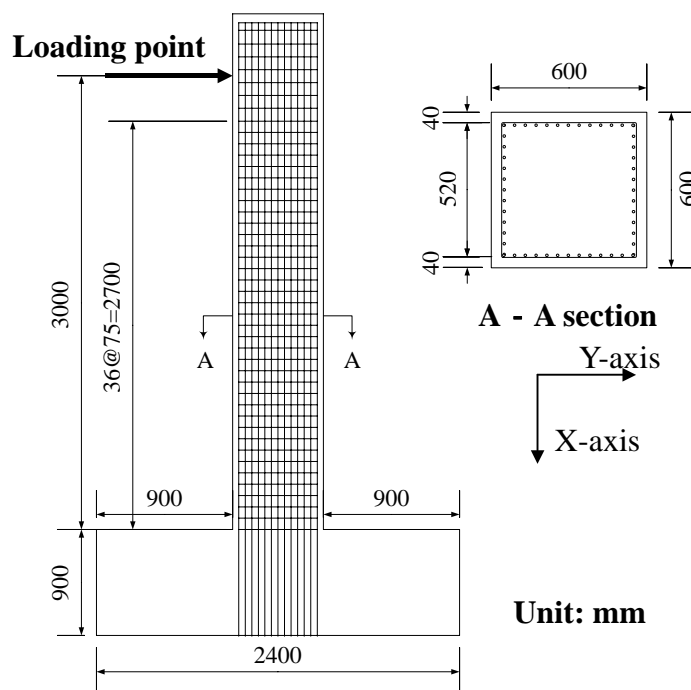
Figure 6.1   Dimensions of the column and loading arrangement
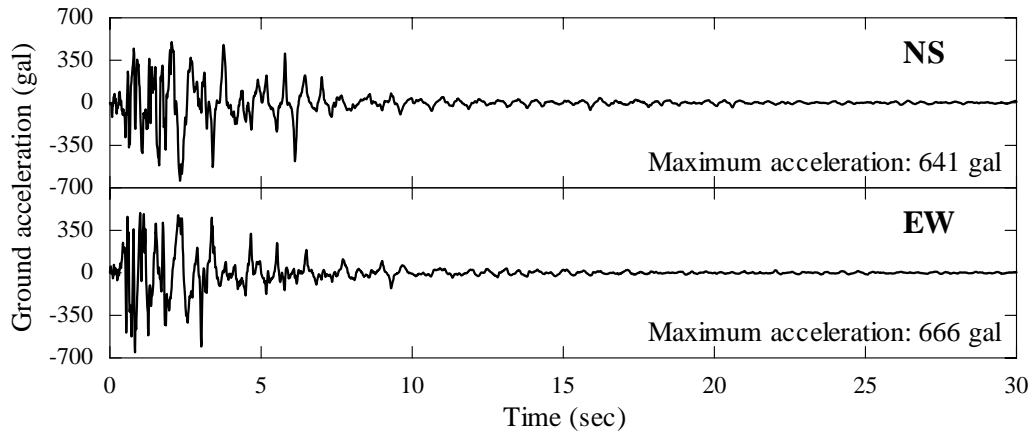
Figure 6.2 Input ground motion recorded at Takatori Station during Hyogo-ken Nanbu Earthquake 1995 (Time axis was condensed to 50 % its original length.)

and NS components were horizontally applied to the direction along X-axis and Y-axis, respectively. In order to make the predominant period of the ground motion closer to the natural period, which is calculated with the initial stiffness of the RC column, the time axis of the motion was condensed to 50 % its original length. The experiments were carried out on two columns subjected to the two levels of maximum accelerations. The maximum acceleration was arranged to be 20 % of original motion with respect to linear level response of the RC column, while 100 % with respect to nonlinear level response of the RC column.

6.2.2   Analytical procedure

The 3D dynamic lattice model used in the analysis for the RC column is shown in **Figure 6.3**. In the analysis, it is assumed that the self-weight of the column is distributed over all nodal points. It is also assumed that a concentrated mass, which is equivalent to the weight of a superstructure, is acting on the top nine nodes of the column. In general, the damping is assumed to be proportional to a combination of the mass and the stiffness matrices, so-called the Rayleigh damping. However, this damping formulation has no physical meaning and may lead to the damping with unexpected vibration mode shapes. From the previous study (Hilber et al. 1977, Sing et al. 1991), it was pointed out that when the factor in the Newmark method, γ was given as the value that was grater than 0.5, the numerical dissipation was present, and consequently it was possible to attain unconditionally stability and a favorable energy dissipation property if $\beta \geq 1/4 \ (\gamma + 0.5)^2$. Therefore, in the analysis, it is assumed that the viscous damping is neglected ($h = 0$). In addition, the numerical damping of the Newmark method with factors $\beta = 0.36$ and $\gamma = 0.70$ is used as time integration (Committee 311 2002). Here, a time interval is set as 0.01 sec. Moreover, since the nonlinear responses

159
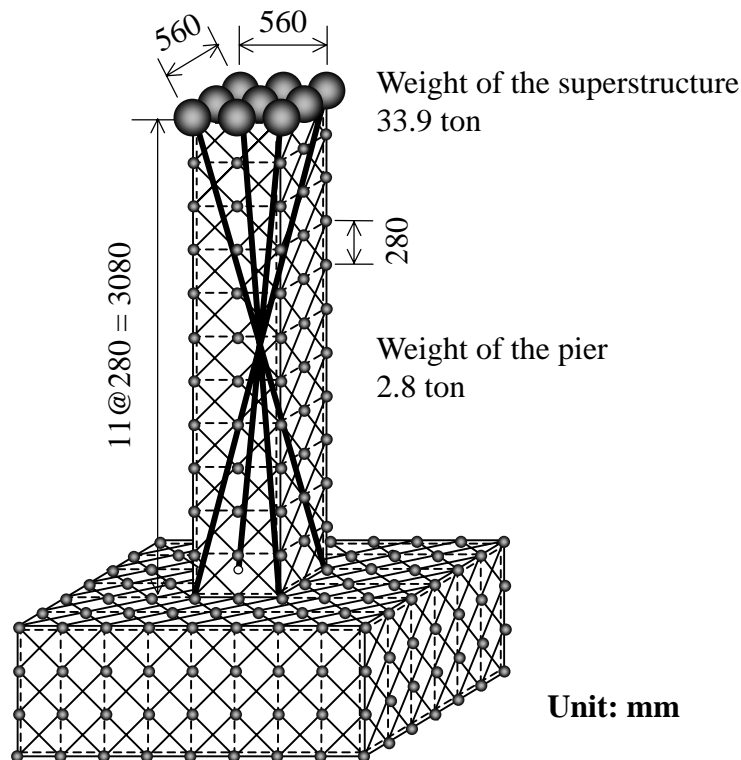
**Figure 6.3**   3D dynamic lattice model

appear when RC structures are subjected to the large ground motions, it is necessary to iterate the calculation until a sufficiently converged solution is obtained.   In this study, the Newton-Raphson iteration method is used to iterate until an adequately converged solution is obtained. In order to check the convergence, the out-of-balance force and the energy increment are compared with each initial value during the iteration.   The convergence tolerances for the out-of-balance force and energy are set at 0.001 and 0.01, respectively.

6.2.3   Analytical results and discussions

The hysteresis loops, which are the relationships between the acceleration and the horizontal displacement at the center of gravity of the weight (a superstructure), are shown in **Figure 6.4** in the case of 20 % level motion and in **Figure 6.5** in the case of 100 % level motion.   These are equivalent to the relationship between the lateral force and the lateral displacement at top of the column, because the product of the acceleration and the mass of a superstructure (33.9 ton) is considered as the lateral force.   The experimental and analytical results of displacement time histories at the top of the column subjected to the bilateral loading are illustrated in **Figure 6.6**.
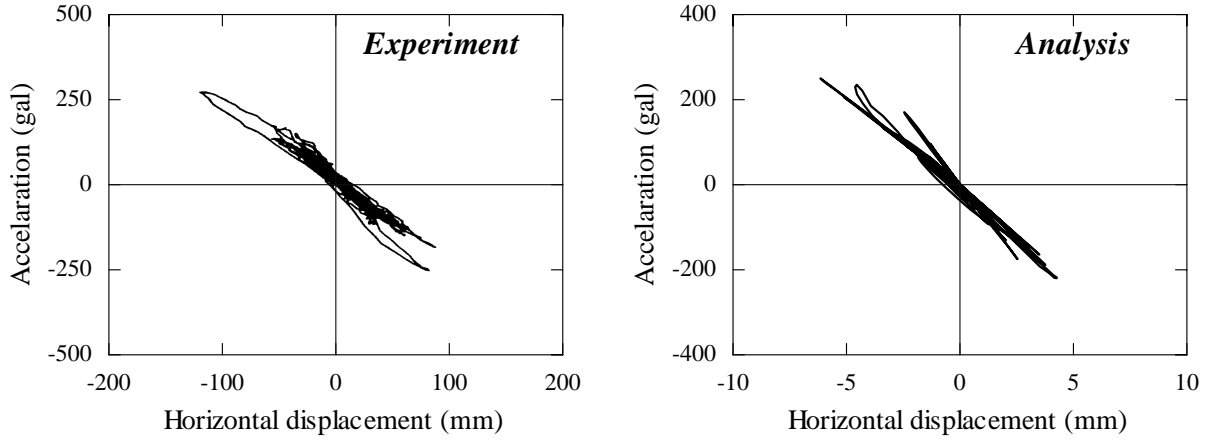
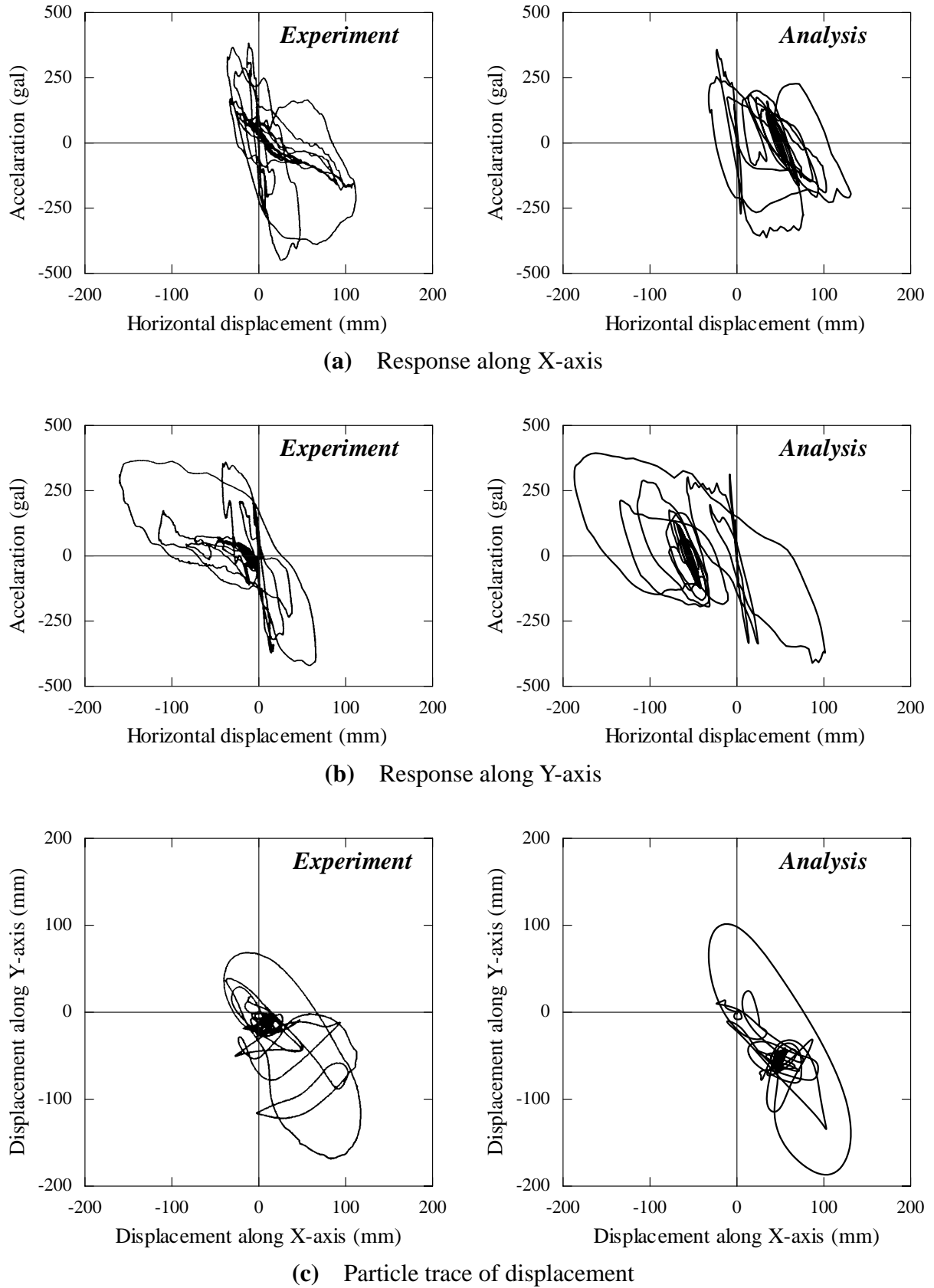(a)   Response along X-axis
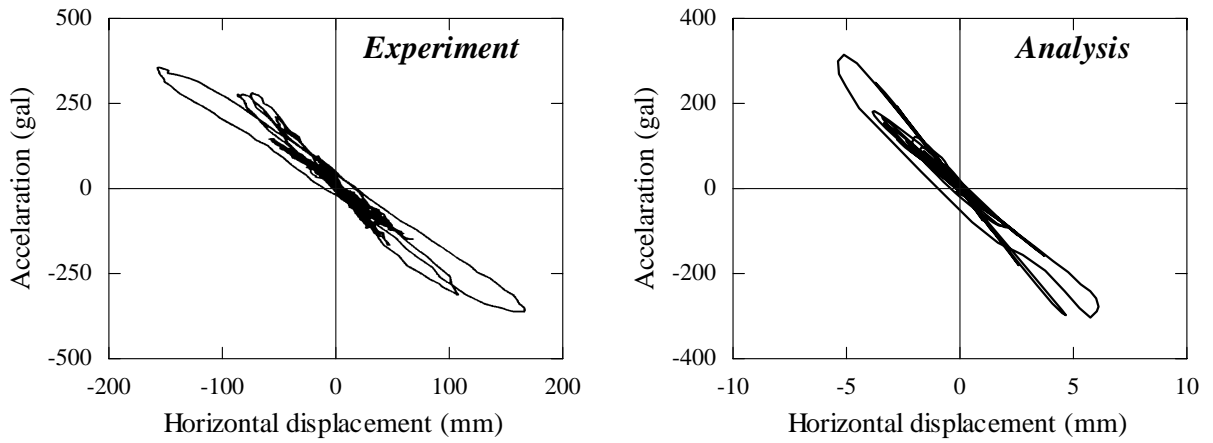
(b)   Response along Y-axis
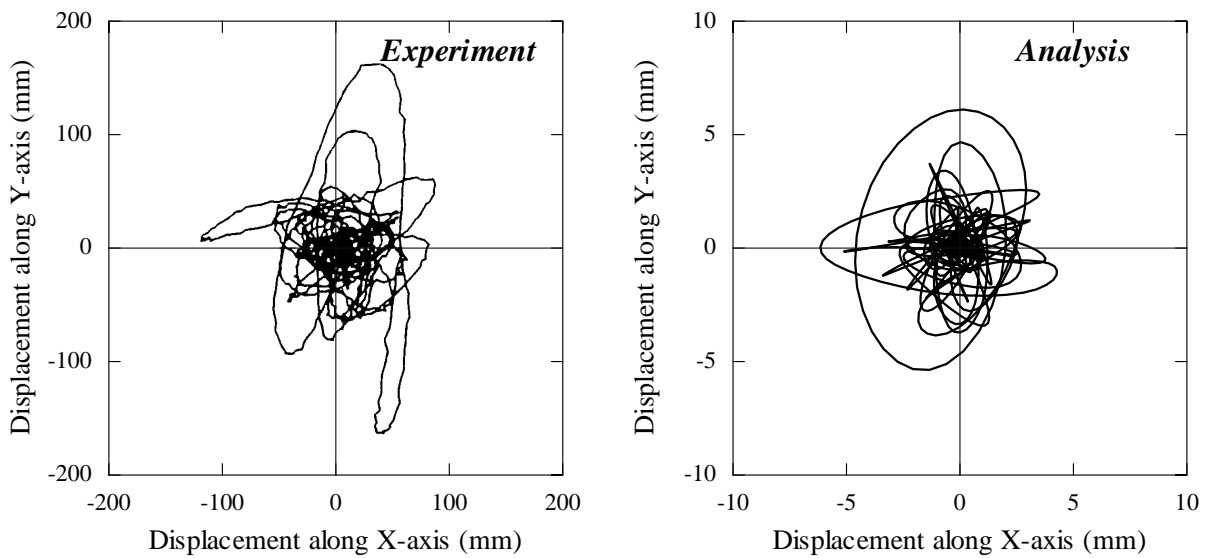
(c)   Particle trace of displacement

Figure 6.4   Comparison with results of bilateral shaking table test and the 3D lattice model analysis (20% level motion)

(a) Response along X-axis

(b) Response along Y-axis

(c) Particle trace of displacement

Figure 6.5   Comparison with results of bilateral shaking table test and the 3D lattice
model analysis (100% level motion)
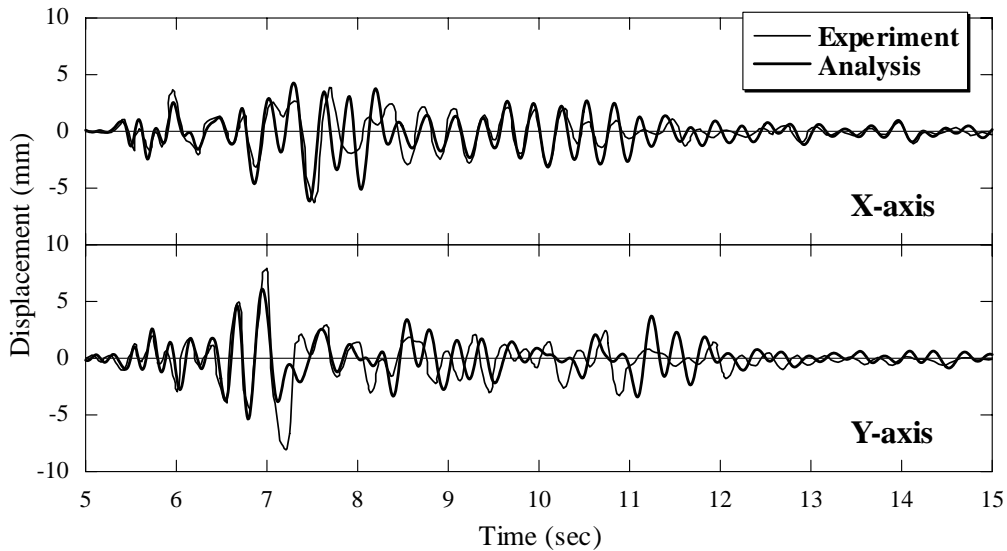
(a) 20% level motion
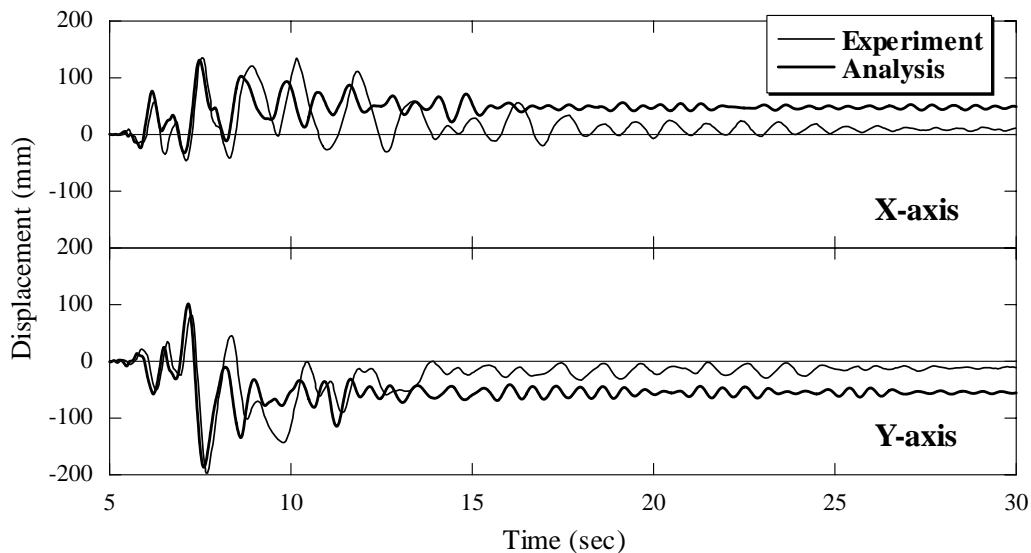
(b) 100% level motion

Figure 6.6 Displacement time histories of the bilateral shaking table test and the 3D lattice model analysis

As for the first low-level shaking (20%), the experimental results indicate the linear response. It can be observed in **Figure 6.4 (b)** that the response along the Y-axis, in which the larger amplitude of acceleration is applied, show slight loops in the hysteresis curves in both experiment and analysis. This is due to the minor cracking at the bottom end of the column. The analytical results from the 3D dynamic lattice model show the good agreement with the experimental results. However, the analytical initial stiffness found to be slightly higher than that in experimental results. This is caused by that the cylindrical strength of concrete is slightly higher than the actual strength of concrete in a RC column. In order to predict the behavior with high accuracy, the dispersion due to the material heterogeneity has to be

considered in the analysis.

In the second shaking test on the full level acceleration, the analytical and experimental results are also found to show the good agreement with each other.   The relationships of the acceleration-displacement in X- and Y-axes of the experiment and analytical results show the curves with higher energy dissipation.   In the analysis, the buckling of reinforcement takes place in 280 mm range from the bottom end of the column.   This is corresponding to the experimental fact.   The buckling length between 300 mm and 400 mm at the bottom of the column is recognized in the experimental observation.   Consequently, the cyclic loops in the acceleration-displacement curves show the smaller energy dissipation capacity after the occurrence of buckling, in both experimental and analytical results.   However, the analytical stiffness after the displacement reached the maximum is predicted stiffer than the experimental one.   This is caused by that the stress-strain model of concrete is not realistic due to the assumption for the stiffness of concrete under reversed cyclic loading.   It is necessary to improve the stress-strain model of concrete including cyclic relationship to obtain accurately predicted results.

As can be seen in **Figure 6.6**, the analytical displacement time histories in both X-axis and Y-axis are also found to be close to the experimental results until the maximum displacement. However, the divergence between the experimental and analytical results is recognized after the first seven seconds.   These are because of the differences for the stiffness of an RC column during the vibration.   The analytical stiffness is higher than that in the experiment since the stiffness in the stress-strain model under cyclic loading is assumed to be the initial stiffness.

Through above discussions, it is confirmed that the newly developed 3D lattice model analysis can predict the biaxial seismic behavior of RC columns subjected to the bilateral ground motions.   The further development to a nonlinear analytical tool for the evaluation of performance of RC structures subjected to general loading patterns will be conducted in the future studies.

6.3   Simulation of RC Columns Subjected to Multi-directional Loading

### 6.3.1   Outlines of experiment and analysis

In order to verify the performance of the dynamic 3D lattice model, the pseudo-dynamic loading test conducted by Osada et al. (1997) is used for the comparison.   The specimen is a cantilever RC column with rectangular cross section and a sufficiently stiff footing as shown in **Figure 6.7**.   The arrangement of reinforcement and loading conditions are also illustrated
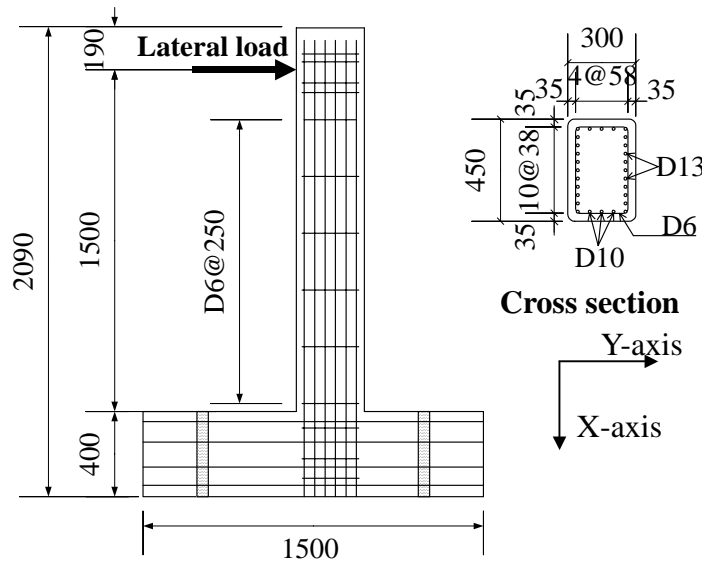
Figure 6.7   Details of a specimen and arrangement of reinforcement

in the figure.   The material properties of concrete and reinforcement are shown in **Table 6.1**.
The load is applied at the height of 1,500 mm from the top of footing.   For the input motion,
NS component recorded at Kobe Marine Meteorological Station in Japan at Hyogo-ken
Nanbu Earthquake (the maximum acceleration of NS component is 818 gal) is used.   In the
experiment, the maximum amplitude of the input ground acceleration was modified to be 298
gal.   The input ground acceleration is shown in **Figure 6.8**.   The duration period of input
acceleration was used as 15 seconds including the principal motion and the acceleration peak
of the earthquake.   The parameters and the initial input data are shown in **Table 6.2**.
During the test, a constant axial compressive load of 79.7 kN (0.59 N/mm^2 in compressive
stress) was maintained at the top of the column.

In addition, two kinds of simulations using the 3D dynamic lattice model are carried out.
The first one deals with the simulation for RC columns subjected to the motion from various
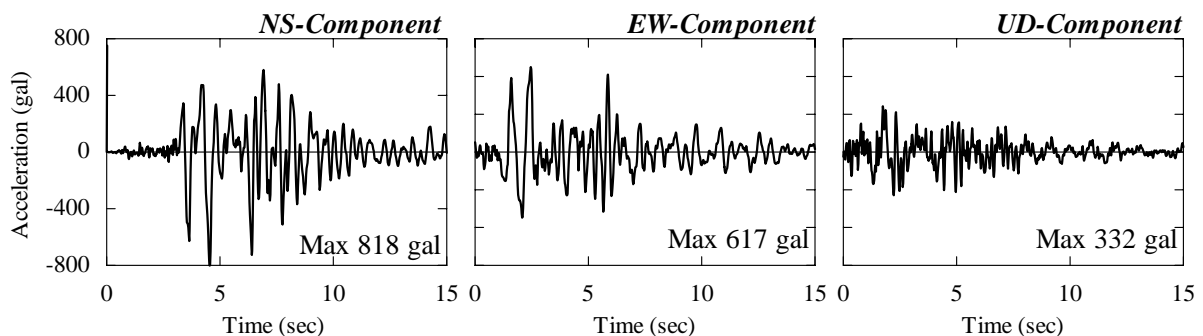
Figure 6.8   Input ground motion (Hyogo-ken Nanbu Earthquake 1995)

165

Table 6.1   Material properties

Concrete	Reinforcement			
$f_c{'}$ (MPa)	Grade	f_y (MPa)	f_u (MPa)	E_s (GPa)
	SD295 D6	360	530	175
27.0	SD295 D10	350	500	172
	SD345 D13	380	560	172

Table 6.2   Initial conditions in pseudo-dynamic loading tests

Mass (ton)	Damping coefficient, h	Yield displacement (mm)	Maximum acceleration (gal)
42	0.03 (After yielding; $h = 0$)	13.9	298

directions.   The second one is related to the simulation of RC columns subjected to 3D simultaneous seismic loads including NS, EW, and UD components of earthquake motion.

In the analysis using the motion from various directions, the directions of loading are set in five cases, such as θ is equal to 0°, 22.5°, 45°, 67.5°, and 90°, where θ indicates the inclined angle to the principal axis.   The input ground acceleration is NS component of Hyogo-ken Nanbu Earthquake as previously shown in **Figure 6.8**, in which the maximum acceleration is modified to be 298 gal.

As for the 3D seismic loading, the input ground motions recorded at Hyogo-ken Nanbu Earthquake that are NS, EW, and UD components as previously shown in **Figure 6.8** are used. The maximum accelerations of NS, EW, and UD components are set to be 409 gal, 309 gal, and 166 gal, respectively.   Here, it is assumed that the ground motion of EW and NS components is applied to the direction along X- and Y-axes in the cross section, respectively.

3D lattice model used to analyze the test specimen is shown in **Figure 6.9**.   In the dynamic analysis, it is assumed that RC bridge piers are connected to a sufficiently stiff footing.   It means that the design ground acceleration directly inputs to the bottom of the pier.   In this analysis, in order to simulate RC bridge piers subjected to reversed cyclic loading, four arch members are considered as mentioned in the previous section.   Since the RC bridge pier is a cantilever type, each arch member is set to be connecting from the loading point to the bottom of piers on the opposite side.
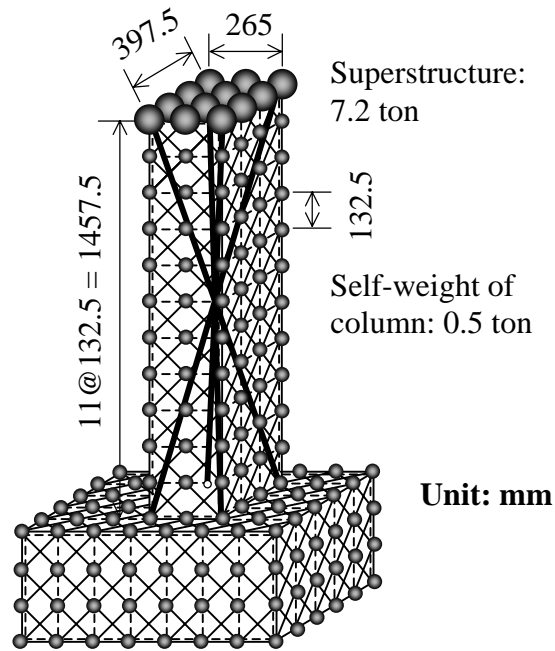
**Figure 6.9** 3D dynamic lattice model

In the analysis, it is assumed that the self-mass of a pier is concentrated at each nodal point based on the idealization of lumped-mass. It is also assumed that the concentrated mass, which is equivalent to the weight of a superstructure (412 kN), is acting to the top of the column. Newmark's β-method ($\beta = 0.25$) with a time spacing of 0.01 second is applied. The damping is introduced by using viscous forces, which are generated from a global damping matrix. Here, the global damping matrix can be obtained by a linear combination of the global stiffness matrix and the mass matrix, which is so-called Rayleigh damping. In the analysis, the damping coefficient is assumed to be 2.0 %.

6.3.2   Comparison with pseudo-dynamic loading tests

The hysteresis loops and the time histories of displacement response at the top of the pier are illustrated in **Figures 6.10** and **6.11**, respectively. Here, the hysteresis loops are defined as the relationships between the lateral force and lateral displacement at the top of the column. One of the examples for the deformed shape of the 3D lattice model with buckling of reinforcing bars is illustrated in **Figure 6.12**. As can be seen from these figures, the results of 2D and 3D analyses are found to be in the good agreement with each other. As can be seen in **Figure 6.12**, the buckling of longitudinal reinforcement at the bottom of the column is also predicted in the analysis. In addition, after the buckling of reinforcement occurs, the analytical results indicate the decrease in the energy dissipation capacity. These analytical responses show the good agreement with the experimental results. Therefore, it is confirmed that 3D lattice model analysis can accurately predict the overall behavior of RC columns
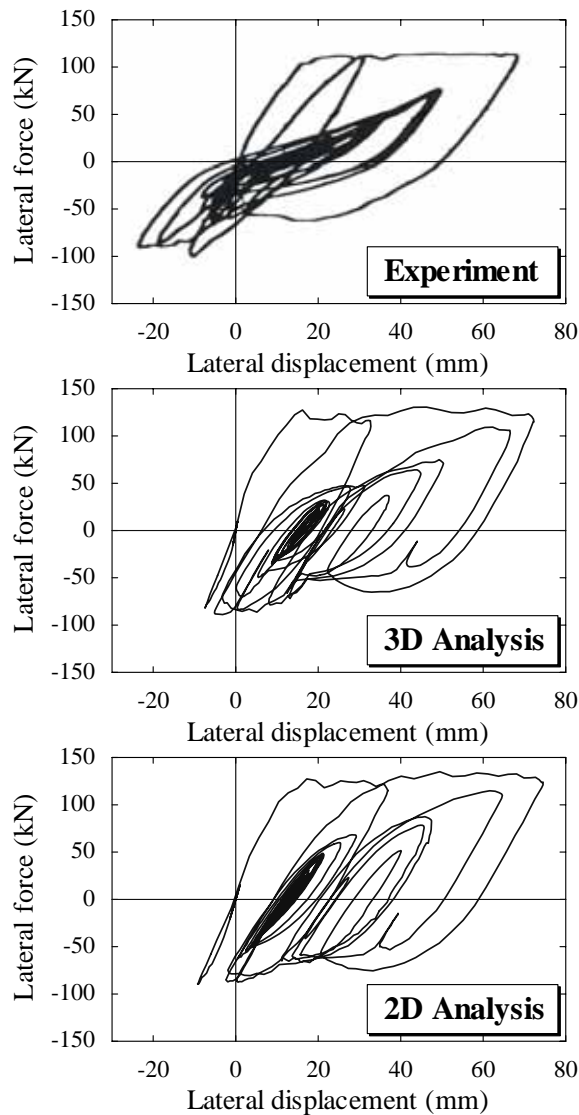
**Figure 6.10** Hysteresis loops (comparison between 3D and 2D analyses)
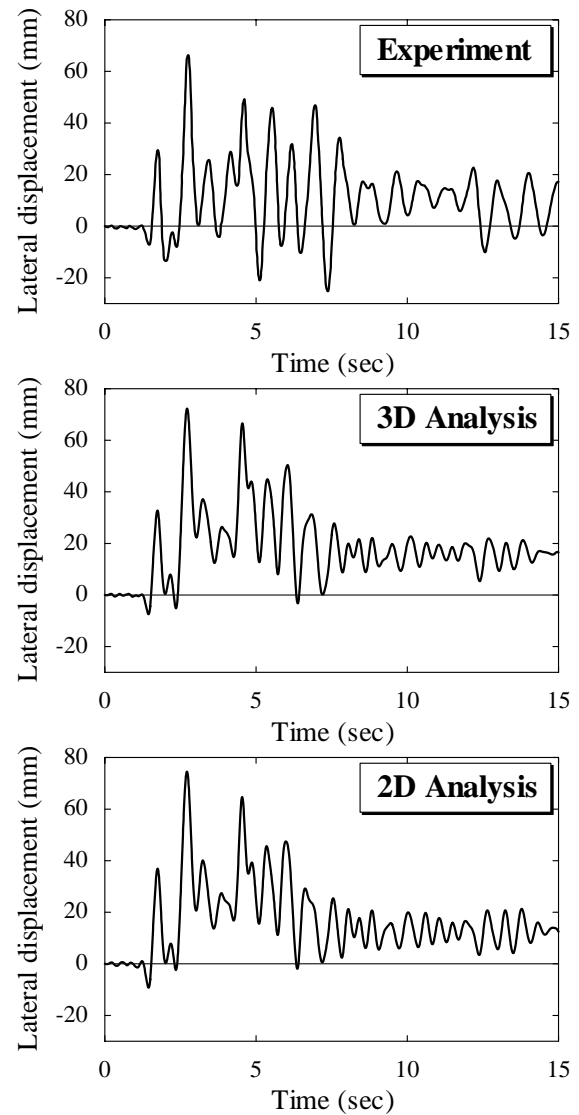
Figure 6.11 Displacement time histories

including the post-peak behavior with same accuracy to 2D analysis. In addition, it can be confirmed that the 3D lattice model analysis predict the response of RC columns under the uniaxial earthquake motion, including the residual displacement and the deformation capacity.

6.3.3 Effect of direction of motion on analytical response

To verify the seismic performance of RC columns subjected to the ground motion in two independent directions, the 3D analyses are carried out. RC columns are identical to ones used in the analysis of **section 6.3.2**. The input ground motion is shown in **Figure 6.8**. The directions of loading are set in five cases, such as θ is equal to 0°, 22.5°, 45°, 67.5° and 90°, where θ indicates the inclined angle to the principal axis. The magnitudes of ground motion
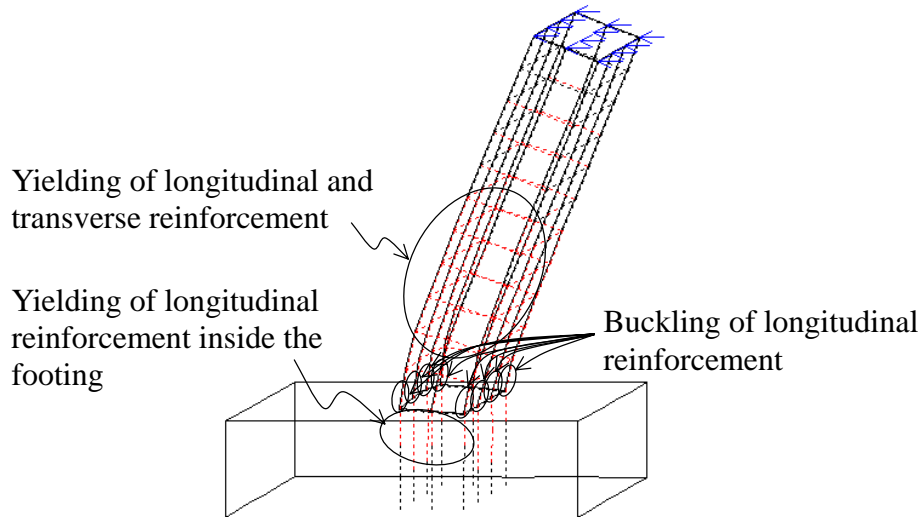
Figure 6.12   Deformed shape by the 3D lattice model considering buckling of longitudinal reinforcement

in X- and Y-axes are determined from **Equation 6.1**.

$$f_x(t) = f(t) \cdot \sin\theta, \quad f_y(t) = f(t) \cdot \cos\theta \tag{6.1}$$

where, $f(t)$, $f_x(t)$, and $f_y(t)$ means the magnitude of ground motion, the magnitude of component along with X-axis (the transverse direction as shown in **Figure 6.7**), and the magnitude of component along with Y-axis (the longitudinal direction), respectively.

The maximum displacement responses of RC columns subjected to ground motion in the inclined direction are shown in **Figure 6.13**.   The magnitude of ground motion is determined from **Equation 6.1**.   Although the direction of applied ground motion is varied for each case, the magnitude of amplitude of input ground motion is identical to that in each loading direction.   Consequently, the applied energy is also identical to each other.   However, as can be observed from **Figure 6.13**, the loading direction affects on the maximum response of displacement.   It is expressed that the flexural strength of RC columns with rectangular cross section subjected to biaxial bending is different depending on each principal axis.   Hence, the maximum displacement response along Y-axis in the case of $\theta = 0°$ is larger than that along X-axis in the case of $\theta = 90°$.

The analytical results of relationships between X- and Y-displacement responses of RC columns subjected to the motion from diagonal direction are shown in **Figure 6.14**.   Two circles centered at the origin with δ_{xmax} or δ_{ymax} as the radius, respectively, are drawn in **Figure 6.14**.   Here, δ_{xmax} and d δ_{ymax} are the maximum displacement responses in X-axis and
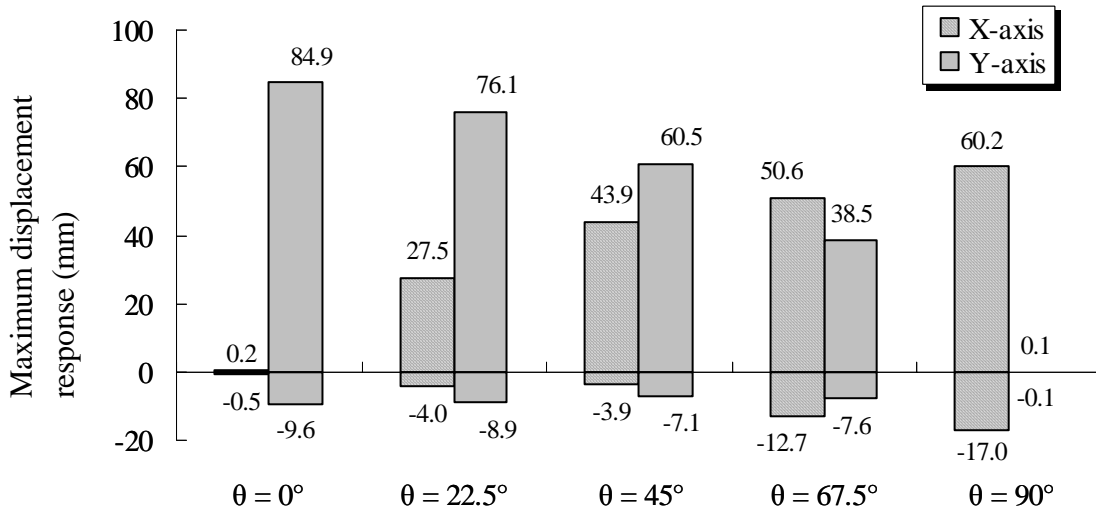
Figure 6.13   Maximum displacement responses of RC columns subjected to ground
motion from various directions

Y-axis.   In addition, the ellipse that is centered at the origin with δ_{ymax} as a major axis length
and δ_{xmax} as a minor axis length is drawn in the figure.   As can be seen from **Figure 6.14**, the
maximum displacement can be predicted approximately in terms of the ellipse in the case of θ
= 22.5° and 45°, while becomes smaller in the case of $\theta = 67.5°$.   Moreover, it is found that
when the inclined angle between the loading direction and X-axis becomes larger, the
discrepancy of responses from the loading direction increases and the column shows the
round behavior.   Especially, the behavior of RC column in the case of $\theta = 67.5°$ seems to be
complex.   It is found that the maximum displacement response of RC columns subjected to
the diagonal direction cannot be simply predicted from the calculation in 2D analysis.
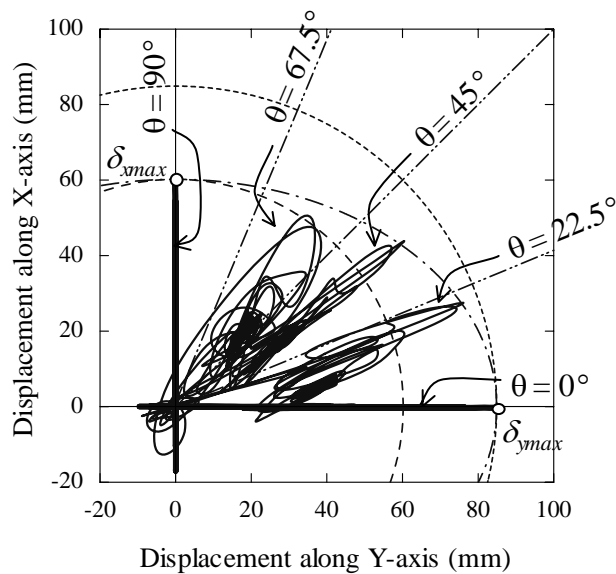

Figure 6.14   Relationship between X- and Y-directional displacements

Moreover, it is confirmed that the 3D lattice model analysis can reasonably predict the biaxial seismic behavior of RC columns subjected to ground motion from the diagonal direction.
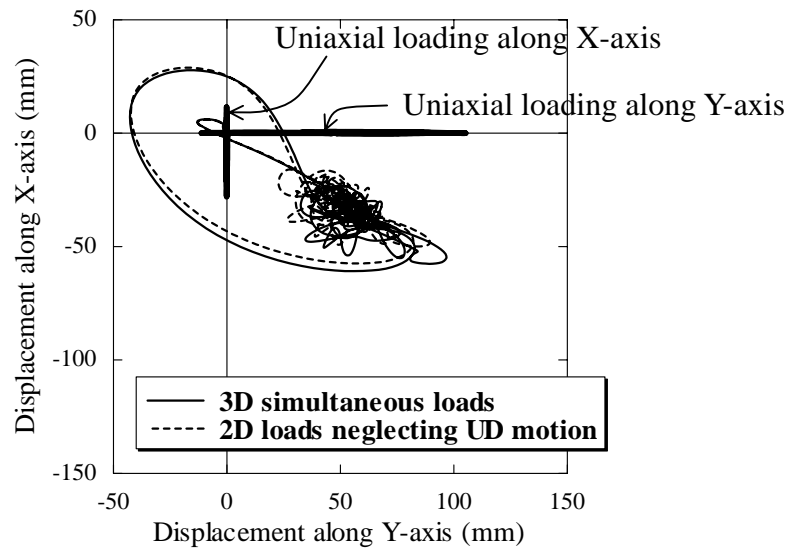
6.3.4 Simulation using 3D earthquake motion

The analytical results of displacement time histories at the top of the column subjected to 3D simultaneous loads or 2D bilateral loads neglecting UD motion are illustrated in **Figure 6.15**. From the results of the 3D lattice model analysis, the maximum displacement of a column subjected to 3D simultaneous loading is larger than that under bilateral loading. As for the residual displacement, there is similar tendency in the cases of columns subjected to 3D simultaneous loads or 2D bilateral loading. Comparing with the case of neglecting UD motion, only a slight increase in the residual and the maximum displacements can be
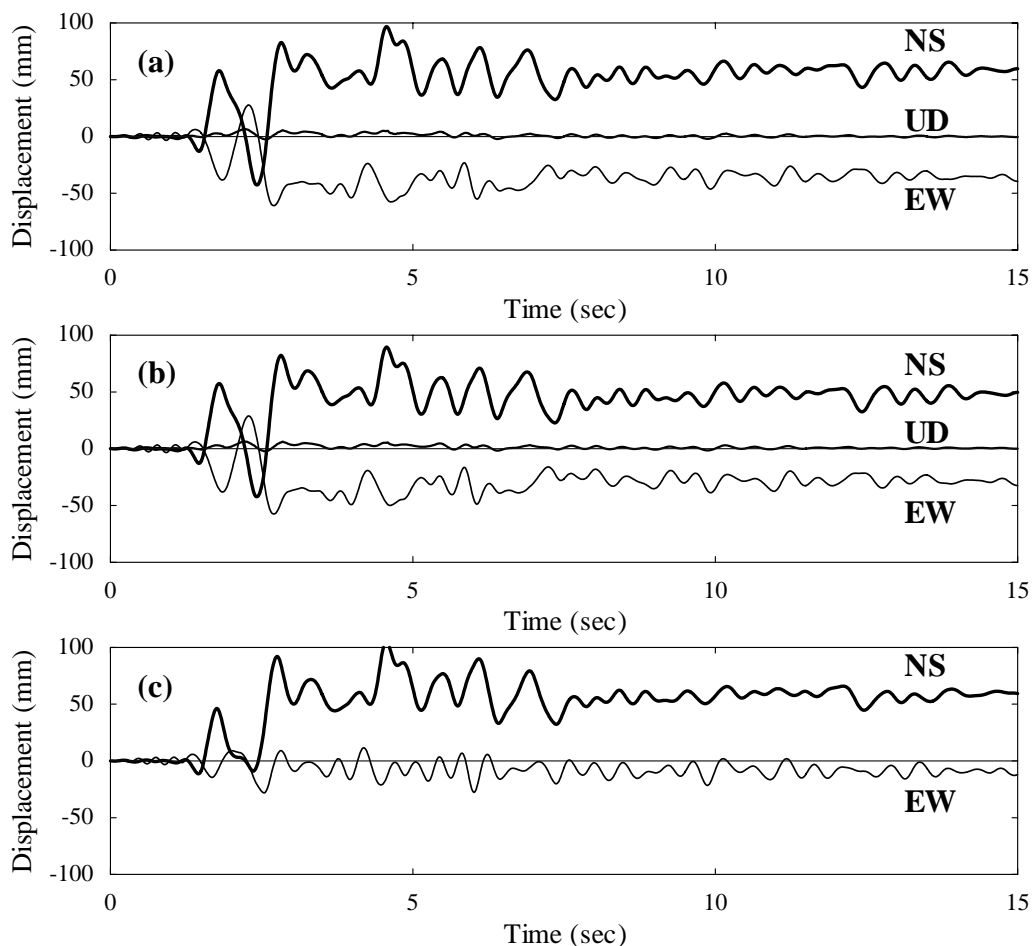
Figure 6.15 Displacement time histories at the top of the column subjected to
(a) 3D simultaneous loading including NS, EW, and UD motions,
(b) 2D biaxial loading along principal axes of cross-section, and
(c) uniaxial loading independently along principal axes of cross-section

Figure 6.16 Particle trace of displacements at the top of the column

observed in the analytical results including UD motion, as shown in **Figures 6.15 (a)** and **(b)**. The analytical result in the case of uniaxial loading shows the smaller displacement response than that in the case of 3D simultaneous loads or 2D bilateral loading.

The analytical results of the particle trace of displacement at the top of a column are shown in **Figure 6.16**. The result shows the relationship between displacements along the principal axes of a column. The response of a column subjected to 3D simultaneous loading, 2D bilateral loading, or uniaxial loading independently along the principal axis of a column is illustrated in this figure. As can be seen from the figure, the maximum displacement under 3D simultaneous loading is larger than that under uniaxial loading along its principal axis. Although current standard specifications permit to analyze the response along each principal axis of a structure independently, the response of a RC column subjected to biaxial bending cannot be completely estimated by the 2D analysis under the uniaxial bending.

The hysteresis loops, which are the relationships between base shear force and the top horizontal displacement during initial four seconds are shown in **Figure 6.17**. The effects of biaxial loading on deformation capacity are particularly evident in the rectangular cross-sectional columns in which the stiffness of column is different depending on each principal axis. The interaction effects are recognized in rectangular columns because of the ellipsoidal shape of interaction surface for its failure condition under biaxial bending and axial load. When a rectangular structural member due to the increase in the bending along strong axis yields, the plastic deformation will become large in the weak axis direction according to the ellipsoidal shape of the failure surface. Therefore, the yielded rectangular columns may maintain the flexural resistance capacity along their strong axis but may

172
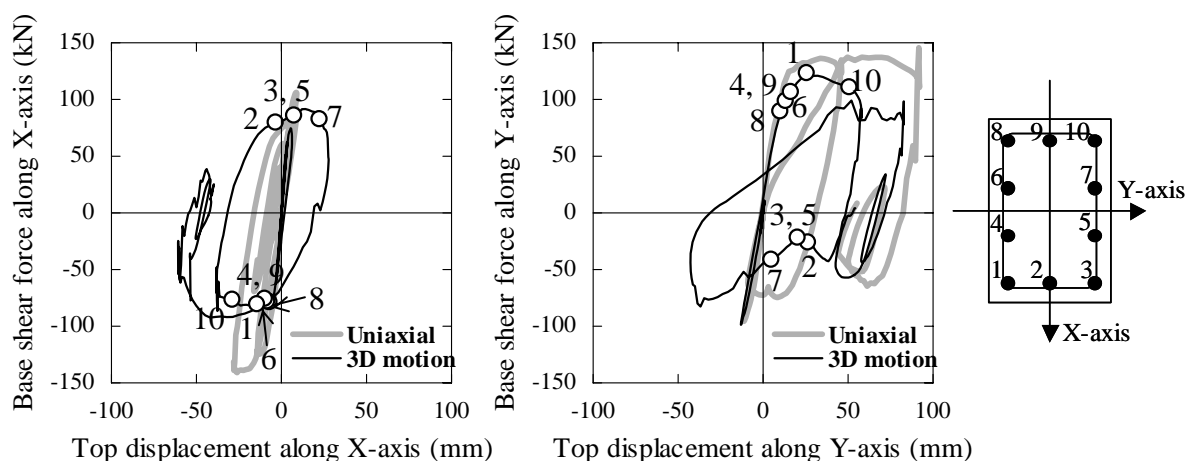
Figure 6.17   Base shear force-top horizontal displacement relationships in case of 3D loading or uniaxial loading during initial 4 seconds

decrease the load carrying capacity in the direction of weak axis.

Hence, it is found that the maximum displacement response of RC columns subjected to ground motion from diagonal direction cannot be simply predicted from the calculation in 2D analysis.   The response in 2D analysis is considered in two orthogonal directions independently.   Moreover, it is confirmed that the 3D lattice model analysis can reasonably predict the biaxial seismic behavior of RC columns subjected to ground motion from the diagonal direction of cross section.

6.4   3D Dynamic Analysis Using Several Earthquake Motions

6.4.1   Introduction

In the previous discussion in **section 6.3**, the validity and applicability of 3D lattice model analysis is confirmed by the verification using the results of bilateral shaking table tests. Here, time-history response analysis using several kinds of strong-motion records as input earthquake motion will be performed to evaluate the seismic performance of RC bridge piers.

It is quite rare that the ground acceleration at a construction site of target RC structures is recorded.   The designer should carefully select the design earthquake motion that adequately represents the ground motion expected at a particular site and in particular the motion that would drive the structure to its critical response, resulting in the highest damage potential. However, the quantification of such ground motion is comparatively difficult.   It requires a sufficient understanding of ground motion parameters, which characterize the severity and the damage potential of the earthquake ground motion (JSCE 2002).   Since these are the

parameters most often associated with the severity of ground motion, the recommendations for the choice of ground motion are on the peak ground acceleration, frequency content, and duration.

The seismic performance verification should be carried out based on the several earthquake motions because the period, the amplitude, the phase, and the frequency of input acceleration influenced the seismic response of structures. Here, near-fault ground motion results in a sudden burst of energy into a structure, in which the energy must be dissipated immediately. This is usually characterized by a single unidirectional large excursion. On the other hand, the sinusoidal type ground motion with longer duration requires a more steady dissipation of energy over a longer period with numerous yield reversals. The dynamic response analyses using these motions are quite useful to obtain the seismic response characteristics of structures.
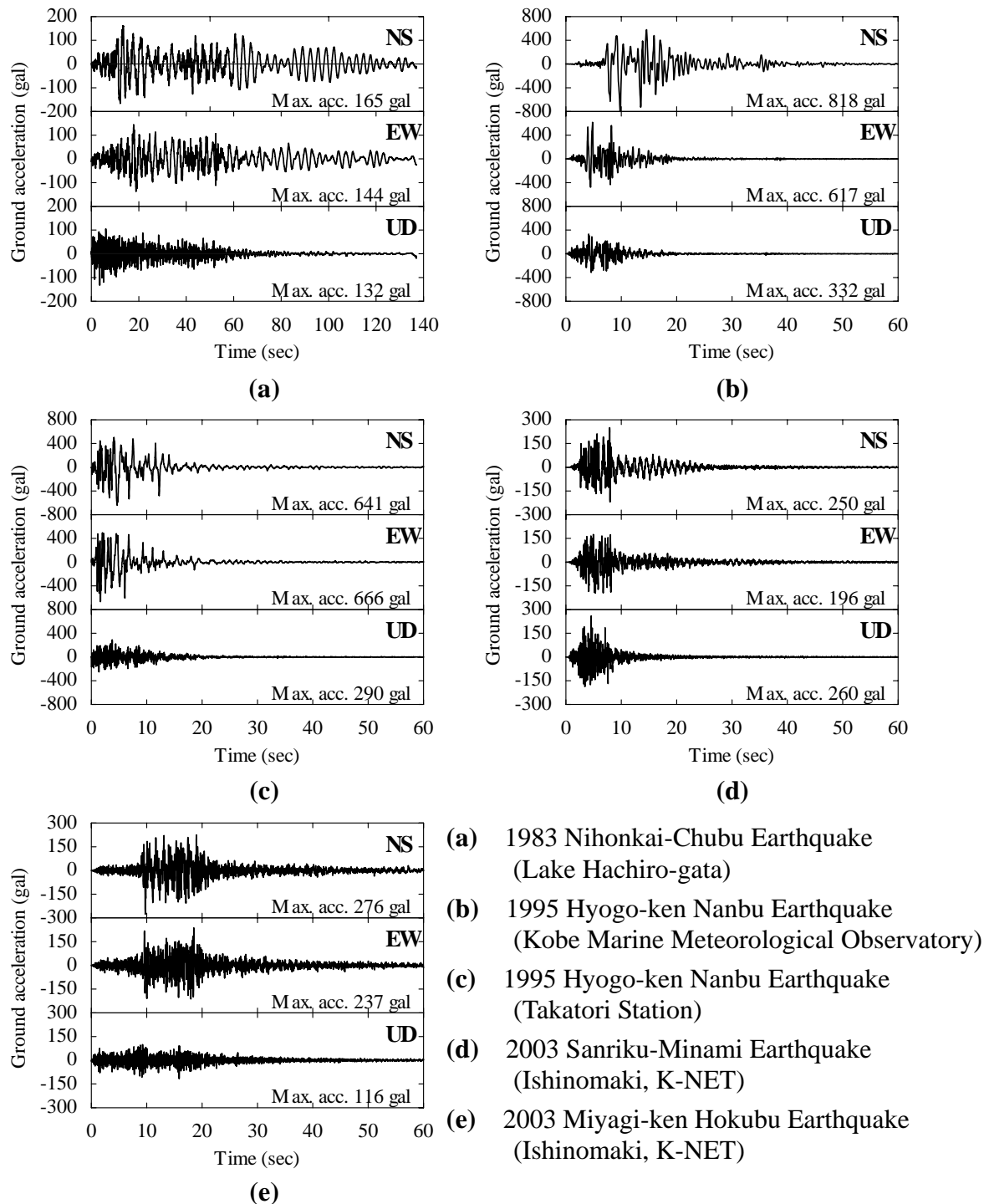
Hence, time-history response analysis using several kinds of strong-motion records is performed in which the strong earthquake motions, such as 1983 Nihonkai-Chubu Earthquake, 1995 Hyogo-ken Nanbu (Kobe) Earthquake, 2003 Sanriku-Minami Earthquake, and 2003 Miyagi-ken Hokubu Earthquake, are used.

6.4.2   Feature of accelerations used in seismic performance verification

The analytical target is a RC column previously used in **section 6.2** (**Figure 6.1**). The input ground motions using in the dynamic analysis are illustrated in **Figure 6.18**.

For Case A, NS, EW, and UD components of 1983 Nihonkai-Chubu Earthquake (**Figure 6.18 (a)**) are used as the input accelerations. The peak accelerations are 165 gal, 144 gal, and 132 gal, respectively. Here, the peak accelerations of each component are similarly arranged following NS component (165 gal) to be 400 gal. In addition, the time axis of motion is condensed by 50 %. The main significant characteristics of this ground motion are the long duration of the principal motion and acceleration peaks that occur at 20 seconds and 50 seconds after the start.

In Case B and Case C, NS, EW, and UD components recorded at Takatori Station and Kobe Marine Meteorological Observatory in Japan at 1995 Hyogo-ken Nanbu (Kobe) Earthquake (**Figures 6.18 (b), (c)**) are used. Here, the peak accelerations of each component are similarly arranged following NS component (641 gal at Takatori Station, and 818 gal at Kobe Marine Meteorological Observatory) to be 450 gal. This kind of motion is classified to the near-field earthquake motions, which consist of a short duration and strong directivity and contain a low frequency impulse in the acceleration.

(a) 1983 Nihonkai-Chubu Earthquake
     (Lake Hachiro-gata)

(b) 1995 Hyogo-ken Nanbu Earthquake
     (Kobe Marine Meteorological Observatory)

(c) 1995 Hyogo-ken Nanbu Earthquake
     (Takatori Station)

(d) 2003 Sanriku-Minami Earthquake
     (Ishinomaki, K-NET)

(e) 2003 Miyagi-ken Hokubu Earthquake
     (Ishinomaki, K-NET)

Figure 6.18   Input ground motions using in the dynamic analysis

In Case D and Case E, NS, EW, and UD components recorded at Ishinomaki (K-NET) at 2003 Sanriku-Minami Earthquake and 2003 Miyagi-ken Hokubu Earthquake (**Figures 6.18 (d), (e)**) are used.   The peak accelerations of each component are similarly arranged following NS component (250 gal in Sanriku-Minami Earthquake motion and 276 gal in Miyagi-ken Hokubu Earthquake motion) to be 400 gal.   The basic features of these motions are the long duration of the principal motion with a significantly high frequency.
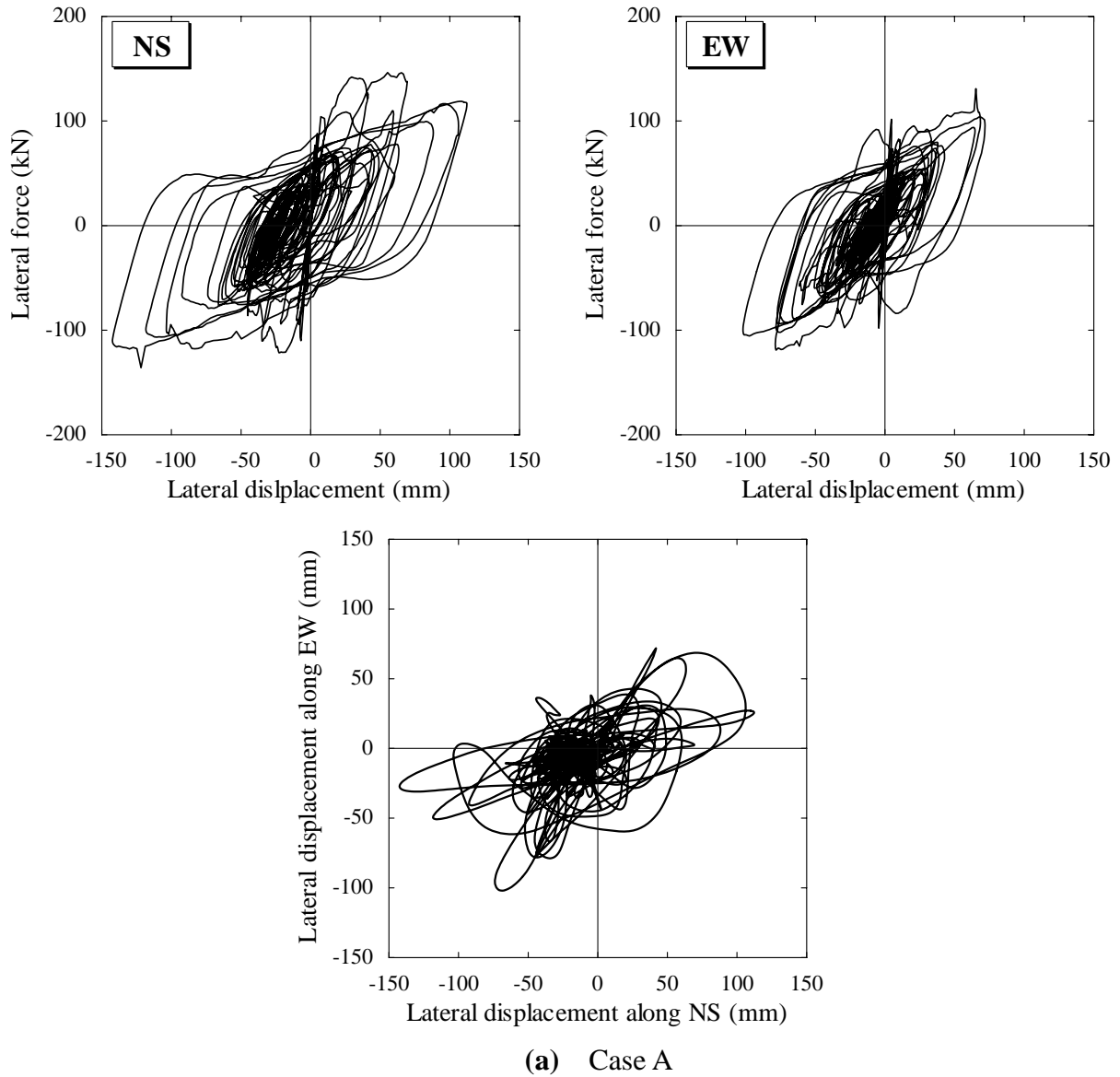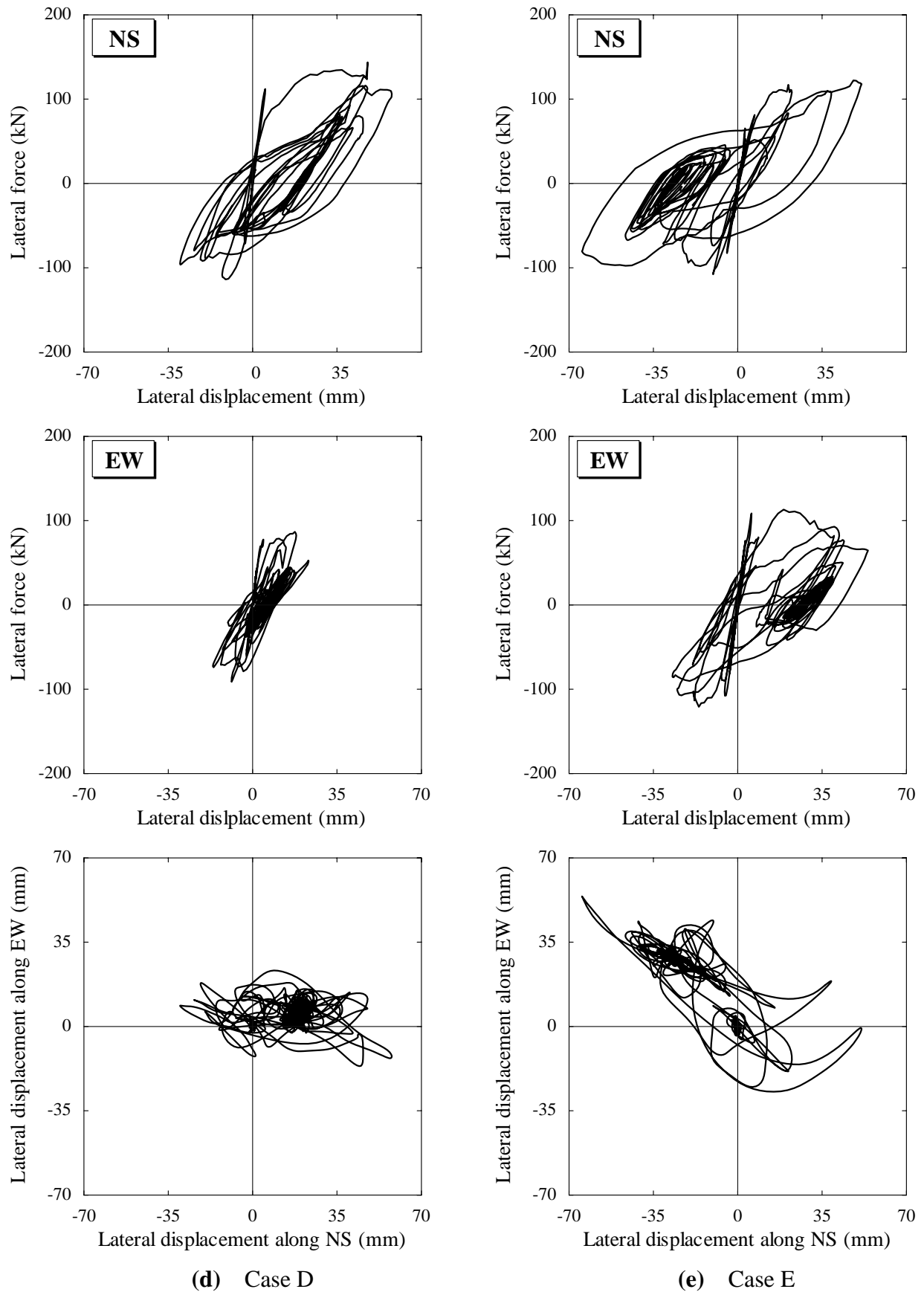
(a) Case A

Figure 6.19 Analytical responses by the 3D dynamic lattice model for RC bridge piers subjected to earthquake motions
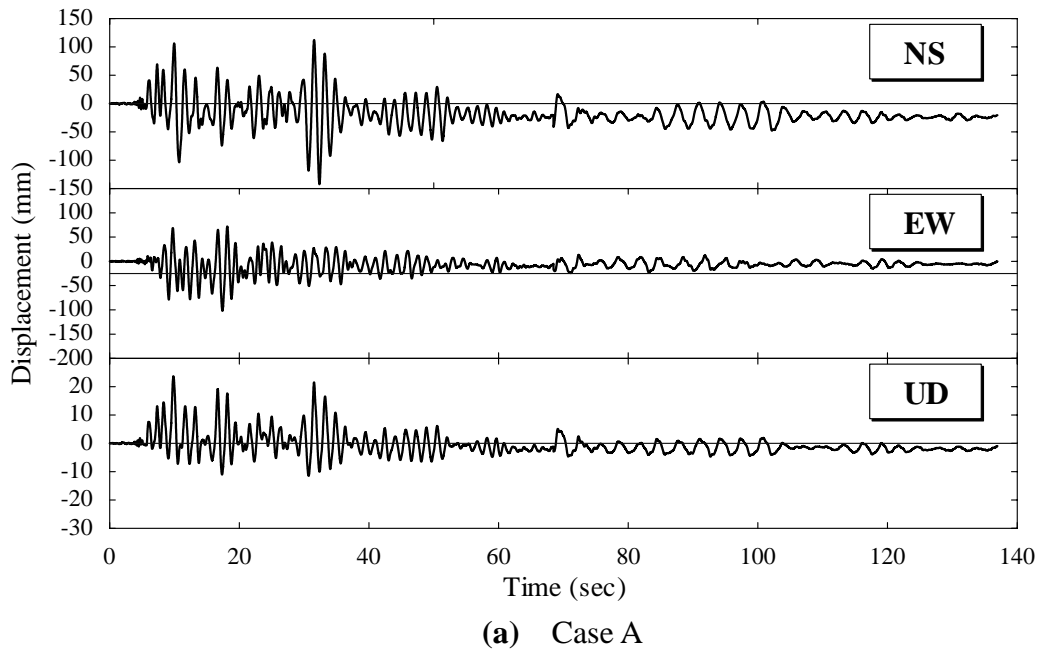
6.4.3 Response of displacement

The results of the 3D dynamic lattice model analysis for RC bridge piers subjected to five earthquake motions are illustrated in **Figure 6.19**. In addition, the displacement time histories by the 3D dynamic lattice model for five RC bridge piers are shown in **Figure 6.20**. In the figure, the hysteresis loops, which are the relationships between the lateral force and the lateral displacement at the top of the pier along X-axis (NS) and Y-axis (EW), are shown.
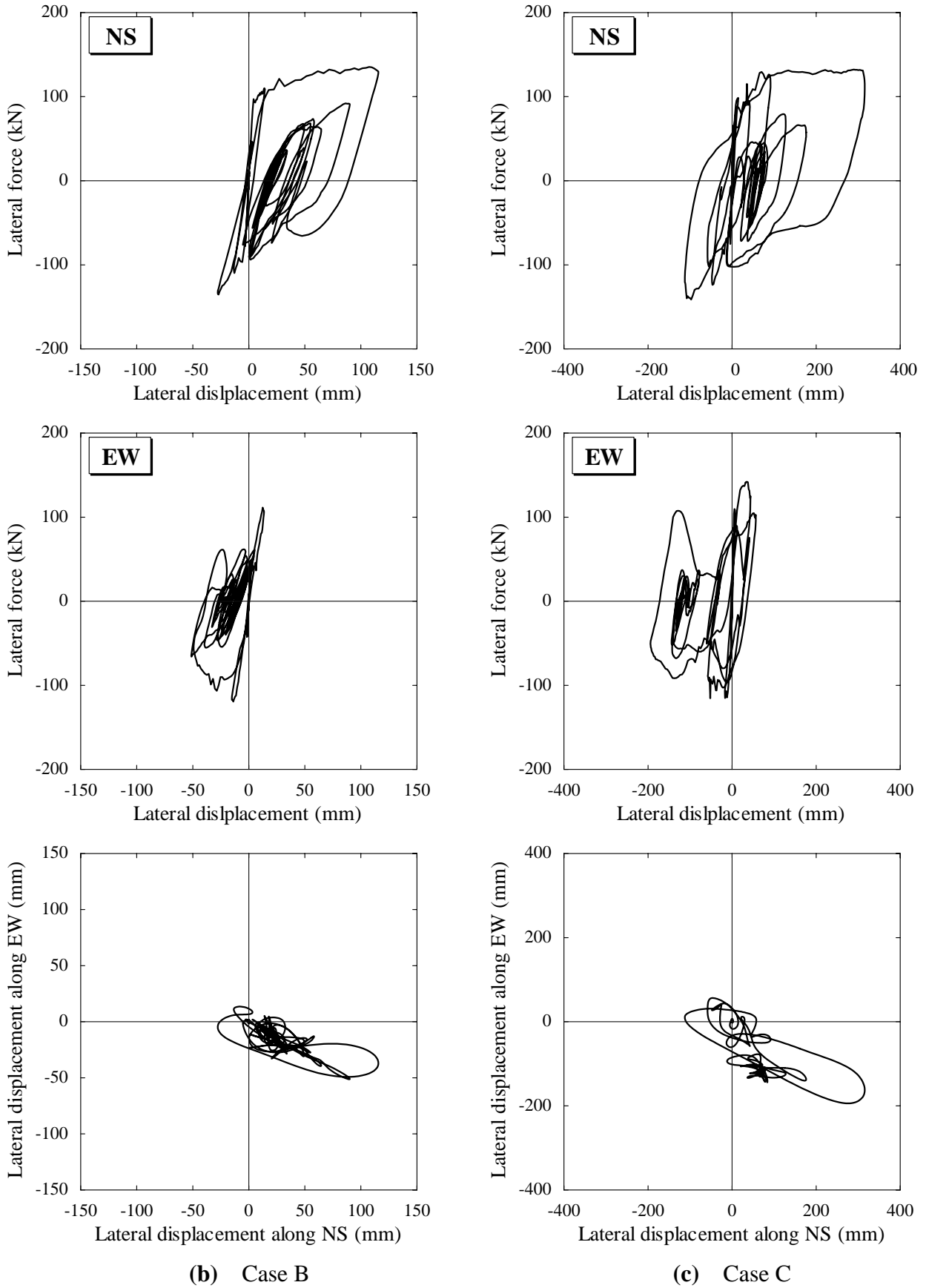
Figure 6.19 Analytical responses by the 3D dynamic lattice model for RC bridge piers subjected to earthquake motions (continued)

177

(d) Case D

(e) Case E

Figure 6.19 Analytical responses by the 3D dynamic lattice model for RC bridge piers subjected to earthquake motions (continued)
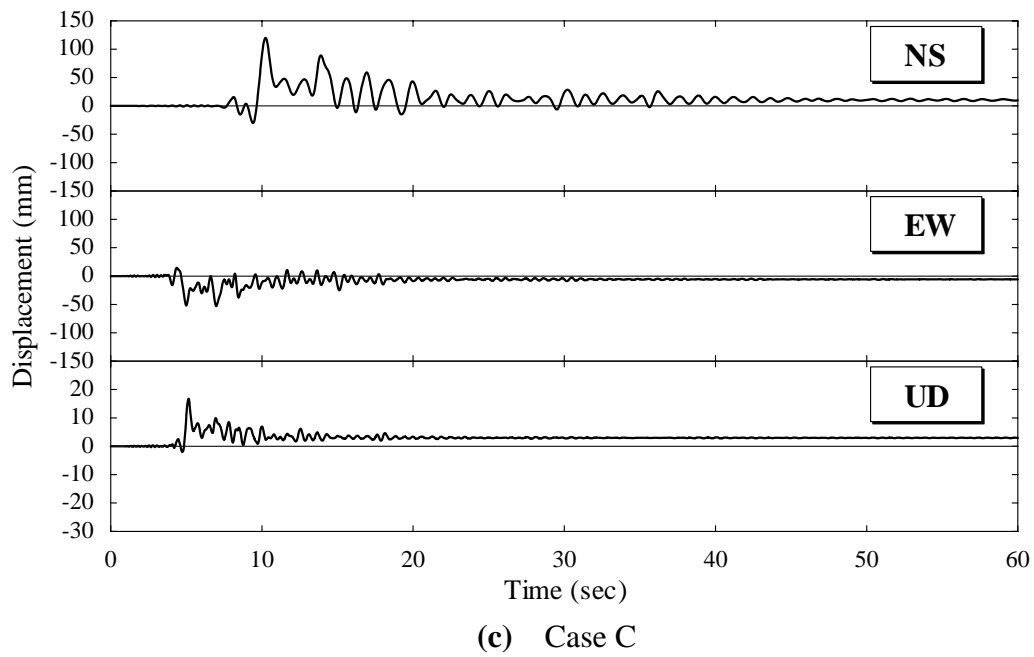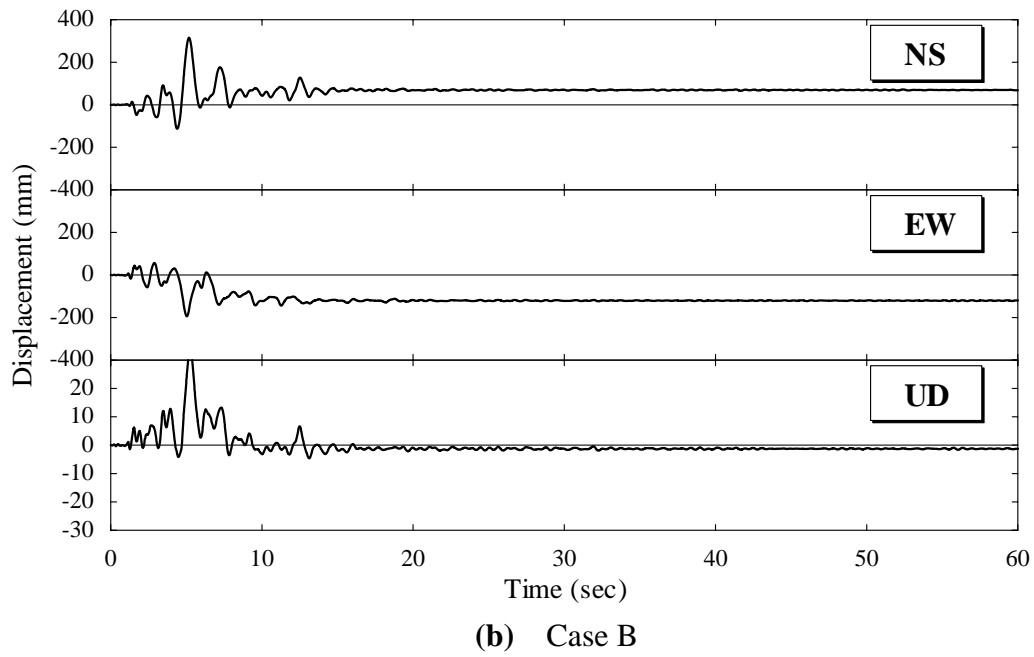
178

(a) Case A

Figure 6.20 Displacement time histories by the 3D dynamic lattice model for RC bridge piers subjected to earthquake motions

In Case A, it is found that the larger displacement responses along both NS and EW directions are predicted both in positive and negative directions, as compared with other cases. It can be seen that the response of the pier shows the significant energy dissipation capacity. The buckling of reinforcement takes place at the bottom of the pier. Hence, after the buckling occurs, the hysteresis loop shows the large deformation with slight pinching behavior.

For Case B and Case C, the comparison with the various results shows that the piers of Case B and Case C have the larger maximum displacement compared to others, in spite of the same peak acceleration and the smaller residual displacement. This is because the pier of Case C is subjected to bilateral motion with similar intensity in each direction. It can be seen that in Case C, the displacement becomes very large in NS direction and considerably small in EW direction. Consequently, when the maximum displacement increases in the positive side, the residual displacement also accumulates. On the other hand, in the results of Case A, the displacement increases in both directions resulting in larger hysteresis and smaller residual displacement.

The behavior of Case B and Case C is because the first yielding takes place in positive side and further loading causes significantly larger positive response so that the response cannot return sufficiently to cause yielding in negative direction during unloading. However, the maximum positive response is larger and consequently, the residual deformation in the positive side accumulates resulting in relatively larger residual deformation than that in the pier of Case A.

179

(b) Case B

(c) Case C

Figure 6.20 Displacement time histories by the 3D dynamic lattice model for RC bridge
piers subjected to earthquake motions (continued)
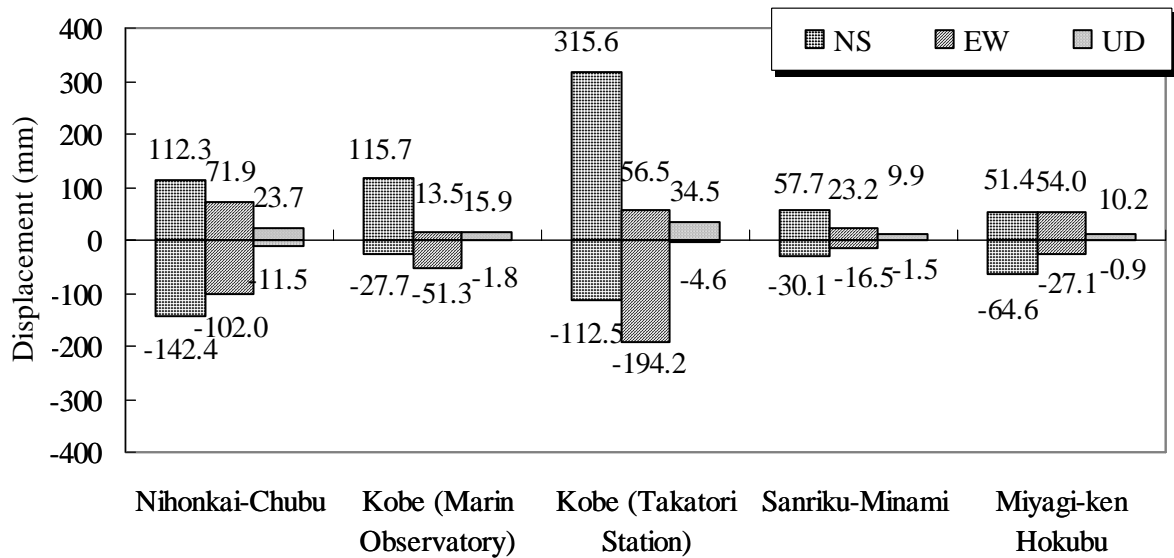
(d) Case D

(e) Case E

Figure 6.20 Displacement time histories by the 3D dynamic lattice model for RC bridge
piers subjected to five earthquake motions (continued)

181
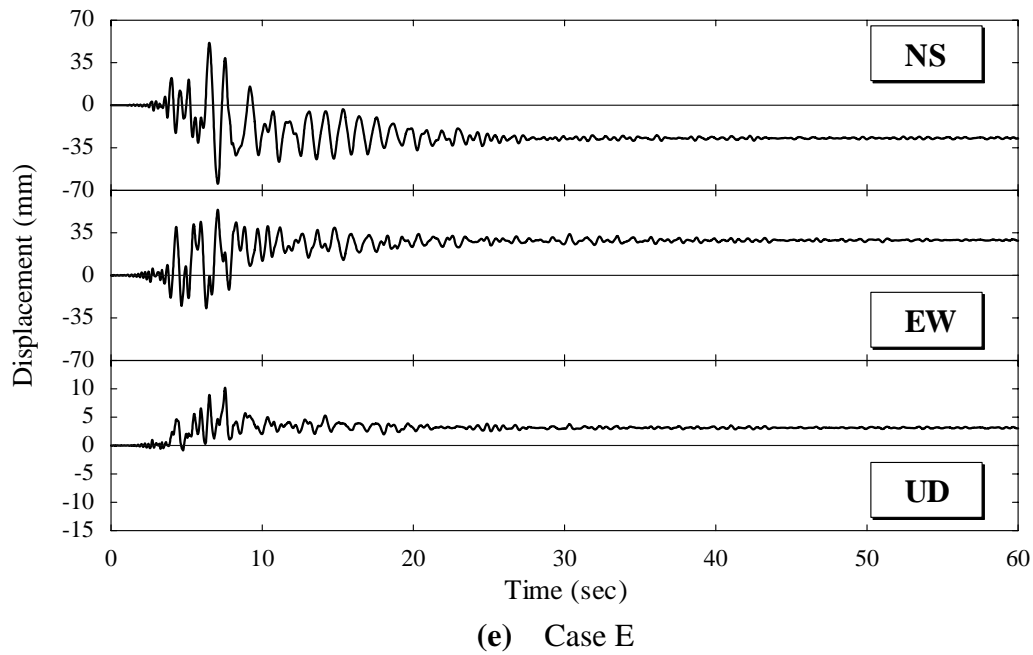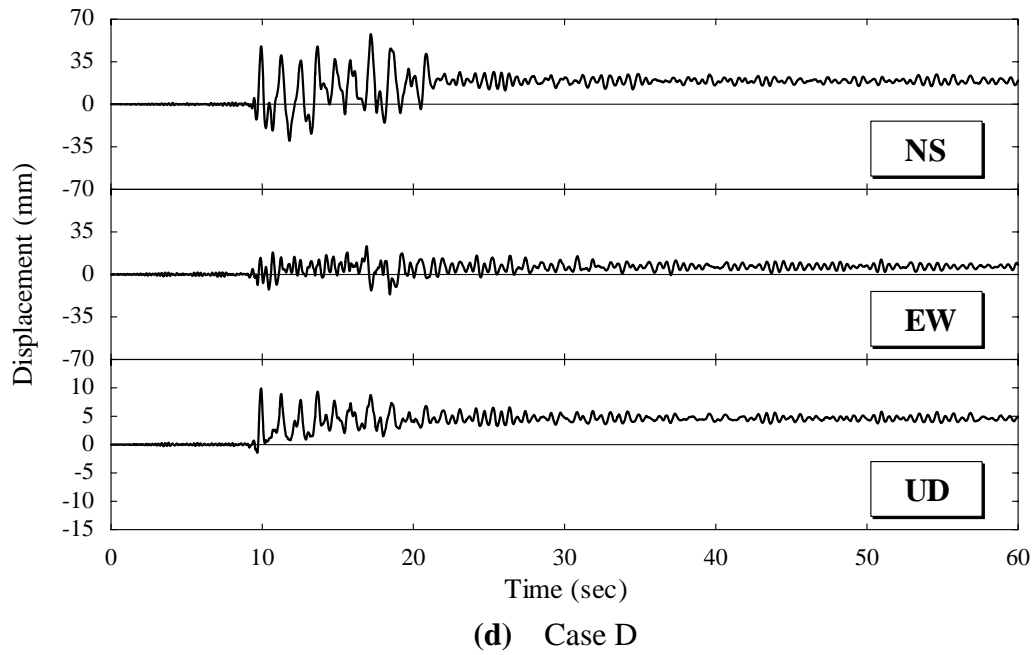
Figure 6.21   Maximum displacement of each case

On the other hand, for Case D and Case E, since the input motion has significantly high frequency, the maximum response is found to be smaller than other cases.   In addition, it is noticed that the residual displacements of Case D and Case E remain in different direction, even though the overall behavior is similar to each other.

The simulation has been performed using the same amplitude of input ground motion. **Figure 6.21** shows the maximum displacements in NS, EW, and UD directions for five RC bridge piers.   From the figure, the analytical results show that the maximum and residual displacements are not necessarily determined from the amplitude of input ground motion, but they are influenced by the characteristics of frequency, duration, and phase of the motion.   In addition, in the large deformation range, the buckling behavior of reinforcement is dominant in the overall response of the pier.   It is found that the analysis considering the buckling of reinforcement can predict the seismic response and cyclic loops representing the energy dissipation capacity of RC columns with proper accuracy.

6.5   Conclusions

In this chapter, the nonlinear analyses using the 3D dynamic lattice models are conducted and verified for RC columns on the shaking table tests.   By considering the appropriate constitutive models of concrete and reinforcement, it is found that the 3D lattice model analysis can reasonably predict the biaxial behavior of RC columns subjected to the bilateral ground motion.   It is also found that the post-peak response of RC columns is strongly

influenced by the buckling behavior of longitudinal reinforcement. The analysis considering the buckling of longitudinal reinforcement can predict the post-peak response as well as the cyclic hysteresis representing the energy dissipation capacity of RC columns with sufficient accuracy.

The analytical simulations are carried out using 3D ground motion including NS, EW, and UD motions. It is found that the maximum displacement response of RC columns subjected to ground motion from the diagonal direction cannot be simply predicted from the calculation by 2D analysis. It is confirmed that the 3D lattice model analysis can reasonably predict the biaxial seismic behavior of RC columns subjected to ground motion from the diagonal direction.

The seismic performance verification is also performed based on the several real-earthquake motions. Here, near-field type and far-field type ground motions are used. The analytical results show that the maximum and residual displacements are not necessarily determined from the amplitude of input ground motion, but influenced by the characteristics of frequency, duration, and phase of the motion. In addition, at the large deformation range, the buckling behavior of reinforcement is dominant in the overall response of the column. Moreover, it is found that the analysis considering the buckling of reinforcement can predict the seismic response and cyclic loops representing the energy dissipation capacity of RC columns with proper accuracy.
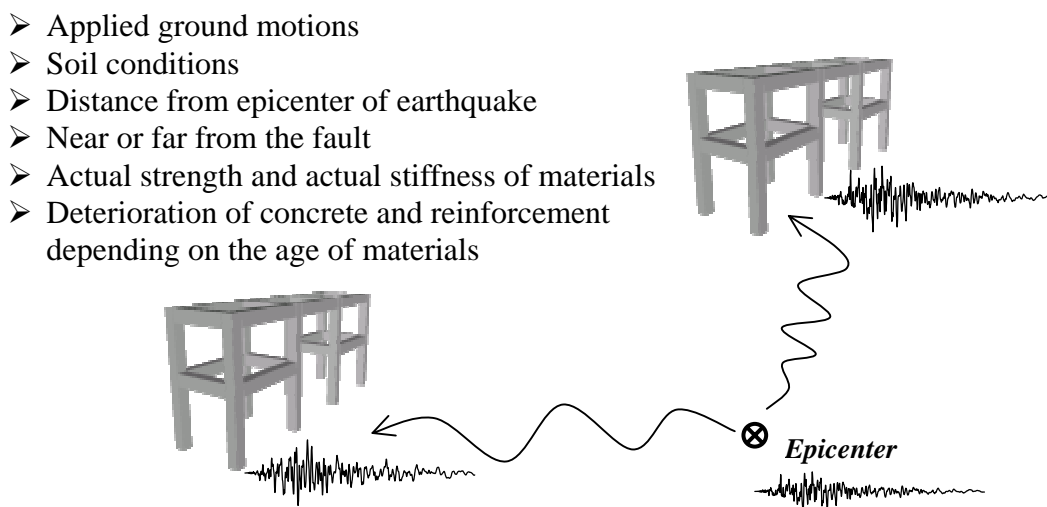
References in Chapter 6

[1]   JSCE (2002): *Standard Specifications for Concrete Structures-2002*, Seismic Performance Verification, December.

[2]   Kyoshin Network (K-NET): http://www.k-net.bosai.go.jp/k-net/.

[3]   Nishida, H., Unjoh S., and Nagaya K. (2001): Shaking Table Test of RC Column Subjected to Bilateral Excitation, *Technical Memorandum of Public Works Research Institute*, No.3843, pp.545-556, November.

[4]   Osada, K., Ohno, S., Yamaguchi, T., and Ikeda, S. (1997): Seismic Behavior of Reinforced Concrete Piers Strengthened with Carbon Fiber Sheets, *Concrete Library of JSCE*, No.30, pp.155-179, December.

[5]   Unjoh, S., Nishida, H., and Nagaya, K. (2002): Shaking Table Test of Square RC Column Subjected to Bilateral Excitation, *Technical Memorandum of Public Works Research Institute*, No.3871, July. (in Japanese)

7 DAMAGE ANALYSIS OF ACTUAL RC VIADUCTS

7.1 Introduction

Hyogo-ken Nanbu Earthquake, which occurred on January 1995 in Japan, caused the destructive collapse to various structures including reinforced concrete (RC) structures. The observations following this earthquake indicate that the main causes of severe damage were due to the overestimation of both shear carrying capacity and deformation capacity of the structural members of columns and beams. These members had low amount of transverse reinforcement. On the other hand, it is noticed that there were many RC structures without almost any damages. The difference of the degree of damage is influenced by several factors even if the dimension of structures and the arrangement of reinforcement are almost identical, as schematically shown in **Figure 7.1**.

Hence, the estimation of the structural performance is difficult because there are many factors influencing the seismic response of structures. With an input ground motion, in recent year, the prediction of earthquake motion at the ground surface is possible due to the development of seismic engineering. In the seismic design for RC structures, it is important to accurately

➤ Applied ground motions
➤ Soil conditions
➤ Distance from epicenter of earthquake
➤ Near or far from the fault
➤ Actual strength and actual stiffness of materials
➤ Deterioration of concrete and reinforcement
   depending on the age of materials

Epicenter

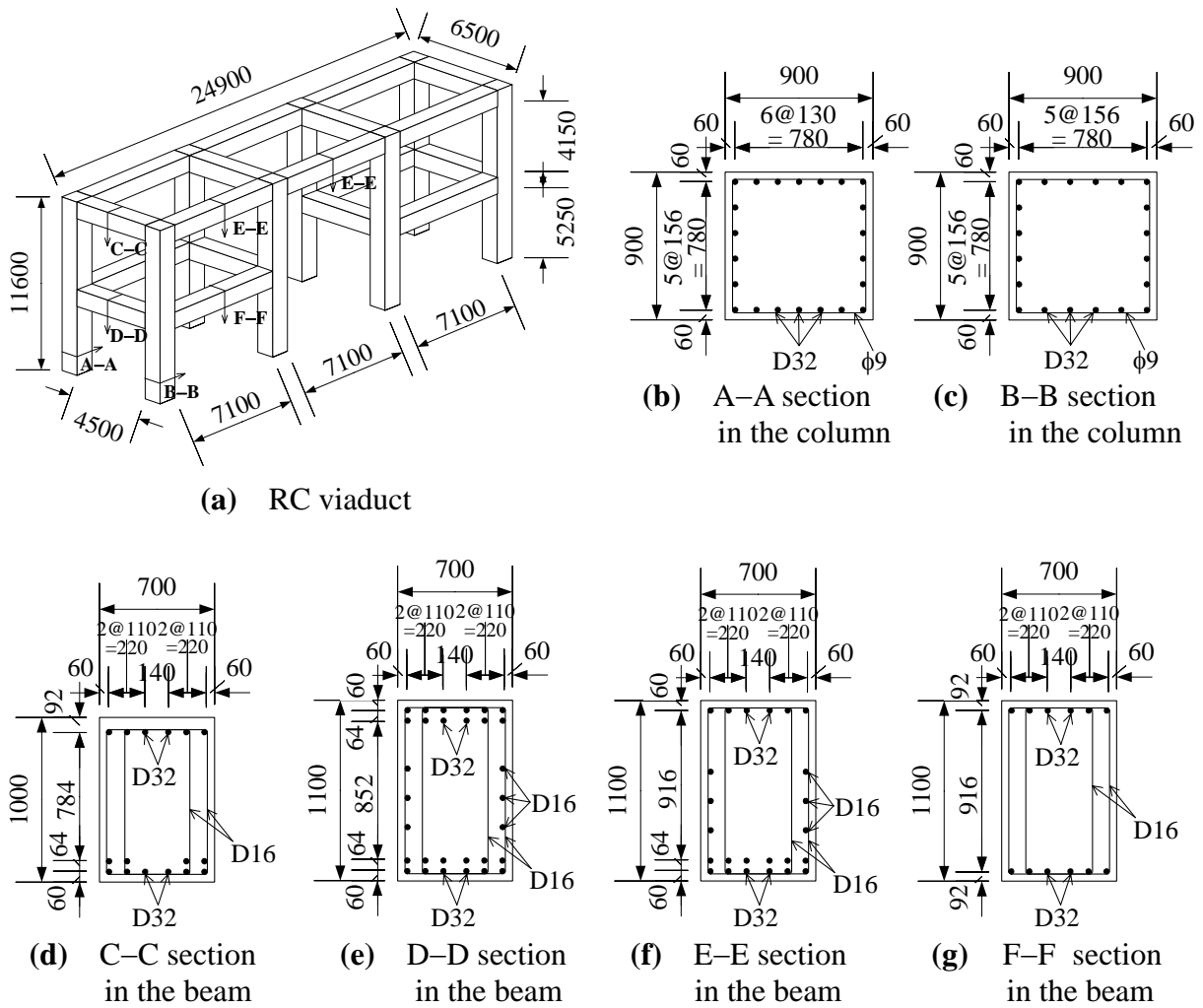**Figure 7.1** Factors on ground motion at soil surface

assess the load carrying capacity and deformation capacity of RC structures with various dimensions of cross section and arrangements of reinforcement. In addition, the information such as the maximum and residual displacements obtained from the dynamic analysis is useful to estimate the behavior of RC structures subjected to large earthquake motion.

Many investigations for the damage of structures and the damage analyses were performed (Committee on Hanshin-Awaji Earthquake Disaster 1996, Ishibashi and Okamura 1998, Committee 311 2000, 2002). In order to evaluate the seismic performance, the response is considered by analyzing along the longitudinal and transverse directions of the structures independently. However, actual structures are generally subjected to the ground motion from different directions of their principal axes. When the damage analysis is carried out, three-dimensional approach is essential to evaluate the effects of the multi-directional input ground motion. Generally, the seismic performance evaluation is performed by the frame analysis based on the moment-curvature restoring characteristics or the fiber technique (Tsuchiya et al. 1999, 2000, Ota et al. 2002). The shortcoming of these models is the difficulty in estimating the behavior in the post-peak range, especially, when RC structural members fail in shear. In addition, these models cannot directly predict the shear deformation and changing of torsional stiffness because the in-plane deformation is not taken into account.

In Chapter 5 and Chapter 6, the performance of 3D lattice model has been confirmed. As mentioned previously, the 3D lattice model is an objective and simple procedure, which can explain the shear resisting mechanism of RC structural members reasonably. In this chapter, RC rigid-frames in railroad viaducts are selected as the analytical target. The seismic response of rigid-frame RC viaducts will be evaluated using the 3D nonlinear dynamic lattice model analysis. The analytical results will be compared with actual damages of the viaducts. The input ground motions determined by Frequency-Dependent Equi-Linearized technique, FDEL (Sugito et al. 1994) are used. The buckling behavior of reinforcement at the end of columns is taken into consideration in the analysis. However, The bond-slip behavior of reinforcing bars at the joint portion is neglected. The interaction between soil and structures is not considered as well.

7.2 Target Structures

The seismic performance evaluation is performed for two rigid-frame railroad viaducts. **Figure 7.2** and **Figure 7.3** show the details and dimensions of rigid-frame RC viaducts. They are beam-slab type rigid-frame RC viaducts with three-span. These viaducts were

(a) RC viaduct

(b) A–A section in the column

(c) B–B section in the column

(d) C–C section in the beam

(e) D–D section in the beam

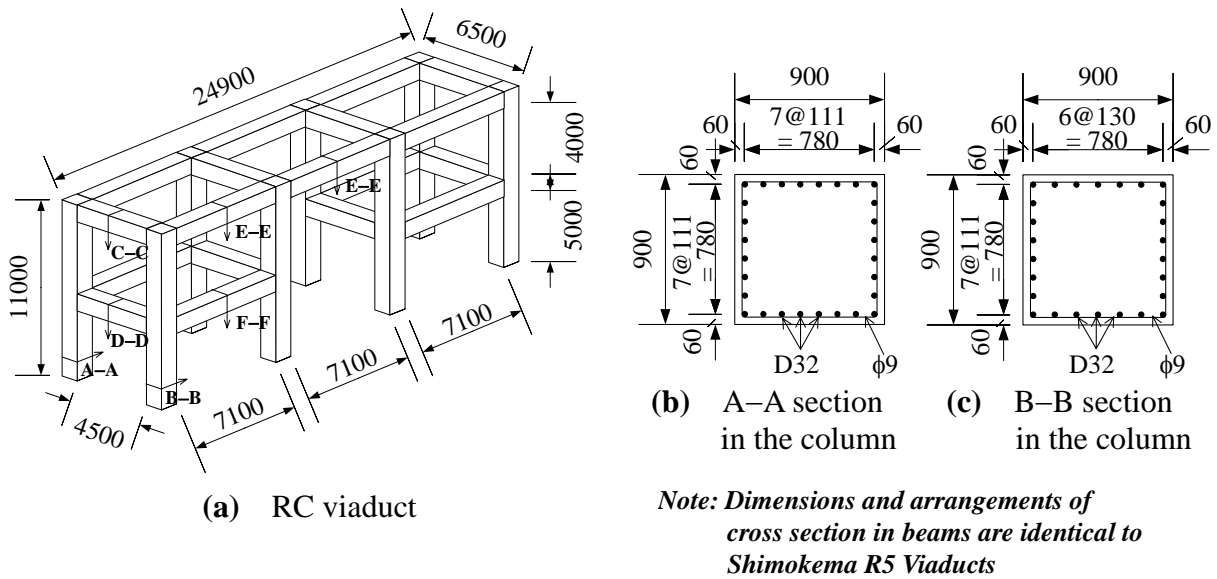**(f)** E–E section in the beam

(g) F–F section in the beam

Figure 7.2 Dimensions and arrangements of reinforcement in Shimokema R5 Viaduct

designed according to Structural Design Standards of Japan National Railways enacted in 1970. Here, the viaducts were designed using the seismic intensity method with a design horizontal seismic intensity of 0.2. The actual damage conditions of two viaducts after the earthquake are shown in **Figure 7.4** (Committee 311 2000). In the observation of actual structures, the degree of damage was determined according to most heavily damaged members in each viaduct. It was observed that there was the slight damage with crossed diagonal cracks and the buckling of longitudinal reinforcement in Shimokema R5 Viaduct. On the other hand, in Hansui R5 Viaduct, the severe shear failure with the collapse of columns and the drops of beams and slabs were observed.

In both of viaducts, the cross section of a column was a square of 900 mm. All reinforcing bars in the columns had a minimum concrete cover of 60 mm. The beams had the rectangular cross section with 700 mm width and 1,000 mm depth for the upper portion in transverse direction, while with 700 mm width and 1,100 mm depth for other portions. In

(b)   A–A section
in the column

(c)   B–B section
in the column

(a)   RC viaduct

*Note: Dimensions and arrangements of
cross section in beams are identical to
Shimokema R5 Viaducts*

Figure 7.3   Dimensions and arrangements of reinforcement in Hansui R5 Viaduct

Shimokema R5 Viaduct, the heights of columns were 5,430 mm and 4,150mm in lower and upper portions, respectively.   On the other hand, in Hansui R5 Viaduct, the heights of columns were 5,000 mm and 4,000 mm in lower and upper portions, respectively.

The compressive strength of concrete of Shimokema R5 Viaduct was slightly stronger than that of Hansui R5 Viaduct.   In Shimokema R5 Viaduct, the longitudinal reinforcement in columns and beams had the yield strength of 349 N/mm^2 and Young's modulus of 197 kN/mm^2.   The yield strength and Young's modulus of transverse reinforcement were 296 N/mm^2 and 204 kN/mm^2, respectively.   The material properties used in these two viaducts are summarized in **Table 7.1**.
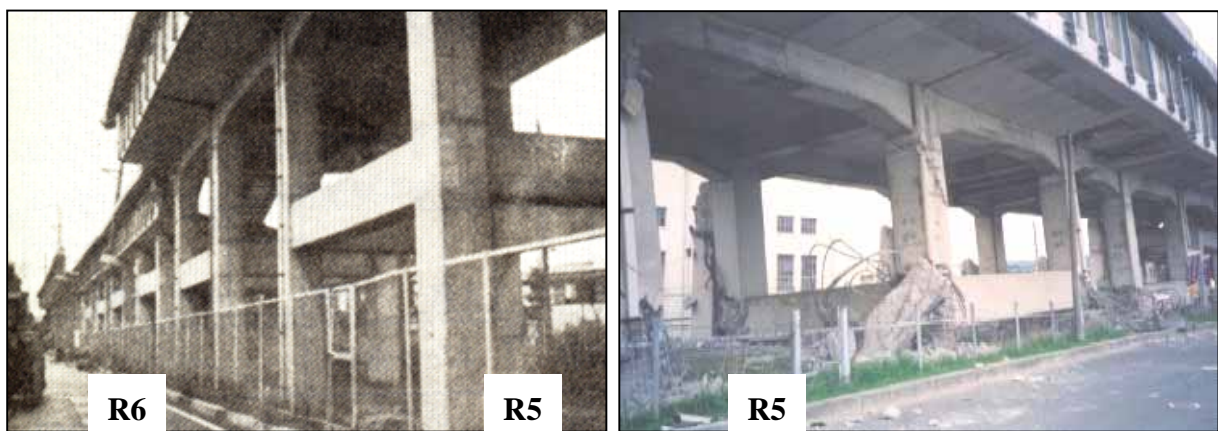
(a)   Shimokema R5 Viaduct

(b)   Hansui R5 Viaduct

Figure 7.4   Damage conditions in Shimokema R5 Viaduct and Hansui R5 Viaduct

188

**Table 7.1** Material properties of concrete and reinforcement

Name of RC viaducts	Concrete			Longitudinal reinforcement			Transverse reinforcement		
	$f_c{}'$ (MPa)	f_t (MPa)	E_c (GPa)	f_y (MPa)	f_u (MPa)	E_s (GPa)	f_y (MPa)	f_u (MPa)	E_s (GPa)
Shimokema R5[*1]	31.7	2.43	16.8	349	533	197	296	436	204
Hansui R5	29.1	1.27	18.4	322	521	203	263	380	183

*1: Material properties of concrete and reinforcement were obtained by strength tests for actual materials used in Shimokema Viaducts.

To predict the input ground motion at each construction point, the motions at the engineering foundation level and at the soil surface are considered.   Generally, the strong motion at the engineering foundation level is predicted by the non-stationary strong motion prediction method and the response spectrum method.   The non-stationary strong motion prediction models were developed based on the rock surface strong motion dataset that consists of 118 components of major Japanese accelerograms including the records from 1995 Hyogo-ken Nanbu Earthquake (Sugito et al. 2000, Committee 311 2002).   Based on the dataset, the non-stationary strong motion is predicted by the earthquake magnitude and the distance from the earthquake epicenter.   On the other hand, for the spectrum method, simulated strong motion is obtained by fitting with the maximum motion and the response spectrum, which are predicted by using an empirical equation.   In the following analysis, these two methods are called as motion-I and motion-II, respectively.

Using the input ground motion at an engineering foundation level, the ground motion at the soil surface can be evaluated.   To analyze the response of soil surface, the multi-reflection theory is generally used.   However, this theory cannot explain the nonlinear behavior of soil that is observed in the cases of large earthquake.   In order to consider the nonlinear behavior of soil, the equi-linearized technique was developed.   For earthquake damage assessment, SHAKE (Schnabel et al. 1972) has been used as the equi-linearized technique.   Recently, the method to consider the frequency-dependent effect of the shear modulus and the damping factor has been developed as FDEL (Sugito et al. 1994).   In the analysis, the input ground motions determined by FDEL (Sugito et al. 1994) are used.   The ground motions at each construction point of RC viaducts are shown in **Figure 7.5**.   These motions are applied to RC viaducts along longitudinal and transverse directions of the viaducts simultaneously.

For both viaducts, the weight of a superstructure including the slab weight is assumed to be 7200 kN.   The self-weight of the structure is calculated by multiplying the volume of

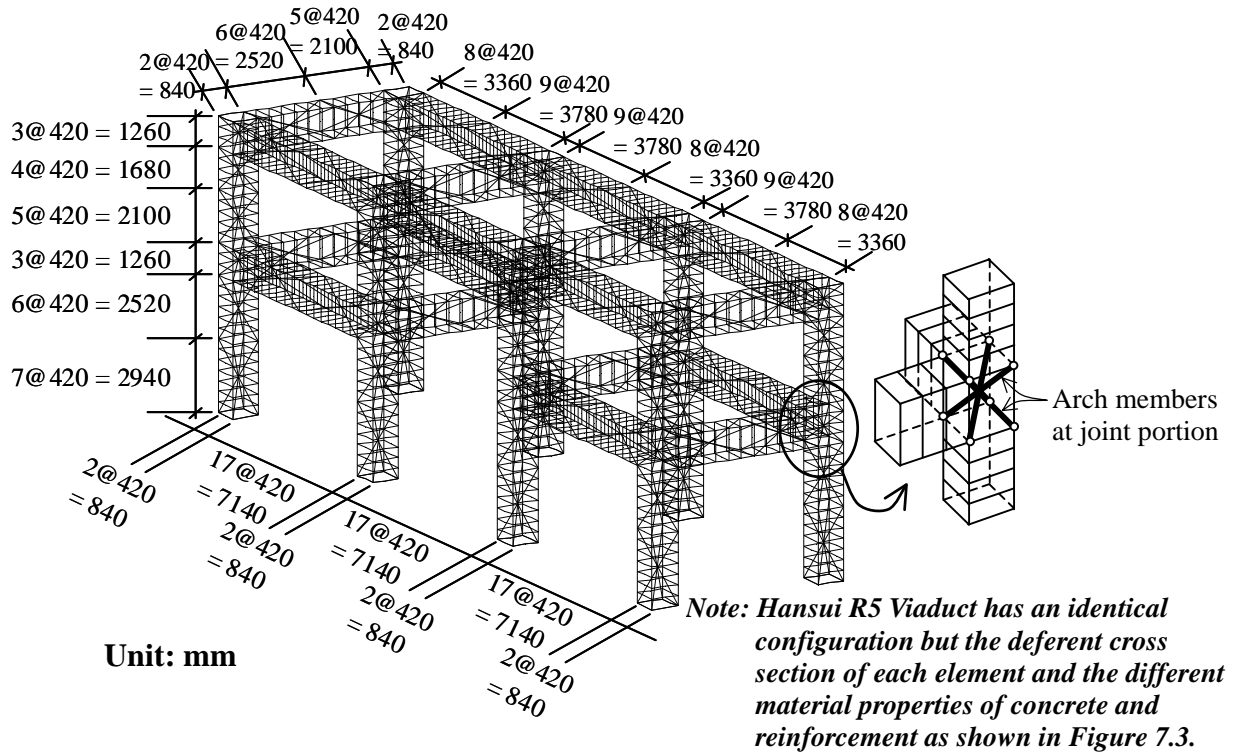**(a)** Shimokema R5 Viaduct

(b) Hansui R5 Viaduct
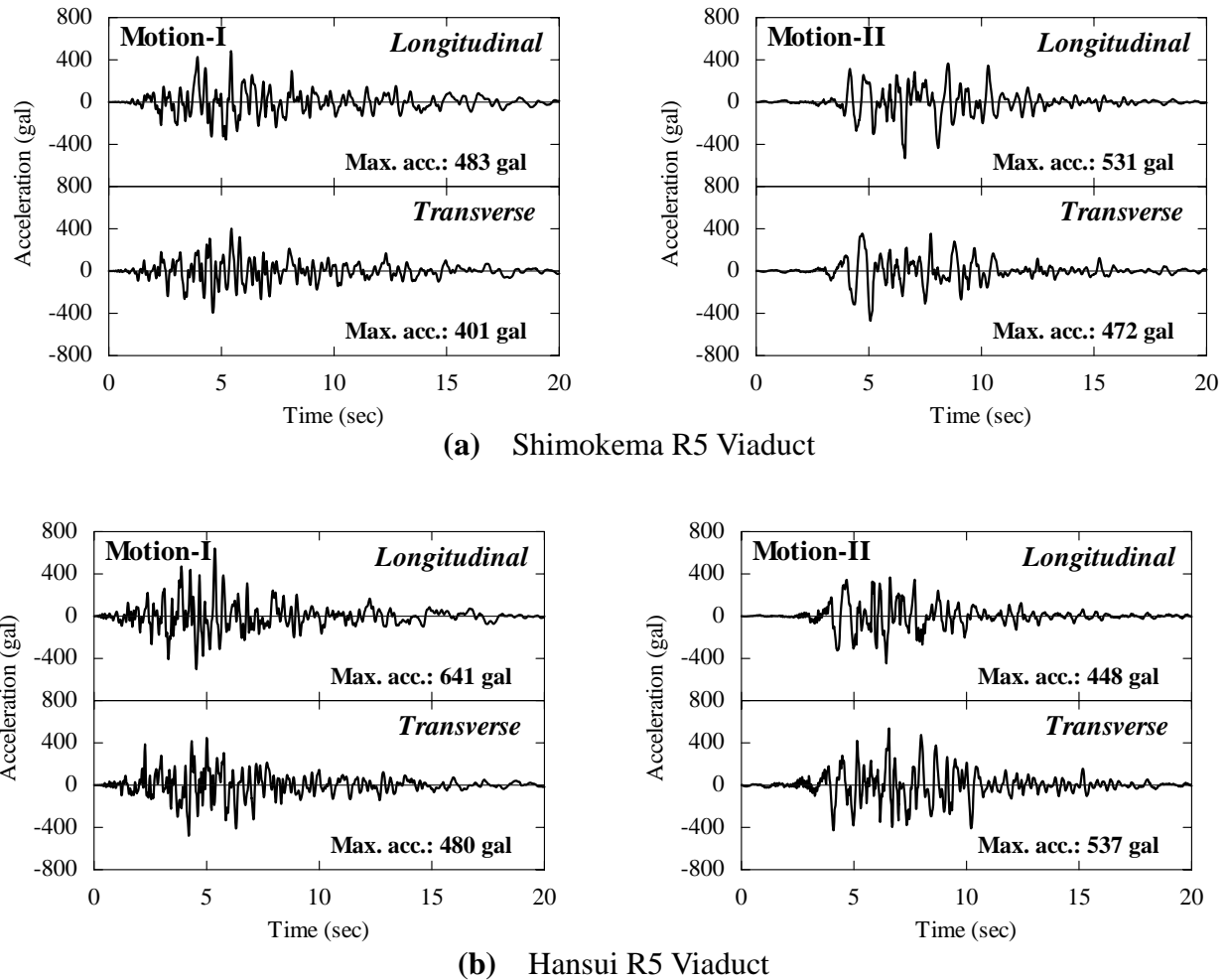
Figure 7.5 Input ground motions at each construction point

columns and beams by the specific gravities of concrete and reinforcement. The mass of the structure is assumed to uniformly distribute over all nodal points of the lattice model.

7.3 Configuration of Lattice Model

The 3D dynamic lattice model and the boundary conditions used in the analysis are illustrated in **Figure 7.6**. The three-span viaduct is treated as a unit of the analytical model. As seen in the figure, the model consists of beams and columns, while the slab is not included. In the analysis, it is assumed that the masses corresponding to the self-weight of viaducts are uniformly distributed over all nodal points, using the lumped-mass idealization. It is also assumed that there is a concentrated mass, which is equal to the weight of the superstructure and the slab, acting on the top nodes of columns and beams.

Figure 7.6 3D dynamic lattice model for Shimokema R5 Viaduct

It is considered that the joints of each column and beam are rigidly connected between each member. According to the flexural deformation of columns and beams, it is appropriate to provide arch members in two layers along the longitudinal direction of the member axis. Hence, the arch members in both columns and beams are modeled into eight concrete members. Similarly, at the column-beam joint portion, four arch members are modeled as shown in **Figure 7.6**. In order to determine the cross-sectional area of arch members in the 3D lattice model, the values of t_b and t_d are determined based on the theorem of minimization of the total potential energy. The calculations for the values of t_b and t_d are conducted on each structural member individually. The distributions of the total potential energy with varied value of t of each member are shown in **Figure 7.7**. Here, the values of t at the column-beam joint portion are assumed to be identical to those obtained in the lower columns for simplicity.

For the boundary conditions at the bottom of a column, the foundation in the actual structure consists of both beams and piles under the ground surface. The N-value of between 30 and 50 was encountered at a depth of 3 m below the ground surface at the sites of Shimokema R5 Viaduct and Hansui R5 Viaduct. Here, the N-value (the standard penetration resistance value) is defined as the number of blows required driving the split-barrel sampler a total distance of 30 cm, the count being started after a penetration of 15 cm. Since RC viaducts
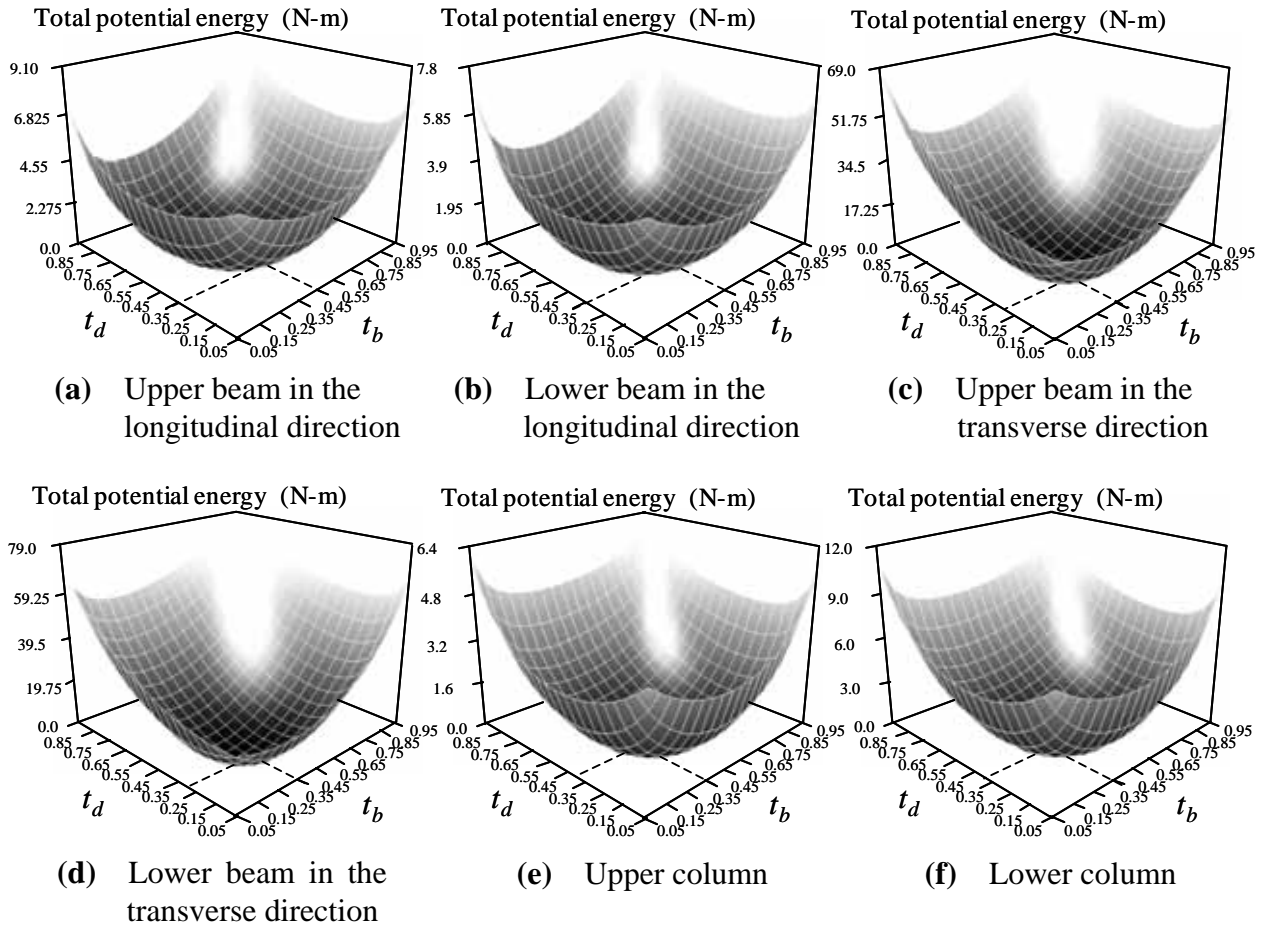
Figure 7.7 Distribution of total potential energy in each beam and column

are founded on the sufficiently stiff ground, it is assumed that the input ground motion is directly applied to the bottom of each lower column. The 3D lattice model treats the RC viaduct that is disregarded the foundation, and consequently the interaction between the structure and soil is not considered in the analysis. For the boundary between neighboring viaducts in the longitudinal direction, the horizontal direction is assumed to be a free condition.

In the dynamic analysis, it is assumed that the viscous damping is neglected ($h = 0$) and the numerical damping of the Newmark method with factors $\beta = 0.36$ and $\gamma = 0.70$ is used as the time integration. Here, a time interval is set to be 0.01 sec. Since the nonlinear responses appear when RC structures are subjected to the large ground motions, the Newton-Raphson iteration method is adopted to iterate the calculations until an adequately converged solution is obtained. In order to check the convergence, the out-of-balance force and energy increment are compared with initial values during the iteration. The convergence tolerances of the out-of-balance force and energy are set to be 0.001 and 0.01, respectively.

7.4   Damage Analysis of Actual RC Viaducts

7.4.1   Seismic response of RC viaducts

The dynamic analysis is carried out by using the 3D lattice model.   Two types of the input ground motions (motion-I and motion-II) that are expressed in the previous section are used for the seismic performance evaluation of rigid-frame RC viaducts.   As mentioned previously, the footing is not modeled and a fixed support is provided at the bottom of each lower column.   Hence, the ground motion is applied to the bottom of each column directly. The results of the analysis are shown in **Figures 7.8** to **7.11**.   In these figures, the analytical results of displacement time histories and particle traces of displacement at the mid-span of an upper beam in the transverse direction are illustrated.

When the general personal computer with Pentium4 1.7GHz is used, the computing time becomes around 3 hours in which the total time and time interval are set to be 10 sec and 0.01 sec, respectively.   That corresponds to be 1,000 steps of the time integration.   Here, the analytical degree of freedom in the actual scale RC viaducts is as follows; the number of nodes is around 5,000, and the number of elements is around 30,000.   It is found that the computing time is comparatively shorter than other analytical methods used in the practice. The shorter computing time is one of the benefits of the 3D lattice model analysis.

Figure 7.8 shows the analytical results by the 3D dynamic lattice model using the motion-I for Shimokema R5 Viaduct.   It can be observed that the stable response during 10 seconds is predicted.   In the bottom of the lower column, the buckling of longitudinal reinforcement takes place.   For the top of each column and the end of each beam, it can be observed in the analytical results that the buckling of reinforcement does not occur.   The cracks occur in the diaconal members of concrete at the upper and lower columns.   These behaviors are matching with actual observations after Hyogo-ken Nanbu Earthquake as shown in **Figure 7.4** (Committee 311 2000).   On the other hand, the brittle behavior is observed in the cases of Shimokema R5 with motion-II and Hansui R5 Viaduct with both motion-I and motion-II as shown in **Figures 7.9**, **7.10**, and **7.11**.   This is caused by the compressive softening of concrete at the diagonal and flexural members in the lower column.   In all upper columns, the cracks at the diagonal members of concrete are predicted in the case of the analysis using the motion-I or the motion-II.   The response also corresponds to the actual damages of Hansui R5 Viaduct.   Actually, it was observed in Hansui R5 Viaduct after the earthquake that the severe shear failure at lower columns happened with the collapse of upper columns and the drops of beams and slabs took place.
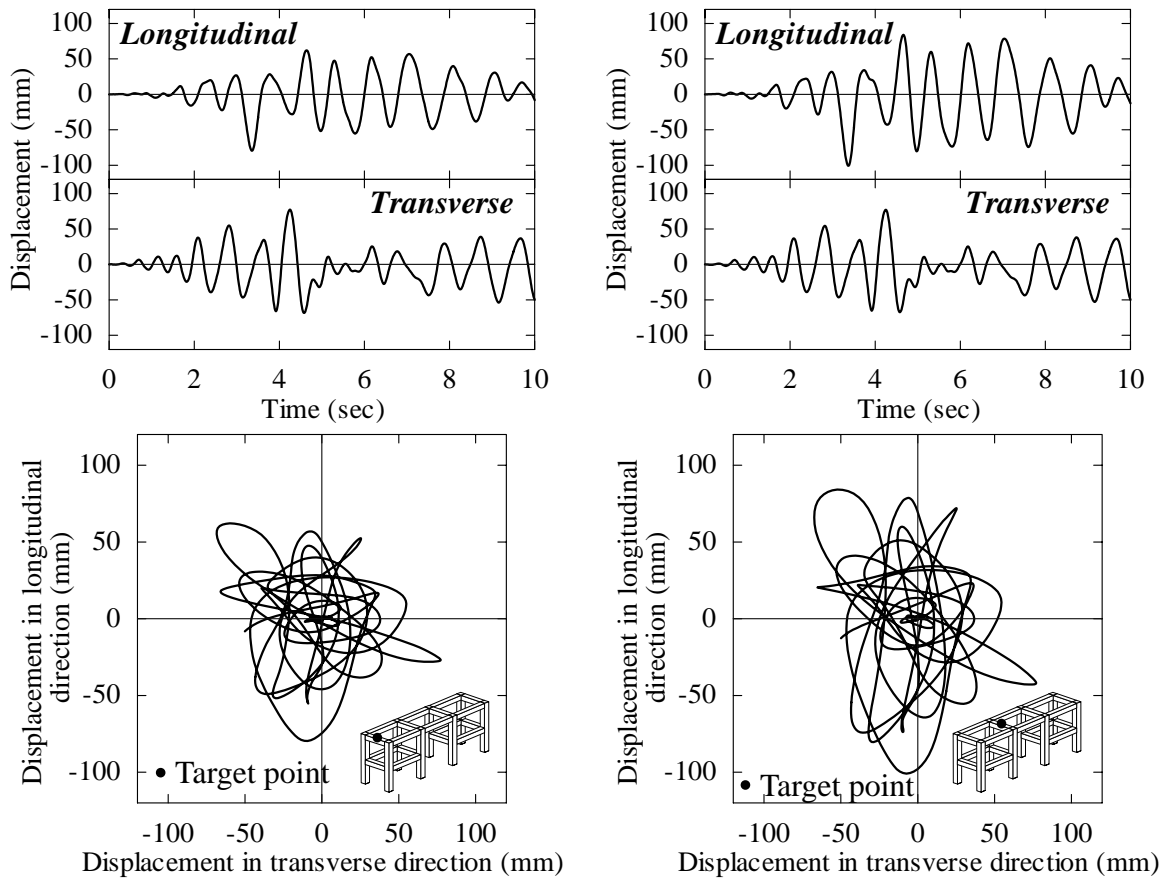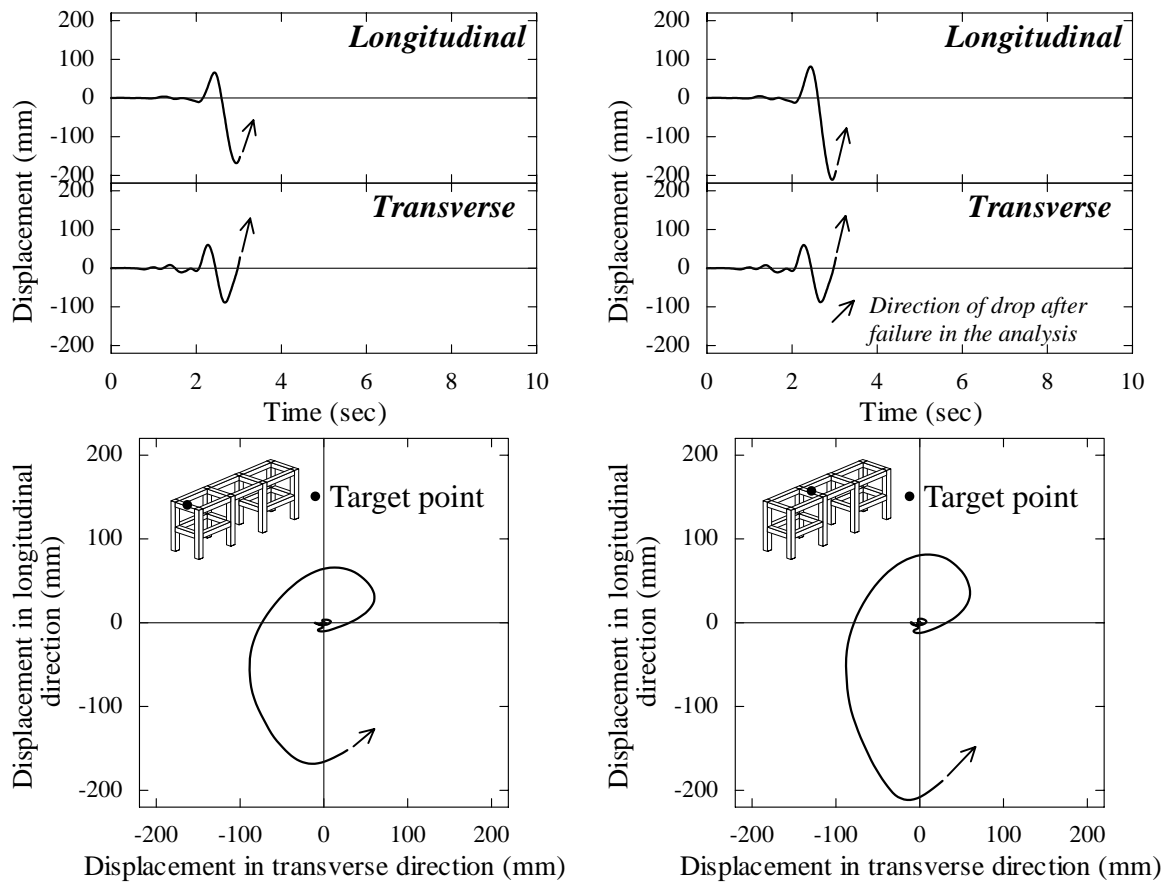
Figure 7.8   Analytical responses for Shimokema R5 Viaduct subjected to motion-I
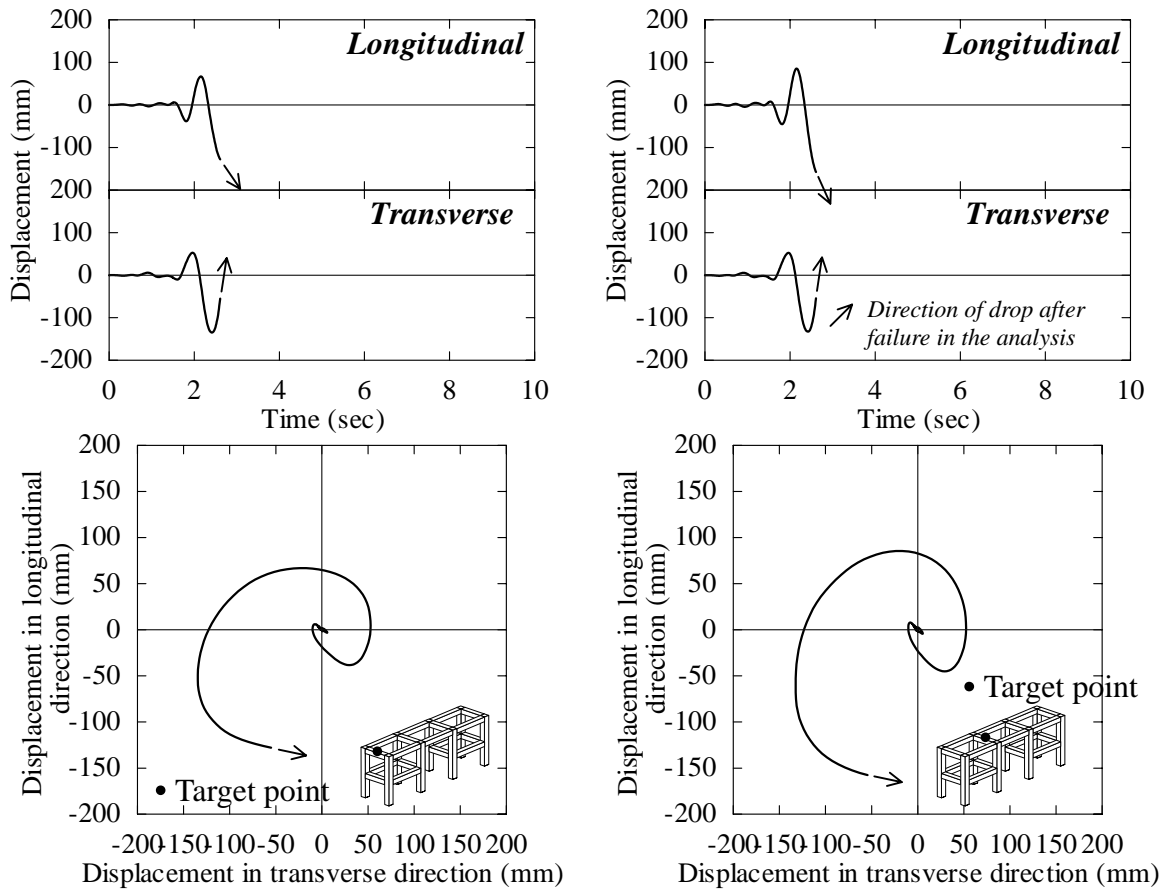
Figure 7.9   Analytical responses for Shimokema R5 Viaduct subjected to motion-II
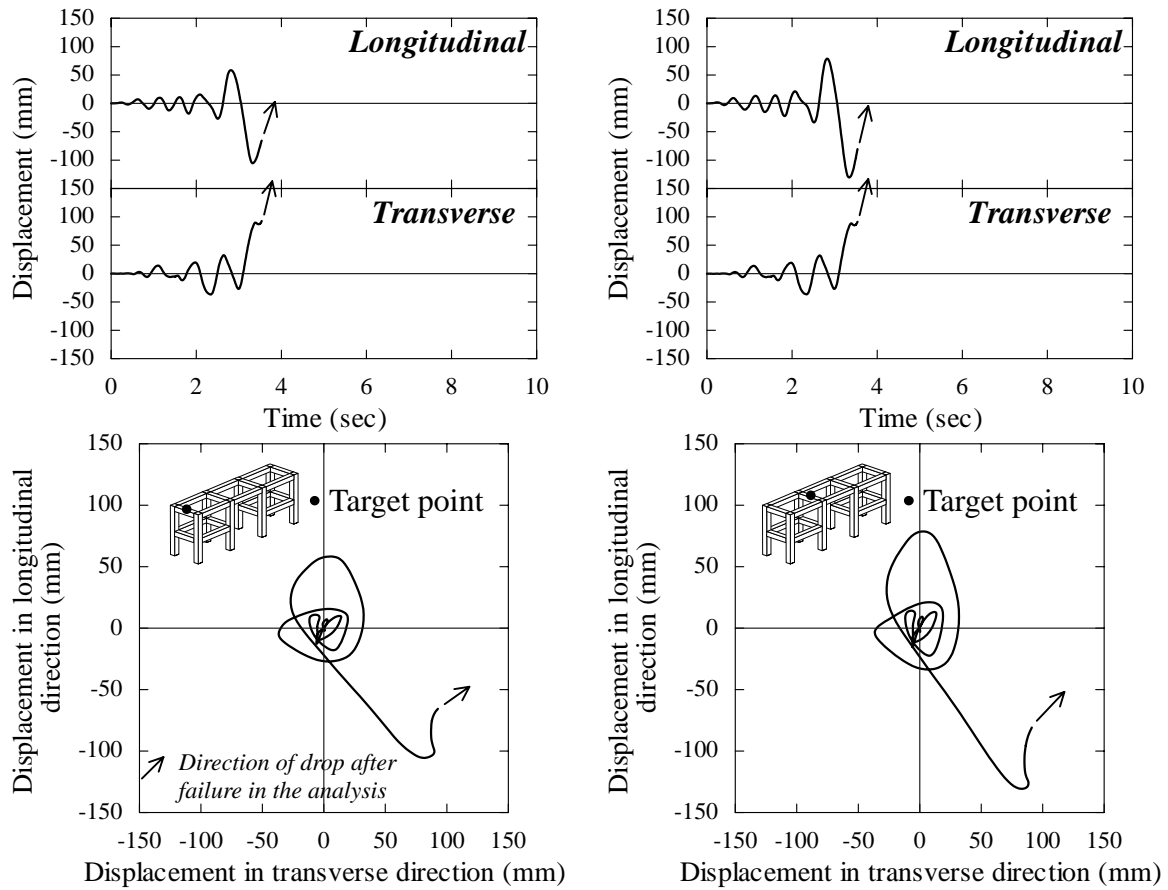
**Figure 7.10** Analytical responses for Hansui R5 Viaduct subjected to motion-I

Figure 7.11 Analytical responses for Hansui R5 Viaduct subjected to motion-II

In the case of Shimokema R5 with motion-II as shown in **Figure 7.9**, it is observed that the large deformation of around −150 mm in the longitudinal direction is predicted. In the analysis, the boundary condition in the longitudinal direction is assumed as a free condition. However, actually, there exist the neighboring viaducts in the longitudinal direction. Therefore, the assumption, which the longitudinal constraint is free, is unrealistic and consequently, the predicted behavior becomes different from the actual response of a structure. It is necessary to consider the interaction with neighboring viaducts when the deformation in the longitudinal direction is dominant at the failure of a structure.

It is also found that the direction, in which the beams and slabs drops down after the lower column fails in shear, can be clearly estimated by the particle traces of displacement in **Figures 7.9**, **7.10**, and **7.11**. In the figure, the arrow indicates the direction of drop after shear failure predicted in the analysis. As can be judged from analytical results, Shimokema R5 Viaduct with the motion-II (**Figure 7.9**) fails toward the longitudinal direction during the increase in the displacement response in the longitudinal direction. On the other hand, it is found that Hansui R5 Viaduct with the motion-I or the motion-II fails toward the transverse direction during the displacement in the longitudinal direction decreases. The information about the state of deformation after the failure of a structure in shear is quite beneficial in terms of the restoration or rehabilitation after the earthquake.

Figure 7.12 shows the deformed shape of Shimokema R5 Viaduct when the maximum displacement at mid-span of the upper beam in transverse direction is reached. The displacements in deformed shapes are magnified by a factor of 30. As can be seen in the

Note: Displacements in the deformed shapes are magnified by a factor of 30.
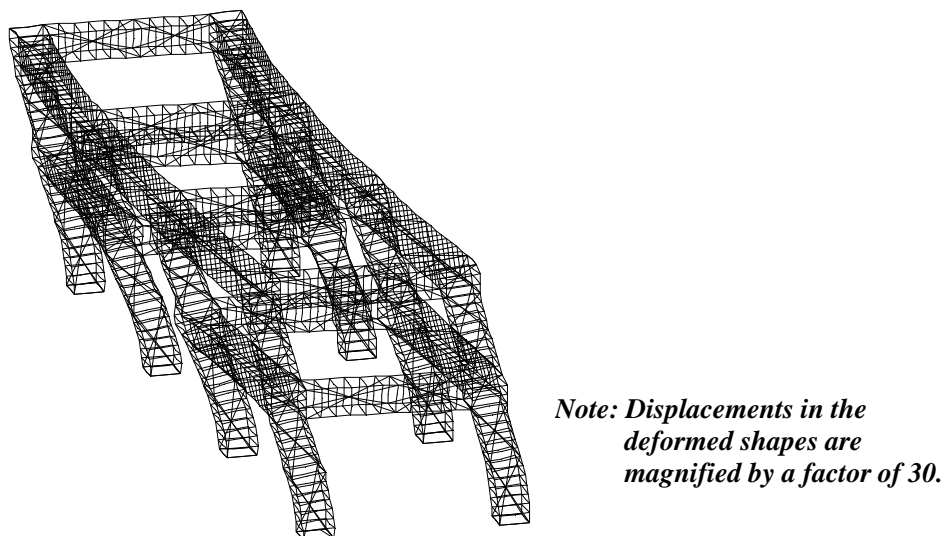
Figure 7.12   Deformed shape of the 3D lattice model for Shimokema R5 Viaduct

figure, the upper layer of columns indicates the torsional behavior when the viaduct is subjected to seismic bilateral loading. The beams and columns in the rigid-frame RC viaduct are found to show the complex responses under the torsion. In this viaduct, since the beams have sufficient amount of transverse reinforcement, the damage is concentrated in the column when the large deformation takes place as shown in **Figure 7.12**. This damage condition is predicted in Hansui R5 Viaduct.

7.4.2   Analytical simulation of shear failure of RC viaducts

In order to verify the response of Hansui R5 Viaduct in which the calculation in the dynamic analysis is terminated by the divergence, the detailed investigation is carried out. The elements in the column at the lower layer in Hansui R5 Viaduct will be focused on. **Figure 7.13** shows the stress-strain relationships of concrete for both diagonal and flexural members. In the figure, the deformed shape of the 3D lattice model for Hansui R5 Viaduct subjected to motion-II is also illustrated. The elements focused on are those in the column at the lower layer in Hansui R5 Viaduct.

It can be seen in the figure that the 3D dynamic lattice model can predict the compressive softening behavior in diagonal members of concrete. The softening behavior is observed in the *elements c* and *d* of the diagonal members of concrete in the 3D lattice model, while the tensile strain increases in the *elements a* and *b* of the diagonal members of concrete. This is caused by that the external energy is locally consumed by a certain portion and the elements in the surrounding portion release the stored energy into localizing elements. Since the external energy becomes large in the actual structure, the brittle failure cannot be predicted in the analysis after the compression softening of concrete occurs. Hence, the iteration procedure in the nonlinear dynamic analysis, which is necessary when the material nonlinearity appears, should be improved in future.

In the analysis, it is assumed that the shear failure takes place at the column or beam when the compression softening behavior of concrete in arch or diagonal members has been predicted. Hence, the shear failure is predicted in spite of the decrease in shear stresses that are transferred across inclined cracks by the aggregate interlock. In addition, the arch member or diagonal member is assumed to include the severe diagonal cracks that have widely opened. Because of widely opened diagonal cracks, the compressive strength of concrete shows the softening response as the tensile strain perpendicular to the compressive direction increases. Consequently, it is found that the analytical response in the post-peak is milder than that in the actual brittle behavior.
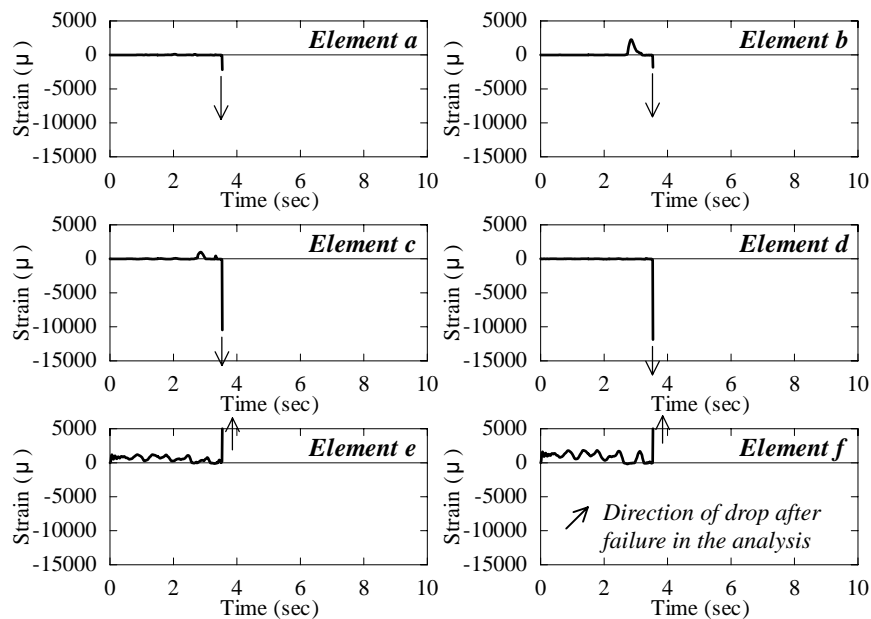
Elements A to C: Flexural members

Element a to f: Diagonal members
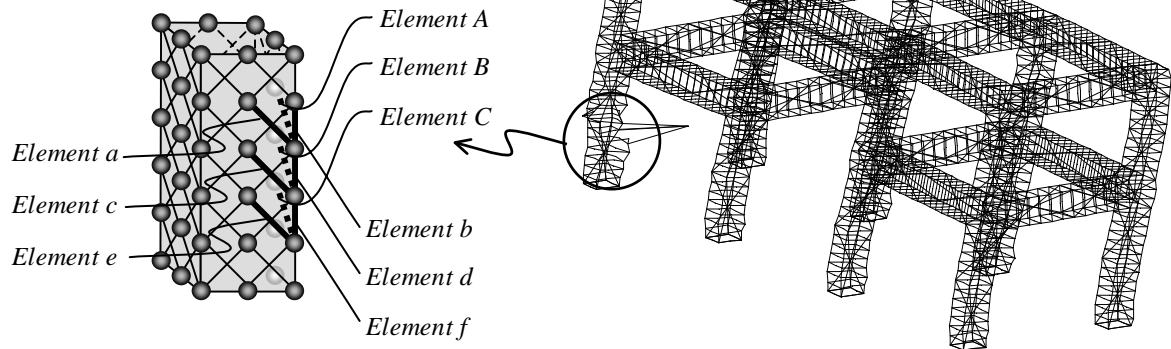
(a) Focused elements of concrete in the 3D dynamic lattice model
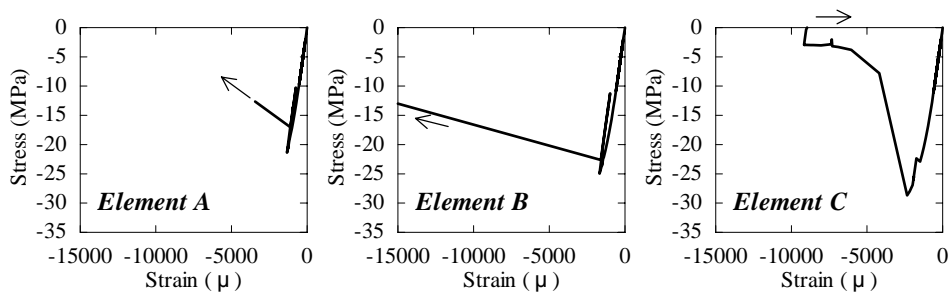
(b) Stress-strain relationships of flexural members of concrete

(c) Stress-strain relationships of diagonal members of concrete

Figure 7.13 Elemental responses of concrete members in the 3D dynamic lattice model for Hansui R5 Viaduct

7.4.3   Influence of vertical loads on seismic response of RC viaducts

In order to investigate the influence of the self-weight on the analytical response of a structure, two analyses with or without the vertical loads are carried out.   In the analysis, the vertical loads correspond to the self-weight of the superstructure and the slab.   **Figures 7.14** to **7.17** show the displacement time histories obtained by the 3D dynamic lattice model analysis with or without vertical loads.

It is found that when the vertical loads are neglected, all analytical results of RC viaducts subjected to the seismic loads show the stable response during 10 seconds.   This stable behavior can be observed even if the analysis considering the vertical loads predicts the shear failure.   Since the additional moment of $P-\Delta$ effect increases as the lateral displacement increases, the analysis neglecting the vertical loads underestimates the lateral displacement. In addition, it is found that the collapse mechanism takes place due to the instability of geometrical nonlinearity, which is associated with comparatively high axial load.

The analysis of RC viaducts shows that the flexural instability occurs with the increase in the vertical loads corresponding to the self-weight and the weight of the superstructure. Therefore, it is recommended that the geometrical nonlinearity as well as the material nonlinearity at the large deformation range should be considered in predicting the allowable ductility of RC columns with heavier weight of a superstructure.

7.4.4   Effect of seismic bilateral loading

The effect of the seismic bilateral loading is verified by comparing the analytical results of RC viaducts subjected to unidirectional and bilateral loadings.   **Figures 7.18** and **7.19** show the displacement time histories at the mid-span of the upper beam in the transverse direction. These are the analytical results of Shimokema R5 Viaduct and Hansui R5 Viaduct with the motion-I.

For Shimokema R5 Viaduct, it can be seen that the maximum analytical displacement in the longitudinal direction obtained by the unidirectional loading is similar to the one by the bilateral loading.   On the other hand, the maximum analytical displacement in the transverse direction obtained in case of the unidirectional loading becomes larger than that in case of the bilateral loading.   In the figure of the displacement trace of particle, it is found that the maximum displacement is larger than that approximated by an ellipse with the maximum displacements obtained from each unidirectional analysis.
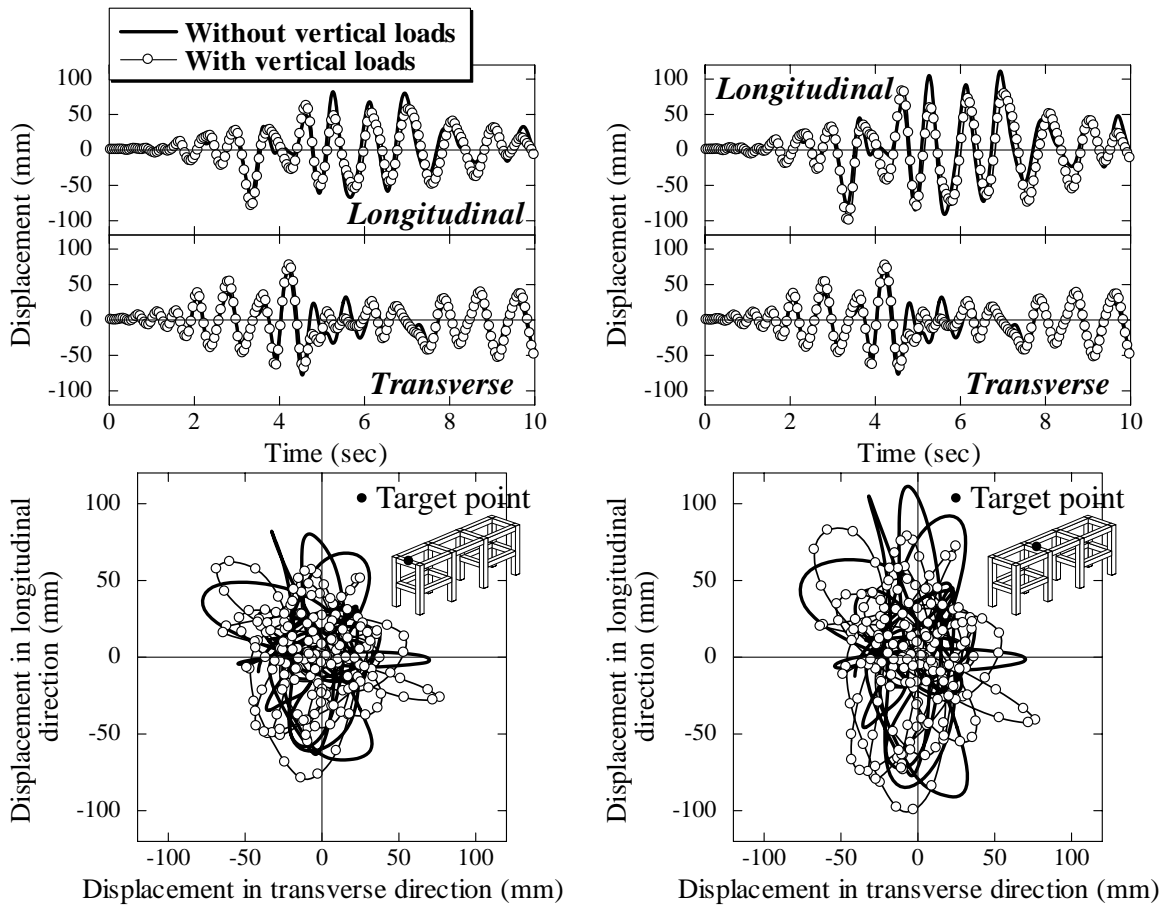
Figure 7.14   Analytical response for Shimokema R5 Viaduct subjected to motion-I
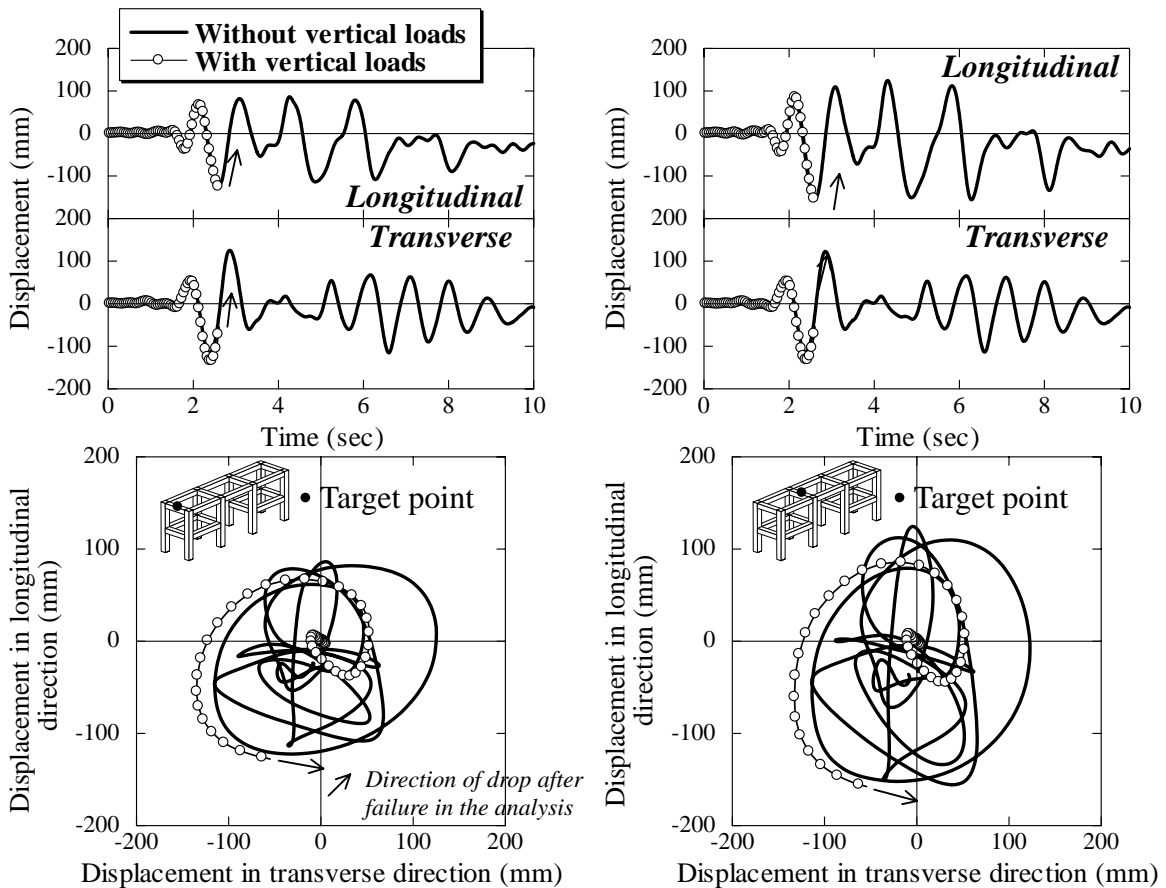
Figure 7.15   Analytical response for Shimokema R5 Viaduct subjected to motion-II
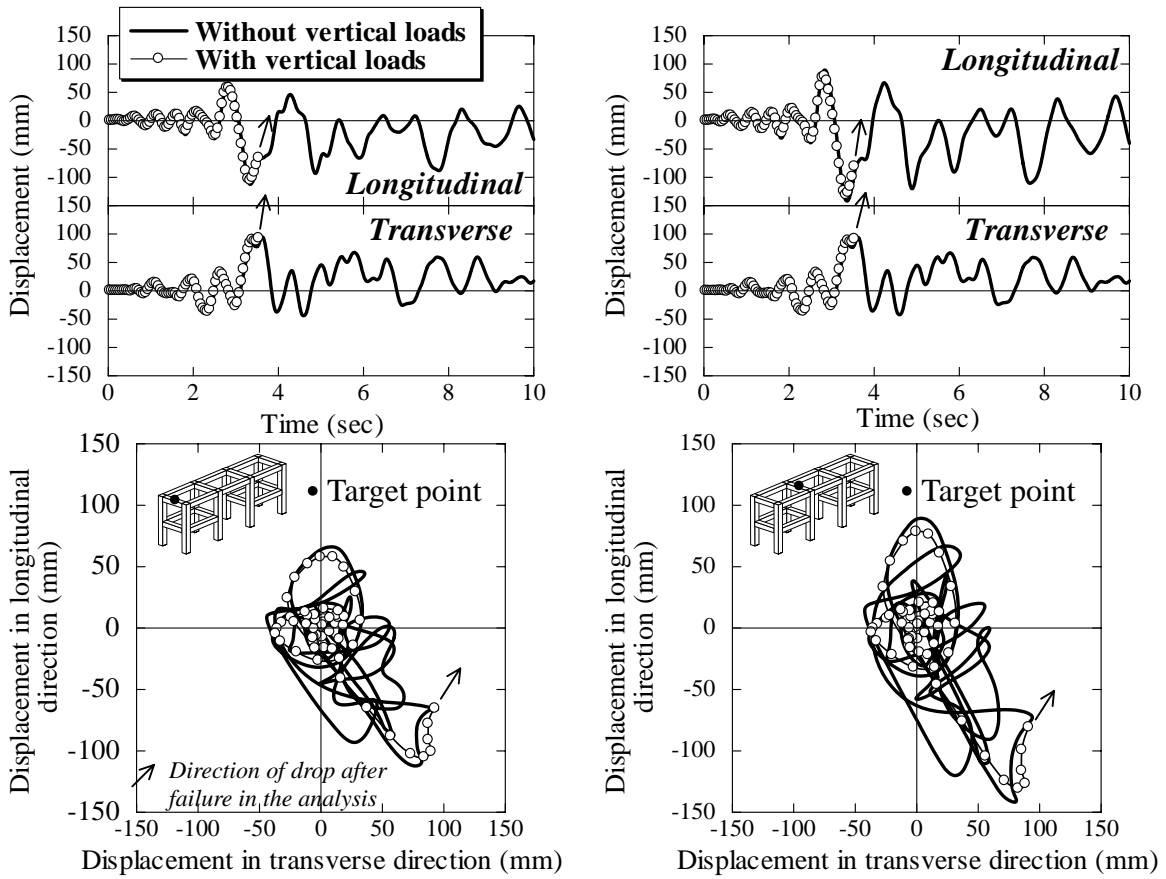
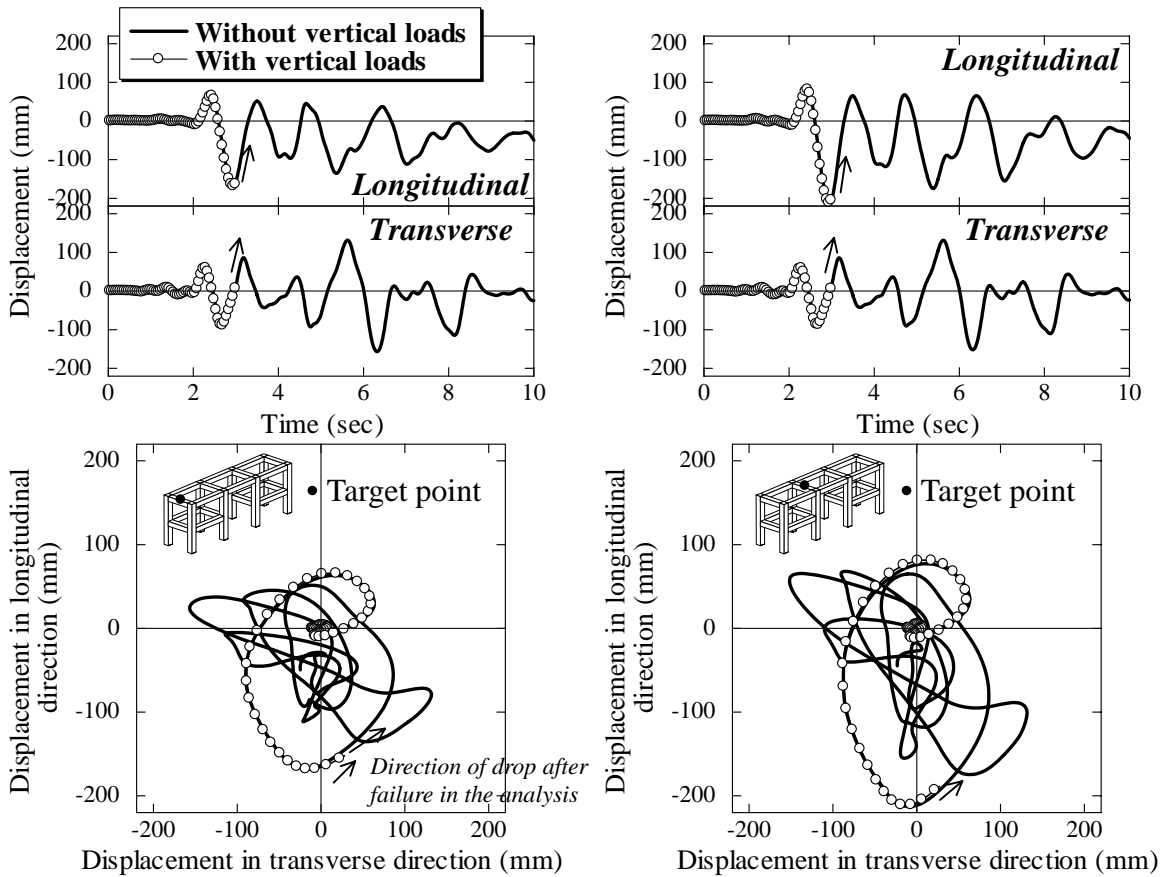**Figure 7.16**   Analytical response for Hansui R5 Viaduct subjected to motion-I

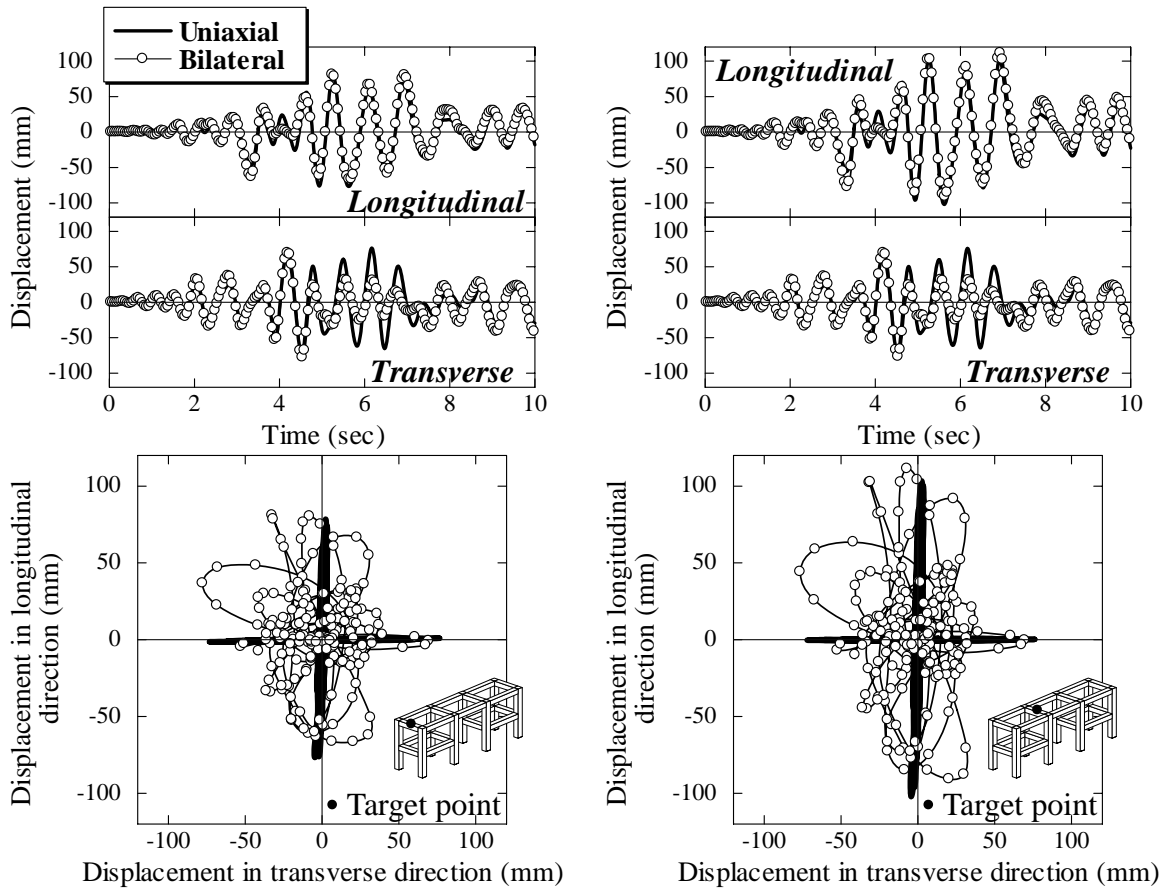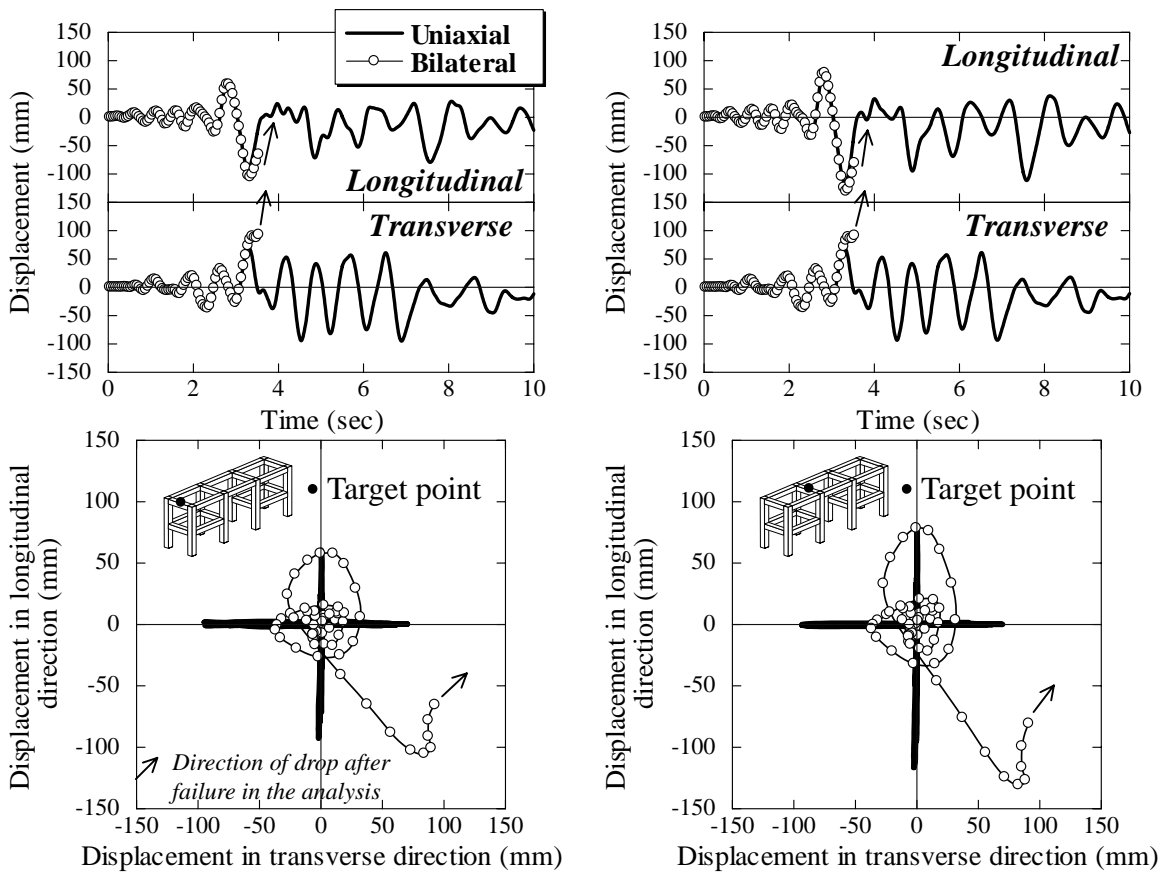**Figure 7.17**   Analytical response for Hansui R5 Viaduct subjected to motion-II

Figure 7.18   Analytical responses for Shimokema R5 Viaduct subjected to motion-I

Figure 7.19   Analytical responses for Hansui R5 Viaduct subjected to motion-I

In Hansui R5 Viaduct, it is found that the maximum displacement increases when the structure is subjected to bilateral loading.   In the analysis with bilateral loading, it is predicted that the lower column fails in shear due to the compression softening of diagonal members of concrete.   Nevertheless, the analytical response in case of the unidirectional loading in longitudinal or transverse direction becomes stable during 10 seconds. Consequently, this behavior cannot be predicted by the 2D analysis conducted independently in longitudinal or transverse direction.   This is caused by that the corner of cross section in the column becomes more severe condition.   In addition, it is found that the maximum displacement of RC viaducts subjected to seismic bilateral loading cannot be predicted from the calculation considering two orthogonal directions separately.

7.5   Seismic Performance Evaluations Using 3D Dynamic Lattice Model

By comparing between the actual damage condition and the analytical response of RC viaducts, the validity of the 3D dynamic lattice model has been confirmed at the structural system level.   The analytical response predicted by the 3D dynamic lattice model is used to evaluate the seismic performance of RC structures.

The maximum displacement during the earthquake and the residual displacement after the earthquake are useful to evaluate the possibility of the restoration or rehabilitation after the earthquake occurs.   In order to evaluate the seismic performance of a RC structure, the predicted response, such as the maximum and residual displacements, ca be compared with the limiting values determined from the importance of target structures.

Since the shear failure of RC structures is not preferable, the evaluation of failure mode including the shear failure and the prediction of shear carrying capacity should be performed appropriately.   As mentioned previously, the shear failure in the lattice model analysis is assumed to take place at a column/beam when the compression softening behavior of concrete in arch or diagonal member is predicted.   This is considered as the shear failure in spite of the decrease in shear stresses that are transferred across inclined cracks.   Because of widely opened diagonal cracks, the compressive strength of concrete decreases as the tensile strain perpendicular to the compressive direction increases.   Therefore, it is important to examine the stress-strain relationships of concrete in arches and diagonal members.

In order to evaluate the damage degree of RC structures quantitatively, it is required to verify whether the buckling behavior of longitudinal reinforcement takes place at the end of structural members.   From the verification at the structural member level, it is found that the

buckling behavior governs the overall response at the large deformation range and that influences the analytical seismic response and the energy dissipation capacity. Therefore, it is important to consider the buckling behavior of longitudinal reinforcement in predicting the seismic response of RC structures. The material models, such as the fracture of longitudinal reinforcements due to the low-cycle fatigue and the stress-strain relationship of concrete subjected to cyclic loading, are required to predict the seismic response with higher accuracy.

7.6 Conclusions

The nonlinear analysis of actual rigid-frame RC viaducts is performed by using the 3D dynamic lattice model. Two analytical targets are selected from actual viaducts damaged during 1995 Hyogo-ken Nanbu Earthquake. The input ground motions at each construction point are determined considering the soil condition and the distance from the epicenter of earthquake. The comparisons between the results of dynamic analysis and the actual damages of RC viaducts reveal the reliability of the 3D lattice model. It is also found that the analysis can predict damage conditions that are including both the buckling behavior of reinforcement in RC columns and their shear failure.

In addition, the dynamic analyses are carried out on the verification with respect to the vertical loading, which represents the self-weight and the weight of a superstructure. The results of the analysis clarify the influence of vertical loads on the maximum displacement in the longitudinal and transverse directions. From the analysis, it is found that when the columns in RC viaducts are subjected to large deformation, the collapse mechanism takes place due to the instability of geometrical nonlinearity. The analysis also shows that this instable behavior due to a high axial load appears when the lateral displacement significantly increases.

Moreover, the analytical simulations are performed for RC viaducts subjected to either unidirectional or bilateral loadings. The results of analysis show that the shear failure cannot be predicted by the 2D simulations analyzed along the longitudinal and transverse directions independently. The analytical results demonstrate that the corner of cross section in the column is deteriorated due to the severe condition under the biaxial loading.

References in Chapter 7

[1]   Editorial Committee for the Report on the Hanshin-Awaji Earthquake Disaster (1996): *Report on the Hanshin-Awaji Earthquake Disaster, Investigation of Causes of Damage to Civil Engineering Structures*, JSCE et al., Maruzen, December.

[2]   Ishibashi, T. and Okamura, H. (1998): Study on the Design Earthquake Resistance and Degree of Earthquake Damage of Reinforced Concrete Viaducts, *Cement and Concrete Composite*, Elsevier, Vol.19, No.3, pp.193-201.

[3]   Ota, T., Tsuchiya, S, and Umehara, H. (2002): Seismic Response Analysis of Railroad Viaducts Damaged by Hyogo-Ken-Nanbu Earthquake, *Proceedings of the JCI*, Vol.24, No.2, pp.1021-1026. (in Japanese)

[4]   Schnabel, P. B., Lysmer, J., and Seed, H. B. (1972): SHAKE A Computer Program for Earthquake Response Analysis of Horizontally Layered Sites, *EERC*, pp.72-12.

[5]   Subcommittee for Damage Analysis of Concrete Structures Caused by Hanshin-Awaji Earthquake (Committee 311) (2000): *Verification of Procedures of Seismic Performance Evaluation based on Damage Analysis for Hanshin-Awaji Earthquake –Examination Issues and Future Plans-*, Concrete Engineering Series No.36, May. (in Japanese)

[6]   Subcommittee for Damage Analysis of Concrete Structures Caused by Hanshin-Awaji Earthquake (Committee 311) (2002): *Verification of Procedures of Seismic Performance Evaluation based on Damage Analysis for Hanshin-Awaji Earthquake –Comparison of Analytical Procedures and its Application–*, Concrete Engineering Series No.49, December. (in Japanese)

[7]   Sugito, M., Goda, H., and Masuda, T. (1994): Frequency Dependent Equi-linearized Technique for Seismic Response Analysis of Multi-layered Ground, *Journal of Geotechnical Engineering*, JSCE, No.493/III-27, pp.49-58, June. (in Japanese)

[8]   Sugito, M., Furumoto, Y., and Sugiyama, T. (2000): Strong Motion Prediction on Rock Surface by Superposed Evolutionary Spectra, *Proceeding of 12th World Conference on Earthquake Engineering*, Auckland, New Zealand, January. (in CD-ROM)

[9]   Tsuchiya, S., Ishii, H., and Umehara, H. (1999): Response Analysis of Reinforced Concrete Rigid-frames in Railroad Viaducts Damaged by Hyogo-ken-Nanbu

Earthquake, *Proceedings of Seminar on Post-peak Behavior of RC Structures Subjected to Seismic Loads*, JCI, Vol.2, pp.245-258, Tokyo, Japan, October.

[10] Tsuchiya, S., Furuya, Y., Kim, I. H., and Okamura, H. (2001): Seismic Performance Evaluation of RC Frames in Railroad Viaducts Using Three-dimensional Nonlinear Dynamic Analysis, *Concrete Library of JSCE*, No.38, pp.105-120, December.

8 GENERAL CONCLUSIONS

The main objective of this study is to develop a 3D nonlinear analytical tool that can evaluate the seismic performance of RC structural members including the post-peak region. The 3D lattice model is proposed and confirmed to be able to predict the cyclic response of RC columns. In the concept of 3D lattice model, the shear resisting mechanism consists of the arch action and the truss action. As for the arch action, the internal stress flow is idealized as the compressive struts. Moreover, as for the truss action, the 3D space comprised of an orthogonal coordinate system is defined by three truss planes. The in-plane 2D constitutive law of concrete considering the softening of compressive stress of concrete is applied.

The essential performance of the lattice model is demonstrated by the verification using 2D lattice model for several types of RC structural members, including columns and beams. The analysis is carried out for three RC columns tested at University of California, San Diego. The verifications show the capability of the 2D static lattice model in predicting the behavior of a RC column that fails in shear. In addition, it is found that the 2D static lattice model provides accurate predictions of the cyclic response of flexural RC columns until the ultimate stage is reached. The comparison of analytical results using 2D dynamic lattice model with results of shaking table tests reveals the applicability of this model for the evaluation of the seismic response of RC columns, including the maximum load and the maximum displacement of the column. However, the analysis using the 2D lattice models is unable to fully predict the post-peak response of RC columns.

From the experimental observations, the necessity to take the buckling behavior of longitudinal reinforcement into consideration is confirmed when the prediction of post-peak response is required. As expected, the significant improvement in predicting the post-peak response can be achieved by the analysis considering the buckling behavior of reinforcement. In the model, the spatially averaged stress-strain model of reinforcement is considered. It is found that the lattice model analysis considering the buckling of longitudinal reinforcement can reliably predict the post-peak response and the energy dissipation capacity of RC columns with sufficient accuracy.

The accuracy of prediction is also improved by considering the pull-out behavior of longitudinal reinforcement at the column-footing connection by the joint element modeling the steel strain-slip relationship. The pull-out behavior of longitudinal reinforcement influences the stiffness and the energy dissipation capacity. The consideration of the pull-out behavior of reinforcement makes analytical results to be close to the experimental results, and consequently, the accuracy is improved.

The simulation of RC columns with different amount of transverse reinforcement clarifies that the maximum base shear force rises with the increase in the amount of transverse reinforcement. On the other hand, it is found that the transverse reinforcement ratio have significant influence on the maximum displacement within the range of amount of the transverse reinforcement studied here. Taking the energy absorption in the individual elements into account, the distribution of energy dissipated in a RC column can be accurately evaluated using the 2D dynamic lattice model. Moreover, it is confirmed that the damage zone in a RC column during an earthquake can be quantitatively predicted by evaluating the distribution of energy dissipation.

The configurations of 3D static lattice model based on the 2D modeling concept are verified for RC columns on unidirectional cyclic loading tests. It is confirmed that the comparison between 2D and 3D lattice model analyses is fairly close to each other in terms of the overall behavior of RC columns. Moreover, from the comparison between experimental and analytical results, it is found that 3D lattice model analysis can accurately predict the overall behavior of RC columns including the post-peak behavior with the same accuracy as 2D analysis.

In order to apply to the arbitrary loading condition, the 3D static lattice model is verified for the experimental results of RC columns subjected to lateral forces from diagonal directions of a section. The comparison between the experimental and analytical results shows that the 3D lattice model analysis can predict successfully the behavior of RC columns under bilateral loading. In addition, the analysis can explain the influence of loading direction on the cyclic behavior of RC columns quantitatively. In the analysis, the severe deterioration in terms of the strain in each element is predicted. However, the divergence of analytical results from experimental results is observed at large deformation range because of the fracture of longitudinal reinforcing bars due to the low-cycle fatigue.

The analyses by 3D static lattice model are also carried out for RC beams with solid and hollow sections subjected to pure torsion and the applicability of the analysis to the prediction of torsional behavior is confirmed. In the pre-analysis, it is found that the ratio of arch part

to the cross-sectional width of a RC beam increased with the increase in reinforcement.   It is found that the torsional analysis by 3D lattice model with appropriate values of t_b and t_d can predict reasonable torque-twist relationships of solid sectional RC beams.   The failure mode of torsional RC beams with various amount of reinforcement is also predicted.   Moreover, the analytical simulation of hollow sectional RC columns subjected to combined cyclic loading of torsion and bending is carried out.   It is confirmed that the 3D lattice model analysis can appropriately predict the 3D response of RC columns subjected to the combined cyclic loads of torsion and bending.   The simulation reveals the effect of combination of torsional and flexural deformation on the load carrying capacity and the deformation capacity.

The results of 3D dynamic lattice model analysis prove that reasonable seismic behavior of RC columns subjected to bilateral ground motion can be estimated.   It is found that the analysis considering the buckling behavior of longitudinal reinforcement can predict the post-peak response as well as the energy dissipation capacity of RC columns with sufficient accuracy.   The seismic performance verification is also performed based on several actual earthquake motions.   The analytical results show that the maximum and residual displacements are not necessarily determined from the amplitude of input ground motion, but influenced by the characteristics of frequency, duration, and phase of the ground motion.   In addition, it is found that the analysis considering the buckling of reinforcement can predict the seismic response and cyclic loops of RC columns.   It also proves the reliability of the 3D lattice model in the prediction of the seismic response of RC structural members including columns and beams.

The nonlinear analysis using the 3D dynamic lattice model is performed on actual RC structures.   The targets used in the analysis are two actual rigid-frame RC viaducts damaged at 1995 Hyogo-ken Nanbu Earthquake.   One of these viaducts has slight damage with diagonal cracks and the buckling of longitudinal reinforcement.   Another has the severe shear failure with the collapse of a column.   The input ground motions for each viaduct are determined by the program of FDEL.   The results of dynamic analysis are compared with actual damages of RC viaducts.   The comparison reveals the reliability of the 3D dynamic lattice model at the structural system level.   It is also found that the analysis can predict the damage conditions including both the buckling behavior of the end of columns and the shear failure of columns.   In addition, the dynamic analyses are carried out on the verification with respect to the vertical loads.   The vertical loads in the analysis correspond to the self-weight and the weight of a superstructure.   The results of dynamic analysis clarify the influence of vertical loads on the maximum displacement and the instable behavior.   Finally, the analytical simulation is performed for RC viaducts subjected to either unidirectional or bilateral loadings.   The comparison between the results of these two analyses shows that the

shear failure cannot be predicted by the 2D simulation along longitudinal and transverse directions separately. Through the analytical investigations, it can be confirmed that newly developed analytical method using the 3D lattice model provides the appropriate evaluation of damaged RC structures subjected to severe seismic loads.